



**HAL**  
open science

# Mono- and bimetallic nanoparticles stabilized by functionalized ionic liquids: synthesis and catalytic applications

Deepthy Krishnan

► **To cite this version:**

Deepthy Krishnan. Mono- and bimetallic nanoparticles stabilized by functionalized ionic liquids: synthesis and catalytic applications. Coordination chemistry. Université Paul Sabatier - Toulouse III; Danmarks pædagogiske universitet, 2023. English. NNT: 2023TOU30270 . tel-04552707

**HAL Id: tel-04552707**

**<https://theses.hal.science/tel-04552707>**

Submitted on 19 Apr 2024

**HAL** is a multi-disciplinary open access archive for the deposit and dissemination of scientific research documents, whether they are published or not. The documents may come from teaching and research institutions in France or abroad, or from public or private research centers.

L'archive ouverte pluridisciplinaire **HAL**, est destinée au dépôt et à la diffusion de documents scientifiques de niveau recherche, publiés ou non, émanant des établissements d'enseignement et de recherche français ou étrangers, des laboratoires publics ou privés.



# THÈSE



**En vue de l'obtention du  
DOCTORAT DE L'UNIVERSITÉ DE TOULOUSE**

**Délivré par l'Université Toulouse 3 - Paul Sabatier**

**Cotutelle internationale: Université technique du Danemark**

**Présentée et soutenue par  
Deepthy KRISHNAN**

Le 28 novembre 2023

**Nanoparticules mono- et bimétallique stabilisées par des liquides  
ioniques fonctionnalisés: synthèse et application en catalyse**

Ecole doctorale : **SDM - SCIENCES DE LA MATIERE - Toulouse**

Spécialité : **Chimie Organométallique et de Coordination**

Unité de recherche :

**LCC - Laboratoire de Chimie de Coordination**

Thèse dirigée par

**Karine PHILIPPOT, Anders RIISAGER et Rosa AXET MARTI**

Jury

**M. Jairton DUPONT, Rapporteur**

**Mme Karine DE OLIVEIRA VIGIER, Rapporteur**

**M. Jens Øllgaard Duus, Examineur**

**M. Eric MANOURY, Examineur**

**Mme Karine PHILIPPOT, Directrice de thèse**

**M. Anders RIISAGER, Directeur de thèse**



# Mono- and bimetallic nanoparticles stabilized by functionalized ionic liquids: synthesis and catalytic applications

**PhD Thesis**  
September 2023

**Author**  
Deepthy Krishnan

**Supervisors**  
Prof. Anders Riisager  
Dr. Karine Philippot  
Dr. M. Rosa Axet

**Co-supervisor**  
Prof. Søren Kegsnæs





---

*Dedicated to Achan and Amma*



## Preface

This PhD thesis is performed as part of the Marie Skłodowska-Curie Innovative Training Network European Joint Doctorate (ITN-EJD) program “Coordination Chemistry Inspires Molecular Catalysis” (CCIMC). The work was conducted in the period October 2020-September 2023 in a collaborative project between two institutes, the Centre for Catalysis and Sustainable Chemistry, Department of Chemistry, Technical University of Denmark (DTU), Denmark, under the supervision of Prof. Anders Riisager and the Engineering of Metal Nanoparticles group at the Laboratoire de chimie de coordination (LCC), CNRS Toulouse, France, under the supervision of Dr. Karine Philippot and Dr. M. Rosa Axet. The industrial partner in the collaboration was IFP *Energies Nouvelles* (IFPEN), Solaize, France, where a three-month internship has been performed. The PhD thesis focuses on the synthesis of monometallic Ru and Ni as well as bimetallic RuRe nanoparticles (NPs) in carefully functionalized ionic liquids (FILs) to obtain metal NP/FILs catalytic systems. The systems have been applied in hydrogenation catalysis, where the structure-activity relationship has been explored. [Chapter 1](#) provides an overview of the thesis by introducing and summarizing the main topics involved including synthesis, characterization, and application of ILs and metal NPs in ILs. It also describes the aims and objectives of the PhD project. [Chapter 2](#) deals with the synthesis of ILs incorporating specific functional groups chosen for their ability to stabilize and alter the surface characteristics of the NPs. [Chapter 3](#) is devoted to the employment of these ILs for the synthesis of Ru NPs and study of the structure-stability relation of the systems as well as reactivity and selectivity patterns in hydrogenation catalysis. The obtained results have been published in *Nanomaterials*, 2023, 13:1459. [Chapter 4](#) concerns the synthesis of Ni NPs in the tailored FILs. The reactivity of the Ni NPs and the impact of their oxidation have been studied through application in hydrogenation catalysis. Given that bimetallic metal NPs can show better catalytic performance than monometallic NPs due to a ‘synergistic effect’ of the two metals, an appropriate combination of desired metals can tune the reactivity of the catalyst. In [Chapter 5](#), efforts have been made to utilize this concept to synthesize RuRe/FILs catalyst suitable for amide hydrogenation, relying on the known H<sub>2</sub> activating property of Ru NPs with the capability of oxophilic Re to activate carbonyl groups. [Chapter 6](#) closes the PhD thesis with main conclusions and perspectives of the work. [Chapter 7](#) provides the materials and characterization methods used.



## Acknowledgement

First and foremost, I extend my sincere gratitude to Prof. Jairton Dupont, Prof. Karine De Oliveira Vigier, Prof. Jens Øllgaard Duus and Dr. Eric Manoury for accepting to be the jury members for my PhD thesis.

As it is said "Words, though powerful, are but feeble vessels to contain the depth of emotions."

I would like to thank my supervisors, Prof. Anders Riisager, Dr. Karine Philippot and Dr. M. Rosa Axet for their constant encouragement and valuable scientific guidance throughout my PhD studies. Their availability despite their busy schedule has been of tremendous support. I thank Anders for all the support he has provided me and for cheering me up during my most challenging moments. Thank you for being an inspiration to me. I am immensely grateful to Karine for the care, affection, and motivation she has shown me from the very first day we met. Thank you for the guidance you have provided me both professionally and personally. Your emails ending with "Bon courage pour tout" have always encouraged me to do my best even when I felt low. You are like family to me. I would like to express my heartfelt thanks to Rosa who has always been one phone call away. Thank you for helping me out and making me realize my potential both in science and in knitting. Thank you for teaching me to be bold and enjoy my PhD studies. I would also like to thank, Prof. Søren Kegnæs, for being my co-supervisor and for all the friendly games we had during the group events.

I would like to thank Dr. Lionel Magna for giving me an opportunity to undertake my internship at *IFP Energies nouvelles (IFPEN)*. Thank you for the scientific advice and guidance you have provided during my stay, through which I was able to gain experience in the industrial sector. A special thanks for helping me out with all the related French administrative procedures and being very kind.

Next, I would like to especially thank Dr. Katerina Soulantica, who provided me with an opportunity that became a turning-point in my life. She has consistently offered her support, provided valuable advice, and expressed genuine interest in my well-being. I express my gratitude to Assoc. Prof. Susmita De and Prof. Girish Kumar for their support and encouragement that inspired me to undertake my master thesis in Europe.

## Acknowledgement

---

I would like to thank all the DTU staff for both technical and administrative assistance. Special thanks to Ishaq for his quick help with all practical issues especially in the autoclave room. Thanks to Jette, Monica, Mariusz, Stephan, Bodil, Charlie, Joanne, Betina, Atli, John and all other for all the help I have received at DTU during the period. I express my gratitude to all scientific and non-scientific staffs for their support.

I have been lucky to have not one but two wonderful groups with lovely members. I thank Betsy, Sakhitha, Mahtab, Li, Wenting, Pablo, Astrid, Leo and Chantal for their help and presence. Thank you for making the AR-group fun and amazing. Special thanks to Leo for helping me out with all the XPS analyses. I would equally like to thank Equipe L, Engineering of metal nanoparticles members, Nuria, Tatiana, Lola, Miquel, François, Emmanuel, Azadeh, Dr. Catherine Amiens, Dr. Alain Igau and Dr. Pierre Sutra for their support and help. I would like to specially thank Vincent Collière for helping me with the TEM analysis and treating me very kindly. I thank all the staff in the different technical services at LCC for their help. Special thanks to Alida and Prof. Rinaldo Poli for helping me with all CCIMC work and administrative procedures. I thank all the 14 ESRs in CCIMC - Aswin, Paven, Agustín, Sara, Massimo, Max, Anastasiia, Joel, Joris, Zinnia, Pawel, Irina, Wimonsiri and Chantal for the experience and culture insights I have received from them during each CCIMC conference and otherwise. Heartfelt thanks to the academic board committee, CCIMC for valuable correction and evaluation of the reports and presentations. The project leading to this application has received funding from the European Union's Horizon 2020 research and innovation programme under the Marie Skłodowska-Curie grant agreement No 860322. It is said 'No thanks needed between true friends, but gratitude finds its way', I would like to thank my best friend Anjali for being my backbone. I would like to thank Aswin for his constant support and endless encouragement each time my reaction fails. Thanks to Ajay, Meenu for treating me as family. I also thank my friends Anand and Tiago for the good company. Last but not least, I express my love and gratitude to my parents who believed in me and supported me throughout my endeavor, without their constant support, care, and advice nothing will be possible.

Thank you All.



Deepthy Krishnan

## Abstract

Metal nanoparticles (NPs) are recognized attractive materials for application in the field of catalysis due to their remarkable high surface-to-volume ratio that induces a high number of potential active sites. It is well known that stabilizers play an important role in synthesis and catalytic performance of metal NPs. They protect the NPs structure, thereby preventing agglomeration or aggregation that may occur due their high surface energy. Additionally, stabilizers can influence the electronic properties of the NPs, optimizing their reactivity and selectivity in catalytic reactions. Thus, appropriate selection and utilization of stabilizers are crucial factors for modifying and enhancing the performance of NPs across a diverse range of catalytic reactions including hydrogenation of various substrates. Among all possible stabilizers for metal NPs, ionic liquids (ILs) can be employed for the synthesis of metal NPs. ILs possesses intriguing physical and chemical properties and presents the advantage to act both as stabilizer and solvent in the reaction, resulting in reduced utilization of chemicals and limit waste, which limits the environmental footprint. Careful tailoring of imidazolium based ILs with functional groups has proven a relevant way to improve catalytic performance of metal NPs. In this context, a series of Ru NPs and Ni NPs were synthesized by the organometallic approach in functionalized imidazolium ionic liquids (FILs) with methoxy- and cyano-groups (abbreviated as MEM, MME and CN). Well-dispersed and narrow-sized Ru NPs ranging from 1.3 to 2.2 nm were obtained as well as Ni NPs ranging between 2.8 and 6.9 nm depending on the IL functionalization. Thermal gravimetric analysis (TGA) and X-ray photoelectron spectroscopy (XPS) allowed to study the interaction between the NPs and the ILs. Ru NPs stabilized by the methoxy-containing FILs (MEM and MME) displayed a good balance between catalytic activity and stability when applied in the hydrogenation of styrene at mild reaction conditions. Moreover, the Ru/FILs showed complete selectivity towards ethylbenzene at milder reaction conditions (5 bar, 30 °C) than reported in literature for other Ru NP catalysts. All the Ni/ILs systems were found to be efficient catalysts for the hydrogenation of 2-cyclohexene-1-one under the applied reaction conditions (substrate/Ni ratio of 100/1, 130 °C, 10 bar H<sub>2</sub>), providing full substrate conversion and complete selectivity towards hydrogenation of the olefinic bond in short reaction time (1 h). Bimetallic RuRe NPs were also synthesized with an average size of 1.6 and 3.3 nm in unfunctionalized (H) and MEM ILs, respectively, but neither of the systems catalyzed the hydrogenation of amides, which is reputed

as a challenging reaction due to the high stability of amides. In summary, the PhD work led to the synthesis of novel Ru, Ni and RuRe bimetallic NPs in MEM and MME ILs, and insights into structure-performance relations in hydrogenation catalysis. The work provides perspectives for future development within both the fields of nanochemistry and selective catalysis.



---

## Resumé

Metal nanopartikler (MNP'er) er attraktive materialer til anvendelse inden for katalyse på grund af deres bemærkelsesværdige høje overflade-til-volumen forhold, som giver et stort antal potentielle aktive steder. Det er velkendt, at stabilisatorer spiller en vigtig rolle i syntese og katalytisk ydeevne af MNP'er, da de beskytter NP-strukturen og forhindrer agglomering eller sammenklumpning, som ellers kan forekomme på grund af deres høje overfladeenergi. Derudover kan stabilisatorer påvirke de elektroniske egenskaber af NP'erne og påvirke deres reaktivitet og selektivitet i katalytiske reaktioner. Derfor er korrekt valg og anvendelse af stabilisatorer afgørende faktorer for at modificere og forbedre NP'ernes præstation på tværs af en bred vifte af katalytiske reaktioner, herunder hydrogenering af forskellige substrater. Ioniske væsker (IL'er) kan med fordel anvendes som stabilisatorer til syntese af MNP'er. Ud over at IL'er besidder særlige fysiske og kemiske egenskaber har de den fordel, at fungere både som stabilisator og opløsningsmiddel i reaktionen, hvilket på grund af reduceret brug af kemikalier og affaldsdannelse fører til mindre miljøpåvirkning. Omhyggelig tilpasning af imidazolium-baserede IL'er med funktionelle grupper har vist sig at være en relevant måde at forbedre MNP'ers katalytiske ydeevne på. I denne sammenhæng er der i nærværende projekt syntetiseret en serie af RuNP'er og NiNP'er ved en organometallisk metode i funktionelle imidazolium-ioniske væsker (FIL'er) med methoxy- og cyano-grupper (forkortet som MEM, MME og CN). Veldispergerede RuNP'er med størrelsen 1,3-2,2 nm med smal størrelsesfordeling, samt NiNP'er med størrelser mellem 2,8-6,9 nm blev opnået afhængigt af IL-funktionaliseringen. Termogravimetrisk analyse (TGA) og røntgenfotoelektron spektroskopi (XPS) gjorde det muligt at studere interaktionen mellem NP'er og IL'er. RuNP'er stabiliseret af de methoxy-baserede FIL'er (MEM og MME) udviste en god balance mellem katalytisk aktivitet og stabilitet, når de blev anvendt i hydrogeneringen af styren under milde reaktionsbetingelser. Derudover viste Ru/IL'erne fuldstændig selektivitet over for dannelse af ethylbenzen under reaktionsbetingelser (5 bar H<sub>2</sub>, 30 °C), der var mildere end rapporteret i litteraturen for andre RuNP-katalysatorer. Alle Ni/IL-systemer viste sig at være effektive katalysatorer til hydrogenering af 2-cyclohexe-1-non under de anvendte reaktionsbetingelser (substrat/Ni-forhold på 100/1, 130 °C, 10 bar H<sub>2</sub>), hvilket gav fuld omdannelse af substratet og fuldstændig selektivitet over for hydrogenering af olefinbindingen på kort reaktionstid (1 time). Bimetalliske RuReNP'er blev også syntetiseret med en gennemsnitlig størrelse på 1,6 og 3,3 nm i

ikke-funktionaliserede (H) og MEM IL'er, men ingen af systemerne katalyserede hydrogenering af amider, hvilket er kendt som en udfordrende reaktion på grund af amiders høje stabilitet. Samlet set førte ph.d.-arbejdet til syntese af nye Ru-, Ni- og RuRe-bimetalliske NP'er i MEM og MME IL'er og indsigt i struktur-præstationsevne i hydrogeneringskatalyse. Arbejdet giver perspektiver for fremtidig udvikling inden for både nanokemi og selektiv katalyse.

## Résumé

Les nanoparticules métalliques (NPMs) sont des matériaux attractifs reconnus pour leur application dans le domaine de la catalyse en raison de leur remarquable rapport surface-volume élevé induisant un grand nombre de sites actifs potentiels. Il est bien connu que les stabilisateurs jouent un rôle important dans la synthèse et la performance catalytique des NPMs. Ils protègent la structure des NP, prévenant ainsi leur agglomération ou agrégation qui peut survenir en raison de leur énergie de surface élevée. De plus, les stabilisateurs peuvent influencer les propriétés électroniques des NP, optimisant leur réactivité et leur sélectivité dans les réactions catalytiques. Ainsi, le choix approprié et l'utilisation des stabilisateurs sont des facteurs cruciaux pour modifier et améliorer la performance des NP dans une large gamme de réactions catalytiques, y compris l'hydrogénation de divers substrats. Parmi tous les stabilisateurs possibles pour les NPMs, les liquides ioniques (LI) peuvent être utilisés pour la synthèse des NPMs. Les LI possèdent des propriétés physiques et chimiques intrigantes et présentent l'avantage d'agir à la fois comme stabilisateur et solvant dans la réaction, entraînant une utilisation réduite de produits chimiques et limitant les déchets, ce qui réduit l'empreinte environnementale. L'ajustement soigneux des LI à base d'imidazolium avec des groupes fonctionnels s'est avéré être une manière pertinente d'améliorer la performance catalytique des NPMs. Dans ce contexte, une série de NPMs de Ru et de Ni a été synthétisée par l'approche organométallique dans des liquides ioniques d'imidazolium fonctionnalisés (LIF) avec des groupes méthoxy- et cyano- (abrévés en MEM, MME et CN). Des RuNPs bien dispersées et de taille étroite, variant de 1,3 à 2,2 nm, ont été obtenues ainsi que des NiNPs variant de 2,8 à 6,9 nm en fonction de la fonctionnalisation des LI. L'analyse thermogravimétrique (TGA) et la spectroscopie photoélectronique à rayons X (XPS) ont permis d'étudier l'interaction entre les NP et les LI. Les RuNPs stabilisées par les LIF contenant du méthoxy (MEM et MME) ont montré un bon équilibre entre l'activité catalytique et la stabilité lorsqu'elles ont été appliquées dans l'hydrogénation du styrène à des conditions de réaction douces. De plus, les Ru/LIF ont montré une sélectivité complète envers l'éthylbenzène à des conditions de réaction plus douces (5 bar, 30 °C) que celles rapportées dans la littérature pour d'autres catalyseurs RuNP. Tous les systèmes Ni/LI se sont avérés être des catalyseurs efficaces pour l'hydrogénation du 2-cyclohexé-1-none dans les conditions de réaction appliquées (rapport substrat/Ni de 100/1,

130 °C, 10 bar H<sub>2</sub>), fournissant une conversion complète du substrat et une sélectivité complète envers l'hydrogénation de la liaison oléfinique en un court laps de temps de réaction (1 h). Des RuReNPs bimétalliques ont également été synthétisées avec une taille moyenne de 1,6 et 3,3 nm dans des LI non fonctionnalisés (H) et MEM, respectivement, mais aucun des systèmes n'a catalysé l'hydrogénation des amides, réputée être une réaction difficile en raison de la haute stabilité des amides. En résumé, le travail de thèse a conduit à la synthèse de nouvelles NPMs Ru, Ni et RuRe dans des LI MEM et MME, ainsi qu'à des perspectives sur les relations entre structure et performance en catalyse d'hydrogénation. Ce travail ouvre des perspectives pour le développement futur dans les domaines de la nanochimie et de la catalyse sélective.

## List of abbreviations

ATR-IR: attenuated total reflection infrared spectroscopy  
AMMIm: 1-(3-aminopropyl)-2,3-dimethylimidazolium  
BF<sub>4</sub>: tetrafluoroborate  
BmIm: 1-butyl-3-methylimidazolium  
BBIm: 1,3-dibutylimidazolium  
BMMIm: 1-butyl-2,3-dimethylimidazolium  
C<sub>2</sub>OHMIm : 1-ethylhydroxyl-3-methylimidazolium  
CAL: cinnamaldehyde  
CBILS®: carbonate based ionic liquid synthesis  
CDCl<sub>3</sub>: deuterated chloroform  
CNT: carbon nanotubes  
COL: cinnamyl alcohol  
COA: cyclooctane  
COD: 1,5-cyclooctadiene  
COT: 1,3,5-cyclooctatriene  
CYD: 1,3-cyclohexadiene  
CYE: cyclohexene  
CYA: cyclohexane  
CYA: 1,3-cyclohexane  
CYD: 1,3-cyclohexadiene  
CYE: 1,3-cyclohexene  
DAMI: 1,3-di(N,N-dimethylaminoethyl)-2-methylimidazolium  
DCM: dichloromethane  
DFT: density functional theory  
DLS: dynamic light scattering  
DMSO-d<sub>6</sub>: deuterated dimethyl sulfoxide  
DTBB: 4,4'-di-tert-butylbiphenyl  
EA: elemental analysis  
ECH: ethylcyclohexane  
EB: ethylbenzene  
EMIm: 1-ethyl-3-methylimidazolium  
EXAFS: X-ray absorption fine structure  
FCC: face-centred cubic  
FWHM: full-width-at-half-maximum  
GC: gas chromatography  
H: 1-hexyl-3-methyl imidazolium bis(trifluoromethanesulfonyl)imide  
H<sub>2</sub>: hydrogen  
HAD: hexadecylamine

HCAL: hydrocinnamaldehyde  
HCOL: hydrocinnamyl alcohol  
HCP: hexagonal close-packed  
HMI<sub>m</sub>: 1-hexyl-3-methylimidazolium  
HRTEM: high resolution transmission electron microscopy  
ICP-MS: inductively coupled plasma-mass spectrometry  
ICP-OES: inductively coupled plasma - optical emission spectroscopy  
IL: Ionic liquid  
LCC: Laboratoire de Chimie de Coordination  
MEM: 1-methoxyethoxymethyl-3-methyl imidazolium bis(trifluoromethanesulfonyl)imide)  
MME: 1-methoxymethoxyethyl-3-methyl imidazolium bis(trifluoromethanesulfonyl)imide)  
MNP: metal nanoparticle  
MOc<sub>3</sub>N: methyltrioctylammonium  
NHC: N-heterocyclic carbenes  
[Ni(COD)<sub>2</sub>]: bis(1,5-cyclooctadiene)nickel(0)  
NMR: nuclear magnetic resonance  
NTf<sub>2</sub>: bis(trifluoromethanesulfonyl)imide  
OMI<sub>m</sub>: 1-octyl-3-methylimidazolium  
PEG: polyethylene glycol  
PA: phenylacetylene  
RTILs: room temperature ionic liquids  
PF<sub>6</sub>: hexafluorophosphate  
[Ru(COD)(2-methylallyl)<sub>2</sub>]: (2-methylallyl)(1,5-cyclooctadiene)ruthenium(0)  
[Ru(COD)(COT)]: (1,5-cyclooctadiene)(1,3,5-cyclooctatriene)ruthenium(0)  
[Re<sub>2</sub>(CO)<sub>10</sub>]: dirhenium decacarbonyl  
SAXS: small angle X-ray scattering  
S: styrene  
SILP: supported ionic liquid phase  
STEM: scanning transmission electron microscopy  
TGA: thermogravimetric analysis  
TEM: transmission electron microscopy  
THF: tetrahydrofuran  
TMGL: 1,1,3,3-tetramethylguanidine lactate  
TOF: turnover frequency  
TSIL: task-specific ionic liquids  
UHV: ultra-high vacuum  
UV-vis - ultraviolet-visible spectroscopy  
VOCs: volatile organic compounds  
WAXS: wide angle X-ray scattering  
XPS: X-ray photoelectron spectroscopy

---

## Table of content

Preface

Acknowledgement

Abstract

Resumé (*Danish*)

Résumé (*French*)

List of abbreviations

Chapter 1. Introduction.....	1
1.1 Ionic liquids.....	1
1.2 Metal nanoparticles.....	22
1.3 Objectives and outlook.....	40
1.4 Summary.....	41
1.5 References.....	41
Chapter 2. Synthesis and characterization of imidazolium ionic liquids.....	54
2.1 Introduction.....	54
2.2 Experimental section.....	57
2.3 Results and discussions.....	59
2.4 Summary.....	74
2.5 References.....	75
Chapter 3. Synthesis, characterization, and application in catalysis of ruthenium nanoparticles in functionalized ionic liquids.....	79
3.1 Introduction.....	79
3.2 Experimental section.....	82
3.3 Results and discussions.....	83
3.4 Summary.....	105
3.5 References.....	106
Chapter 4. Synthesis, characterization, and catalytic application of nickel- and nickel oxide nanoparticles in functionalized ionic liquids.....	109
4.1 Introduction.....	109
4.2 Experimental section.....	112
4.3 Results and discussions.....	113
4.4 Summary.....	142
4.5 References.....	143

## Table of content

---

Chapter 5.	Synthesis and characterization of ruthenium-rhenium nanoparticles in ionic liquids.....	147
5.1	Introduction.....	147
5.2	Experimental section.....	149
5.3	Results and discussions.....	149
5.4	Summary.....	163
5.5	References.....	163
Chapter 6.	General conclusion and perspectives.....	165
Chapter 7.	Materials and characterization methods.....	170
Appendix A.	List of publications and conferences.....	173
Appendix B.	Supplementary information for Chapter 2.....	175
Appendix C.	Supplementary information for Chapter 3.....	179
Appendix D.	Supplementary information for Chapter 4.....	187
Appendix E.	Supplementary information for Chapter 5.....	194



## 1. Introduction

This bibliographic chapter will provide general information on ionic liquids (**section 1**) and metal nanoparticles (**section 2**). After giving the definition of these two types of species, main synthesis methods as well as main physico-chemical properties and usages will be presented and illustrated by relevant examples from literature linked with the objectives of this PhD project.

### 1.1 Ionic liquids

The most practical definition of an ionic liquid (IL) is ‘a liquid composed entirely of ions’ [1]. There are diverse salts which are liquids at ambient temperature. ILs that are liquid at room temperature are called room temperature ionic liquids (RTILs). Most ILs are composed of a large organic cation of low symmetry, and a much smaller inorganic polyatomic anion with the charge highly delocalized. The liquid state is favored by small lattice enthalpy and large entropy changes, attributed to the large size and conformational flexibility of the two weakly coordinating ions [2]. While the structural arrangement of IL resembles that of a salt, the main difference is that the coulombic interactions between the ions in a salt is much stronger than in ILs as the result of the similarity between the size and nature of the ions, giving them a strong crystalline structure with relative high melting point, *e.g.* is the melting point of NaCl (s) 801 °C [3]. ILs exhibit notably distinct physical characteristics which includes negligible vapor pressure, high charge density, high polarity, high dielectric constant and capability to form supramolecular networks [4]. These properties can be designed through combination of various cations and anions as presented hereafter.

#### 1.1.1 Cation

The cationic center of an IL involves typically a positively charged nitrogen, phosphorus or sulfur atom. Those described thus far involve mainly ammonium, sulphonium, imidazolium, pyridinium, pyrrolidinium, phosphonium, oxazolium, *etc.* cations substituted with alkyl chains (**Figure 1.1**).

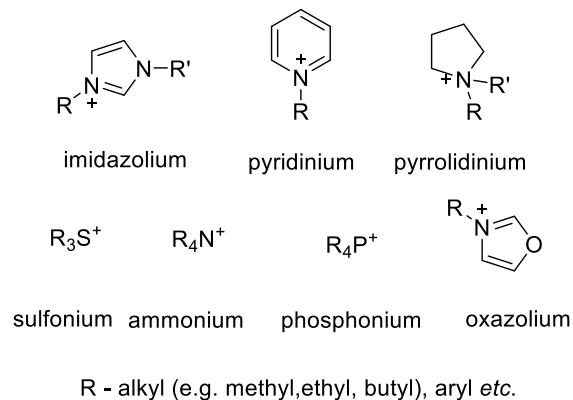


**Figure 1.1** Some commonly used cations for ILs.

Modification of the cation can have a significant influence on the IL properties like melting point, viscosity, and miscibility with other solvents, *etc.* [5]. Based on the cations, ILs may be divided into the following groups (**Figure 1.2**):

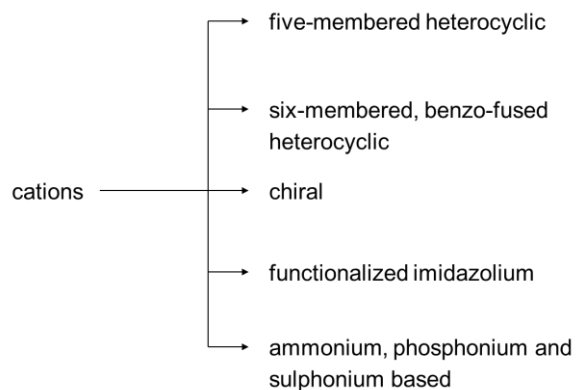


**Figure 1.2** Different groups of cations [5].

### 1.1.2 Anion

Anions of ILs are usually organic or inorganic weakly basic compounds with a delocalized negative charge [5]. ILs can be divided into six groups based on their anions: ILs based on anions like 1)  $[\text{PF}_6]^-$ ,  $[\text{BF}_4]^-$  and  $[\text{SbF}_6]^-$ ; 2) metal halides like  $\text{AlCl}_3$ ; 3) bis(trifluoromethanesulfonyl)imides, tris(trifluoromethanesulfonyl)methanide, *etc.*; 4) alkylsulphonates, alkylphosphonates, *etc.*; 5), acetate ( $\text{CH}_3\text{CO}_2^-$ ), triflate ( $\text{CF}_3\text{SO}_3^-$ ), tosylate ( $\text{CH}_3\text{PhSO}_3^-$ ) *etc.*; 6) borates and carboranes. **Figure 1.3** depicts some of the commonly used anions.

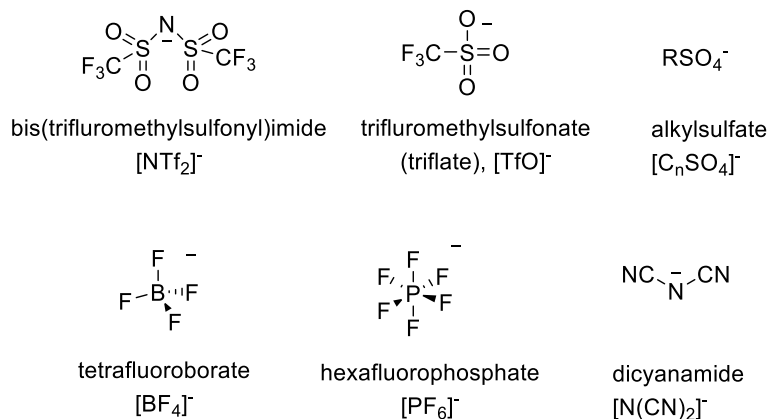


**Figure 1.3** Some commonly used anions for ILs.

### 1.1.3 Structural classification and general properties of ILs

Based on the combination of a cation and an anion and their unique physical, thermal, chemical, and biological properties, ILs can be classified into several categories, as shown in **Figure 1.4** [6,7].

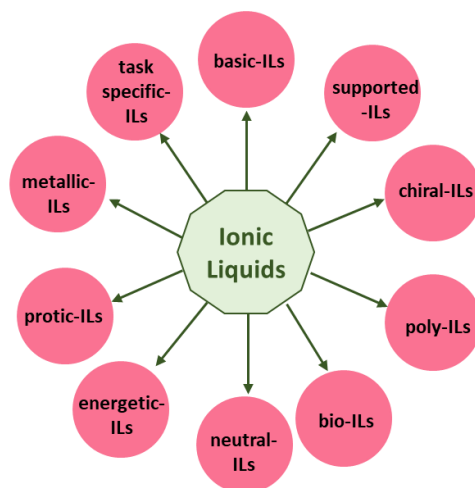


**Figure 1.4** Classification of ILs redrawn from [7].

The specific properties of ILs that make them unique alternatives to traditional aqueous or organic solvents include [3]: (i) ILs remain liquid over a wide range of temperatures, (ii) tunable acidic and basic trends, (iii) negligible vapor pressure, (iv) highly polar nature, (v) tunable hydrophilic and hydrophobic nature, (vi) tunable viscosity, (vii) long range of solubility in solvents due to

tunable combination of cations and anions, (vii) high thermal stability, and (viii) high degree of organization.

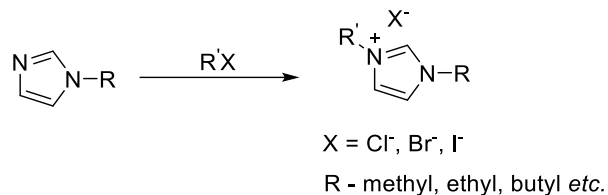
#### 1.1.4 Synthesis of ILs

The first report on the synthesis of ILs concerned the preparation of ethylammonium nitrate in 1914 [8]. The product was formed by the addition of concentrated nitric acid to ethylamine, providing a pure salt (mp. 12-14 °C) after water removal by distillation. While the protonation of appropriate amines or phosphines remains the most straightforward approach for producing IL, this method is constrained by potential for decomposition due to deprotonation [9]. However, different other methods can be used to produce ILs. The synthesis of ILs can be broadly split into two steps: 1) the formation of the desired cation and 2) an anion exchange resulting in the desired IL. Generally, most cations are available commercially, commonly as a halide salt. This PhD project focuses on the synthesis and application of 1,3-dialkylimidazolium cation based ILs.

##### a) Alkylation reactions

The synthesis of IL cations may be carried out through the protonation with free acids as mentioned above or by  $S_N2$  quaternization of an amine (Menschutkin reaction) [10,11], phosphine, or sulfide, most commonly by using an alkyl halide [9]. The alkylation process to form halide salts presents dual advantages: 1) a wide range of alkyl halides are available that are comparatively inexpensive, and 2) the substitution reactions generally occur smoothly at reasonable temperatures. The resulting halide IL can be readily converted to ILs with other anions. The alkylation reaction may be carried out using alkyl chlorides, -bromides or -iodides, with the reaction conditions required being harsher in the order  $I < Br < Cl$  corresponding to the order of the halide anions as leaving group. The quaternization reactions are quite simple to perform; the amine is mixed/stirred with the desired alkylating agent at an elevated temperature [9,12]. The reaction time and temperature are dependent on the alkylating agent employed, alkyl chlorides displaying the least reactive and alkyl iodides the most. One of the many reported examples of the synthesis of imidazolium ILs is the work of Dzyuba and coworkers, who reported the preparation of 1-alkyl-3-methylimidazolium halides and analogues in high yields with shorter reaction times than synthesized before through the alkylation of 1-methylimidazole [13]. One of the important requirements of such reaction is

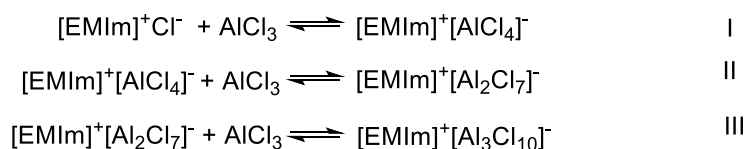
that the reaction mixture is kept moisture free as the products formed often are extremely hygroscopic which can effect their physical properties [14]. **Scheme 1.1** describes a general alkylation reaction for the preparation of imidazolium cation based ILs.



**Scheme 1.1** Alkylation of imidazole to obtain imidazolium-based IL.

### b) Anion-exchange reactions

The anion exchange can be carried out either by direct reaction of halide salts with Lewis acids to form Lewis acid based ILs or *via* anion metathesis. The early and most widely studied Lewis acid based ILs are salts with  $\text{AlCl}_3$  [15–17]. Such salts can be synthesized by mixing of the Lewis acid ( $\text{MX}_n$ ) and the halide salt. This results in the formation of more than one anion species, depending on the ratio of quaternary halide salt  $\text{Q}^+\text{X}^-$  and Lewis acid  $\text{MX}_n$ . This can be illustrated by the reaction of  $[\text{EMIm}]\text{Cl}$  with  $\text{AlCl}_3$  (**Scheme 1.2**, I-III).

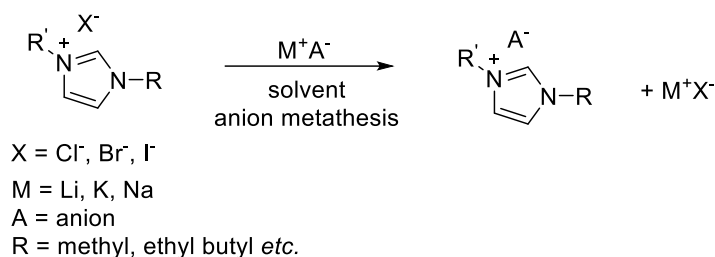


**Scheme 1.2** Series of equilibria in the reaction between  $[\text{EMIm}]\text{Cl}$  and  $\text{AlCl}_3$  [18].

Only equilibrium I in **Scheme 1.2** needs to be considered if  $[\text{EMIm}]\text{Cl}$  is present in molar excess compared to  $\text{AlCl}_3$  and the formed IL is basic. A molar excess of  $\text{AlCl}_3$  results in the formation of acidic ILs and equilibria II and III predominate. Other Lewis acids used apart from  $\text{AlCl}_3$  are  $\text{BCl}_3$  [19] and  $\text{AlEtCl}_2$  [20], among others. The preparative methods applied for all these salts are generally very similar.

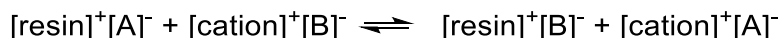
Anion metathesis stands out as a favorable technique to produce water- and air stable ILs based on 1,3-dialkylimidazolium cations. The first water-insoluble IL  $[\text{EMIm}][\text{PF}_6]$  was prepared by the

reaction of [EMIm]Cl and  $\text{HPF}_6$  in aqueous solution [21]. The water solubility is dependent on both the cation and anion, where generally water-solubility decreases with increasing alkyl chain length on cation [22]. The primary objective of all anion exchange reactions is to create the intended ILs without the presence of undesired cations or anions. This goal is more easily achieved in the case of ILs that are immiscible with water, facilitating easy product separation after reaction (phase separation). **Scheme 1.3** describes a general metathesis step for the preparation of imidazolium cation based ILs.



**Scheme 1.3** Anion metathesis of imidazolium ILs.

Ion-exchange resin is another preparative method used for the large-scale synthesis of ILs [23]. Essentially, ion-exchange materials are salts where one ion is fixed in a stationary (solid/gel) phase and the counter-ion present in the solution is exchangeable (**Scheme 1.4**). During an anion exchange, the counter ion  $[\text{B}]^-$  in the solution equilibrates with the counter-ion present on the ion-exchange material  $[\text{A}]^-$ . If the equilibrium constant is large and the exchange column is of sufficient length, complete exchange will take place and only  $[\text{cation}]^+[\text{A}]^-$  is eluted as pure solution [5].



**Scheme 1.4** Ion exchange reaction.

Ion-exchange is generally a reversible process, and it is therefore always preferred that the ion-exchange material shows strong affinity for the counter-ion of the starting material over the corresponding ion of the product. Literature on the use of ion-exchange for ILs synthesis is comparatively scarce, however, one example is the work reported by Mizute and group on the use

of anion exchange material for the synthesis of [EMIm][DCA] from [EMIm][Br] on an industrial scale [24].

Carbonate based ionic liquid synthesis (CBILS® - registered trademark of proionic GmbH [25]) stands out as a cutting-edge commercial process, known for its environmentally conscious approach and halide free and waste free synthesis of ILs [26]. This method utilizes carbonic acid esters as quaternization reagents and the formation of quaternized alkylcarbonate intermediate is the crucial step in the process [27]. This then reacts with Brønsted acids to obtain the final IL. During this reaction, the alkylcarbonate anion undergoes protonation and hydrolysis with the release of CO<sub>2</sub> and the formation of the corresponding alcohol. Simultaneously, the Brønsted acid is deprotonated, resulting in the formation of the conjugated anion. The removal of volatiles under vacuum conditions gives the desired IL [26].

### 1.1.5 Purification of ILs

The main challenge in synthesizing ILs lies in the purification of the final products. Lack of significant vapor pressure prevents the purification of ILs through distillation and low melting points makes crystallization difficult. Thus, impurities that are present from the beginning or generated during the synthesis process and byproducts are difficult to remove. This is a delicate point as even traces of impurities can have an impact on the physical and chemical properties of ILs for example melting point, decomposition temperature *etc.* [28]. Some of the common IL impurities are water, halides, unreacted organic starting materials, and residual organic reaction solvents. Suspended particles are a class of impurities that are often overlooked. These can come from metathesis byproduct, molecular sieves, sorbents, *etc.* [5]. The low volatility of the ILs allows the removal of water by placing them under vacuum for several hours. However, this procedure is not appropriate for many protic ILs as the conjugated acid and base can be volatile resulting in loss of one of the IL components [5]. ILs have a remarkable capacity to incorporate water thus, relying solely on vacuum conditions does not effectively reduce the water content to an acceptable level (depending on the application) within a reasonable timeframe. While it can be sensible to subject the sample to heat during vacuum, it is important to exercise caution, as heat can accelerate the decomposition of ILs. Alternative approaches may involve employing vacuum azeotropic distillation with solvents like toluene. Another requirement is to perform the synthesis of ILs by

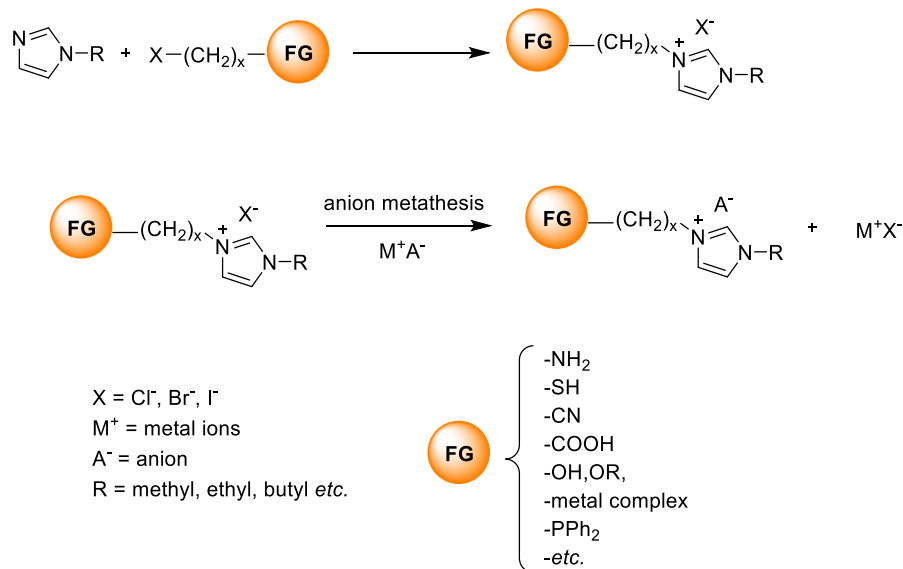
using highly pure starting materials. This can be achieved through distillation or recrystallization of the starting materials. All solvents used for quaternization, and anion metathesis should be dried and distilled before. If precautions are not taken it often leads to the formation of colored ILs (for *e.g.* from carbene formation). The common way of removing color is by using insoluble sorbents like activated charcoal [29], silica [30], and alumina [5]. One of the other purification methods include zone melting [5].

### 1.1.6 Task-specific ionic liquids

Task-specific ionic liquids (TSIL) can be defined as ILs which incorporate a covalently linked reactive functionality [31]. The functional group (FG) like carboxylic acid (-COOH) [32], amine (-NR<sub>3</sub>) [33] or nitrile (-CN) [34] can be incorporated either into the anion or cationic part or both [18]. Such functionalities can impart additional properties to the ILs that can be thus employed for specific tasks, with several objectives. For instance, ILs with appended amines have been developed to favor the separation of CO<sub>2</sub> from gas stream *via* carbamate formation [35]. ILs modified with a hydroxyl group (-OH) have been used as a phase transfer catalyst for ethoxybenzene synthesis [36]. Metal-ligating groups incorporated into ILs can be used for metal-ion extraction from aqueous solution [37]. The physicochemical properties of these TSILs like solubility in molecular solvents, thermal stability and chemical properties like reactivity, depend on the nature of the functional groups incorporated [38]. A TSIL can be a RTIL with covalently attached FG that can act not only as a reaction medium but also as a reagent/catalyst. A TSIL can also be a binary system of functionalized salts, which may be solid at room temperature that can be dissolved in a conventional IL [39].

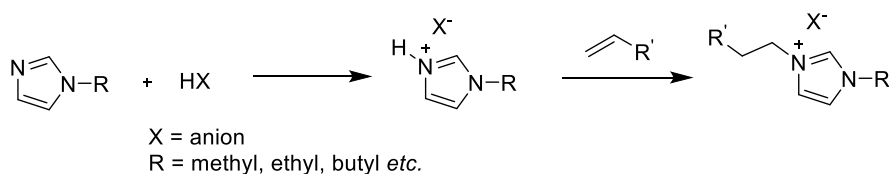
Synthesis of TSILs can be analogous to that of non-functionalized ILs. The quaternization of tertiary amines, phosphines and sulfides with a functional group-incorporated alkyl halide can afford the desired TSILs [40]. These salts can be further modified through ion metathesis, anion exchange or ion-exchange resin methods. **Scheme 1.5** shows the synthesis of imidazolium-based TSIL through quaternization of imidazole followed by anion metathesis.





**Scheme 1.5** Synthesis of TSILs.

Wasserscheid and coworkers introduced a new method for the synthesis of TSIL by employing a sequence of protonation and Michael reactions [41]. In this approach, the imidazole or nucleophile of interest is protonated using an acid form of the anion which eventually incorporates into the IL, *e.g.*, HPF<sub>6</sub> forms PF<sub>6</sub>-ILs. The desired Michael acceptor is then added to the salt formed, which inserts into the N<sup>+</sup>-H bond (**Scheme 1.6**).



**Scheme 1.6** Synthesis of TSIL using a protonation-Michael reaction sequence.

The purification and characterization methods of the products are similar to the conventional ILs. The techniques used to characterize ILs and TSILs are described in **section 1.1.8**.

### 1.1.7 Thermophysical properties of ILs

*Liquidus range* – This property refers to the temperature range where the ILs are in their liquid forms – the difference between the melting point and the decomposition temperature [42]. It is

difficult to obtain accurate values for the melting points of ILs as melting points ( $T_{mp}$ ) and glass transition temperatures ( $T_g$ ) can be strongly affected by the presence of impurities [43,44]. Ngo and coworkers showed that larger asymmetric cations yielded ILs with lower  $T_{mp}$  and that the highest  $T_{mp}$  is associated with symmetric cations [45]. They also showed that branched alkyl chains displayed higher  $T_{mp}$  than straight ones. Larger anions tend to result in the lowering of  $T_{mp}$  of ILs due to the reduced influence of Coulombic attractions within the crystal lattice and the increase of covalent character of the ions [46].

*Density* - Extensive experimental data have been collected for density as a function of temperature across a series of various ILs [42], including those derived from imidazolium, pyridinium, ammonium, phosphonium, *etc.* In the case of pure ILs, the values exhibit variability, depending on the combinations of cations and anions used. For a given cation, *e.g.* [BMIm]<sup>+</sup> and temperature, the density of IL increases in the order [BF<sub>4</sub>]<sup>-</sup> < [OTf]<sup>-</sup> < [PF<sub>6</sub>]<sup>-</sup> < [NTf<sub>2</sub>]<sup>-</sup> [47]. It has been reported that increasing halide (Cl<sup>-</sup> and Br<sup>-</sup>) and H<sub>2</sub>O contamination also tends to decrease the density over a wide range of values [48].

*Viscosity* - Generally, ILs are more viscous than most of the molecular solvents and this property is strongly dependent of the temperature [49,50]. For example, the viscosity of [BMIm][PF<sub>6</sub>] increases by 27% with a temperature increase from 20 to 25 °C [50]. The presence of impurities can also have a dramatic impact of the viscosity of the ILs. Considering ILs with the same anions and compositions, larger alkyl substituents on the imidazolium cation result in increased viscosity [16]. An additional element contributing to the cation's impact on viscosity is the extent of asymmetry in alkyl substitutions. Notably asymmetric substitutions have been recognized as a crucial factor in achieving reduced viscosities. This is also the case with anions. ILs with highly symmetric or spherical anions are more viscous compared to others. For a given IL, *e.g.* [C<sub>n</sub>mim][NTf<sub>2</sub>], the viscosity trends is as follows: Cl<sup>-</sup> > [CH<sub>3</sub>COO]<sup>-</sup> > [PF<sub>6</sub>]<sup>-</sup> > [C<sub>1</sub>SO<sub>4</sub>]<sup>-</sup> > [C<sub>2</sub>SO<sub>4</sub>]<sup>-</sup> > [BF<sub>4</sub>]<sup>-</sup> > [OTf]<sup>-</sup> > [NTf<sub>2</sub>]<sup>-</sup> [42].

### 1.1.8 Characterization of ILs

Given the substantial impact of impurities on the properties of ILs, it is essential to thoroughly characterize them prior to data reporting. Mass spectrometry (MS), nuclear magnetic resonance (NMR) spectroscopy, elemental analysis (EA) [51] are usual techniques which proves relevant to

confirm the structure of ILs. Nonetheless, it is important to note that certain impurities cannot be directly quantified through these methods. For example, if ILs are contaminated with LiCl, neither  $\text{Li}^+$  nor  $\text{Cl}^-$  will appear in MS because of their small masses, and they may not significantly alter the C, H, and N content (%) in EA. As discussed earlier the main impurities in ILs include water, organics, halides, and metal-ions. Water content can be assessed using  $^1\text{H}$  NMR and infrared (IR) spectroscopy but below 1000 ppm, Karl-Fischer titration needs to be employed [52]. IR and NMR analyses can also be employed to characterize the functional groups present in TSIL [53]. The unreacted organic starting materials like 1-methylimidazole and alkyl halides can be easily detected using NMR spectroscopy (mainly  $^1\text{H}$ ,  $^{13}\text{C}$ ). Halide impurities can be assessed using several techniques like  $^{19}\text{F}$ ,  $^{35}\text{Cl}$  NMR (>1 mol%), titration with silver nitrate which can be monitored visually for qualitative analysis or using the Volhard procedure (>10 ppm), ion chromatography (IC, >10 ppm), inductively coupled plasma-mass spectrometry (ICP-MS, >10 ppb) [5]. Metal-ion impurities exist in two primary forms: 1) as halide salts resulting from metathesis by-products and 2) as unreacted metallic starting material salts. Direct analysis of the metal itself is not consistently carried out; instead, focus is placed on analyzing the counterions originating from metathesis by-products or halide salts. If the amounts of these counterions are adequately low, it is assumed that the content of metal is also sufficiently minimal [5]. Thermal properties of the ILs can be analyzed using thermal gravimetric analysis (TGA) and differential scanning calorimetry (DSC) [45]. The thermal degradation profiles of ILs can be readily acquired by exposing the samples to a progressively rising temperature [54]. Other characterization techniques include X-ray photoelectron spectroscopy (XPS) [55], UV-visible spectroscopy (UV-vis) [56] and small angle X-ray scattering (SAXS) [57].

### **1.1.9 Applications of ILs**

Over the past decade, ILs have gained significant attention across various fields, including chemistry, biochemistry, and material engineering due to their distinct properties, including non-volatility, high thermal stability, wide electrochemical range, and high ionic conductivity [58–60] as mentioned earlier. However, certain limitations of ILs, such as their sensitivity to moisture and their acidic or basic nature, could potentially influence their applicability in some fields. Additionally, there has been a recent focus on investigating other aspects such as the toxicity,

degradation, and ecotoxicity of ILs [60]. Despite that, the fact that ILs can be tailored or customized to meet specific requirements make them highly attractive. Some applications of ILs are described in the following section. **Figure 1.5** reports some examples of IL application.

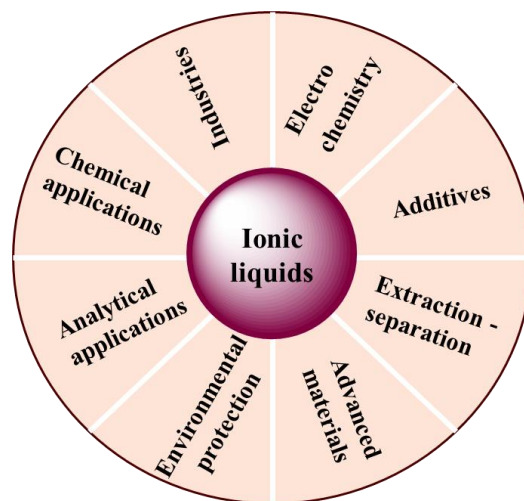


**Figure 1.5** Applications of ILs.

### 1.1.9.1 ILs catalyst and reaction media for organic synthesis

ILs are widely utilized in various organic reactions, offering several advantages. These include management of product distribution, enhanced reaction rates and reactivity, ease of product separation, catalyst immobilization, and facilitate the recycling [61,62]. ILs can effectively substitute traditional volatile organic compounds (VOCs) as solvents in organic reactions [62]. The incompatibility of imidazolium-based ILs with bases finds application in diverse reactions that do not require a base, such as the creation of N-heterocyclic carbenes, Heck reactions, and the generation of nanoparticles (NPs) within ILs [62,63].

*Transition metal complexes in ILs* - Many transition metal complexes dissolve readily in ILs, thus making them a suitable solvent for transition metal complex catalysis. Based on the anion coordinative attributes and the cation reactivity level, the ILs can assume various roles, such as acting as an “innocent” solvent, a ligand or precursor to a ligand, a co-catalyst, or even as the catalyst itself. ILs consisting of weakly coordinating anions like  $[\text{NTf}_2]^-$ ,  $[\text{BF}_4]^-$ ,  $[\text{PF}_6]^-$ , etc., paired with cations that do not coordinate to the catalyst and do not form species under reaction

conditions can be categorized as relatively “innocent” solvents in the realm of transition metal catalysis. The primary function of such ILs is to serve as a more or less polar, and more or less weakly coordinating environment for the transition metal catalysts [64]. ILs synthesized by the reaction of a halide salt and a Lewis acid like chloroaluminate typically serve as a solvent as well as a co-catalyst in transition metal catalysis. This is due to the Lewis acidity or basicity, which lead to interaction with the catalyst complex [64]. The cation and anion can serve as ligands or precursors of ligands for a transition metal complex that is dissolved within the ILs. When the catalytic center is cationic, the anion within the ILs can exhibit ligand-like behavior, depending on their coordination capabilities. Notably, it has been shown that when the anion of a cationic transition metal complex differs from that of the IL, there is a substantial replacement of the metal complex anion by the anion from the IL [65].

*Organic reactions* - ILs exhibit high potential as effective catalysts over a wide range of organic reactions, acting as a substitute for traditional catalysts that often present limitations in terms of selectivity, yield, and reaction conditions. Kore and coworkers reported the acylation of isobutylbenzene using chloroaluminate-based ILs and liquid coordination complexes as catalysts to replace the conventional catalysts like HF and AlCl<sub>3</sub> [66]. Bhongale *et al.* synthesized five sulfonic acid-functionalized ILs with different cations [67]. They showed that these ILs were efficient catalysts for the O-alkylation of hydroquinone with methanol in the presence of a small amount of benzoquinone. Thus, ILs exhibit remarkable potential as catalysts in diverse organic reactions, addressing limitations associated with conventional catalysts and contributing to the development of more efficient and environmentally conscious processes.

*Nanoparticle synthesis* – ILs have emerged as versatile components that can act both as solvent and stabilizers for the synthesis of metal nanoparticles (NPs), providing an efficient synthesis method. For instance, Guleria and coworkers used an imidazolium-based RTIL as a solvent, reducing and stabilizing agent to synthesize stable  $\alpha$ -Se NPs ( $d_m = 34$  nm) exhibiting antioxidant properties [7]. On a similar note, Garg *et al.* reported the synthesis of palladium NPs ( $d_m = 1.4$  and 1.7 nm) by employing a choline-based IL [68]. These IL-stabilized Pd NPs exhibited notable catalytic efficiency in hydrogenation reactions on substrates with various functional groups. A detailed review of metal NPs in ILs is provided in **section 1.2.3**.

### 1.1.9.2 Electrochemistry

ILs find wide applications in the field of electrochemistry due to their diverse physico-chemical properties which include efficient conducting electrolytes, broad electrochemical potential window, high thermal stability, adjustable solubility, *etc.* [7]. The efficiency of any electrochemical device is generally based on the equilibrium between IL properties and electrode characteristics [69]. The properties of ILs and electrodes are associated to three primary factors: 1) conductivity, 2) viscosity and 3) electrochemical potential of ILs. ILs exhibit exceptional ionic conductivity due to their ionic nature [70,71]. Although ILs possess high viscosity, this can be tailored through appropriate combination of cations and anions [72]. The electrochemical potential of ILs is closely related to their oxidation and reduction tendencies. ILs offer a wide range of electrochemical potential windows, both in their pure form and when coupled with additives. This characteristic is of significant import, as it influences their utility and adaptability in various electrochemical applications [73,74].

### 1.1.9.3 Other applications

Some of the other application of ILs are summarized below [75]:

- i) extraction and separation processes - micro-extraction, biomass extraction, extraction of flavonoids *etc.*
- ii) industries - food and bioproduct, biodiesel production, pharmaceuticals, *etc.*
- iii) additives - lubricating agents, corrosion inhibitors, surface-active agents, *etc.*
- iv) analytical applications - gas chromatography columns, stationary phase for high-performance liquid chromatography (HPLC), *etc.*

### 1.1.10 Supported ionic liquid phase (SILP)

Supported ionic liquid phase (SILP) technology is a convenient approach to obtain liquid-solid combinations comprising a solid material that effectively retain a liquid on that does not evaporate [76]. This method involves the surface modification of a porous solid by dispersing a thin layer of IL on it, as illustrated in **Figure 1.6**.

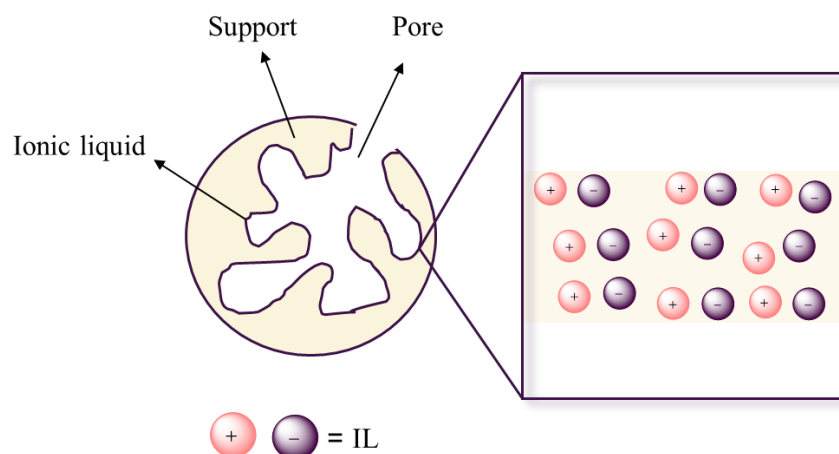
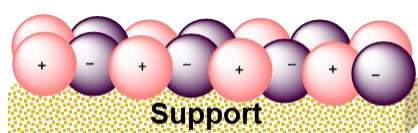


**Figure 1.6** Schematic representation of SILP technology where an IL film is dispersed in a porous material. Redrawn from [76].

By this way it is feasible to transfer distinct characteristics of the fluid onto the surface of a solid material by choosing appropriate ions for the IL and confining it to the material surface. As a result, the SILP framework allows the tailored production of solid materials, yielding uniform and well-defined surface structures with distinct properties and controlled chemical reactivity, thus offering a strategy to overcome the non-uniformity often present in traditional materials science. Additionally, the SILP technique has the potential to generate materials with novel surface properties [76]. The common methods to immobilize ILs onto the surface of a solid material are given in **Figure 1.7**.

Covalent anchoring of a monolayer of IL onto a solid material support – the IL blends in with the support and loses certain of its bulk properties like solvation, conductivity, viscosity, *etc.* If the IL contains functionality such as acidity, hydrophobicity, this can render the surface properties of the support.

a)



Immobilizing multi-layers of IL onto the solid material support – the IL bulk properties can be maintained. Metal salts/complexes, nanoparticles can be dissolved to render functionalities.

b)

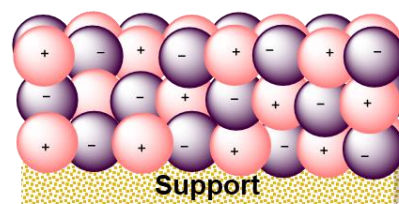


**Figure 1.7** Main methods to obtain SILP materials based in SILP films according to the phase behavior. Redrawn with modification from [76].

The SILP materials offer several advantages compared to liquid-liquid and gas-liquid systems, which are [76,77]:

- i) high surface area - due to the nature of the support structure, thus enabling the interaction with a large number of reactant molecules simultaneously when applied in catalysis, leading to enhanced reaction rates and efficiencies.
- ii) thin film formation - ILs can form a thin film over the support and thus limit mass transport issues.
- iii) adjustable solvent properties - solvent properties, like solubility can be tailored to meet specific requirements. Varying the composition of the IL, the reactants solubility can be optimized, leading to improved reaction yields and selectivity. Additionally, the solubility of the products can be controlled, allowing for easy separation and recovery.
- iv) thermal stability - most ILs are thermally stable up to 200 °C and above, making them suitable for employing in high-temperature applications. For instance, ILs have been successfully heterogenized in silica, nanoporous materials, or polymers to use them as both catalysts and reaction media for production of biodiesel [78].



- v) application in reactor technology – the materials can effectively be utilized in fixed-bed or fluidized-bed reactor technology.
- vi) efficient catalyst immobilization in a defined environment.

### 1.1.10.1 Synthesis of SILPs

There are two different types of SILPs based on the nature of IL fixation. The first type involves the straightforward physisorption of the IL onto the high-surface-area support. Here, the interaction is relatively weak, encompassing van der Waals forces and hydrogen bonding between the IL and the support surface, and the IL is dispersed across the support surface. The second type is based on chemisorption of the IL onto the surface where more robust connections, including covalent bonding, arise between the support and the IL [79].

*Support materials* - supports for SILP involve commercially available porous silica gels, which have moderate-to-high surface area ranging between 300 and 500 m<sup>2</sup> g<sup>-1</sup> [80,81]. The number of reactive silanol groups on the silica gel can be reduced by thermal pretreatment [82]. By such passivation stable catalyst performance can be achieved as the reaction of these silanol groups with the ligands or catalyst reduce the actual concentration of the latter [83]. These silanol groups also offer possibilities for the chemical fixation of ILs *e.g.*, the reaction of these silanol groups with triethoxysilanes, as reported by Mehnert and coworkers [84] (**Figure 1.8**). Some of the other materials used as supports include mesoporous silica materials (MCM-41, MCM-48), silica-alumina materials like zeolites and clays, or other inorganic metal oxide supports like Al<sub>2</sub>O<sub>3</sub>, TiO<sub>2</sub>, ZrO<sub>2</sub>, *etc.* (6).

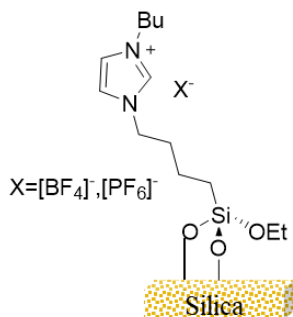


**Figure 1.8** Covalent bonding of IL fragments to the surface of silica gel. Redrawn from [84].

Various techniques have been developed for the synthesis of SILP materials. Some of them include incipient wetness impregnation, freeze-drying, spray coating for dispersion of ILs. Chemically bound ILs are synthesized traditionally through sol-gel synthesis. The incipient wetness impregnation method and sol-gel synthesis are described briefly below.

*Incipient wetness impregnation* - Generally, the IL, and if necessary, the catalyst complex, are dissolved in an appropriate organic solvent or water. The support is then added, and the mixture is stirred for a defined time. The solvent is subsequently evaporated under mild vacuum conditions. This protocol results in the formation of a thin IL layer on the support surface. The volumetric ratio between the IL volume ( $V_{IL}$ ) and the overall pore volume ( $V_{pore, total}$ ) of the support is given as the liquid loading,  $\alpha_{IL}$  (vol%) (**Equation 1.1**)

$$\alpha_{IL} = \frac{V_{IL}}{V_{pore, total}} \quad (\text{Eq. 1.1})$$

One example of successful application of the SILP concept is the continuous gas-phase Rh-catalyzed hydroformylation reported by Riisager and coworkers. The catalytic material was prepared by the impregnation of a transition metal complex containing IL onto a commercially available silica gel 100 (surface area  $300 \text{ m}^2 \text{ g}^{-1}$ , pore volume  $1.0 \text{ cm}^3 \text{ g}^{-1}$ , pore diameter  $137 \text{ \AA}$ ). The ILs used were [BMIm][PF<sub>6</sub>] or [BMIm][*n*-C<sub>8</sub>H<sub>17</sub>OSO<sub>3</sub>] and as catalysts a combination of [Rh(acac)(CO)<sub>2</sub>] and three different phosphine ligands [85].

*Sol-gel synthesis* - A separate IL phase does not exist; instead, the IL acts as a covalently tethered ligand. The grafting of the IL is followed by ion exchange to replace certain anionic components. This supports the anchoring of anionic catalyst species, including [WO<sub>4</sub>]<sup>2-</sup>, [RuO<sub>4</sub>]<sup>2-</sup>, [PdCl<sub>2</sub>]<sup>2-</sup>, [NiCl<sub>4</sub>]<sup>2-</sup>, [CuCl<sub>4</sub>]<sup>2-</sup>, [Al<sub>2</sub>Cl<sub>7</sub>]<sup>-</sup>, and [SnCl<sub>5</sub>]<sup>-</sup> [86]. Anchoring the anionic portion of the IL enables the immobilization of cationic catalysts. One of many examples, is the work of Mehnert and coworkers [84] who reported the synthesis of a SILP catalyst for application in liquid-phase hydroformylation. The synthesis included grafting IL fragments onto the surface of silica gel. The initial step involved introducing a triethoxysilyl functionality to a butylimidazole moiety to provide 1-butyl-3-(3-triethoxysilylpropyl)-4,5-dihydroimidazolium chloride. The anion exchange for [BF<sub>4</sub>]<sup>-</sup> or [PF<sub>6</sub>]<sup>-</sup> led to the grafting of the desired IL to the silica surface. Subsequent grafting of the imidazolium fragment onto the

pretreated silica gel, by reflux-heating approach in  $\text{CHCl}_3$ , resulted in formation of an IL-monolayer-modified support material.

### 1.1.10.2 Application of SILPs in catalysis

A precise understanding of the specific site, required to provide the catalytic function **F**, is essential for effective conversion of substrates to desired products. Catalysts can be categorized into four types (A1, A2, B and C), based on the supported ionic liquid films according to the nature of the catalytic function **F** [87] (**Figure 1.9, Tables 1.1 and 1.2**).

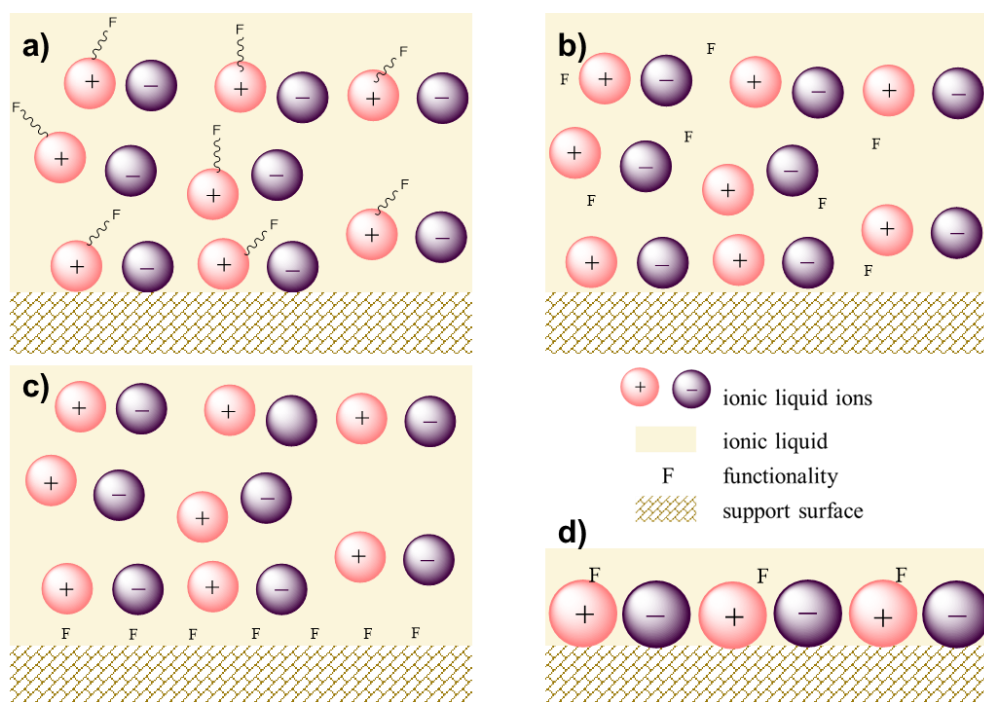


**Figure 1.9** Categorization of catalysts based on supported ionic liquid films according to the nature of the catalytic function **F**. a) Type A1, b) Type A2, c) Type B and d) Type C redrawn from [87].

**Table 1.1** Categorization of catalysts based on supported ionic liquid films according to the nature of the catalytic function **F** [87].

<b>Type A1</b> - task-specific ILs	<b>Type A2</b> - immobilized homogeneous catalysts and metal nanoparticles (NPs)
<p>1) The catalytic function <b>F</b> may be introduced by a moiety that is chemically attached either to the cation or the anion (or both) of the ILs.</p> <p>2) This arrangement provides a high concentration of active sites, which is beneficial for slow reactions where the reaction occurs in the catalytic phase.</p> <p>3) To address the potential diffusion limitations across the phase boundary during faster reactions, a thin IL film can be used, or the functionalized IL can be diluted with non-functionalized IL.</p>	<p>1) The molecular catalysts can be dissolved within a narrow IL film, functioning similarly to homogeneous catalysts (<b>F</b>). To reduce leaching the catalyst needs to have high solubility in the IL compared to the fluid phase.</p> <p>2) After the substrate molecules pass the phase boundary, they exhibit easy diffusion within the catalyst phase towards the molecular catalyst. Here, they get converted into products. These products must then diffuse back across the phase boundary and into the bulk fluid.</p> <p>3) Metal NPs can be immobilized in thin films of ILs [80]. The NPs can either be synthesized directly in the ILs that will act a stabilizer [88], or they can be synthesized outside, using a suitable stabilizer, and then transferred into the ILs.</p>

**Table 1.2** Categorization of catalysts based on supported ionic liquid films according to the nature of the catalytic function **F** [87].

<b>Type B</b> – heterogeneous catalysts coated with ILs	<b>Type C</b> – chemically bound monolayers of ILs
<p>1) A support with catalytically active sites on its surface (heterogeneous catalyst) can be coated with a thin layer of IL. This serves a dual function: it provides the necessary reactive sites</p>	<p>1) A reduced quantity of IL leads to the formation of a monolayer coating on the entire support surface or appears as IL islands, coating specific areas of the support. The IL is used to</p>

---

<p>and also acts as a stationary carrier for the IL film.</p> <p>2) The thin IL film has a transformative effect on how substrate molecules access the active centers residing on the support surface. This change in access influences the catalytic process.</p> <p>3) Compared to traditional heterogeneous catalysis, the substrate encounters two steps: passage through phase boundary between the bulk fluid and the IL film, as well as the IL film itself. The relative concentration of substrate, intermediates, and products in the vicinity of the active sites is influenced by the actual concentrations in the fluid phase and the partitioning coefficients for each molecule between the bulk fluid and IL.</p> <p>4) Metal NPs can also be attached on the surface of the support and then coated with thin layer of ILs. The morphology of the NPs may vary in the presence of the ILs. It is controlled by the strength of interaction between support and NPs, support and IL, and NPs and IL.</p>	<p>transfer the functionality <b>F</b> to the support surface.</p> <p>2) The bonding between the IL and support usually involves chemisorption, providing specific interaction between the cation of the IL and reactive sites present on the surface of the support. Such monolayers are resistant to leaching.</p> <p>3) A notable advantage of IL monolayers is their ability to avoid the limitations arising from slow diffusion of reactants and products across the phase boundary.</p>
--	--

---

Several examples report the application of the SILP concept for catalysis. Some of them include hydrogenation [89,90], hydroamination [91,92], hydroformylation [82], carboxylation [93] reactions, among others. Selected systems used in hydrogenation reactions are summarized in **Table 1.3**.

**Table 1.3** Selected examples for the use of supported ionic liquid catalysts in hydrogenation reactions. Adapted from [87].

Type of catalyst	Ionic Liquid	Support	Reaction medium	Operation mode	Ref.
Ru, Rh complexes	Phosphonium salt	Silica	Slurry	Batch	[94]
Rh complex	[BMIm][PF <sub>6</sub> ]	Silica gel	Fixed-bed	Continuous	[95]
FeRu NPs	[1-butyl-3-(3-triethoxysilylpropyl)-imidazolium][NTf <sub>2</sub> ]	SiO <sub>2</sub>	Fixed-bed	Batch	[96]
Pd NPs	TMGL	Molecular sieve	Slurry	Batch	[90]
Pt NPs	[BM <sub>2</sub> Im][OTf]	Flame-dried silica	Fixed-bed	Continuous	[97]
Pd NPs	[BMIm][SbF <sub>6</sub> ]	Modified CNT	Slurry	Batch	[98]

TMGL: 1,1,3,3-tetramethylguanidine lactate; NTf<sub>2</sub>: bis(trifluoromethylsulfonyl)imide; OTf: trifluoromethylsulfonate; CNT: carbon nanotubes.

## 1.2 Metal nanoparticles

Nanotechnology is a scientific discipline that deals with the preparation and use of nano-size particles within the size range of 1 to 100 nm. The term 'nanoparticle' originates from the Greek word 'nano,' meaning 'small' and, when used as a prefix, denotes a size of 10<sup>-9</sup> meter (= 1 nm) [99]. Metal nanoparticles (NPs) including transition metal NPs find versatile applications in various fields like molecular biology, medicine, physics, organic and inorganic chemistry, and material science [100,101]. Decreasing particle size to the nanoscale imparts unique and enhanced characteristics like morphology and particle size distribution, which are not exhibited by larger bulk materials [102]. Electronic properties of metal NPs are situated at the frontier between molecular species and bulk compounds [103]. Their surface-to-volume ratio is significantly higher than that of larger particles or atoms, leading to a high number of potential active sites on the surface [104]. This unique extrinsic property of the surface area of NPs contributes to them being

highly attractive and influences also various intrinsic properties, including their strong surface reactivity which is size-dependent [105]. The properties observed at the nanoscale are mainly due to two key factors:

- 1) *Quantum size effect* [106]: In bulk metals, the electronic behavior is characterized by the presence of energy bands. The valence band contains the valence electrons, typically s- and d-electrons in the case of transition metals. The conduction band of metals partially overlaps with the valence band and hence is partially occupied by electrons responsible for the electrical conductivity of metals. In semiconductors the valence and conduction bands are separated by a specific energy gap, which is considerably larger in insulators. When a metal particle undergoes continuous size reduction the bands turn into discrete energy levels. At this stage, the bulk properties of the metal disappear and are substituted by "quantum dot," which are governed by the principles of quantum mechanics. Such confinement of charge carriers within a small space, resulting in discrete energy levels, is referred to as the "quantum size effect." It brings changes in the electronic properties of metals in NPs.
- 2) *Surface/interface effect* [107,108]: Metal NPs offer a higher number of potential active sites compared to bulk catalytic materials due to their high surface-to-volume ratio making them highly attractive as catalysts. Furthermore, the diverse shapes, crystallographic facets and different fractions of surface atoms located at their corners and edges can contribute to their versatility in catalytic applications.

Different synthesis methods (see next section) allow to have metal NPs in a reproducible way to study their properties.

### **1.2.1 Synthesis of metal nanoparticles (NPs)**

Various chemical and physical techniques like chemical reduction, electrochemical reduction, thermal decomposition *etc.* have been employed for the synthesis and stabilization of metal NPs [109]. The choice of the method to synthesize metal NPs is key as during the synthesis, processes like kinetics of interaction of metal ions and reducing agents, adsorption of stabilizing agents with metal NPs have strong influence on the structure and size (morphology), stability and physicochemical properties of the metal NPs [110]. The different techniques for the synthesis of

metal NPs are categorized into two main types: 1) bottom-up methods - where atoms and molecules are employed as starting materials and 2) top-down methods - where a bulk material is used as the starting material and particles size is reduced to NPs regime [110,111] (**Figure 1.10, Table 1.4**).

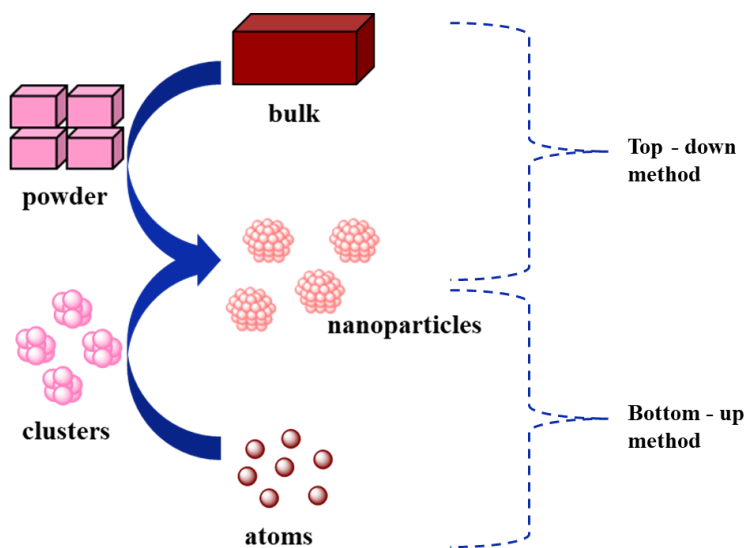


**Figure 1.10** Synthesis methods for MNPs.

**Table 1.4** Methods for synthesis of metal NPs.

Top-down methods	Bottom-up methods
Mechanical milling – ball milling, mechanochemical synthesis	Solid state methods - physical and chemical vapor deposition
Thermal evaporation	Liquid state methods - sol-gel, chemical reduction, hydrothermal, solvothermal
Laser ablation	Gas phase spray pyrolysis, laser ablation, organometallic synthesis.
Sputtering	Other methods -electrodeposition, microwave, and ultrasound technique.



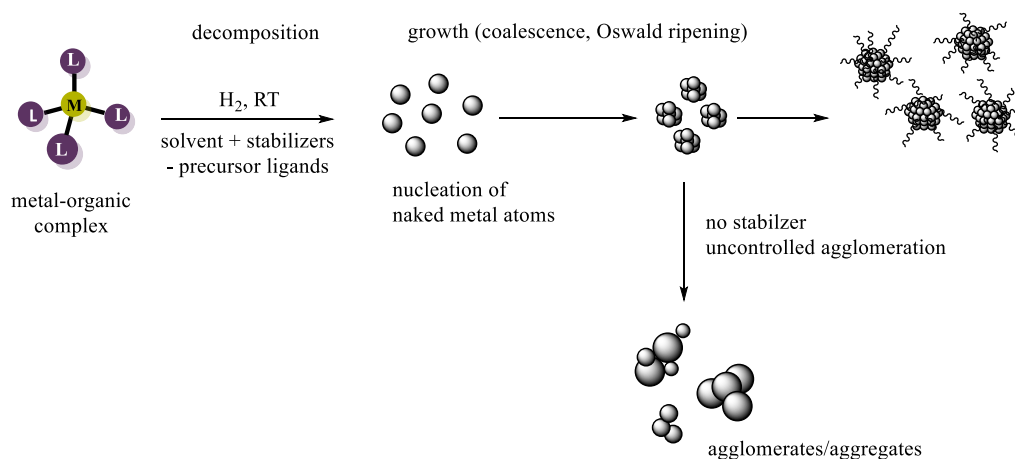
The establishment of reproducible and controlled synthesis methods to obtain well-defined NPs in terms of shape, size and composition is of utmost significance in the field of nanochemistry. In this context, the organometallic approach refined by Chaudret and Philippot and collaborators for over 25 years, provides an effective method for the synthesis of small and well-defined metal NPs [112,113]. The following section will focus on the utilization of the organometallic approach for synthesizing metal NPs as developed within my research team at LCC-CNRS, Toulouse. This section will include a discussion of the overall methodology, recent advancements, and the selection of organometallic precursors.

### 1.2.2 Organometallic approach for the synthesis of metal NPs

Organometallic compounds (or metal-organic complexes) are the source of metal atoms for the organometallic approach [113]. Organometallic complexes involve the association of one or more metal atoms with carbon-containing fragments and they can be  $\sigma$ -bonds (metal-alkyl),  $\pi$ -bonds (metal-olefin/arene), or a combination of both, as seen in compounds like allyl, cyclopentadienyl, cyclooctadiene *etc.* [114]. Pleass and coworkers [115] reported the first example of organometallic complex reaction with reducing gases where they synthesized nickel nanopowders using hydrogen to reduce nickelocene and study the kinetic of the deposition of Ni onto powder surface. Chaudret, Bradley and coworkers later developed the synthesis of Pd NPs and PdCu alloy by employing the organometallic approach [116–118]. The Pd based organometallic complexes employed for metal NPs synthesis include palladium acetate, Pd(OAc)<sub>2</sub> and bis(dibenzylideneacetone)palladium, Pd(dba)<sub>2</sub> and the copper precursor was copper acetate hydrate, Cu(OAc)<sub>2</sub>.xH<sub>2</sub>O. The controlled decomposition of (1,3-cyclooctadiene)(1,3,5-cyclooctatriene) ruthenium, [Ru( $\eta^4$ -C<sub>8</sub>H<sub>12</sub>)( $\eta^6$ -C<sub>8</sub>H<sub>10</sub>)] or [Ru(COD)(COT)], in the presence of small amounts of various stabilizers like polymers and ligands to synthesize Ru NPs were also reported [113].

In the organometallic approach, the metal-organic complexes (metal precursors) with zero or low oxidation state of the metal are decomposed at mild reaction conditions in the presence of carefully chosen ligands (**Scheme 1.7**). Olefinic complexes are preferred as hydrogenation of such complexes results in the reduction of the unsaturated ligands within their coordination sphere into their corresponding alkanes, which are inert towards the metallic surface [113]. For example, [Ru(COD)(COT)] is easily decomposed under hydrogen (1-3 bar) at room temperature [119],

bis(1,5-cyclooctadiene)nickel,  $[\text{Ni}(\text{C}_8\text{H}_{12})_2]$  or  $[\text{Ni}(\text{COD})_2]$  can be employed for the preparation of Ni NPs [120] and dirhenium(II) tetraallyl complex,  $[\text{Re}_2(\text{C}_3\text{H}_5)_4]$  allowed to get pure Re NPs [121]. All these precursors generate byproducts like propane and cyclooctane which are inert to the metal surface and can be removed under vacuum. The stabilizing agent introduced at the beginning of the reaction plays a crucial role, as it governs the characteristics of the resulting nanostructures [113]. Some of the stabilizers include simple ligands such as alcohols [122], thiols [123], silanes [124], aminoalcohols [125], 3-aminopropyltriethoxysilane [126], amines [123], diphosphines [127] and ionic liquids [128] as well as polymers [129] can also be used. Through this method, a wide variety of metal nanostructures can be obtained by adjusting the choice of metals, reaction conditions, and stabilizing agents.



**Scheme 1.7** Schematic representation for the synthesis of metal nanoparticles (NPs) by the organometallic approach adapted from [113].

The organometallic approach for the synthesis of metal NPs provides numerous advantages, which are primarily centered around the precise control of the reaction conditions (which in-turn affect the surface of the particles) and the control over particle characteristics (size, size distribution and shape). Such control allows to obtain monodispersed NPs with desired properties. One potential challenge lies in the synthesis and handling of organometallic complexes that require inert conditions. Nevertheless, the advantages gained in terms of controlling the characteristics of NPs make the efforts involved justifiable. Indeed, having well-controlled metal NPs allow to finely investigate their properties for applications in different domains, including catalysis among others.

Some of the experimental techniques that are used for NPs characterization are listed in **Table 1.5** [130].

**Table 1.5** Techniques applicable for characterization of NPs.

Technique	Information obtained	Ref
NMR (all types)	Influence of ligands on NP shape and morphology, density and arrangement of	[131]
Nuclear magnetic resonance	ligand, atomic composition	[132]
SAXS	Particle size, size distribution	[133]
Small-angle X-ray scattering		
XPS	Oxidation states, electronic structure,	[134]
X-ray photoelectron spectroscopy	elemental composition	
FTIR	Ligand binding and surface composition,	[135]
Fourier transform infrared spectroscopy		[136]
TGA	Mass and composition of stabilizers,	[137]
Thermal gravimetric analysis	ligand stability on the surface.	
ICP-OES, ICP-MS	Elemental composition, size, NP metal	[138]
Inductively coupled plasma optical emission spectroscopy and mass spectrometry	concentration	[139]
TEM, HRTEM, STEM	NP size, size monodispersity, shape,	[130]
Transmission electron microscopy	aggregation, crystal structure of single	
High-resolution TEM	particles. crystallinity: monocrystalline,	
Scanning electron microscopy	polycrystalline and amorphous NPs. Combined with HAADF (High-angle annular dark-field imaging), EDX (Electron diffraction) for morphology study, crystallinity	
SQUID-nanoSQUID	Magnetization saturation, blocking	[140]
	temperature	[141]
DLS	Hydrodynamic size, detection of	[142]
Dynamic light scattering	agglomerates	

---

Technique	Information obtained	Ref
UV-Vis	Optical properties, size, concentration,	[143]
Ultraviolet-visible spectrophotometry	agglomeration state	
WAXS	Size, crystal structure/crystallinity,	[144]
Wide-angle X-ray scattering	interparticle distance.	
Powder-XRD	Size, crystal structure	[145]
X-ray diffraction		

---

### 1.2.3 Metal nanoparticles in ionic liquids (ILs)

It is well-established that ILs, particularly those derived from imidazolium salts, can be effectively used for the *in-situ* generation and stabilization of metal NPs [146]. These ILs are excellent stabilizing agents and, importantly, exhibit high self-organization at the nanoscale. ILs form extensive hydrogen-bond networks in their liquid state, rendering these supramolecular fluids with structural directionality [147,148]. The structural organization can act as "entropic driver," for the spontaneous and well-defined ordering of nanostructures [146,149,150]. The properties of ILs, especially those based on imidazolium salts, are primarily based on the formation of aggregates rather than the individual cations and anions [149,150]. The basic unit typically consists of one imidazolium cation surrounded by at least three anions, and reciprocally, each anion is encircled by at least three imidazolium cations. The network structure gives rise to continuous three-dimensional ionic channels within the ILs, coexisting with non-polar regions which can form dispersed microphases in some cases, while in others continuous phases [146]. The segregation of polar and non-polar domains in imidazolium based ILs profoundly influences their solvation properties and their interactions with various species. As a result, polar substances tend to dissolve preferentially in polar domains, while non-polar compounds find affinity within non-polar regions [73]. Thus, non-polar transition-metal precursors (organometallic compounds) tend to dissolve in the non-polar domains of the IL, while polar precursors have an affinity for the polar regions. The volume of these nano-regions within the IL influences the size and shape of the metal nanoparticles. **Figure 1.11** shows the different stabilization/interaction by IL/TSIL towards metal NPs [128,151].

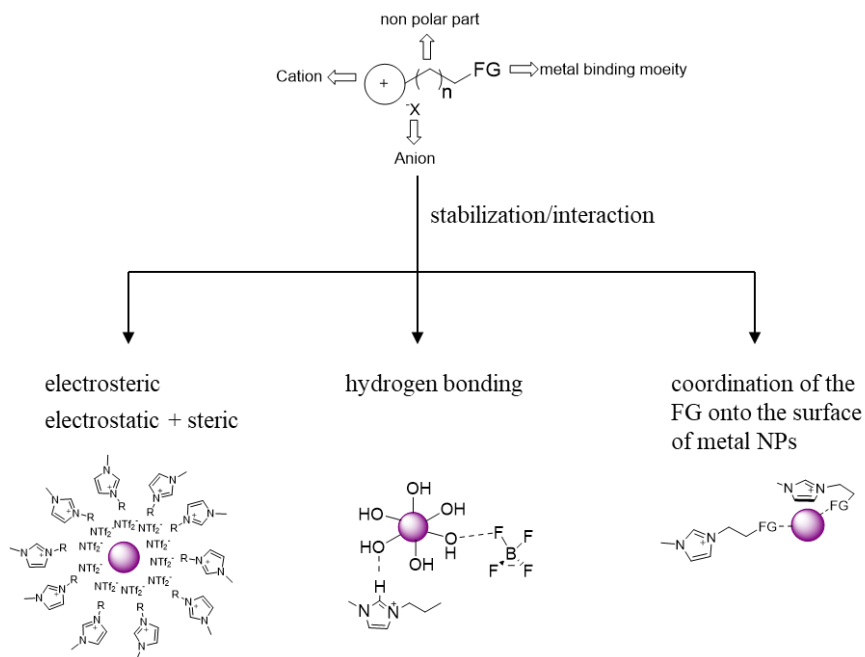


**Figure 1.11** Different types of stabilization provided by ILs/TSILs.

#### 1.2.4 Catalytic applications of metal NPs in ILs

In the field of heterogeneous catalysis, the utilization of metal NPs is firmly established mainly due to their exceptional reactivity. One of the key attributes is the increase in the number of surface atoms with decreasing particle size. These surface atoms serve as the active sites, being thus crucial for catalytic processes. Since the number of surface atoms influences their catalytic reactivity a precise control over the metal NP size holds great importance [152]. In the case of metal NPs synthesized in ILs, the choice of cations and anions may impact the morphology and electronic properties of metal NPs and in turn strongly influence their performance in catalysis [153]. Several families of small and well dispersed metal NPs synthesized in ILs have been employed in catalytic reactions including hydrogenation, hydroformylation, coupling reactions, *etc.* [153].

Since this PhD project mainly involves Ru and Ni NPs synthesis and application in hydrogenation reactions, a main focus has been given in the following to recently reported Ru- and Ni-based nanocatalysts in ILs for hydrogenation reactions of different substrates.

#### 1.2.4.1 Hydrogenation with Ru NPs in ILs

**Table 1.6** summarizes recent examples of the application of Ru NPs in ILs for hydrogenation reactions. The examples evidence that Ru NPs in ILs have been employed for the selective hydrogenation of different functional groups including CO, CO<sub>2</sub>, quinoline, ketone and aldehydes. One of the challenging reactions, the hydrogenation of CO<sub>2</sub> to either methane or formic acid preferentially, can be achieved by Ru NPs, employing the appropriate ILs and reaction conditions. Many Ru NPs stabilized by ILs like [BMIm][NTf<sub>2</sub>] and [BMIm][PF<sub>6</sub>] have also been employed for the selective hydrogenation of arenes like benzene, toluene, o-xylene [156]. Additional literature review on the synthesis and catalysis of Ru NPs in different ILs have been provided in Chapter 3.

**Table 1.6** Recent examples of the application of Ru NPs in ILs for hydrogenation reactions.

Catalyst	Synthetic methodology	Characterization techniques	Catalytic reaction conditions	Comments	Ref.
Ru NP/ [OMIm][NTf <sub>2</sub> ]  (average diameter 2.5 nm)	1) Reduce [Ru(COD)(methylallyl) <sub>2</sub> ] in IL, 40 - 60 bar H <sub>2</sub> room temperature	NMR, UV-Vis, TEM	0.03 to 0.26 mol % catalyst, 1 mL IL 80 bar H <sub>2</sub> : CO <sub>2</sub> = (1:1, 3:1) 100 - 150 °C 12 - 48 h	CO <sub>2</sub> hydrogenation  Best yield 69% of CH <sub>4</sub> using 0.24% Ru catalyst, 1:1 H <sub>2</sub> : CO <sub>2</sub> ratio, 150 °C	[154]
Ru NP/ [DAMI][TfO]  (average diameter 7.1 - 14.1 nm)	1) Reduce [RuCl <sub>2</sub> (C <sub>6</sub> H <sub>6</sub> ) <sub>2</sub> ] / [Ru(COD)(methylallyl) <sub>2</sub> ] in 1 mL, 50 °C, 4 bar H <sub>2</sub> , 2 h.  2) Evaporate the black solution.	XRD, XPS, ICP-OES, TEM SAXS	50 wt.% Ru metal, 5 h, 50 - 100 °C H <sub>2</sub> : CO <sub>2</sub> = (1:1)	CO <sub>2</sub> hydrogenation  22,689 TON towards formic acid formation	[155]

**Table 1.6** Recent examples of the application of Ru NPs in ILs for hydrogenation reactions.

Catalyst	Synthetic methodology	Characterization	Catalytic reaction conditions	Comments	Ref.
Ru NP/ILs	1) Reduce [Ru(2-methylallyl)2COD] in 0.3 g IL. 90 °C, argon, 18 h	TEM, ATR - IR	2 mol% Ru metal, 5 h, 80 °C, 10 bar H <sub>2</sub>	Quinoline hydrogenation	[156]
ILs = [BMMIm][NTf <sub>2</sub> ] [BMIm][NTf <sub>2</sub> ] [C <sub>10</sub> MMIm][NTf <sub>2</sub> ] [C <sub>1</sub> C <sub>1</sub> (EG)Im][NTf <sub>2</sub> ] [C <sub>2</sub> OHMIm][NTf <sub>2</sub> ] (average diameter 1.6 - 3.4 nm)	2) Evaporate the black solution.			Best catalyst - Ru NP/ [C <sub>1</sub> C <sub>1</sub> (EG)Im][NTf <sub>2</sub> ] 100% conversion and 99% selectivity towards 1,2,3,4- tetrahydroquinoline (THQ)	



**Table 1.6** Recent examples of the application of Ru NPs in ILs for hydrogenation reactions.

Catalyst	Synthetic methodology	Characterization	Catalytic reaction conditions	Comments	Ref.
RuNP@ 1) O PPh <sub>2</sub> -PIILS 2) O PPh <sub>2</sub> -PEGPIIL 3) O PPh <sub>2</sub> -PIILS 4) O PPh <sub>2</sub> -PEGPIILS (phosphine oxide-decorated polymer immobilized ionic liquid PIIL)	1) Suspend stabilizer in 25 mL ethanol and add RuCl <sub>3</sub> ·3H <sub>2</sub> O in 5 mL ethanol. 2) Stir vigorously for 4h at room temperature. 3) Cool mixture to 0 °C and add NaBH <sub>4</sub> dropwise and stir mixture overnight. 4) Concentrate solvent under reduced pressure. 5) Add cold acetone 300 mL and stir for 1 h. 6) Collect filtrate wash with water, acetone and diethyl ether and dry the black powder.	ICP-OES, TEM, XPS, ATR - IR	0.1 mol% of Ru metal, 3 h, 50 °C, 5 bar H <sub>2</sub>	CO Hydrogenation (aryl and heteroaryl ketones and aldehydes)  RuNP@O=PPh <sub>2</sub> - PEGPIILP was found to be the most efficient catalyst.	[157]

**Table 1.6** Recent examples of the application of Ru NPs in ILs for hydrogenation reactions.

Catalyst	Synthetic methodology	Characterization	Catalytic reaction conditions	Comments	Ref.
Ru@PIL(CL)	1) Dissolve PIL (X = Cl, Br, I) and the required quantity of RuCl <sub>3</sub> ·H <sub>2</sub> O or RuBr <sub>3</sub> ·H <sub>2</sub> O in 40 ml of ethylene glycol.	TGA, TEM, XRD, XPS, UV-Vis	0.33 mol% of Ru catalyst, 60 min, 110 °C, 25 bar H <sub>2</sub> .	Phenol, styrene Hydrogenation	[158]
Ru@PIL(Br)					
Ru@PIL(I)					
Ru@PIL(NTf <sub>2</sub> )					
PIL = poly(1-butyl-3-vinyl-imidazolium) (average diameter 1.2 - 2.6 nm)	2) Stir for 4 h and the black solution heated to 170 °C for 1.5 h. 3) Dissolve the resulting sticky black in 5 mL of methanol and centrifuge with 25 mL of diethyl ether.			Activity and selectivity could simply be manipulated through counter-anion exchange: for instance, NTf <sub>2</sub> results in 100% selectivity towards ethyl cyclohexane and I anion shows 100% selectivity towards ethylbenzene.	
	4) Collected the PIL stabilized NPs and centrifuge 5 ml of NP solution with a 30 ml mixture of diethyl ether and acetone.				
	5) Vacuum dry the resulting shiny black product at 35 °C				

#### 1.2.4.2 Hydrogenation with Ni NPs in ILs

Selective hydrogenation reaction is traditionally facilitated by noble metals like Pd, Ru, and Pt. Nickel-based metal NPs were initially considered as poor catalysts because of their sensitivity to oxidation when exposed to air or solvents such as water. Despite of this, Ni NPs synthesized using various stabilizers, including ILs, have emerged as providing good conversion and selectivity in various hydrogenation reactions with substrates such as olefins, nitro compounds and  $\alpha,\beta$ -unsaturated aldehydes. Examples of different catalytic hydrogenation reactions using Ni NPs synthesized in ILs have been provided in **Table 1.7** and additionally in Chapter 4.

**Table 1.7** Examples of the application of Ni NPs in ILs for hydrogenation reactions.

Catalyst	Synthetic methodology	Characterization	Catalytic reaction conditions	Comments	Ref.
IL-NH <sub>2</sub> -Ni	1) Dissolve Ni(OAc) <sub>2</sub> ·4H <sub>2</sub> O in 20 mL ethanol and add IL in 2 mL methanol to it and mix for 4h at room temperature.	EA, TEM, TGA, XRD, XPS, UV-Vis	27 mmol/L Ni 2 mL solvent (H <sub>2</sub> O, IL-s), 10 min, 90 °C, 30 bar H <sub>2</sub>	CO, C=C bond Hydrogenation	[159]
IL-NH <sub>2</sub> = 1-(3-aminopropyl)-2,3-dimethylimidazolium bromide ([AMMIm] Br) (average diameter 6 - 7 nm)	2) Add NaOH and 1 mL N <sub>2</sub> H <sub>4</sub> ·H <sub>2</sub> O to the mixture at 90 °C and stir for 10 min.  3) Washed with methanol and dry under reduced pressure.		IL.s = [BMMIm][PF <sub>6</sub> ] [BMMIm][BF <sub>4</sub> ] [BMMIm][CH <sub>3</sub> SO <sub>3</sub> ]	90% conversion and selectivity towards -phenyl-2-butanone when H <sub>2</sub> O was used as a solvent in reaction medium	

**Table 1.7** Examples of the application of Ni NPs in ILs for hydrogenation reactions.

Catalyst	Synthetic methodology	Characterization	Catalytic reaction conditions	Comments	Ref.
Ni NPs/ [BMMIm]OAc - Pluronic - P123 mixed micelle. (average diameter 8 ± 1.4 nm)	1) Stir 5 ml anhydrous ethanol containing triblock polymers and Ni(OAc) <sub>2</sub> ·4H <sub>2</sub> O under nitrogen atmosphere. After stirred at RT for 5 h. 2) Add 4 mg NaOH slowly to the solution, followed by 13 mg N <sub>2</sub> H <sub>4</sub> ·H <sub>2</sub> O reductant at 70 °C. After 10 min, the color of the solution will change from green to brownish black. 3) Cooled mixture to RT, and then use a dialysis membrane to remove residual ethanol and base. 4) Concentrated the resulting Ni NP aqueous solution to 2 ml, and under N <sub>2</sub> atmosphere.	UV-Vis, XRD, XPS, TEM	0.05 mmol Ni catalyst, 2 mL solvent (H <sub>2</sub> O), 5 h, 65 °C, 15 bar H <sub>2</sub> .	olefins and α, β - unsaturated aldehydes, nitro compound Hydrogenation  >99% selectivity towards CC bonds reduction in α, β - unsaturated aldehydes and >95% selectivity towards NO <sub>2</sub> reduction in nitro compounds.	[160]

### 1.2.5 Bimetallic nanoparticles

Apart from monometallic NPs, NPs containing a mixture of two (bimetallic) or more metals are also interesting species for catalytic applications. They generally present an improvement of properties due to the synergistic effects between the metals, and the rich variety of structures, compositions, and properties [161]. The organometallic approach is also performant for the synthesis of bimetallic NPs [162,163]. The four main types of bimetallic nanostructures are shown in **Figure 1.12** and are: a) core-shell, b) subcluster segregated, c) mixed and d) three-shell NPs [161].

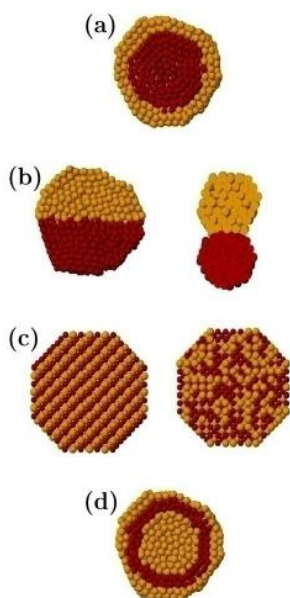


**Figure 1.12** Schematic representation of some possible mixing patterns in bimetallic MNPs: a) core-shell, b) subcluster segregated, c) mixed and d) three-shell NPs [154].

#### 1.2.5.1 Bimetallic NPs in catalysis

Alloying allows the fine-tuning and modification of metal properties, including catalytic activity [164]. The mutual influence between different neighboring atoms can result in catalytic behavior that is different and often better from that of monometallic clusters due to “synergistic effects” [165]. Bimetallic catalysts using Pt with Ir or Re have seen widespread application in

petrochemical reforming [161]. Bimetallic NPs containing different transition metals have been used in hydrogenation reactions for substrates like CO<sub>2</sub> as well as biomass-derived substrates among others. For instance, Philippot, Axet and coworkers reported the synthesis of core-shell Ru@Pt (core@shell) and Pt@Ru NPs by two step decomposition of [Ru(COD)(COT)] and [Pt(CH<sub>3</sub>)<sub>2</sub>(COD)] in different molar ratios (1:1, 1:2, 1:4) using 4-(3-phenylpropyl)pyridine (PPP) as a stabilizer [162]. They employed the NPs for the selective hydrogenation of cinnamaldehyde (CAL). They observed a direct correlation between the catalytic activity and surface Pt content with higher surface Pt resulting in higher activity. Thus, Ru<sub>1</sub>Pt<sub>4</sub> NPs exhibited higher activity compared to other compositions in the RuPt series, and similarly, Pt<sub>1</sub>Ru<sub>1</sub> NPs in the PtRu series. The same group also synthesized RuNi NPs by the decomposition of [Ru(COD)(COT)] and [Ni(COD)<sub>2</sub>] by H<sub>2</sub> in the presence of polyvinylpyrrolidone (PVP) as ligand using different Ru/Ni ratio. The catalytic activity of the NPs was studied by applying it for the selective hydrogenation of furfural. They showed that catalysts presenting Ni on the surface were highly selective towards the partially hydrogenated products, while those with Ru were able to hydrogenate the heteroaromatic ring [166].

Bimetallic NPs synthesized in ILs have also proved to be efficient catalysts for hydrogenation reactions. For example, Dietrich *et al.* reported the synthesis of PtSn NPs with an average diameter of 2-3 nm by chemical reduction of the metal salt precursors PtCl<sub>2</sub> and Sn(OAc)<sub>2</sub> in [MOc<sub>3</sub>N][NTf<sub>2</sub>] (methyltrioctylammonium bis(trifluoromethylsulfonyl)imide) IL using triethylborohydride as reducing agent. The catalyst was employed in the selective hydrogenation of cinnamaldehyde. The PtSn NPs showed higher selectivity (80-100%) towards the  $\alpha,\beta$ -unsaturated cinnamic alcohol whereas monometallic Pt NPs showed 100% selectivity towards hydrocinnamic aldehyde [167]. Dupont and coworkers [168], reported the synthesis of bimetallic core@shell Ru@Pt NPs by the decomposition of [Ru(COD)(2-methylallyl)<sub>2</sub>] followed by [Pt<sub>2</sub>(dba)<sub>3</sub>] in [BMIm][PF<sub>6</sub>] (1-butyl-3-methylimidazolium hexafluorophosphate) and obtained NPs with average size 2.9  $\pm$  0.2 nm. They performed the hydrogenation of benzene by dissolving the NPs in n-heptane which afforded 5% benzene conversion with 21% selectivity towards 1,3-cyclohexadiene, a performance which was not observed when using monometallic Pt or Ru NPs under the same reaction conditions. Dupont and coworkers [169] also reported the synthesis of RuNi NPs with an average diameter of 2-3 nm, containing a Ru rich shell and Ni-rich core in

[BMIm][NTf<sub>2</sub>] IL using the precursors [Ni(COD)<sub>2</sub>] and [Ru(COD)(2-methylallyl)<sub>2</sub>]. They employed the NPs for CO<sub>2</sub> hydrogenation and found that the RuNi NPs in [BMIm][NTf<sub>2</sub>] (hydrophobic IL) allowed 30% conversion of CO<sub>2</sub> to light hydrocarbons (79% alkanes, 16% olefins and 5% CH<sub>4</sub>) under very mild reaction conditions, whereas [BMIm][BF<sub>4</sub>] (hydrophilic IL) mainly afforded CO. The same group immobilized RuPd NPs in [BMIM][PF<sub>6</sub>] IL using [Ru(COD)(2-methylallyl)<sub>2</sub>] and [Pd<sub>2</sub>(dba)<sub>3</sub>] as precursors and obtained well-dispersed RuPd NPs with an average diameter of 2.2 ± 1.1 nm (RuPd 1:1), 2.2 ± 0.5 nm (RuPd 1:9) and 3.6 ± 1.8 nm (RuPd 9:1), respectively. The catalytic activity of the bimetallic NPs was evaluated in the hydrogenation of benzene and phenol under biphasic conditions (N-heptane/IL mixture). In benzene hydrogenation, NPs generated from a 1:1 ratio of Ru:Pd showed 94% benzene conversion and 99% selectivity towards cyclohexane. However, the conversion decreased under the same reaction conditions when the Ru:Pd ratio was 9:1 or 1:9 showing that decreasing the Pd content made the bimetallic material to behave as pure Ru NP, whereas increasing the Pd content indicated preferable Pd catalytic behavior and reduced the activity towards hydrogenation of arenes. The RuPd NPs were also examined for the selective hydrogenation of phenol, where the bimetallic RuPd NPs (1:1) promoted the hydrogenation of phenol to exclusively form cyclohexanone [170].

### 1.3 Objectives and outlook

The main objectives of the thesis include:

- 1) The synthesis and characterization of ionic liquids (IL) and functionalized ionic liquids (FILs).
- 2) Utilization of the synthesized ILs for synthesis of transition metal nanoparticles (NPs) mainly employing ruthenium, nickel and rhenium metals. Complete characterization of these metal NPs/ILs systems through state of art techniques including TEM, TGA, XPS, NMR, ATR-IR *etc.*
- 3) Employment of the series of metal NPs/ILs systems in catalytic hydrogenation of substrates like styrene, cinnamyl alcohol, 2,3-benzofuran, trans-2-hexen-1-al, hexanal, benzonitrile, benzylamine, phenylacetylene and (R)-(+)-limonene to study the activity and reactivity of such systems.



## 1.4 Summary

The organometallic approach has several advantages and is widely utilized for the synthesis of a diverse range of metal NPs. ILs are potential stabilizers for metal NPs synthesis rendering NPs with different size, shape, morphology, and catalytic properties. Their dual role as solvents during NPs synthesis provide the additional benefit to reduce chemical waste. Metal NPs prepared using ILs have been employed in a wide variety of hydrogenation reactions of CO<sub>2</sub>, ketones and aldehydes, olefins *etc.* Ru and Ni NPs have in particular been found to be effective catalysts in hydrogenation reactions due to their high catalytic efficiency and selectivity, as seen from the plethora of works reported in literature. Careful choice of the ion composition in ILs can impart good catalytic efficiency to the metal NPs and coherently modify the surface, and this PhD work relies in this domain of research. In the next chapters, the synthesis of Ru-, Ni- NPs in FILs (H, MEM, MME and CN) have been performed and their application in hydrogenation catalysis will be described. Synthesis of bimetallic RuRe NPs has also been attempted.

## 1.5 References

1. MacFarlane, D.R.; Kar, M.; Pringle, J.M. *Fundamentals of Ionic Liquids from Chemistry to Applications*, 1st ed.; Wiley-VCH: Weinheim, Germany, **2017**; ISBN 9783527340033.
2. Krossing, I.; Slattery, J.M.; Daguene, C.; Dyson, P.J.; Oleinikova, A.; Weingärtner, H. Why Are Ionic Liquids Liquid? A Simple Explanation Based on Lattice and Solvation Energies. *J. Am. Chem. Soc.* **2006**, *128*, 13427–13434, doi:10.1021/ja0619612.
3. Ehsan Kianfar; Sajjad Mafi Ionic Liquids: Properties, Application, and Synthesis. *Fine Chem. Eng.* **2020**, *22–31*, doi:10.37256/fce.212021693.
4. Consorti, C.S.; Suarez, P.A.Z.; De Souza, R.F.; Burrow, R.A.; Farrar, D.H.; Lough, A.J.; Loh, W.; da Silva, L.H.M.; Dupont, J. Identification of 1,3-Dialkylimidazolium Salt Supramolecular Aggregates in Solution. *J. Phys. Chem. B* **2005**, *109*, 4341–4349, doi:10.1021/jp0452709.
5. Clare, B.; Sirwardana, A.; MacFarlane, D.R. Synthesis, Purification and Characterization of Ionic Liquids. *Top. Curr. Chem.* **2009**, *290*, 1–40, doi:10.1007/128\_2008\_31.
6. Handy, S. Room Temperature Ionic Liquids: Different Classes and Physical Properties. *Curr. Org. Chem.* **2005**, *9*, 959–988, doi:10.2174/1385272054368411.
7. Singh, S.K.; Savoy, A.W. Ionic Liquids Synthesis and Applications: An Overview. *J. Mol. Liq.* **2020**, *297*, 112038, doi:10.1016/j.molliq.2019.112038.
8. Walden, P. *Bull. Acad. Imper. Sci. St. Petersbourg* **1914**, *8*, 405–422.

- 
9. Gordon, C.M.; Muldoon, M.J.; Wagner, M.; Hilgers, C.; Davis, J.H.; Wasserscheid, P. *Synthesis and Purification of ionic liquids*. 2<sup>nd</sup> ed.; John Wiley and Sons, **2008**; Vol.1, pp. 7–55. ISBN 9783527312399.
  10. Menshutkin, N. Über Die Affinitätskoeffizienten Der Alkylhaloide Und Der Amine. *Zeitschrift für Physikalische Chemie* **1890**, *6U*, 41–57, doi:10.1515/zpch-1890-0607.
  11. Menshutkin, N. Beiträge Zur Kenntnis Der Affinitätskoeffizienten Der Alkylhaloide Und Der Organischen Amine. *Zeitschrift für Physikalische Chemie* **1890**, *5U*, 589–600, doi:10.1515/zpch-1890-0546.
  12. Burrell, A.K.; Del Sesto, R.E.; Baker, S.N.; McCleskey, T.M.; Baker, G.A. The Large-Scale Synthesis of Pure Imidazolium and Pyrrolidinium Ionic Liquids. *Green Chem.* **2007**, *9*, 449–45, doi:10.1039/b615950h.
  13. Dzyuba, S. V.; Bartsch, R.A. Efficient Synthesis of 1-Alkyl(Aralkyl)-3-Methyl(Ethyl)Imidazolium Halides: Precursors for Room-Temperature Ionic Liquids. *J Heterocycl. Chem.* **2001**, *38*, 265–268, doi:10.1002/jhet.5570380139.
  14. Cao, Y.; Chen, Y.; Wang, X.; Mu, T. Predicting the Hygroscopicity of Imidazolium-Based ILs Varying in Anion by Hydrogen-Bonding Basicity and Acidity. *RSC Adv.* **2014**, *4*, 5169–5176, doi:10.1039/c3ra44464c.
  15. Hurley, F.H.; Wier, T.P. Electrodeposition of Metals from Fused Quaternary Ammonium Salts. *J. Electrochem. Soc.* **1951**, *98*, 203, doi:10.1149/1.2778132.
  16. Wilkes, J.S.; Levisky, J.A.; Wilson, R.A.; Hussey, C.L. Dialkylimidazolium Chloroaluminate Melts: A New Class of Room-Temperature Ionic Liquids for Electrochemistry, Spectroscopy, and Synthesis. *Inorg. Chem.* **1982**, *21*, 1263–1264, doi:10.1021/IC00133A078.
  17. Robinson, J.; Osteryoung, R.A. An Electrochemical and Spectroscopic Study of Some Aromatic Hydrocarbons in the Room Temperature Molten Salt System Aluminum Chloride-n-Butylpyridinium Chloride. *J. Am. Chem. Soc.* **1979**, *101*, 323–327, doi:10.1021/JA00496A008.
  18. Ratti, R. Ionic Liquids: Synthesis and Applications in Catalysis. *Adv. Chem.* **2014**, *2014*, 1–16, doi:10.1155/2014/729842.
  19. Williams, S.D.; Schoebrechts, J.P.; Selkirk, J.C.; Mamantov, G. A New Room Temperature Molten Salt Solvent System: Organic Cation Tetrachloroborates. *J. Am. Chem. Soc.* **1987**, *109*, 2218–2219, doi:10.1021/JA00241A069.
  20. Chauvin, Y.; Einloft, S.; Olivier, H. Catalytic Dimerization of Propene by Nickel-Phosphine Complexes in 1-Butyl-3-Methylimidazolium Chloride/AlEt<sub>x</sub>Cl<sub>3-x</sub> (x = 0, 1) Ionic Liquids. *Ind. Eng. Chem. Res.* **1995**, *34*, 1149–1155, doi:10.1021/ie00043a017.
  21. Fuller, J.; Carlin, R.T.; De Long, H.C.; Haworth, D. Structure of 1-Ethyl-3-Methylimidazolium Hexafluorophosphate: Model for Room Temperature Molten Salts. *J. Chem. Soc. Chem. Commun.* **1994**, 299, doi:10.1039/c39940000299.
  22. Holbrey, J.D.; Seddon, K.R. The Phase Behaviour of 1-Alkyl-3-Methylimidazolium Tetrafluoroborates; Ionic Liquids and Ionic Liquid Crystals. *J. Chem. Soc., Dalton Trans.* **1999**, 2133–2140, doi:10.1039/a902818h.
  23. Helfferich, F. Ion exchange McGraw-Hill Book Co. *Inc., New York*, **1962** 90.
  24. Mizuta, K.; Kasahara, T.; Hashimoto, H.; Arimoto, Y. **2006** PCT/JP2006/322693
-

- 
25. a) R. S. Kalb, W. Wesner, R. Hermann, M. Kotschan, M. Schelch and W. Staber, Patents WO2005021484, EP1658262B1, US8075803B2; (b) R. S. Kalb, Patents 55 WO2008052860, EP2079705B1; (c) R. S. Kalb, Patents WO2008052863, E P2079707B1; (d) R. S. Kalb, Patent Application WO2008052861
  26. Kalb, R.S.; Damm, M.; Verevkin, S.P. Carbonate Based Ionic Liquid Synthesis (CBILS®): Development of the Continuous Flow Method for Preparation of Ultra-Pure Ionic Liquids. *React. Chem. Eng.* **2017**, *2*, 432–436, doi:10.1039/C7RE00028F.
  27. Kalb, R.S.; Stepurko, E.N.; Emel'yanenko, V.N.; Verevkin, S.P. Carbonate Based Ionic Liquid Synthesis (CBILS®): Thermodynamic Analysis. *Phys. Chem. Chem. Phys.* **2016**, *18*, 31904–31913, doi:10.1039/C6CP06594E.
  28. Andanson, J.M.; Meng, X.; Traïkia, M.; Husson, P. Quantification of the Impact of Water as an Impurity on Standard Physico-Chemical Properties of Ionic Liquids. *J. Chem. Thermodyn.* **2016**, *94*, 169–176, doi:10.1016/j.jct.2015.11.008.
  29. Appetecchi, G.B.; Scaccia, S.; Tizzani, C.; Alessandrini, F.; Passerini, S. Synthesis of Hydrophobic Ionic Liquids for Electrochemical Applications. *J. Electrochem. Soc.* **2006**, *153*, A1685, doi:10.1149/1.2213420.
  30. Anderson, J.L.; Armstrong, D.W.; Wei, G.T. Ionic Liquids in Analytical Chemistry. *Anal. Chem.* **2006**, *78*, 2893–2902, doi:10.1021/AC069394O.
  31. Pucheault, M.; Vaultier, M. Task Specific Ionic Liquids and Task Specific Onium Salts. *Top. Curr. Chem.* **2009**, *290*, 83–126, doi:10.1007/128\_2008\_33.
  32. Han, L.; Choi, S.J.; Park, M.S.; Lee, S.M.; Kim, Y.J.; Kim, M. Il; Liu, B.; Park, D.W. Carboxylic Acid Functionalized Imidazolium-Based Ionic Liquids: Efficient Catalysts for Cycloaddition of CO<sub>2</sub> and Epoxides. *React. Kinet. Mech. Catal.* **2012**, *106*, 25–35, doi:10.1007/s11144-011-0399-8.
  33. Cai, Y.Q.; Lu, F.; Peng, Y.Q.; Song, G.H. Preparation and Characterization of Amino or Carboxyl-Functionalized Ionic Liquids. *Chin. Chem. Lett.* **2007**, *18*, 21–23, doi:10.1016/j.ccl.2006.11.018.
  34. Fei, Z.; Zhao, D.; Pieraccini, D.; Ang, W.H.; Geldbach, T.J.; Scopelliti, R.; Chiappe, C.; Dyson, P.J. Development of Nitrile-Functionalized Ionic Liquids for C-C Coupling Reactions: Implication of Carbene and Nanoparticle Catalysts. *Organometallics* **2007**, *26*, 1588–1598, doi:10.1021/om060950e.
  35. Bates, E.D.; Mayton, R.D.; Ntai, I.; Davis, J.H. CO<sub>2</sub> Capture by a Task-Specific Ionic Liquid. *J. Am. Chem. Soc.* **2002**, *124*, 926–927, doi:10.1021/ja017593d.
  36. Feng, G.R.; Peng, J.J.; Qiu, H.Y.; Jiang, J.X.; Tao, L.; Lai, G.Q. Synthesis of Novel Greener Functionalized Ionic Liquids Containing Appended Hydroxyl. *Synth. Commun.* **2007**, *37*, 2671–2675, doi:10.1080/00397910701465230.
  37. Visser, A.E.; Swatloski, R.P.; Reichert, W.M.; Mayton, R.; Sheff, S.; Wierzbicki, A.; Davis, J.; Rogers, R.D. Task-Specific Ionic Liquids for the Extraction of Metal Ions from Aqueous Solutions. *Chem. Comm.* **2001**, 135–136, doi:10.1039/b008041l.
  38. Fei, Z.; Geldbach, T.J.; Zhao, D.; Dyson, P.J. From Dysfunction to Bis-Function: On the Design and Applications of Functionalised Ionic Liquids. *Chem. Eur. J.* **2006**, *12*, 2122–2130, doi:10.1002/chem.200500581.
-

- 
39. Lee, S.G. Functionalized Imidazolium Salts for Task-Specific Ionic Liquids and Their Applications. *Chem. Comm.* **2006**, 1049–1063, doi:10.1039/b514140k.
  40. Davis, J.H. Task-Specific Ionic Liquids. *Chem. Lett.* **2004**, *33*, 1072–1077, doi:10.1246/CL.2004.1072.
  41. Wasserscheid, P.; Driessen-Hölscher, B.; Van Hal, R.; Steffens, H.C.; Zimmermann, J. New, Functionalised Ionic Liquids from Michael-Type Reactions—a Chance for Combinatorial Ionic Liquid Development. *Chem. Comm.* **2003**, *3*, 2038–2039, doi:10.1039/b306084e.
  42. Rooney, D.; Jacquemin, J.; Gardas, R. Thermophysical Properties of Ionic Liquids. *Top. Curr. Chem.* **2009**, *290*, 185–212, doi:10.1007/128\_2008\_32.
  43. Suarez, P.A.Z.; Einloft, S.; Dullius, J.E.L.; De Souza, R.F.; Dupont, J. Synthesis and Physical-Chemical Properties of Ionic Liquids Based on 1- n-Butyl-3-Methylimidazolium Cation. *J. Chim. Phys. Physicochim. Biol.* **1998**, *95*, 1626–1639, doi:10.1051/jcp:1998103.
  44. Dzyuba, S. V.; Bartsch, R.A. Influence of Structural Variations in 1-Alkyl(Aralkyl)-3-Methylimidazolium Hexafluorophosphates and Bis(Trifluoromethylsulfonyl)Imides on Physical Properties of the Ionic Liquids. *ChemPhysChem* **2002**, *3*, 161–166, doi:10.1002/1439-7641(20020215)3.
  45. Ngo, H.L.; LeCompte, K.; Hargens, L.; McEwen, A.B. Thermal Properties of Imidazolium Ionic Liquids. *Thermochim. Acta* **2000**, *357–358*, 97–102, doi:10.1016/S0040-6031(00)00373-7.
  46. Holbrey, J.D.; Rogers, R.D.; Mantz, R.A.; Trulove, P.C.; Cocalia, V.A.; Visser, A.E.; Anderson, J.L.; Anthony, J.L.; Brennecke, J.F.; Maginn, E.J.; et al. Physicochemical Properties. In *Ionic Liquids in Synthesis: Second Edition*; John Wiley and Sons, **2008**; Vol. 1, pp. 57–174 ISBN 9783527312399.
  47. Jacquemin, J.; Ge, R.; Nancarrow, P.; Rooney, D.W.; Costa Gomes, M.F.; Pádua, A.A.H.; Hardacre, C. Prediction of Ionic Liquid Properties. I. Volumetric Properties as a Function of Temperature at 0.1 MPa. *J. Chem. Eng. Data* **2008**, *53*, 716–726, doi:10.1021/je700707y.
  48. Troncoso, J.; Cerdeiriña, C.A.; Sanmamed, Y.A.; Romaní, L.; Rebelo, L.P.N. Thermodynamic Properties of Imidazolium-Based Ionic Liquids: Densities, Heat Capacities, and Enthalpies of Fusion of [Bmim][PF6] and [Bmim][NTf2]. *J. Chem. Eng. Data* **2006**, *51*, 1856–1859, doi:10.1021/je060222y.
  49. Baker, S.N.; Baker, G.A.; Kane, M.A.; Bright, F. V. The Cybotactic Region Surrounding Fluorescent Probes Dissolved in 1-Butyl-3-Methylimidazolium Hexafluorophosphate: Effects of Temperature and Added Carbon Dioxide. *J. Phys. Chem. B* **2001**, *105*, 9663–9668, doi:10.1021/jp0103528.
  50. Harris, K.R.; Woolf, L.A.; Kanakubo, M. Temperature and Pressure Dependence of the Viscosity of the Ionic Liquid 1-Butyl-3-Methylimidazolium Hexafluorophosphate. *J. Chem. Eng. Data* **2005**, *50*, 1777–1782, doi:10.1021/IE050147B.
  51. Noorhisham, N.A.; Amri, D.; Mohamed, A.H.; Yahaya, N.; Ahmad, N.M.; Mohamad, S.; Kamaruzaman, S.; Osman, H. Characterisation Techniques for Analysis of Imidazolium-Based Ionic Liquids and Application in Polymer Preparation: A Review. *J. Mol. Liq.* **2021**, *326*, 115340, doi:10.1016/j.molliq.2021.115340.
-

- 
52. Margreth, M.; Schlink, R.; Steinbach, A. Water Determination By Karl Fischer Titration. *Pharmaceutical Sciences Encyclopedia* **2010**, doi:10.1002/9780470571224.PSE415.
  53. Liu, D.; Gui, J.; Zhu, X.; Song, L.; Sun, Z. Synthesis and Characterization of Task-Specific Ionic Liquids Possessing Two Brønsted Acid Sites. *Synth. Commun.* **2007**, *37*, 759–765, doi:10.1080/00397910601131429.
  54. Pillai, P.; Pal, N.; Mandal, A. Synthesis, Characterization, Surface Properties and Micellization Behaviour of Imidazolium-Based Ionic Liquids. *J. Surfactants Deterg.* **2017**, *20*, 1321–1335, doi:10.1007/s11743-017-2021-1.
  55. Kolbeck, C.; Killian, M.; Maier, F.; Paape, N.; Wasserscheid, P.; Steinrück, H.P. Surface Characterization of Functionalized Imidazolium-Based Ionic Liquids. *Langmuir* **2008**, *24*, 9500–9507, doi:10.1021/la801261h.
  56. AL-Aqmar, D.M.; Abdelkader, H.I.; Abou Kana, M.T.H. Imidazolium Based Ionic Liquids as Novel Benign Media for Liquid-Dye Laser Systems. *J. Mol. Liq.* **2017**, *231*, 370–378, doi:10.1016/j.molliq.2017.02.019.
  57. Martinelli, A.; Maréchal, M.; Östlund, Å.; Cambedouzou, J. Insights into the Interplay between Molecular Structure and Diffusional Motion in 1-Alkyl-3-Methylimidazolium Ionic Liquids: A Combined PFG NMR and X-Ray Scattering Study. *Phys. Chem. Chem. Phys.* **2013**, *15*, 5510–5517, doi:10.1039/C3CP00097D.
  58. Pan, X.; Wang, M.; Fang, X.; Zhang, C.; Huo, Z.; Dai, S. Ionic Liquid Crystal-Based Electrolyte with Enhanced Charge Transport for Dye-Sensitized Solar Cells. *Sci. China Chem.* **2013**, *56*, 1463–1469, doi:10.1007/s11426-013-4904-y.
  59. Moriel, P.; García-Suárez, E.J.; Martínez, M.; García, A.B.; Montes-Morán, M.A.; Calvino-Casilda, V.; Bañares, M.A. Synthesis, Characterization, and Catalytic Activity of Ionic Liquids Based on Biosources. *Tetrahedron Lett.* **2010**, *51*, 4877–4881, doi:10.1016/j.tetlet.2010.07.060.
  60. Ranke, J.; Stolte, S.; Störmann, R.; Aming, J.; Jastorff, B. Design of Sustainable Chemical Products - The Example of Ionic Liquids. *Chem. Rev.* **2007**, *107*, 2183–2206, <https://doi.org/10.1021/cr050942s>.
  61. Ehsan Kianfar; Sajjad Mafi Ionic Liquids: Properties, Application, and Synthesis. *Fine Chem. Eng.* **2020**, 22–31, doi:10.37256/fce.212021693.
  62. Chowdhury, S.; Mohan, R.S.; Scott, J.L. Reactivity of Ionic Liquids. *Tetrahedron* **2007**, *63*, 2363–2389, doi:10.1016/J.TET.2006.11.001.
  63. Patel, D.D.; Lee, J.M. Applications of Ionic Liquids. *Chem. Rec.* **2012**, *12*, 329–355, doi:10.1002/tcr.201100036.
  64. Loupy, A. *Microwaves in Organic Synthesis*; Wiley-VCH, **2006**; ISBN 9783527314522.
  65. Bösmann, A.; Franci, G.; Janssen, E.; Solinas, M.; Leitner, W.; Wasserscheid, P. Activation, Tuning, and Immobilization of Homogeneous Catalysts in an Ionic Liquid/Compressed CO<sub>2</sub> Continuous-Flow System. *Angew. Chem., Int. Ed. Engl.* **2001**, *40*, 2697–2699, doi:10.1002/1521-3773
  66. Kore, R.; Uppara, P.V.; Rogers, R.D. Replacing HF or AlCl<sub>3</sub> in the Acylation of Isobutylbenzene with Chloroaluminate Ionic Liquids. *ACS Sustain. Chem. Eng.* **2020**, *8*, 10330–10334, doi:10.1021/acssuschemeng.0c03951.
-

- 
67. Bhongale, P. V.; Joshi, S.S.; Mali, N.A. Selective Monoalkylation of Hydroquinone in the Presence of SO<sub>3</sub>H-Functionalized Ionic Liquids as Catalysts. *Chem. Pap.* **2020**, *74*, 4461–4471, doi:10.1007/s11696-020-01230-1.
  68. Garg, G.; Foltran, S.; Favier, I.; Pla, D.; Medina-González, Y.; Gómez, M. Palladium Nanoparticles Stabilized by Novel Choline-Based Ionic Liquids in Glycerol Applied in Hydrogenation Reactions. *Catal. Today* **2020**, *346*, 69–75, doi:10.1016/j.cattod.2019.01.052.
  69. Endres, F. Physical Chemistry of Ionic Liquids. *Phys. Chem. Chem. Phys.* **2010**, *12*, 1648–1648, doi:10.1039/c001176m.
  70. Tomida, D. Thermal conductivity of ionic liquids. *Impact of Thermal Conductivity on Energy Technologies* **2018**, 17-31, doi:10.5772/intechopen.76559
  71. Sánchez-Ramírez, N.; Assresahegn, B.D.; Bélanger, D.; Torresi, R.M. A Comparison among Viscosity, Density, Conductivity, and Electrochemical Windows of N-n-Butyl-N-Methylpyrrolidinium and Triethyl-n-Pentylphosphonium Bis(Fluorosulfonyl Imide) Ionic Liquids and Their Analogues Containing Bis(Trifluoromethylsulfonyl) Imide Anion. *J. Chem. Eng. Data* **2017**, *62*, 3437–3444, doi:10.1021/acs.jced.7b00458.
  72. Yu, G.; Zhao, D.; Wen, L.; Yang, S.; Chen, X. Viscosity of Ionic Liquids: Database, Observation, and Quantitative Structure-Property Relationship Analysis. *AIChE Journal* **2012**, *58*, 2885–2899, doi:10.1002/aic.12786.
  73. Schröder, U.; Wadhawan, J.D.; Compton, R.G.; Marken, F.; Suarez, P.A.Z.; Consorti, C.S.; De Souza, R.F.; Dupont, J. Water-Induced Accelerated Ion Diffusion: Voltammetric Studies in 1-Methyl-3-[2,6-(S)-Dimethylocten-2-Yl]Imidazolium Tetrafluoroborate, 1-Butyl-3-Methylimidazolium Tetrafluoroborate and Hexafluorophosphate Ionic Liquids. *New J. Chem.* **2000**, *24*, 1009–1015, doi:10.1039/b007172m.
  74. Hultgren, V.M.; Mariotti, A.W.A.; Bond, A.M.; Wedd, A.G. Reference Potential Calibration and Voltammetry at Macrodisk Electrodes of Metallocene Derivatives in the Ionic Liquid [Bmim][PF<sub>6</sub>]. *Anal. Chem.* **2002**, *74*, 3151–3156, doi:10.1021/ac015729k.
  75. Kaur, G.; Kumar, H.; Singla, M. Diverse Applications of Ionic Liquids: A Comprehensive Review. *J Mol. Liq.* **2022**, *351*.118556, doi.org/10.3390/molecules28093836.
  76. Fehrmann, R.; Haumann, M.; Riisager, Supported Ionic liquids : fundamentals and applications. John Wiley & Sons, **2014**. ISBN:9783527654789
  77. Kukawka, R.; Pawlowska-Zygarowicz, A.; Dzialkowska, J.; Pietrowski, M.; Maciejewski, H.; Bica, K.; Smiglak, M. Highly Effective Supported Ionic Liquid-Phase (SILP) Catalysts: Characterization and Application to the Hydrosilylation Reaction. *ACS Sustain. Chem. Eng.* **2019**, *7*, 4699–4706, doi:10.1021/acssuschemeng.8b04357.
  78. Gholami, A.; Pourfayaz, F.; Maleki, A. Recent Advances of Biodiesel Production Using Ionic Liquids Supported on Nanoporous Materials as Catalysts: A Review. *Front Energy Res.* **2020**, *8*,144, doi.org/10.3389/fenrg.2020.00144
  79. Meijboom, R.; Haumann, M.; Müller, T.E.; Szesni, N. Synthetic Methodologies for Supported Ionic Liquid Materials. *Supported Ionic Liquids: Fundamentals and Applications* **2014**, 75–94, doi:10.1002/9783527654789
  80. Gu, Y.; Li, G. Ionic Liquids-Based Catalysis with Solids: State of the Art. *Adv. Synth. Catal.* **2009**, *351*, 817–847, doi:10.1002/ADSC.200900043
-

- 
81. Bridier, B.; López, N.; Pérez-Ramírez, J. Molecular Understanding of Alkyne Hydrogenation for the Design of Selective Catalysts. *Dalton Trans.* **2010**, *39*, 8412–8419, doi:10.1039/c0dt00010h.
  82. Riisager, A.; Fehrmann, R.; Flicker, S.; Van Hal, R.; Haumann, M.; Wasserscheid, P. Very Stable and Highly Regioselective Supported Ionic-Liquid-Phase (SILP) Catalysis: Continuous-Flow Fixed-Bed Hydroformylation of Propene. *Angew. Chem., Int. Ed. Engl.* **2005**, *44*, 815–819, doi:10.1002/anie.200461534.
  83. Joni, J.; Haumann, M.; Wasserscheid, P. Development of a Supported Ionic Liquid Phase (SILP) Catalyst for Slurry-Phase Friedel-Crafts Alkylations of Cumene. *Adv. Synth. Catal.* **2009**, *351*, 423–431, doi:10.1002/adsc.200800672.
  84. Mehnert, C.P.; Cook, R.A.; Dispenziere, N.C.; Afeworki, M. Supported Ionic Liquid Catalysis - A New Concept for Homogeneous Hydroformylation Catalysis. *J. Am. Chem. Soc.* **2002**, *124*, 12932–12933, doi:10.1021/ja0279242.
  85. Riisager, A.; Wasserscheid, P.; Van Hal, R.; Fehrmann, R. Continuous Fixed-Bed Gas-Phase Hydroformylation Using Supported Ionic Liquid-Phase (SILP) Rh Catalysts. *J. Catal.* **2003**, *219*, 452–455, doi:10.1016/S0021-9517(03)00223-9.
  86. Yamaguchi, K.; Yoshida, C.; Uchida, S.; Mizuno, N. Peroxotungstate Immobilized on Ionic Liquid-Modified Silica as a Heterogeneous Epoxidation Catalyst with Hydrogen Peroxide. *J. Am. Chem. Soc.* **2005**, *127*, 530–531, doi:10.1021/ja043688e.
  87. Müller, T.E. Supported Ionic Liquids as Part of a Building-Block System for Tailored Catalysts. *Supported Ionic Liquids: Fundamentals and Applications* **2014**, 209–232, doi:10.1002/9783527654789
  88. *Handy, S, Applications of Ionic Liquids in Science and Technology.* **2011**, ISBN 9789533076058.
  89. Fow, K.L.; Jaenicke, S.; Müller, T.E.; Sievers, C. Enhanced Enantioselectivity of Chiral Hydrogenation Catalysts after Immobilisation in Thin Films of Ionic Liquid. *J. Mol. Catal. A Chem.* **2008**, *279*, 239–247, doi:10.1016/j.molcata.2006.11.050.
  90. Huang, J.; Jiang, T.; Gao, H.; Han, B.; Liu, Z.; Wu, W.; Chang, Y.; Zhao, G. Pd Nanoparticles Immobilized on Molecular Sieves by Ionic Liquids: Heterogeneous Catalysts for Solvent-Free Hydrogenation. *Angew. Chem., Int. Ed.* **2004**, *43*, 1397–1399, doi:10.1002/anie.200352682.
  91. Sievers, C.; Jiménez, O.; Knapp, R.; Lin, X.; Müller, T.E.; Türler, A.; Wierczinski, B.; Lercher, J.A. Palladium Catalysts Immobilized in Thin Films of Ionic Liquid for the Direct Addition of Aniline to Styrene. *J. Mol. Catal. A Chem.* **2008**, *279*, 187–199, doi:10.1016/j.molcata.2007.06.016.
  92. Breitenlechner, S.; Fleck, M.; Müller, T.E.; Suppan, A. Solid Catalysts on the Basis of Supported Ionic Liquids and Their Use in Hydroamination Reactions. *J. Mol. Catal. A Chem.* **2004**, *214*, 175–179, doi:10.1016/j.molcata.2003.12.032.
  93. Riisager, A.; Jørgensen, B.; Wasserscheid, P.; Fehrmann, R. First Application of Supported Ionic Liquid Phase (SILP) Catalysis for Continuous Methanol Carbonylation. *Chem. Comm.* **2006**, 994–996, doi:10.1039/b516314e.
-



- 
94. Fow, K.L.; Jaenicke, S.; Müller, T.E.; Sievers, C. Enhanced Enantioselectivity of Chiral Hydrogenation Catalysts after Immobilisation in Thin Films of Ionic Liquid. *J. Mol. Catal. A Chem* **2008**, *279*, 239–247, doi:10.1016/j.molcata.2006.11.050.
  95. Plechkova, N. V.; Seddon, K.R. Applications of Ionic Liquids in the Chemical Industry. *Chem. Soc. Rev.* 2008, *37*, 123–150, doi:10.1039/B006677J
  96. Luska, K.L.; Bordet, A.; Tricard, S.; Sinev, I.; Grünert, W.; Chaudret, B.; Leitner, W. Enhancing the Catalytic Properties of Ruthenium Nanoparticle-SILP Catalysts by Dilution with Iron. *ACS Catal.* **2016**, *6*, 3719–3726, doi:10.1021/acscatal.6b00796.
  97. Knapp, R.; Wyrzgol, S.A.; Reichelt, M.; Hammer, T.; Morgner, H.; Müller, T.E.; Lercher, J.A. Corrugated Ionic Liquid Surfaces with Embedded Polymer Stabilized Platinum Nanoparticles. *J. Phys. Chem. C* **2010**, *114*, 13722–13729, doi:10.1021/jp103250k.
  98. Chun, Y.S.; Shin, J.Y.; Song, C.E.; Lee, S.G. Palladium Nanoparticles Supported onto Ionic Carbon Nanotubes as Robust Recyclable Catalysts in an Ionic Liquid. *Chem. Comm.* **2008**, 942–944, doi:10.1039/b715463a.
  99. You, H.; Yang, S.; Ding, B.; Yang, H. Synthesis of Colloidal Metal and Metal Alloy Nanoparticles for Electrochemical Energy Applications. *Chem. Soc. Rev.* **2013**, *42*, 2880–2904, doi:10.1039/c2cs35319a.
  100. Heiligtag, F.J.; Niederberger, M. The Fascinating World of Nanoparticle Research. *Materials Today* 2013, *16*, 262–271, doi:10.1016/J.MATTOD.2013.07.004
  101. De, M.; Ghosh, P.S.; Rotello, V.M. Applications of Nanoparticles in Biology. *Advanced Materials* **2008**, *20*, 4225–4241, doi.org/10.1002/adma.200703183
  102. Willems VD *Roadmap Report on Nanoparticles.*; Barcelona, Spain, 2005; Willems VD. Roadmap report on nanoparticles. W&W Espana sl, Barcelona, Spain. **2005**, 157.
  103. Philippot, K.; Serp, P. *Concepts in Nanocatalysis*, Wiley-vch Verlag GmbH & Co., **2013**, 1-54, ISBN 978-3-527-33124-6.
  104. D. Astruc *Nanoparticles and Catalysis*; Wiley-VCH, Weinheim, **2008**, ISBN: 978-3-527-31572-7.
  105. Auffan, M.; Rose, J.; Wiesner, M.R.; Bottero, J.Y. Chemical Stability of Metallic Nanoparticles: A Parameter Controlling Their Potential Cellular Toxicity in Vitro. *Environmental Pollution* 2009, *157*, 1127–1133, doi:10.1016/J.ENVPOL.2008.10.002
  106. Corain, B; Schmid, Toshima N, Metal Nanoclusters in Catalysis and Materials Science: The Issue of Size Control, eds. B. Corain, G. Schmid, and N. Toshima, Elsevier, Amsterdam, The Netherlands, **2008**, pp. 3–20, ISBN: 9780444530578
  107. Narayanan, R.; Tabor, C.; El-Sayed, M.A. Can the Observed Changes in the Size or Shape of a Colloidal Nanocatalyst Reveal the Nanocatalysis Mechanism Type: Homogeneous or Heterogeneous? *Top. Catal.* **2008**, *48*, 60–74, doi:10.1007/s11244-008-9057-4.
  108. Narayanan, R.; El-Sayed, M.A. Catalysis with Transition Metal Nanoparticles in Colloidal Solution: Nanoparticle Shape Dependence and Stability. *J. Phys. Chem. B* **2005**, *109*, 12663–12676, doi:10.1021/jp051066p.
  109. Chen, W.; Cai, W.; Zhang, L.; Wang, G.; Zhang, L. Sonochemical Processes and Formation of Gold Nanoparticles within Pores of Mesoporous Silica. *J. Colloid Interface Sci.* **2001**, *238*, 291–295, doi:10.1006/jcis.2001.7525.
-



- 
110. Jamkhande, P.G.; Ghule, N.W.; Bamer, A.H.; Kalaskar, M.G. Metal Nanoparticles Synthesis: An Overview on Methods of Preparation, Advantages and Disadvantages, and Applications. *J. Drug Deliv. Sci. Technol.* 2019, *53*, doi.org/10.1016/j.jddst.2019.101174
  111. Abid, N.; Khan, A.M.; Shujait, S.; Chaudhary, K.; Ikram, M.; Imran, M.; Haider, J.; Khan, M.; Khan, Q.; Maqbool, M. Synthesis of Nanomaterials Using Various Top-down and Bottom-up Approaches, Influencing Factors, Advantages, and Disadvantages: A Review. *Adv. Colloid Interface Sci* 2022, *300*, doi: 10.1016/j.cis.2021.102597
  112. Chaudret, B. Organometallic Approach to Nanoparticles Synthesis and Self-Organization. *C R Phys* 2005, *6*, 117–131, doi.org/10.1016/j.crhy.2004.11.008
  113. Amiens, C.; Chaudret, B.; Ciuculescu-Pradines, D.; Collière, V.; Fajerweg, K.; Fau, P.; Kahn, M.; Maisonnat, A.; Soulantica, K.; Philippot, K. Organometallic Approach for the Synthesis of Nanostructures. *New J. Chem.* **2013**, *37*, 3374–3401, doi:10.1039/c3nj00650f.
  114. Mingos, D.M.P.; Crabtree, R.H.; Theopold, K.H *Comprehensive Organometallic Chemistry III*; Elsevier Ltd., Vol. 12, **2007**, 981,
  115. Pleass, C.M.; Schimmel, D.G. Kinetics of the Deposition of Nickel onto Powder Surfaces from Solutions of Dicyclopentadienylnickel. *J. Catal.* **1972**, *24*, 424–433, doi:10.1016/0021-9517(72)90126-1.
  116. Bradley, J.S.; Hill, E.W.; Chaudret, B.; Duteil, A. Surface Chemistry on Colloidal Metals. Reversible Adsorbate-Induced Surface Composition Changes in Colloidal Palladium-Copper Alloys. *Langmuir* **1995**, *11*, 693–695, doi:10.1021/LA00003A002.
  117. Bradley, J.S.; Millar, J.M.; Hill, E.W.; Behal, S.; Chaudret, B.; Duteil, A. Surface Chemistry on Colloidal Metals: Spectroscopic Study of Adsorption of Small Molecules. *Faraday Discuss* **1991**, *92*, 255–268, doi:10.1039/FD9919200255
  118. Bradley, J.S.; Hill, E.W.; Behal, S.; Klein, C.; Chaudret, B.; Duteil, A. Preparation and Characterization of Organosols of Monodispersed Nanoscale Palladium. Particle Size Effects in the Binding Geometry of Adsorbed Carbon Monoxide. *Chem. Mater* **1992**, *4*, 1234–1239, doi:10.1021/CM00024A023.
  119. Philippot, K.; Lignier, P.; Chaudret, B. Organometallic Ruthenium Nanoparticles and Catalysis. *Top. Organomet. Chem.* **2014**, *48*, 319–370, doi:10.1007/3418\_2014\_83.
  120. Costa, N.J.S.; Guerrero, M.; Collière, V.; Teixeira-Neto, É.; Landers, R.; Philippot, K.; Rossi, L.M. Organometallic Preparation of Ni, Pd, and NiPd Nanoparticles for the Design of Supported Nanocatalysts. *ACS Catal.* **2014**, *4*, 1735–1742, doi:10.1021/cs500337a.
  121. Ayvalı, T.; Lecante, P.; Fazzini, P.F.; Gillet, A.; Philippot, K.; Chaudret, B. Facile Synthesis of Ultra-Small Rhenium Nanoparticles. *Chem. Comm.* **2014**, *50*, 10809–10811, doi:10.1039/c4cc04816d.
  122. Pelzer, K.; Vidoni, O.; Philippot, K.; Chaudret, B.; Collière, V. Organometallic Synthesis of Size-Controlled Polycrystalline Ruthenium Nanoparticles in the Presence of Alcohols. *Adv. Funct. Mater* **2003**, *13*, 118–126, doi:10.1002/ADFM.200390017.
  123. Pan, C.; Pelzer, K.; Philippot, K.; Chaudret, B.; Dassenoy, F.; Lecante, P.; Casanove, M.J. Ligand-Stabilized Ruthenium Nanoparticles: Synthesis, Organization, and Dynamics. *J. Am. Chem. Soc.* **2001**, *123*, 7584–7593, doi:10.1021/JA003961M.
-

- 
124. Pelzer, K.; Laleu, B.; Lefebvre, F.; Philippot, K.; Chaudret, B.; Candy, J.P.; Basset, J.M. New Ru Nanoparticles Stabilized by Organosilane Fragments. *Chem. Mater.* **2004**, *16*, 4937–4941, doi:10.1021/CM049086B.
125. Jansat, S.; Picurelli, D.; Pelzer, K.; Philippot, K.; Gómez, M.; Muller, G.; Lecante, P.; Chaudret, B. Synthesis, Characterization and Catalytic Reactivity of Ruthenium Nanoparticles Stabilized by Chiral N-Donor Ligands. *New J. Chem.* **2006**, *30*, 115–122, doi:10.1039/B509378C.
126. Zahmakiran, M.; Tristany, M.; Philippot, K.; Fajerweg, K.; Özkaz, S.; Chaudret, B. Aminopropyltriethoxysilane Stabilized Ruthenium(0) Nanoclusters as an Isolable and Reusable Heterogeneous Catalyst for the Dehydrogenation of Dimethylamine-Borane. *Chem. Comm.* **2010**, *46*, 2938–2940, doi:10.1039/C000419G.
127. García-Antón, J.; Axet, M.R.; Jansat, S.; Philippot, K.; Chaudret, B.; Pery, T.; Buntkowsky, G.; Limbach, H.H. Reactions of Olefins with Ruthenium Hydride Nanoparticles: NMR Characterization, Hydride Titration, and Room-Temperature C-C Bond Activation. *Angew. Chem. Int. Ed.* **2008**, *47*, 2074–2078, doi:10.1002/ANIE.200704763.
128. Wegner, S.; Janiak, C. Metal Nanoparticles in Ionic Liquids. *Top Curr Chem* **2017**, *375*, 65, doi:10.1007/s41061-017-0148-1.
129. Grubbs, R.B. Roles of Polymer Ligands in Nanoparticle Stabilization. *Polym. Rev.* **2007**, *47*, 197–215, doi:10.1080/15583720701271245.
130. Mourdikoudis, S.; Pallares, R.M.; Thanh, N.T.K. Characterization Techniques for Nanoparticles: Comparison and Complementarity upon Studying Nanoparticle Properties. *Nanoscale* **2018**, *10*, 12871–12934, doi:10.1039/C8NR02278J.
131. Marbella, L.E.; Millstone, J.E. NMR Techniques for Noble Metal Nanoparticles. *Chem. Mater* **2015**, *27*, 2721–2739, doi:10.1021/cm504809c.
132. Sharma, R.; Holland, G.P.; Solomon, V.C.; Zimmermann, H.; Schiffenhaus, S.; Amin, S.A.; Buttry, D.A.; Yarger, J.L. NMR Characterization of Ligand Binding and Exchange Dynamics in Triphenylphosphine-Capped Gold Nanoparticles. *J. Phys. Chem. C* **2009**, *113*, 16387–16393, doi:10.1021/JP90514.
133. Ingham, B. X-Ray Scattering Characterisation of Nanoparticles. *Crystallogr Rev* **2015**, *21*, 229–303, doi:10.1080/0889311X.2015.1024114.
134. Sarma, D.D.; Santra, P.K.; Mukherjee, S.; Nag, A. X-Ray Photoelectron Spectroscopy: A Unique Tool to Determine the Internal Heterostructure of Nanoparticles. *Chem. Mater* **2013**, *25*, 1222–1232, doi:10.1021/CM303567
135. Shukla, N.; Liu, C.; Jones, P.M.; Weller, D. FTIR Study of Surfactant Bonding to FePt Nanoparticles. *J Magn Magn Mater* **2003**, *266*, 178–184, doi:10.1016/S0304-8853(03)00469-4.
136. Busó-Rogero, C.; Brimaud, S.; Solla-Gullon, J.; Vidal-Iglesias, F.J.; Herrero, E.; Behm, R.J.; Feliu, J.M. Ethanol Oxidation on Shape-Controlled Platinum Nanoparticles at Different PHs: A Combined in Situ IR Spectroscopy and Online Mass Spectrometry Study. *J. Electroanal. Chem* **2016**, *763*, 116–124, doi:10.1016/J.JELECHEM.2015.12.034.
-

- 
137. Green, L. Synthesis and Characterization of FePt Magnetic Nanoparticles. *Doctoral thesis, UCL (University College London)*. **2014**.
138. Harkness, K.M.; Cliffel, D.E.; McLean, J.A. Characterization of Thiolate-Protected Gold Nanoparticles by Mass Spectrometry. *Analyst* **2010**, *135*, 868–874, doi:10.1039/B922291J.
139. Elzey, S.; Tsai, D.H.; Rabb, S.A.; Yu, L.L.; Winchester, M.R.; Hackley, V.A. Quantification of Ligand Packing Density on Gold Nanoparticles Using ICP-OES. *Anal Bioanal. Chem.* **2012**, *403*, 145–149, doi:10.1007/S00216-012-5830-0/FIGURES/2.
140. Herrling, M.P.; Fetsch, K.L.; Delay, M.; Blauert, F.; Wagner, M.; Franzreb, M.; Horn, H.; Lackner, S. Low Biosorption of PVA Coated Engineered Magnetic Nanoparticles in Granular Sludge Assessed by Magnetic Susceptibility. *Sci. Total Environ* **2015**, *537*, 43–50, doi:10.1016/J.SCITOTENV.2015.07.161.
141. Yang, T.Q.; Abe, M.; Horiguchi, K.; Enpuku, K. Detection of Magnetic Nanoparticles with Ac Susceptibility Measurement. *Physica. C Supercond* **2004**, *412–414*, 1496–1500, doi:10.1016/J.PHYSC.2004.01.146.
142. H. Kato, S. C. Singh, H. Zeng, C. Guo and W. Cai, Size Determination of NPs by Dynamic Light Scattering, *Nanomaterials: Processing and Characterization with Lasers*, Wiley-VCH, **2012**, ISBN: 978-0-470-17795-2
143. Paramelle, D.; Sadovoy, A.; Gorelik, S.; Free, P.; Hobley, J.; Fernig, D.G. A Rapid Method to Estimate the Concentration of Citrate Capped Silver Nanoparticles from UV-Visible Light Spectra. *Analyst*. **2014**, *139*, 4855–4861, doi:10.1039/C4AN00978A.
144. Casanove, M.-J.; Lecante, P.; Snoeck, E.; Mosset, A.; Roucau, C. HREM and WAXS Study of the Structure of Metallic Nanoparticles. *J. Phys. III* **1997**, *7*, 505–515, doi:10.1051/jp3:1997138.
145. Phung, X.; Groza, J.; Stach, E.A.; Williams, L.N.; Ritchey, S.B. Surface Characterization of Metal Nanoparticles. *Mater. Sci. Eng. A* **2003**, *359*, 261–268, doi:10.1016/S0921-5093(03)00348-4.
146. Dupont, J.; Scholten, J.D. On the Structural and Surface Properties of Transition-Metal Nanoparticles in Ionic Liquids. *Chem. Soc. Rev.* **2010**, *39*, 1780, doi:10.1039/b822551f.
147. Dupont, J.; Suarez, P.A.Z. Physico-Chemical Processes in Imidazolium Ionic Liquids. *Phys. Chem. Chem. Phys.* **2006**, *8*, 2441, doi:10.1039/b602046a.
148. Tsuzuki, S.; Tokuda, H.; Hayamizu, K.; Watanabe, M. Magnitude and Directionality of Interaction in Ion Pairs of Ionic Liquids: Relationship with Ionic Conductivity. *J. Phys. Chem. B* **2005**, *109*, 16474–16481, doi:10.1021/jp0533628.
149. Gozzo, F.C.; Santos, L.S.; Augusti, R.; Consorti, C.S.; Dupont, J.; Eberlin, M.N. Gaseous Supramolecules of Imidazolium Ionic Liquids: ?Magic? Numbers and Intrinsic Strengths of Hydrogen Bonds. *Chem. Eur. J* **2004**, *10*, 6187–6193, doi:10.1002/chem.200305742.
150. Suarez, P.A.Z.; Einloft, S.; Dullius, J.E.L.; de Souza, R.F.; Dupont, J. Synthesis and Physical-Chemical Properties of Ionic Liquids Based on 1-n-Butyl-3-Methylimidazolium Cation. *J. Chim. Phys. Physicochim. Biol* **1998**, *95*, 1626–1639, doi:10.1051/jcp:1998103.
151. Janiak, C. Ionic Liquids for the Synthesis and Stabilization of Metal Nanoparticles. *Zeitschrift für Naturforschung B* **2013**, *68*, 1059–1089, doi:10.5560/znb.2013-3140.
-

- 
152. Somorjai, G.A.; Bruno Chaudret *Nanomaterials in Catalysis*; John Wiley & Sons, **2012**, ISBN: 978-3-527-65687-5
153. Qadir, M.I.; Simon, N.M.; Dupont, J. Catalytic Properties of Metal Nanoparticles Confined in Ionic Liquids. In *Nanoparticles in Catalysis*; Wiley, 2021; pp. 123–138.
154. Melo, C.I.; Szczepańska, A.; Bogel-Lukasik, E.; Nunes da Ponte, M.; Branco, L.C. Hydrogenation of Carbon Dioxide to Methane by Ruthenium Nanoparticles in Ionic Liquid. *ChemSusChem* **2016**, *9*, 1081–1084, doi:10.1002/cssc.201600203.
155. Upadhyay, P.R.; Srivastava, V. Ionic Liquid Mediated In Situ Synthesis of Ru Nanoparticles for CO<sub>2</sub> Hydrogenation Reaction. *Catal. Letters* **2017**, *147*, 1051–1060, doi:10.1007/s10562-017-1995-7.
156. Konnerth, H.; Precht, M.H.G. Selective Hydrogenation of N-Heterocyclic Compounds Using Ru Nanocatalysts in Ionic Liquids. *Green Chem.* **2017**, *19*, 2762–2767, doi:10.1039/C7GC00513J.
157. Doherty, S.; Knight, J.G.; Backhouse, T.; Tran, T.S.T.; Paterson, R.; Stahl, F.; Alharbi, H.Y.; Chamberlain, T.W.; Bourne, R.A.; Stones, R.; et al. Highly Efficient and Selective Aqueous Phase Hydrogenation of Aryl Ketones, Aldehydes, Furfural and Levulinic Acid and Its Ethyl Ester Catalyzed by Phosphine Oxide-Decorated Polymer Immobilized Ionic Liquid-Stabilized Ruthenium Nanoparticles. *Catal. Sci. Technol.* **2022**, *12*, 3549–3567, doi:10.1039/D2CY00205A.
158. Parida, D.; Bakkali-Hassani, C.; Lebraud, E.; Schatz, C.; Grelier, S.; Taton, D.; Vignolle, J. Tuning the Activity and Selectivity of Polymerised Ionic Liquid-Stabilised Ruthenium Nanoparticles through Anion Exchange Reactions. *Nanoscale* **2022**, *14*, 4635–4643, doi:10.1039/D1NR07628K.
159. Hu, Y.; Yu, Y.; Hou, Z.; Yang, H.; Feng, B.; Li, H.; Qiao, Y.; Wang, X.; Hua, L.; Pan, Z.; et al. Ionic Liquid Immobilized Nickel(0) Nanoparticles as Stable and Highly Efficient Catalysts for Selective Hydrogenation in the Aqueous Phase. *Chem. Asian J.* **2010**, *5*, 1178–1184, doi:10.1002/asia.200900628.
160. Yu, Y.; Zhu, W.; Hua, L.; Yang, H.; Qiao, Y.; Zhang, R.; Guo, L.; Zhao, X.; Hou, Z. Ionic Liquid-Pluronic P123 Mixed Micelle Stabilized Water-Soluble Ni Nanoparticles for Catalytic Hydrogenation. *J. Colloid Interface Sci.* **2014**, *415*, 117–126, doi:10.1016/J.JCIS.2013.10.023.
161. Ferrando, R.; Jellinek, J.; Johnston, R.L. Nanoalloys: From Theory to Applications of Alloy Clusters and Nanoparticles. *Chem. Rev.* **2008**, *108*, 845–910, doi: 10.1021/cr040090g
162. Qi, X.; Axet, M.R.; Philippot, K.; Lecante, P.; Serp, P. Seed-Mediated Synthesis of Bimetallic Ruthenium–Platinum Nanoparticles Efficient in Cinnamaldehyde Selective Hydrogenation. *Dalton. Trans.* **2014**, *43*, 9283–9295, doi:10.1039/C3DT53539H.
163. Braga, A.H.; Costa, N.J.S.; Philippot, K.; Gonçalves, R. V.; Szanyi, J.; Rossi, L.M. Structure and Activity of Supported Bimetallic NiPd Nanoparticles: Influence of Preparation Method on CO<sub>2</sub> Reduction. *ChemCatChem* **2020**, *12*, 2967–2976, doi:10.1002/cctc.201902329.
164. Sinfelt, J.H. Supported “Bimetallic Cluster” Catalysts. *J Catal* **1973**, *29*, 308–315, doi:10.1016/0021-9517(73)90234-0.
-

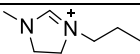
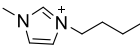
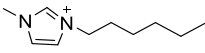
165. Schmid, G.; Lehnert, A.; Malm, J.-O.; Bovin, J.-O. Ligand-Stabilized Bimetallic Colloids Identified by HRTEM and EDX. *Angew. Chem., Int. Ed. Engl.* **1991**, *30*, 874–876, doi:10.1002/anie.199108741.
166. Cardona-Farreny, M.; Lecante, P.; Esvan, J.; Dinoi, C.; del Rosal, I.; Poteau, R.; Philippot, K.; Axet, M.R. Bimetallic RuNi Nanoparticles as Catalysts for Upgrading Biomass: Metal Dilution and Solvent Effects on Selectivity Shifts. *Green Chem.* **2021**, *23*, 8480–8500, doi:10.1039/D1GC02154K.
167. Dietrich, C.; Schild, D.; Wang, W.; Kübel, C.; Behrens, S. Bimetallic Pt/Sn-Based Nanoparticles in Ionic Liquids as Nanocatalysts for the Selective Hydrogenation of Cinnamaldehyde. *Z Anorg. Allg. Chem.* **2017**, *643*, 120–129, doi:10.1002/zaac.201600391.
168. Weilhard, A.; Abarca, G.; Viscardi, J.; Prechtel, M.H.G.; Scholten, J.D.; Bernardi, F.; Baptista, D.L.; Dupont, J. Challenging Thermodynamics: Hydrogenation of Benzene to 1,3-Cyclohexadiene by Ru@Pt Nanoparticles. *ChemCatChem* **2017**, *9*, 204–211, doi:10.1002/cctc.201601196.
169. Qadir, M.I.; Bernardi, F.; Scholten, J.D.; Baptista, D.L.; Dupont, J. Synergistic CO<sub>2</sub> Hydrogenation over Bimetallic Ru/Ni Nanoparticles in Ionic Liquids. *Appl. Catal. B* **2019**, *252*, 10–17, doi:10.1016/j.apcatb.2019.04.005.
170. Abarca, G.; Gonçalves, W.D.G.; Albuquerque, B.L.; Dupont, J.; Prechtel, M.H.G.; Scholten, J.D. Bimetallic RuPd Nanoparticles in Ionic Liquids: Selective Catalysts for the Hydrogenation of Aromatic Compounds. *New J. Chem.* **2021**, *45*, 98–103, doi:10.1039/D0NJ02674C.

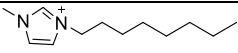
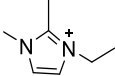
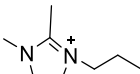
## 2. Synthesis and characterization of imidazolium ionic liquids

### 2.1 Introduction

Imidazolium-based ionic liquids (ILs) have attracted significant interest in the area of metal nanoparticle (NPs) synthesis and catalysis. This is primarily attributed to two main reasons: 1) their capacity to tune the metal nanoparticle size according to the alkyl side chain of the imidazolium and 2) their convenient functionalization to introduce various functionalities that can act as a coordinating capping ligand [1] for the stabilization of the NPs during their synthesis, for *e.g.*, nitrile [2], phosphine [3] *etc.* Additionally, imidazolium cations are precursors to N-heterocyclic carbenes (NHCs) that can be formed by the *in-situ* deprotonation of the acidic C-2 proton of the ring [4]. These NHCs can also serve as a surface coordinating ligand for the NPs stabilization. Many imidazolium salts exist as liquids at room temperature due to their low melting points [5]. These ILs can be synthesized with different counter anions, such as Cl<sup>-</sup>, [BF<sub>4</sub>]<sup>-</sup>, [PF<sub>6</sub>]<sup>-</sup>, and [NTf<sub>2</sub>]<sup>-</sup> (bis(trifluoromethanesulfonyl)imide) [6]. Specifically, the [NTf<sub>2</sub>]<sup>-</sup> anion imparts high thermal stability to imidazolium ILs [7] and provides hydrophobic properties to the ILs [8,9]. As illustration, the decomposition temperature (T<sub>dec</sub>) of some imidazolium-based ILs with different anions is reported in **Table 2.1**, [NTf<sub>2</sub>]<sup>-</sup> based ILs displaying the highest T<sub>dec</sub> [7]. Thermal stability being essential for catalysis as it can be performed at high reaction temperatures [10], high thermal stability for catalysts based in IL is a desirable goal. The hydrophobicity in ILs is interesting as it allows an efficient purification of the ILs by removal of salts with water allowing to obtain high purity compounds.

**Table 2.1** Decomposition temperature T<sub>dec</sub> (°C) of imidazolium based ILs established with thermogravimetric analysis.<sup>a</sup>

Cation	Anions			
	Cl <sup>-</sup>	[BF <sub>4</sub> ] <sup>-</sup>	[PF <sub>6</sub> ] <sup>-</sup>	[NTf <sub>2</sub> ] <sup>-</sup>
C <sub>1</sub> C <sub>3</sub> Im <sup>b</sup> 	269	393	440	453
C <sub>1</sub> C <sub>4</sub> Im 	150	280	349	439
C <sub>1</sub> C <sub>6</sub> Im 	253	425	417	461

	Cation	Anions			
		Cl <sup>-</sup>	[BF <sub>4</sub> ] <sup>-</sup>	[PF <sub>6</sub> ] <sup>-</sup>	[NTf <sub>2</sub> ] <sup>-</sup>
C <sub>1</sub> C <sub>8</sub> Im		243	-	376	425
C <sub>1</sub> C <sub>1</sub> C <sub>2</sub> Im <sup>b</sup>		290	-	500	456
C <sub>1</sub> C <sub>1</sub> C <sub>3</sub> Im		260	390	399	462

<sup>a</sup> Selected data taken from reference [7]. The heat rate is 10 °C.min<sup>-1</sup> and <sup>b</sup> 20 °C.min<sup>-1</sup>

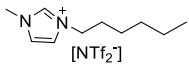
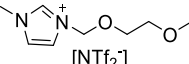
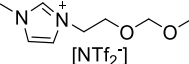
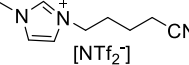
Given their advantages in terms of purification and functionalization, imidazolium type cation and [NTf<sub>2</sub>]<sup>-</sup> anion ILs were chosen to stabilize the metal NPs. Thus, a series of imidazolium-based ILs was synthesized using the Menshutkin reaction, where a tertiary amine is converted into a quaternary ammonium salt by a nucleophilic substitution with an alkyl halide, see chapter 1, **section 1.1.4** for more details. A subsequent anion exchange produces the desired pair of ILs [11]. This chapter focuses on synthesizing task-specific (TS) ILs, namely MEM (1-methoxyethoxymethyl-3-methyl imidazolium bis(trifluoromethanesulfonyl)imide) and MME (1-methoxymethoxyethyl-3-methyl imidazolium bis(trifluoromethanesulfonyl)imide) (**Table 2.3**). This choice is inspired by the literature data evidence that methoxy functionality (**Table 2.2**) can lead to well dispersed and highly active metal nanoparticles for catalysis. Numerous examples can be found in the literature of metal nanoparticles that have been synthesized using polyethylene glycol (PEG) as stabilizer and that have shown high catalytic activity in several reactions. For instance, palladium (Pd) NPs stabilized by PEG demonstrated remarkable catalytic activity and recyclability towards styrene and nitrobenzene hydrogenation under mild reaction conditions. The formed nanoparticles were well dispersed and had an average diameter of 4 nm [12]. As another non-exhaustive example, Sun and coworkers synthesized homogeneously distributed PEG-stabilized Rh nanoparticles of 1.7 nm in size by simple reduction of RhCl<sub>3</sub>.3H<sub>2</sub>O under hydrogen. The formed Rh NPs were found as a highly efficient and recyclable catalyst for the hydroformylation of olefins [13].

**Table 2.2** Selected examples of metal NPs synthesized in stabilizers bearing a methoxy functionality.

Metal precursor	Stabilizer	NP size (nm)	Ref.
Pd(OAc) <sub>2</sub>	PEG <sub>400, 800, 1000, 2000, 4000, 6000</sub>	4 - 5	[12]
RhCl <sub>3</sub> .3H <sub>2</sub> O	PEG <sub>4000</sub>	1.7 ± 0.4	[13]
Pd(OAc) <sub>2</sub>	C <sub>12</sub> Im-PEG IL	1.9 ± 0.3	[14]
Pd(OAc) <sub>2</sub>	PEG <sub>2000, 4000, 6000</sub>	3 - 6	[15]

Given that, our concept entailed to combine the stabilization effect of the methoxy groups and the versatile nature of the ILs by synthesizing imidazolium ILs incorporating the methoxy functionality. A non-functionalized IL, 1-hexyl-3-methyl imidazolium bis(trifluoromethanesulfonyl)imide, H, [16] and one functionalized IL 1-butylcyano-3-methylimidazolium bis(trifluoromethanesulfonyl)imide, CN, [17] (**Table 2.3**) were synthesized for comparison purposes. To gain a comprehensive understanding of the physical and chemical properties of the obtained ILs, a thorough characterization has been performed. This includes analyses by infrared (IR) spectroscopy, thermal gravimetry (TG), differential scanning calorimetry (DSC), X-ray photoelectron spectroscopy (XPS), nuclear magnetic resonance (NMR) spectroscopy (<sup>1</sup>H, <sup>13</sup>C{<sup>1</sup>H}, <sup>19</sup>F, <sup>13</sup>C dept-135) and small angle X-ray scattering (SAXS).

**Table 2.3** Structure of synthesized imidazolium-based ionic liquids.

Ionic liquid	Structure
H	
MEM	
MME	
CN	



## 2.2 Experimental section

### 2.2.1 Synthesis of functionalized ionic liquids (FILs)

**(1-Hexyl-3-methyl imidazolium bis(trifluoromethanesulfonyl)imide (H)).** The synthesis of H was carried out by modifying a previously described procedure [16]. 1-Chlorohexane (13.36 g, 110.7 mmol) was added dropwise to 1-methyl imidazole (8.24 g, 100.2 mmol) in a round bottom flask and the mixture was stirred for 24 h at 80 °C. Then, the solution was washed several times with diethyl ether (50 mL) and dried in vacuo before the addition of Li[NTf<sub>2</sub>] (30.17 g, 104.9 mmol) dissolved in distilled water (20 mL). The mixture was stirred for 24 h at room temperature. The resulting IL (lower phase) was then separated and washed several times with distilled water (≈ 100 mL) until no precipitate of AgCl formed when aqueous AgNO<sub>3</sub> was added to the washing water. Finally, the remaining water was removed by stirring the IL under vacuum (≈ 0.05 mbar) at 60 °C overnight.

**Yield:** 38.90 g (85%).

**<sup>1</sup>H NMR** (400 MHz, CDCl<sub>3</sub>): δ (ppm) 8.97 (s, 1H), 7.29 (t, 3H), 7.26 (t, 1H), 4.17 (t, 2H), 3.95 (s, 3H), 1.86 (m, 2H), 1.32 (m, 6H), 0.88 (t, 2H). **<sup>13</sup>C{<sup>1</sup>H} NMR** (101 MHz, CDCl<sub>3</sub>): δ (ppm) 136.44, 123.71, 122.22, 118.33, 50.42, 36.56, 31.07, 30.15, 25.89, 22.42, 13.96. **<sup>19</sup>F NMR** (376 MHz, CDCl<sub>3</sub>): δ (ppm) -79.01 (s, CF<sub>3</sub>).

**ESI-MS:** positive, ([%]) m/z 167.1 [HMIm]<sup>+</sup> (100); negative, ([%]) m/z 279.9 [NTf<sub>2</sub>]<sup>-</sup> (100).

**IR ν<sub>max</sub>/cm<sup>-1</sup>:** 3157 (w), 2924 (w), 2862 (w), 1346 (s), 1180 (s), 1050 (s).

**Elemental analysis (%)**; Calculated for C<sub>12</sub>H<sub>19</sub>N<sub>3</sub>O<sub>4</sub>S<sub>2</sub>F<sub>6</sub>: C, 32.21; H, 4.28; N, 9.39; Found: C, 32.01; H, 4.22; N, 9.35.

### **1-Methoxyethoxymethyl-3-methyl imidazolium bis(trifluoromethanesulfonyl)imide (MEM).**

The synthesis of MEM was achieved through a similar route as previously described [18]. 2-Methoxyethoxymethyl chloride (6.10 g, 49.0 mmol) was added dropwise to 1-methyl imidazole (4.12 g, 50.1 mmol) dissolved in dry DCM (70 mL) in a Schlenk tube under inert atmosphere. After stirring at room temperature for 24 h, DCM was removed under vacuum, and the remaining IL was washed several times with diethyl ether (≈ 50 mL) followed by removal of excess solvent under vacuum (≈ 0.05 mbar). A solution of Li[NTf<sub>2</sub>] (14.53 g, 52.2 mmol) in distilled water (20 mL) was then added and the mixture stirred at room temperature for 24 h. The resulting IL (lower

phase) was then separated and washed several times with distilled water ( $\approx 100$  mL) until no precipitate of AgCl formed when aqueous AgNO<sub>3</sub> was added to the washing water. Finally, remaining water was removed by stirring the IL under vacuum ( $\approx 0.05$  mbar) at 60 °C overnight.

**Yield:** 20.23 g (90%).

**<sup>1</sup>H NMR** (400 MHz, CDCl<sub>3</sub>):  $\delta$  (ppm) 8.91 (s, 1H), 7.45 (t, 1H), 7.33 (t, 1H), 5.59 (s, 2H), 3.98 (s, 3H), 3.74 (t, 2H), 3.54 (t, 2H), 3.34 (s, 3H). **<sup>13</sup>C{<sup>1</sup>H} NMR** (400 MHz, CDCl<sub>3</sub>):  $\delta$  (ppm) 136.37, 123.80, 121.32, 118.08, 79.38, 71.23, 69.70, 58.91, 36.52. **<sup>19</sup>F NMR** (400 MHz, CDCl<sub>3</sub>):  $\delta$  (ppm) -81.00 (s, CF<sub>3</sub>).

**ESI-MS:** positive, ([%]) m/z 171.1 [MEMmim]<sup>+</sup> (100); (negative, ([%]) m/z 279.9 [NTf<sub>2</sub>]<sup>-</sup> (100).

**IR  $\nu_{\max}/\text{cm}^{-1}$ :** 3162 (w), 2943 (w), 2833 (w), 1346 (s), 1180 (s), 1098 (s), 1050 (s).

**Elemental analysis (%)**; Calculated for C<sub>10</sub>H<sub>15</sub>N<sub>3</sub>O<sub>6</sub>S<sub>2</sub>F<sub>6</sub>: C, 26.60; H, 3.35; N, 9.31. Found: C, 26.02; H, 3.30; N, 9.52.

### **1-Methoxymethoxyethyl-3-methyl imidazolium bis(trifluoromethanesulfonyl)imide (MME).**

The synthesis of MME was performed by modifying a previous described procedure [19]. 1-Bromo-2-(methoxymethoxy)ethane (8.69 g, 51.40 mmol) was added dropwise to 1-methyl imidazole (4.20 g, 51.20 mmol) dissolved in dry acetone (40 mL) in a round bottom flask. The reaction mixture was refluxed at 65 °C for 48 h before washing with acetone ( $\approx 50$  mL) and removing of volatiles *in vacuo*. A solution of Li[NTf<sub>2</sub>] (14.53 g, 52.20 mmol) in distilled water (20 mL) was then added and the reaction mixture stirred at room temperature for 24 h. The resulting IL (lower phase) was then separated and washed several times with distilled water ( $\approx 100$  mL) until no precipitate of AgBr formed when aq. AgNO<sub>3</sub> was added to the washing water. Remaining water was removed by stirring the IL under vacuum ( $\approx 0.05$  mbar) at 60 °C overnight.

**Yield:** 19.16 g (83%).

**<sup>1</sup>H NMR** (400 MHz, CDCl<sub>3</sub>):  $\delta$  (ppm) 8.77 (s, 1H), 7.42 (t, 1H), 7.28 (t, 1H), 4.61 (s, 2H), 4.39 (t, 2H), 3.95 (s, 3H), 3.86 (t, 2H), 3.30 (s, 3H). **<sup>13</sup>C{<sup>1</sup>H} NMR** (400 MHz, CDCl<sub>3</sub>):  $\delta$  (ppm) 136.65, 123.17, 121.37, 118.17, 96.54, 65.20, 55.61, 50.12, 36.41. **<sup>19</sup>F NMR** (400 MHz, CDCl<sub>3</sub>):  $\delta$  (ppm) -81.00 (s, CF<sub>3</sub>).

**ESI-MS:** positive, ([%]) m/z 171.1 [MME<sup>+</sup>mim]<sup>+</sup> (100); negative, ([%]) m/z 279.9 [NTf<sub>2</sub>]<sup>-</sup> (100).

**IR  $\nu_{\max}/\text{cm}^{-1}$ :** 3162 (w), 2943 (w), 2833 (w), 1346 (s), 1180 (s), 1098 (s), 1050 (s).

**Elemental analysis (%)**; Calculated for  $C_{10}H_{15}N_3O_6S_2F_6$ : C, 26.61; H, 3.35; N, 9.31. Found: C, 26.10; H, 3.02; N, 9.52.

**1-Butylcyano-3-methylimidazolium bis(trifluoromethanesulfonyl)imide (CN)**. The synthesis of CN was carried out following a previously described procedure [17]. 5-Chlorovaleronitrile (8.46 g, 71.90 mmol) was slowly added to 1-methyl imidazole (4.92 g, 59.9 mmol) and the mixture stirred at 80 °C for 4 h. Next, the temperature was increased to 110 °C and the reaction was stirred for 24 h. The resulting brownish-yellow liquid was washed several times with diethyl ether ( $\approx$  50 mL) and then decolorized by stirring with a mixture of activated charcoal (0.7 g, 58.2 mmol) in distilled water (10 mL) overnight. After removal of the activated charcoal by filtration,  $Li[NTf_2]$  (20.09 g, 69.9 mmol) in distilled water (20 mL) was added and the reaction mixture stirred at room temperature for 24 h. The resulting IL (lower phase) was then separated and washed several times with distilled water ( $\approx$  100 mL) until no precipitate of AgCl formed when aqueous  $AgNO_3$  was added to the washing water. Remaining water was removed by stirring the IL under vacuum ( $\approx$  0.05 mbar) at 60 °C overnight.

**Yield**: 21.27 g (80%).

**$^1H$  NMR** (400 MHz,  $DMSO-d_6$ ):  $\delta$  (ppm) 8.97 (s, 1H), 7.94 (s, 1H), 7.90 (s, 1H), 4.72 (t, 2H), 4.38 (s, 3H), 2.50 (m, 2H), 2.19 (m, 2H).  **$^{13}C\{^1H\}$  NMR** (400 MHz,  $DMSO-d_6$ ):  $\delta$  (ppm) 135.47, 123.79, 122.26, 48.68, 35.88, 28.69, 21.79, 16.07.  **$^{19}F$  NMR** (400 MHz,  $DMSO-d_6$ ):  $\delta$  (ppm) -80.40 (s,  $CF_3$ ).

**ESI-MS**: positive, ([%])  $m/z$  164.1 [ $C_4CNmim$ ] $^+$  (100); negative, ([%])  $m/z$  279.9 [ $NTf_2$ ] $^-$  (100).

**IR  $\nu_{max}/cm^{-1}$** : 3161(w), 2963(w), 2252(w), 1346(s), 1180(s), 1050(s).

**Elemental analysis (%)**; Calculated for  $C_{11}H_{14}N_4O_4S_2F_6$ : C, 29.73; H, 3.10; N, 12.61. Found: C, 29.70; H, 2.75; N, 12.56.

The materials and characterization methods used have been provided in Chapter 7.

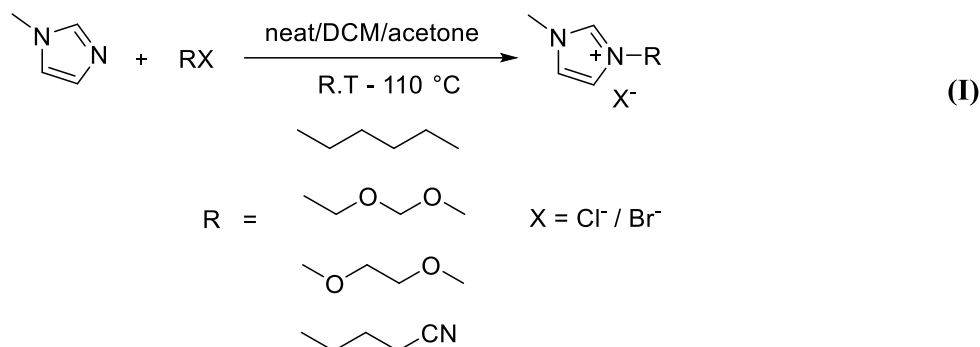
## 2.3 Results and discussion

### 2.3.1 Synthesis of the ILs

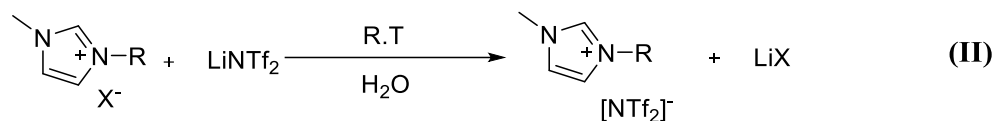
As first step, imidazole was reacted with an alkyl halide (RX) containing the desired functionality. This was done at given temperatures (room temperature (R.T) to 110 °C), in a solvent or under

---

neat condition. This led to the imidazolium halide ( $\text{Cl}^-/\text{Br}^-$ ) IL as the result of the quaternization of the imidazole (**I**).



After washing and drying the obtained imidazolium halide IL with diethyl ether/ethyl acetate or acetone in the case of MME,  $\text{LiNTf}_2$  dissolved in water was added to the IL and the mixture was stirred at R.T (**II**) to perform an anion exchange.



The anion exchange reaction resulted in the formation of water insoluble imidazolium  $[\text{NTf}_2]^-$  IL with  $\text{LiX}$  ( $\text{X} = \text{Cl}^-/\text{Br}^-$ ) as byproduct in the aqueous phase. The aqueous phase was then separated, and the formed IL was repeatedly washed with water to remove the  $\text{LiX}$  ( $\text{X} = \text{Cl}^-/\text{Br}^-$ ). A reaction test was performed to ensure the complete removal of the  $\text{LiX}$ , by addition of  $\text{AgNO}_3$  to the washing aqueous phase. The IL was thus, washed several times until no precipitate of  $\text{AgX}$  was formed.

The so-synthesized ILs were then thoroughly characterized in order to determine their physical and chemical properties, details are given in the next sections.

### 2.3.2 Characterization of the ILs

#### a) ATR-IR analysis

Infrared (IR) spectroscopy is one of the most established and standard technique to characterize ILs [20–22]. This technique allows to identify the functional groups present. Vibrational studies of ILs with imidazolium as cation have been widely discussed in literature [23,24]. The region of

high frequencies ranging from 2800 to 3200  $\text{cm}^{-1}$  displays a composite arrangement of overlapping bands that are specific to various stretching modes of C-H bonds. Within the range of 800 to 1600  $\text{cm}^{-1}$ , distinct bands that correspond to the vibrations of the imidazolium ring can be observed. The range of 400 to 800  $\text{cm}^{-1}$  also encompasses ring vibrations [25]. The stretching frequency of  $[\text{NTf}_2]^-$  anion ranges between 400 – 2000  $\text{cm}^{-1}$  [26]. **Figure 2.1** depicts the IR analyses of the ionic liquids H, MEM, MME, and CN. The bands at 1050, 1180, 1346  $\text{cm}^{-1}$  can be assigned to the stretching frequencies of SN,  $\text{CF}_3$ ,  $\text{SO}_2$ , respectively, in  $[\text{NTf}_2]^-$ . The bands at 1099 and 1098  $\text{cm}^{-1}$  correspond to the C-O stretching of MEM and MME, respectively. The CN stretching can be seen at 2248  $\text{cm}^{-1}$ . The bands at the high frequency region 2800 to 3200  $\text{cm}^{-1}$  correspond to the C-H bonds of the imidazolium cation (**Table 2.4**). The absence of O-H stretching mode of water in the range 3400–3800  $\text{cm}^{-1}$  confirmed the high purity of all the ILs.

**Table 2.4** Infrared spectral bands of ILs.

Wavenumber ( $\text{cm}^{-1}$ )				Assignment	Ref.
H	MEM	MME	CN		
1051 (s)	1049 (s)	1050 (s)	1051 (s)	CC str, $\text{NCH}_3$ twist, SNS asym str	[26]
-	1097 (m)	1097(m)	-	CO str	[27]
1130 (s)	1131(s)	1132 (s)	1130 (s)	$\text{SO}_2$ sym str	
1179 (s)	1179 (s)	1180 (s)	1177 (s)	$\text{CF}_3$ asym str	[26]
1328 (m); 1349 (m)	1346 (m)	1346 (m)	1328 (m); 1348 (m)	$\text{SO}_2$ asym str	
-	-	-	2248 (vw)	CN str	[28]
2931 (w)	2936 (w)	2934 (w)	2963 (vw)	$\text{CH}_3(\text{N})\text{HCH}$ asym Str	
3124 (w)	3120 (w)	3116 (w)	3118 (w)	C-H str	[26]
3151 (w)	3157 (w)	3154 (w)	3158 (w)	C-H str	

vw=very weak; w=weak; m=medium; s=strong; str=stretch, sym=symmetric, asym=asymmetric

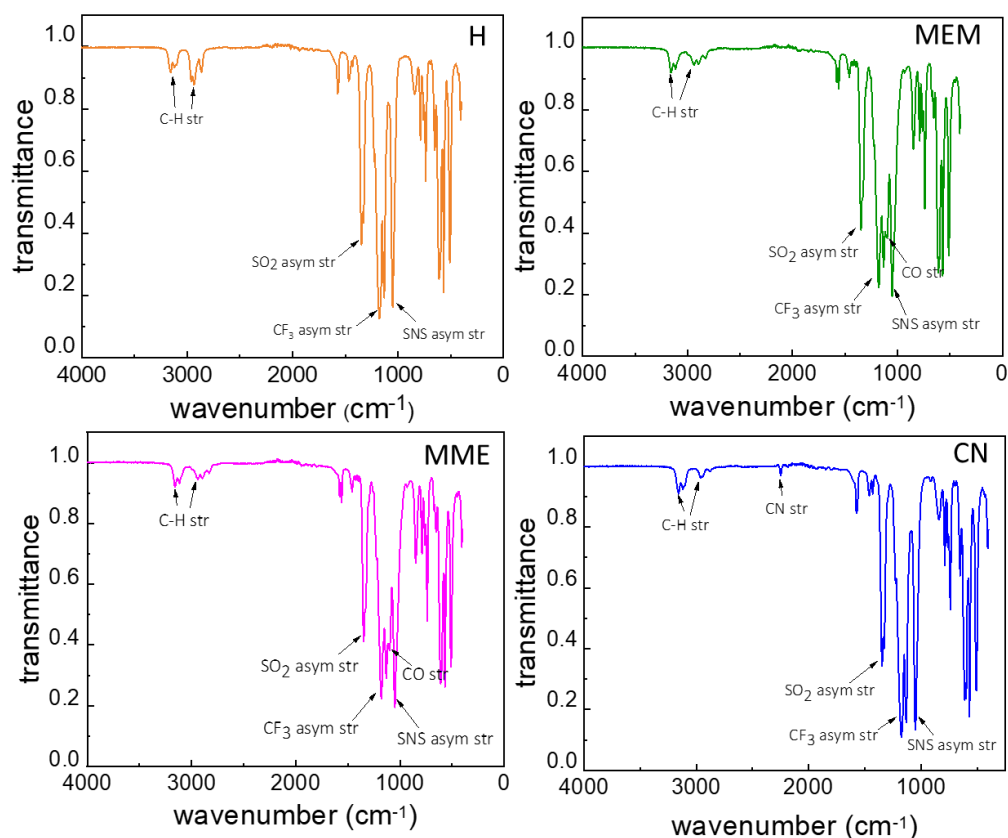


**Figure 2.1** ATR-IR spectra of ILs.

### b) TG and DSC analysis

Thermal gravimetry (TG) and differential scanning calorimetry (DSC) analyses were performed to evaluate the thermal properties of the synthesized ILs. It is known that the side chain of the cation and the nature of the anion influence the thermal stability of the ILs [5]. The thermal decomposition temperature ( $T_{\text{dec}}$ ) of non-functionalized imidazolium-based ILs primarily relies on the nature of the anion, regardless of the specific cation [5]. ILs derived from halides consistently exhibit the lowest  $T_{\text{dec}}$ , whereas the fluorinated anions show the highest  $T_{\text{dec}}$  [29–31]. The order of stability for anions is:  $[\text{NTf}_2]^- > [\text{PF}_6]^- \geq [\text{BF}_4]^- > \text{Cl}^-$  [7]. ILs containing weakly coordinating anions are usually more stable due to their reduced nucleophilic nature. The most common decomposition mechanism resulting in the formation of alkyl halides is the  $\text{S}_{\text{N}}1$  or  $\text{S}_{\text{N}}2$  nucleophilic substitution mechanism [32]. The loss of alkyl chain resulting from the nucleophilic substitution ( $\text{S}_{\text{N}}2$ ) by the anion (reverse Menshutkin reaction) [33,34], the Hofmann elimination yielding alkenes from the

break of the N-C bond [35,36] and rearrangement reactions [37] to obtain different isomers of the alkenes are some of the reactions reported during the decomposition process. N-heterocyclic carbene (NHC), cation ring openings and SO<sub>2</sub> are some of the other products observed [7]. Presence of a functional group can also influence the thermal stability of the imidazolium ILs [38], as a potential decomposition of the functionalized part can happen at lower temperatures. Evidence suggests that  $T_{dec}$  of imidazolium ILs is not sensitive to the presence of oxygen, as similar decomposition behavior is noticed in both N<sub>2</sub> and O<sub>2</sub> environment [5]. However, there is also evidence that some imidazolium salts, namely the tetrafluoroborate and hexafluorophosphates decompose at lower temperature in the presence of oxygen [39]. Impurities (starting materials, Li<sup>+</sup>, H<sub>2</sub>O > 1 wt.%) can also have a significant effect on  $T_{dec}$  [40], requiring a careful removal of impurities by repeated washing with solvents. Water content can be reduced by stirring and heating under high vacuum overnight. In our case, such a treatment afforded a H<sub>2</sub>O amount less than 50 ppm in all ILs. TG analysis of all purified ILs were then performed in N<sub>2</sub> atmosphere in order to compare their thermal stability (**Figure 2.2**).

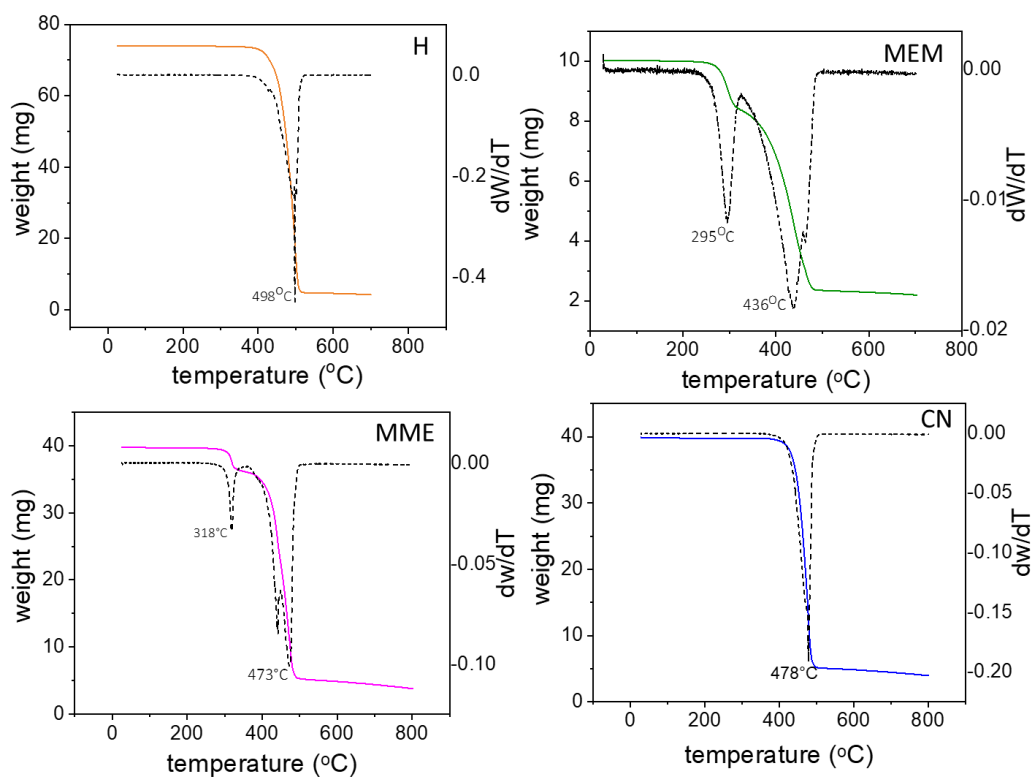


**Figure 2.2** TG analyses of ILs

The H and CN FILs proved to be the most thermally stable, presenting the highest  $T_{\text{dec}}$  with a  $T_{\text{onset}}$  of 404 °C and 454 °C, respectively. In contrast, MEM and MME showed an initial weight loss, attributed to the ether functionalities based on the calculated wt.% loss, between 230–320 °C (18.6 wt.%) and 308–360 °C (7.8 wt.%), respectively, evidencing that the methoxy-containing FILs were thermally less stable. Nevertheless, all the four ILs exhibited good thermal stability.

The DSC curve of ILs generally exhibits four different peaks which are glass transition temperature ( $T_g$ ), crystallization temperature ( $T_c$ )/freezing point ( $T_{\text{fp}}$ ), melting point ( $T_{\text{mp}}$ ) and decomposition temperature ( $T_{\text{dec}}$ ) [41]. The analysis of the calorimetric data for H and MEM, showed supercooling since the freezing point ( $T_{\text{fp}}$ ) was lower than the melting point ( $T_{\text{mp}}$ ) while MME and CN only showed a glass transition ( $T_g$ ) temperature (**Figure 2.3**). **Table 2.5** depicts the melting point ( $T_{\text{mp}}$ ), freezing point ( $T_{\text{fp}}$ ), super cooling ( $\Delta T$ ), and the glass transition temperature ( $T_g$ ) of the four ILs.

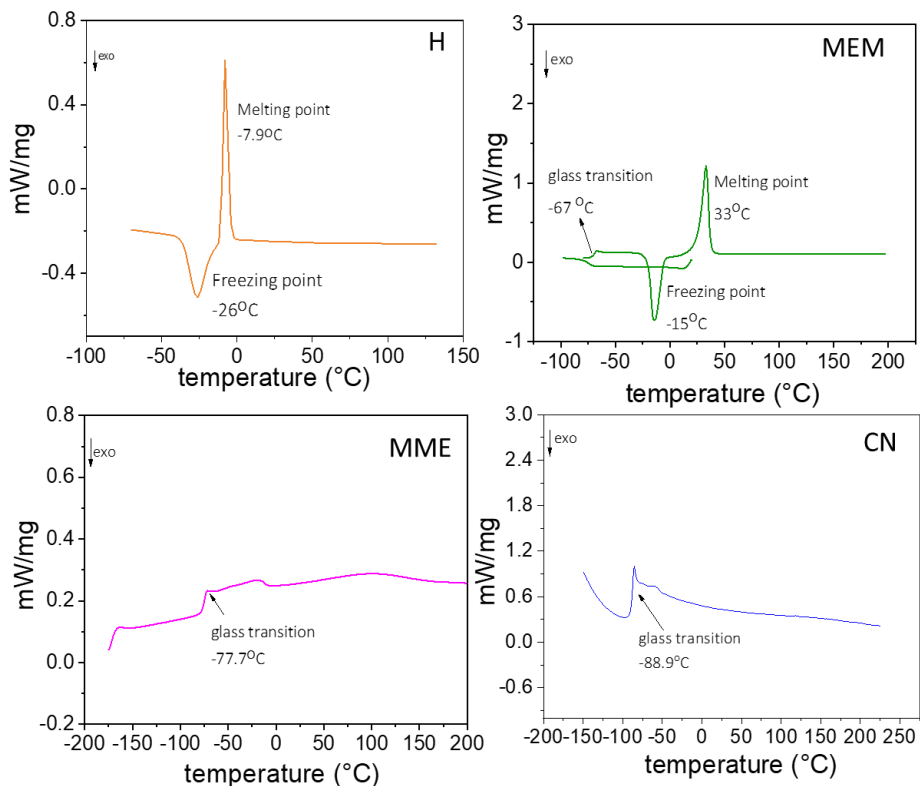


**Figure 2.3** DSC analyses of ILs



**Table 2.5** Melting and freezing points of ILs.<sup>a</sup>

ILs	Melting point (T <sub>mp</sub> ) °C	Freezing point (T <sub>fp</sub> ) °C	Super cooling ( $\Delta T$ ) °C	Glass transition temperature (T <sub>g</sub> ) °C
H	-8	-26	18	-
MEM	33	-15	48	-67
MME	-	-	-	-78
CN	-	-	-	-89

<sup>a</sup> determined from DSC data

### c) XPS analysis

X-ray photoelectron spectroscopy (XPS) analyses were performed on the four ILs. XPS is a surface sensitive technique that can be used to study the surface-interface properties of the ILs and the chemical composition of the near-surface region [42]. Due to the unavoidable vapor pressure, investigation of conventional liquids is generally very difficult, as the XPS technique requires ultra-high vacuum (UHV) conditions, with pressure  $< 10^{-6}$  mbar. However, ILs are out of such restriction due to their low vapor pressure. Survey scans (**Figure 2.4**) and high-resolution spectra (**Appendix B**) for all the ILs were recorded. Due to the differential charging that occurs during probing, the spectra were referenced by setting the C 1s binding energy at 284.9 eV.

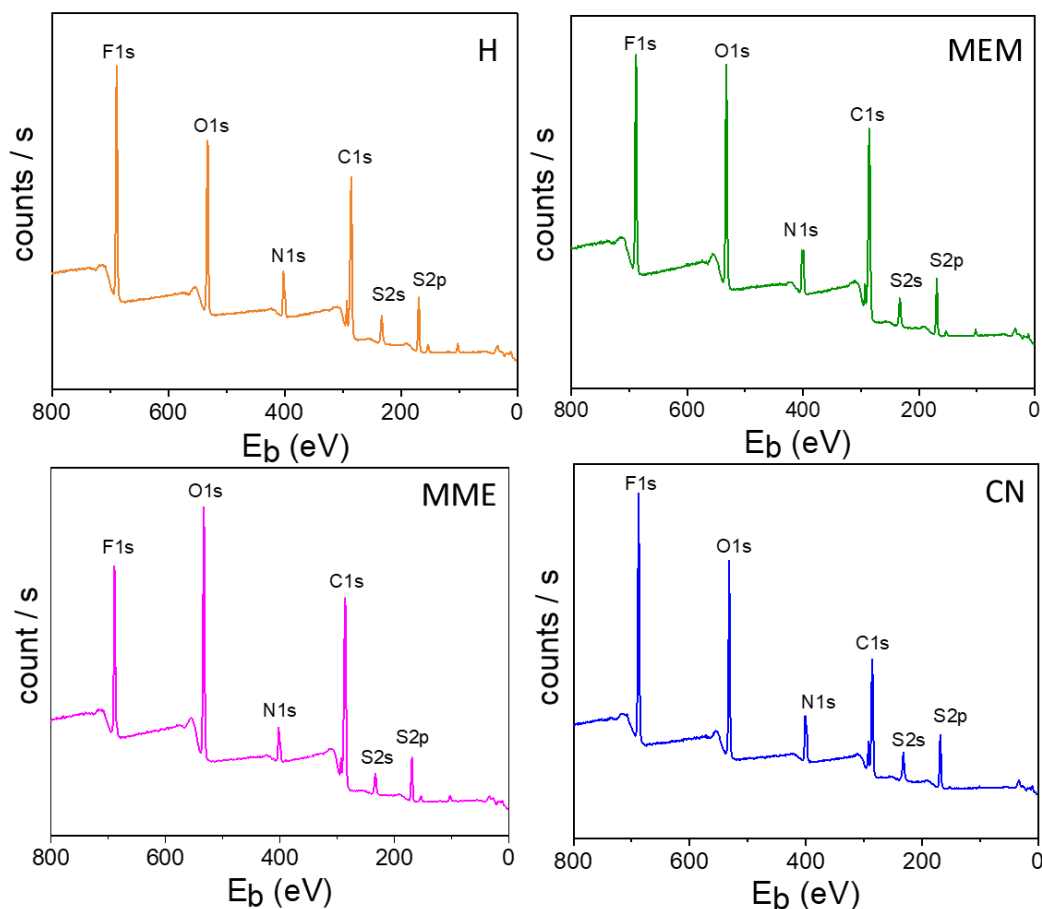


**Figure 2.4** XPS survey of ILs

For all the ILs, the N 1s spectrum contains two peaks, one at the lower binding energy attributed to the N 1s<sub>anion</sub> and the other at higher binding energy to that of N 1s<sub>cation</sub>. The S 2p (2p<sub>3/2</sub>, 2p<sub>1/2</sub>) contains a single doublet peak due to the spin orbital coupling. The peak positions observed on the spectra are consistent with the literature data [43–45]. The O 1s<sub>cation</sub> and O 1s<sub>anion</sub> in MEM and MME display similar binding energies and hence only a single peak is observed [42,46]. Among the high-resolution spectra of all elements, C 1s exhibits the highest complexity. It contains five fitted compounds attributed to five different carbons of both the cation and anion. The C 1s peaks between binding energy (E<sub>b</sub>) 290 – 290 eV correspond to the C 1s environment of the cation and the peak with the higher E<sub>b</sub> attributes to that of the anion [47]. The binding energies (E<sub>b</sub>), atomic ratio (%) and the full-width-at-half-maximum - FWHM (eV) of the C 1s and N 1s, O 1s, S 2p and

F 1s of the ILs are summarized in **Table 2.6** and **Table 2.7**, respectively. **Figure 2.5** shows the chemical structure related to the different ILs and the corresponding numbering of atoms.

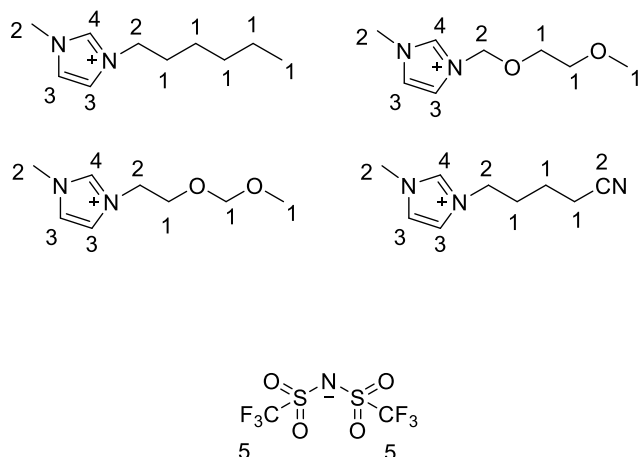


**Figure 2.5** Chemical structures of the ILs with numbering of atoms.

**Table 2.6** Binding energies (eV) of C 1s for the carbon atoms in the ILs.

Atom <sup>a</sup>	Binding energy IL (E <sub>IL</sub> )	Atomic ratio (%)	FWHM (eV)
<b>H</b>			
C <sub>1</sub>	284.80	52.73	1.37
C <sub>2</sub>	286.43	26.55	1.29
C <sub>3</sub>	287.41	5.310	1.14
C <sub>4</sub>	288.85	3.710	1.14
C <sub>5</sub>	292.59	10.15	1.13
<b>MEM</b>			
C <sub>1</sub>	284.80	28.00	1.30
C <sub>2</sub>	286.36	11.10	1.20
C <sub>3</sub>	287.59	3.10	1.20
C <sub>4</sub>	288.39	5.00	1.00
C <sub>5</sub>	292.59	2.10	1.00
<b>MME</b>			
C <sub>1</sub>	284.80	28.0	1.30

Atom <sup>a</sup>	Binding energy IL (E <sub>IL</sub> )	Atomic ratio (%)	FWHM (eV)
C <sub>2</sub>	286.31	11.10	1.20
C <sub>3</sub>	287.51	3.10	1.20
C <sub>4</sub>	288.75	5.00	1.00
C <sub>5</sub>	292.38	2.10	1.00
<b>CN</b>			
C <sub>1</sub>	284.80	46.03	1.44
C <sub>2</sub>	286.12	35.50	1.44
C <sub>3</sub>	287.72	2.07	1.21
C <sub>4</sub>	288.66	7.25	1.18
C <sub>5</sub>	292.30	7.83	1.14

<sup>a</sup> C<sub>1</sub>-C<sub>5</sub> correspond to the carbon atoms in the ILs as numbered in Figure S32.

**Table 2.7** Binding energies (eV) of the chemical states of the atoms in the ILs.

Element	Binding energy IL (E <sub>IL</sub> )	Atomic ratio (%)	FWHM (eV)
<b>H</b>			
N 1s (anion)	399.08	35.00	1.25
N 1s (cation)	401.71	65.00	1.27
S 2p <sub>3/2</sub>	168.78	64.58	1.18
S 2p <sub>1/2</sub>	170.00	35.42	1.25
F 1s	688.38	100.00	1.79
O 1s (cation/anion)	532.17	89.39	1.44
H <sub>2</sub> O <sub>absorbed</sub>	533.62	10.61	1.44
<b>MEM</b>			
N 1s (anion)	399.14	49.80	1.44
N 1s (cation)	401.70	50.21	1.44
S 2p <sub>3/2</sub>	168.70	66.84	1.22
S 2p <sub>1/2</sub>	169.97	33.16	1.19
F 1s	688.44	100.00	1.82
O 1s (cation/anion)	532.29	70.18	1.44
H <sub>2</sub> O <sub>absorbed</sub>	533.10	29.82	1.44
<b>MME</b>			
N 1s (anion)	398.91	36.85	1.29

Atom <sup>a</sup>	Binding energy IL (E <sub>IL</sub> )	Atomic ratio (%)	FWHM (eV)
N 1s (cation)	401.52	61.42	1.32
S 2p <sub>3/2</sub>	168.54	67.40	1.24
S 2p <sub>1/2</sub>	169.79	32.60	1.22
F 1s (LiF)	684.24	6.03	1.70
F 1s (anion)	688.19	93.97	1.79
O 1s (CO <sub>3</sub> <sup>2-</sup> )	530.22	9.15	1.44
O 1s (cation/anion)	532.03	68.25	1.44
H <sub>2</sub> O <sub>absorbed</sub>	533.25	22.60	1.44
<b>CN</b>			
N 1s (anion)	398.99	59.91	1.37
N 1s (cation)	401.50	40.36	1.19
S 2p <sub>3/2</sub>	168.47	65.51	1.19
S 2p <sub>1/2</sub>	169.71	34.49	1.23
F 1s	688.08	97.39	1.77
O 1s (CO <sub>3</sub> <sup>2-</sup> )	530.09	10.39	1.44
O 1s (cation/anion)	531.86	74.04	1.44
H <sub>2</sub> O <sub>absorbed</sub>	533.23	15.57	1.44

#### d) NMR analysis

Characterization of the ILs was also performed using nuclear magnetic resonance (NMR) spectroscopy (<sup>1</sup>H, <sup>13</sup>C{<sup>1</sup>H}, <sup>19</sup>F, <sup>13</sup>C dept-135). Through this, purity of the synthesized ionic liquid with respect to the starting materials and the molecular structure was evaluated. The <sup>1</sup>H NMR for all ILs showed the characteristic peaks between 7.25 and 10.25 ppm which can be attributed to the imidazolium protons (C2-H, C4-H, C5-H). The analysis of <sup>13</sup>C{<sup>1</sup>H} and <sup>13</sup>C dept-135 NMR revealed peaks located between 120 and 145 ppm corresponding to the three imidazolium carbon atoms present in the ionic liquids (ILs). <sup>19</sup>F analysis showed a single peak at negative chemical shift value corresponding to the 6 fluorine atoms present on the [NTf<sub>2</sub>]<sup>-</sup> anion of the ILs. No peak of impurities was observed thus qualitatively stating that if present, the impurities were present only in negligible amounts below the detection value of NMR. The <sup>1</sup>H NMR showed negligibly small peak of H<sub>2</sub>O. The <sup>1</sup>H, <sup>13</sup>C{<sup>1</sup>H}, <sup>19</sup>F, <sup>13</sup>C dept-135 NMR spectra for all IL are provided below (Figure 2.6, 2.7, 2.8).

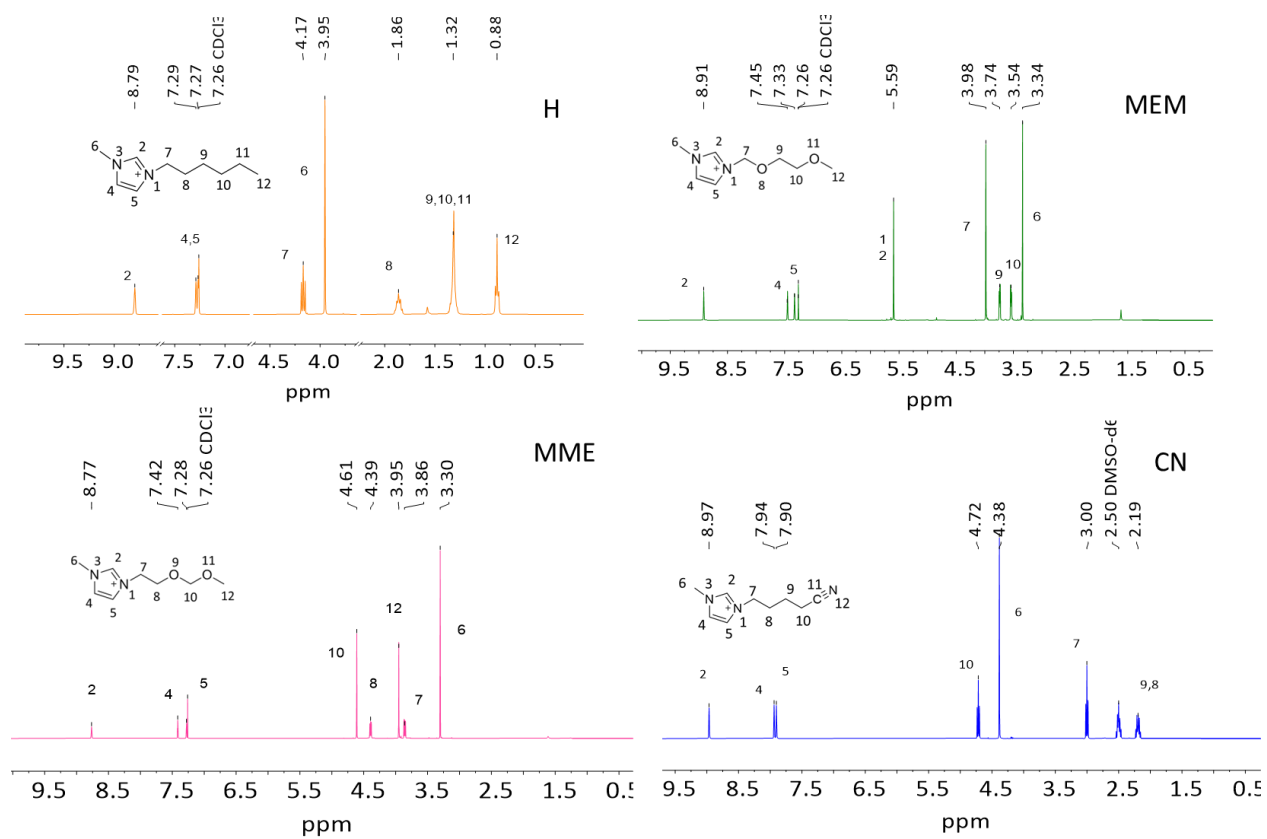


Figure 2.6  $^1\text{H}$  NMR of ILs

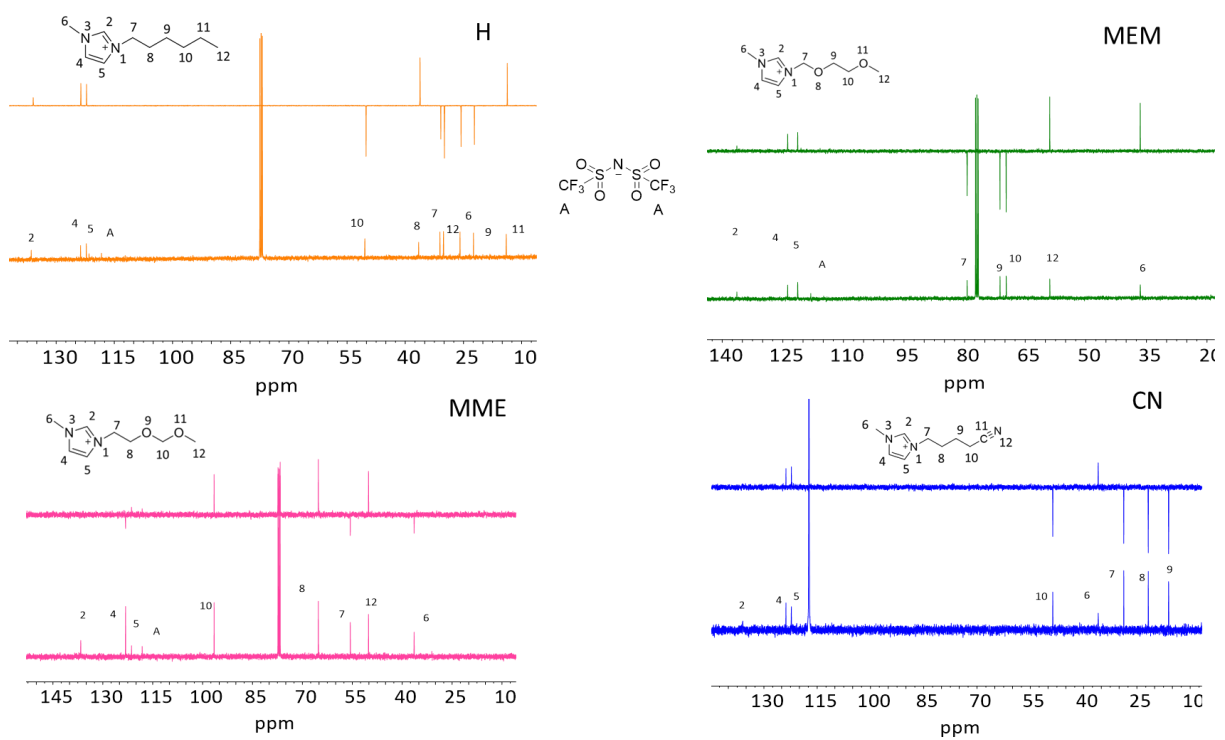
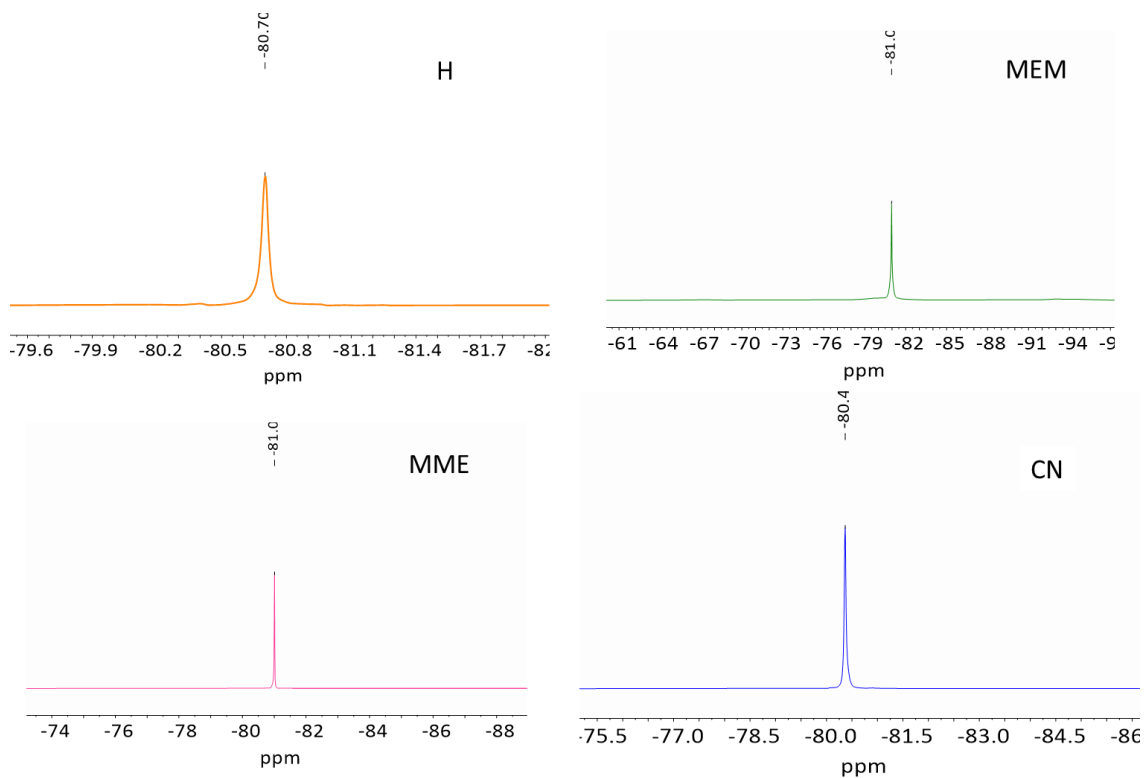
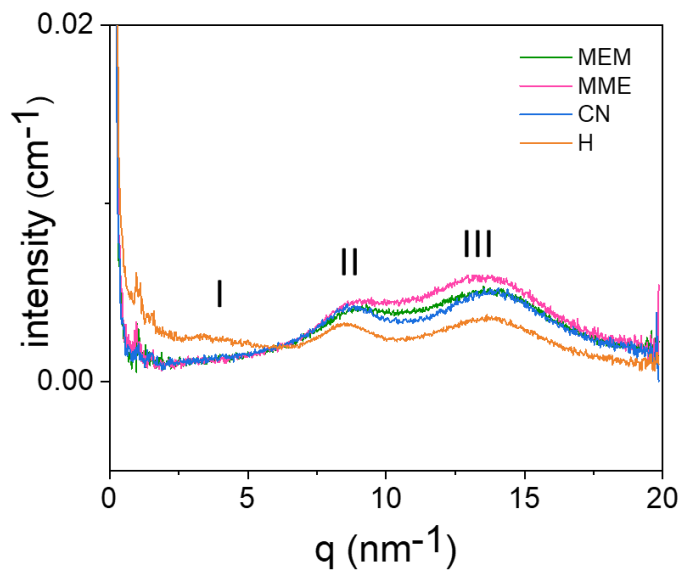


Figure 2.7  $^{13}\text{C}\{^1\text{H}\}$  NMR of ILs.



**Figure 2.8**  $^{19}\text{F}$  NMR of ILs

e) SAXS analysis



**Figure 2.9** X-ray diffraction patterns for the series of ILs



Small angle X-ray scattering (SAXS) analysis was performed on all the ILs in collaboration with Prof. John Slattery and Dr. Naomi Elstone at University of York, UK to study the nature of cation-cation, anion-anion, and cation-anion ordering (**Figure 2.9**). Two primary diffraction peaks can be observed in the ranges  $q \approx 8\text{-}9 \text{ nm}^{-1}$  (peak II) and  $q \approx 12.9$  (peak III). The  $q$ -value is called the scattering vector and is a function of the scattering angle:

$$q = \frac{4\pi \sin\theta}{\lambda}, \quad 2\theta \text{ is the angle of deflection}$$

For H, one additional peak at  $q \approx 2\text{-}4 \text{ nm}^{-1}$  can also be seen. Previous studies of imidazolium ionic liquids with different anions have observed similar diffraction features [48–50]. Peak I depends strongly on the alkyl chain length and reflects on the structural heterogeneity on the nanometer scale of the ILs. Peak II at  $\sim 8.8 \text{ nm}^{-1}$ , which is commonly called the "charge-ordering peak" (COP) is interpreted as relating to correlations between like charges (anion-anion and cation-cation separations) [51]. Comparing the ILs, the order of intensity of the peak is as follows  $\text{MME} > \text{MEM} \sim \text{CN} > \text{H}$  which can be seen by plotting the intensity of the peaks against the different ILs (**Figure 2.10 a**). Peak III at  $\sim 13.5 \text{ nm}^{-1}$  is commonly referred to as the "contact peak" (CP). The CP is interpreted as relating to correlations between ions of opposite charges i.e., the typical separation of the anions and cations [52]. The ILs follow the same intensity order as peak II. **Figure 2.10 b** shows the special correlation length  $L_{\text{II}}$  ( $L = 2\pi/q_{\text{II}}$ ) and  $L_{\text{III}}$  ( $L = 2\pi/q_{\text{III}}$ ) for the four ILs. The special correlation length was found to be similar in all ILs for both the peaks.

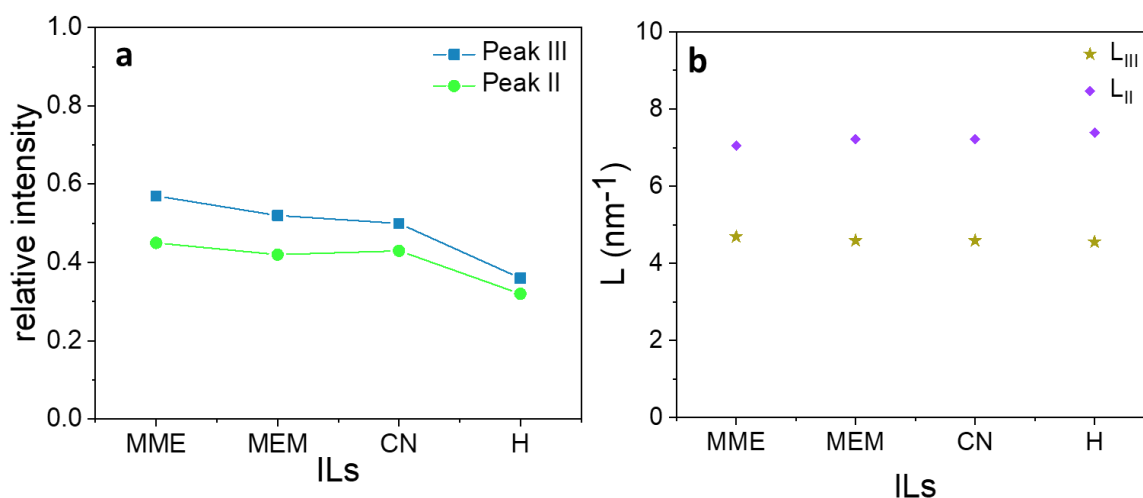


**Figure 2.10** a) Intensity of peak I and II vs. ILs and b) correlation length ( $L$ ) vs. ILs

## 2.4 Summary

A series of four imidazolium-based ILs, one non-functionalized and three functionalized, namely H, MEM, MME, and CN, were synthesized in good yields by using the standard quaternization and anion exchange reaction synthesis procedure. A complete characterization including IR, TG, DSC, NMR, XPS and SAXS analyses was performed for all synthesized ILs. IR analysis allowed to establish the stretching frequency and the different functional groups of both the anion and the cation (CN, CO, SO<sub>2</sub>, CF<sub>3</sub>, *etc.*) thus confirming the identity of each IL. TG and DSC analyses gave information on the thermal behavior of the ILs. They were found to be thermally stable above 200°C for MEM and MME and 450°C in the case of H and CN. The binding energies ( $E_b$ ) of the elements present in each IL were obtained through XPS analysis. The purity of the ILs was evaluated from the NMR analysis. The presence of the characteristic <sup>1</sup>H and <sup>13</sup>C peaks also contributed to confirm the structure of the ILs. The interactions and ordering of the cations and anions of the ILs were studied using SAXS technique. These synthesized and fully characterized ILs have been then used for the stabilization of transition metal nanoparticles of ruthenium (Chapter 3) and nickel (Chapter 4). The IL was also tested for the synthesis of ruthenium-rhenium bimetallic nanoparticles (Chapter 5).

## 2.5 References

1. Migowski, P.; Dupont, J. Catalytic Applications of Metal Nanoparticles in Imidazolium Ionic Liquids. *Chem. Eur. J.* **2007**, *13*, 32–39, doi:10.1002/chem.200601438.
2. Prechtel, M.H.G.; Scholten, J.D.; Dupont, J. Tuning the Selectivity of Ruthenium Nanoscale Catalysts with Functionalised Ionic Liquids: Hydrogenation of Nitriles. *J. Mol. Catal. A Chem* **2009**, *313*, 74–78, doi:10.1016/j.molcata.2009.08.004.
3. Stratton, S.A.; Luska, K.L.; Moores, A. Rhodium Nanoparticles Stabilized with Phosphine Functionalized Imidazolium Ionic Liquids as Recyclable Arene Hydrogenation Catalysts. *Catal. Today* **2012**, *183*, 96–100, doi:10.1016/j.cattod.2011.09.016.
4. Wegner, S.; Janiak, C. Metal Nanoparticles in Ionic Liquids. *Top. Curr. Chem.* **2017**, *375*, 65, doi:10.1007/s41061-017-0148-1.
5. Ngo, H.L.; LeCompte, K.; Hargens, L.; McEwen, A.B. Thermal Properties of Imidazolium Ionic Liquids. *Thermochim. Acta* **2000**, *357–358*, 97–102, doi:10.1016/S0040-6031(00)00373-7.
6. Burrell, A.K.; Del Sesto, R.E.; Baker, S.N.; McCleskey, T.M.; Baker, G.A. The Large Scale Synthesis of Pure Imidazolium and Pyrrolidinium Ionic Liquids. *Green Chem.* **2007**, *9*, 449–45, doi:10.1039/b615950h.
7. Chancelier, L.; Boyron, O.; Gutel, T.; Santini, C. Thermal Stability of Imidazolium-Based Ionic Liquids. *French-Ukrainian J. of Chem.* **2016**, *4*, 51–64, doi:10.17721/fujcV4I1P51-64.
8. Schröder, U.; Wadhawan, J.D.; Compton, R.G.; Marken, F.; Suarez, P.A.Z.; Consorti, C.S.; de Souza, R.F.; Dupont, J. Water-Induced Accelerated Ion Diffusion: Voltammetric Studies in 1-Methyl-3-[2,6-(S)-Dimethylocten-2-Yl]Imidazolium Tetrafluoroborate, 1-Butyl-3-Methylimidazolium Tetrafluoroborate and Hexafluorophosphate Ionic Liquids. *New J. Chem.* **2000**, *24*, 1009–1015, doi:10.1039/b007172m.
9. Wadhawan, J.D.; Schröder, U.; Neudeck, A.; Wilkins, S.J.; Compton, R.G.; Marken, F.; Consorti, C.S.; de Souza, R.F.; Dupont, J. Ionic Liquid Modified Electrodes. Unusual Partitioning and Diffusion Effects of Fe(CN)<sub>6</sub><sup>4–/3–</sup> in Droplet and Thin Layer Deposits of 1-Methyl-3-(2,6-(S)-Dimethylocten-2-Yl)-Imidazolium Tetrafluoroborate. *J. Electroanal. Chem.* **2000**, *493*, 75–83, doi:10.1016/S0022-0728(00)00308-9.
10. Axet, M.R.; Philippot, K. Organometallic Metal Nanoparticles for Catalysis. In *Nanoparticles in Catalysis*; Wiley-VCH:Weinheim, **2021**; pp. 73–97. <https://doi.org/10.1002/9783527821761.ch4>
11. MacFarlane, D.R.; Kar, M.; Pringle, J.M. Fundamentals of Ionic Liquids. *Fundamentals of Ionic Liquids*, Wiley-VCH:Weinheim, Germany, **2017**; ISBN 9783527340033.
12. Harraz, F.A.; El-Hout, S.E.; Killa, H.M.; Ibrahim, I.A. Palladium Nanoparticles Stabilized by Polyethylene Glycol: Efficient, Recyclable Catalyst for Hydrogenation of Styrene and Nitrobenzene. *J. Catal.* **2012**, *286*, 184–192, doi:10.1016/j.jcat.2011.11.001.
13. Sun, Z.; Wang, Y.; Niu, M.; Yi, H.; Jiang, J.; Jin, Z. Poly(Ethylene Glycol)-Stabilized Rh Nanoparticles as Efficient and Recyclable Catalysts for Hydroformylation of Olefins. *Catal. Commun.* **2012**, *27*, 78–82, doi:10.1016/j.catcom.2012.07.001.
14. Zhu, W.; Yang, H.; Yu, Y.; Hua, L.; Li, H.; Feng, B.; Hou, Z. Amphiphilic Ionic Liquid Stabilizing Palladium Nanoparticles for Highly Efficient Catalytic Hydrogenation. *Phys. Chem. Chem. Phys.* **2011**, *13*, 13492–13500, doi:10.1039/c1cp20255c.
15. Harraz, F.A.; El-Hout, S.E.; Killa, H.M.; Ibrahim, I.A. Catalytic Hydrogenation of Crotonaldehyde and Oxidation of Benzene over Active and Recyclable Palladium

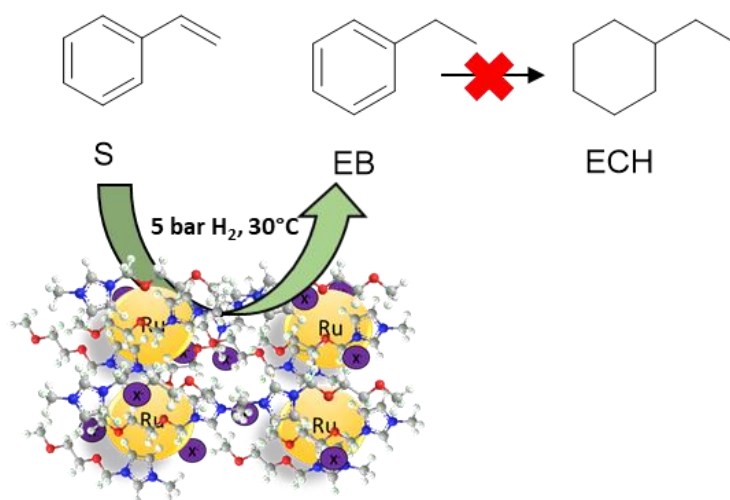
- Nanoparticles Stabilized by Polyethylene Glycol. *J. Mol. Catal. A Chem.* **2013**, *370*, 182–188, doi:10.1016/j.molcata.2013.01.011.
16. Dzyuba, S. V.; Bartsch, R.A. Efficient Synthesis of 1-Alkyl(Aralkyl)-3-Methyl(Ethyl)Imidazolium Halides: Precursors for Room-Temperature Ionic Liquids. *J. Heterocycl. Chem.* **2001**, *38*, 265–268, doi:10.1002/jhet.5570380139.
  17. Zhao, D.; Fei, Z.; Scopelliti, R.; Dyson, P.J. Synthesis and Characterization of Ionic Liquids Incorporating the Nitrile Functionality. *Inorg. Chem.* **2004**, *43*, 2197–2205, doi:10.1021/ic034801p.
  18. Nokami, T.; Matsumoto, K.; Itoh, T.A.; Fukaya, Y.; Itoh, T. Synthesis of Ionic Liquids Equipped with 2-Methoxyethoxymethyl/Methoxymethyl Groups Using a Simple Microreactor System. *Org. Process Res. Dev.* **2014**, *18*, 1367–1371, doi:10.1021/op500131u.
  19. Lockett, V.; Sedev, R.; Bassell, C.; Ralston, J. Angle-Resolved X-Ray Photoelectron Spectroscopy of the Surface of Imidazolium Ionic Liquids. *Phys. Chem. Chem. Phys.* **2008**, *10*, 1330–1335, doi:10.1039/b713584j.
  20. Yamada, T.; Tominari, Y.; Tanaka, S.; Mizuno, M. Infrared Spectroscopy of Ionic Liquids Consisting of Imidazolium Cations with Different Alkyl Chain Lengths and Various Halogen or Molecular Anions with and without a Small Amount of Water. *J. Phys. Chem. B* **2017**, *121*, 3121–3129, doi:10.1021/acs.jpcc.7b01429.
  21. Yamada, T.; Mizuno, M. Infrared Spectroscopy in the Middle Frequency Range for Various Imidazolium Ionic Liquids - Common Spectroscopic Characteristics of Vibrational Modes with In-Plane +C(2)-H and +C(4,5)-H Bending Motions and Peak Splitting Behavior Due to Local Symmetry Breaking of Vibrational Modes of the Tetrafluoroborate Anion. *ACS Omega* **2021**, *6*, 1709–1717, doi:10.1021/acsomega.0c05769.
  22. Moumene, T.; Belarbi, E.H.; Haddad, B.; Villemin, D.; Abbas, O.; Khelifa, B.; Bresson, S. Vibrational Spectroscopic Study of Ionic Liquids: Comparison between Monocationic and Dicationic Imidazolium Ionic Liquids. *J. Mol. Struct.* **2014**, *1065–1066*, 86–92, doi:10.1016/j.molstruc.2014.02.034.
  23. Yamada, T.; Tominari, Y.; Tanaka, S.; Mizuno, M. Infrared Spectroscopy of Ionic Liquids Consisting of Imidazolium Cations with Different Alkyl Chain Lengths and Various Halogen or Molecular Anions with and without a Small Amount of Water. *J. Phys. Chem. B* **2017**, *121*, 3121–3129, doi:10.1021/acs.jpcc.7b01429.
  24. Yamada, T.; Mizuno, M. Characteristic Spectroscopic Features Because of Cation-Anion Interactions Observed in the 700-950  $\text{cm}^{-1}$  Range of Infrared Spectroscopy for Various Imidazolium-Based Ionic Liquids. *ACS Omega* **2018**, *3*, 8027–8035, doi:10.1021/acsomega.8b00938.
  25. Paschoal, V.H.; Faria, L.F.O.; Ribeiro, M.C.C. Vibrational Spectroscopy of Ionic Liquids. *Chem. Rev.* **2017**, *117*, 7053–7112, doi:10.1021/acs.chemrev.6b00461.
  26. Noack, K.; Schulz, P.S.; Paape, N.; Kiefer, J.; Wasserscheid, P.; Leipertz, A. The Role of the C2 Position in Interionic Interactions of Imidazolium Based Ionic Liquids: A Vibrational and NMR Spectroscopic Study. *Phys. Chem. Chem. Phys.* **2010**, *12*, 14153–14161, doi:10.1039/c0cp00486c.
  27. Tiongson, J.K.A.; Bruzon, D.A. V.; Tapang, G.A.; Martinez, I.S. Syntheses and Properties of Methoxy and Nitrile Functionalized Imidazolium Tris(Pentafluoroethyl)Trifluorophosphate Ionic Liquids. *J. Chem. Eng. Data* **2018**, *63*, 1135–1145, doi:10.1021/acs.jced.7b00281.

28. Zhang, Q.; Li, Z.; Zhang, J.; Zhang, S.; Zhu, L.; Yang, J.; Zhang, X.; Deng, Y. Physicochemical Properties of Nitrile-Functionalized Ionic Liquids. *J. Phys. Chem. B* **2007**, *111*, 2864–2872, doi:10.1021/jp067327s.
29. Cao, Y.; Mu, T. Comprehensive Investigation on the Thermal Stability of 66 Ionic Liquids by Thermogravimetric Analysis. *Ind. Eng. Chem. Res.* **2014**, *53*, 8651–8664, doi:10.1021/ie5009597.
30. Clough, M.T.; Geyer, K.; Hunt, P.A.; Mertes, J.; Welton, T. Thermal Decomposition of Carboxylate Ionic Liquids: Trends and Mechanisms. *Phys. Chem. Chem. Phys.* **2013**, *15*, 20480–20495, doi:10.1039/c3cp53648c.
31. Blake, D.M.; Moens, L.; Rudnicki, D.; Pilath, H. Lifetime of Imidazolium Salts at Elevated Temperatures. *J. Sol. Energy Eng. Trans. ASME* **2006**, *128*, 54–57, doi:10.1115/1.2148976.
32. Glenn, A.G.; Jones, P.B. Thermal Stability of Ionic Liquid BMI(BF<sub>4</sub>) in the Presence of Nucleophiles. *Tetrahedron Lett.* **2004**, *45*, 6967–6969, doi:10.1016/j.tetlet.2004.07.050.
33. Clough, M.T.; Geyer, K.; Hunt, P.A.; Mertes, J.; Welton, T. Thermal Decomposition of Carboxylate Ionic Liquids: Trends and Mechanisms. *Phys. Chem. Chem. Phys.* **2013**, *15*, 20480–20495, doi:10.1039/c3cp53648c.
34. Meine, N.; Benedito, F.; Rinaldi, R. Thermal Stability of Ionic Liquids Assessed by Potentiometric Titration. *Green Chem.* **2010**, *12*, 1711–1714, doi:10.1039/c0gc00091d.
35. Wooster, T.J.; Johanson, K.M.; Fraser, K.J.; MacFarlane, D.R.; Scott, J.L. Thermal Degradation of Cyano Containing Ionic Liquids. *Green Chem.* **2006**, *8*, 691–69, doi:10.1039/b606395k.
36. Zhuravlev, O.E.; Verolainen, N. V.; Voronchikhina, L.I. Thermal Stability of 1,3-Disubstituted Imidazolium Tetrachloroferrates, Magnetic Ionic Liquids. *Russ. J. Appl. Chem* **2011**, *84*, 1158–1164, doi:10.1134/S1070427211070068.
37. Hallett, J.P.; Welton, T. Room-Temperature Ionic Liquids: Solvents for Synthesis and Catalysis. 2. *Chem. Rev.* **2011**, *111*, 3508–3576, doi:10.1021/CR1003248
38. Xu, C.; Cheng, Z. Thermal Stability of Ionic Liquids: Current Status and Prospects for Future Development. *Processes 2021, Vol. 9, Page 337* **2021**, *9*, 337, doi:10.3390/PR9020337.
39. Awad, W.H.; Gilman, J.W.; Nyden, M.; Harris, R.H.; Sutto, T.E.; Callahan, J.; Trulove, P.C.; DeLong, H.C.; Fox, D.M. Thermal Degradation Studies of Alkyl-Imidazolium Salts and Their Application in Nanocomposites. *Thermochim. Acta* **2004**, *409*, 3–11, doi:10.1016/S0040-6031(03)00334-4.
40. Burrell, A.K.; Del Sesto, R.E.; Baker, S.N.; McCleskey, T.M.; Baker, G.A. The Large Scale Synthesis of Pure Imidazolium and Pyrrolidinium Ionic Liquids. *Green Chem.* **2007**, *9*, 449–45, doi:10.1039/b615950h.
41. Noorhisham, N.A.; Amri, D.; Mohamed, A.H.; Yahaya, N.; Ahmad, N.M.; Mohamad, S.; Kamaruzaman, S.; Osman, H. Characterisation Techniques for Analysis of Imidazolium-Based Ionic Liquids and Application in Polymer Preparation: A Review. *J. Mol. Liq.* **2021**, *326*, 115340, doi:10.1016/j.molliq.2021.115340.
42. Kolbeck, C.; Killian, M.; Maier, F.; Paape, N.; Wasserscheid, P.; Steinrück, H.P. Surface Characterization of Functionalized Imidazolium-Based Ionic Liquids. *Langmuir* **2008**, *24*, 9500–9507, doi:10.1021/la801261h.
43. Arcifa, A.; Rossi, A.; Spencer, N.D. Adsorption and Tribochemical Factors Affecting the Lubrication of Silicon-Based Materials by (Fluorinated) Ionic Liquids. *J. Phys. Chem. C* **2017**, *121*, 7259–7275, doi:10.1021/acs.jpcc.6b13028.

44. Cremer, T.; Stark, M.; Deyko, A.; Steinrück, H.P.; Maier, F. Liquid/Solid Interface of Ultrathin Ionic Liquid Films: [C<sub>1</sub>C<sub>1</sub>Im][Tf<sub>2</sub>N] and [C<sub>8</sub>C<sub>1</sub>Im][Tf<sub>2</sub>N] on Au(111). *Langmuir* **2011**, *27*, 3662–3671, doi:10.1021/la105007c.
45. Beattie, D.A.; Arcifa, A.; Delcheva, I.; Le Cerf, B.A.; MacWilliams, S. V.; Rossi, A.; Krasowska, M. Adsorption of Ionic Liquids onto Silver Studied by XPS. *Colloids Surf. A Physicochem. Eng. Asp.* **2018**, *544*, 78–85, doi:10.1016/j.colsurfa.2018.02.007.
46. Heller, B.S.J.; Kolbeck, C.; Niedermaier, I.; Dommer, S.; Schatz, J.; Hunt, P.; Maier, F.; Steinrück, H.P. Surface Enrichment in Equimolar Mixtures of Non-Functionalized and Functionalized Imidazolium-Based Ionic Liquids. *ChemPhysChem* **2018**, *19*, 1733–1745, doi:10.1002/cphc.201800216.
47. Villar-Garcia, I.J.; Smith, E.F.; Taylor, A.W.; Qiu, F.; Lovelock, K.R.J.; Jones, R.G.; Licence, P. Charging of Ionic Liquid Surfaces under X-Ray Irradiation: The Measurement of Absolute Binding Energies by XPS. *Phys. Chem. Chem. Phys.* **2011**, *13*, 2797–2808, doi:10.1039/c0cp01587c.
48. Zheng, W.; Mohammed, A.; Hines, L.G.; Xiao, D.; Martinez, O.J.; Bartsch, R.A.; Simon, S.L.; Russina, O.; Triolo, A.; Quitevis, E.L. Effect of Cation Symmetry on the Morphology and Physicochemical Properties of Imidazolium Ionic Liquids. *J. Phys. Chem. B* **2011**, *115*, 6572–6584, doi:10.1021/jp1115614.
49. Triolo, A.; Russina, O.; Fazio, B.; Triolo, R.; Di Cola, E. Morphology of 1-Alkyl-3-Methylimidazolium Hexafluorophosphate Room Temperature Ionic Liquids. *Chem. Phys. Lett.* **2008**, *457*, 362–365, doi:10.1016/j.cplett.2008.04.027.
50. Triolo, A.; Russina, O.; Bleif, H.J.; Di Cola, E. Nanoscale Segregation in Room Temperature Ionic Liquids. *J. Phys. Chem. B* **2007**, *111*, 4641–4644, doi:10.1021/jp067705t.
51. Murphy, T.; Atkin, R.; Warr, G.G. Scattering from Ionic Liquids. *Curr. Opin. Colloid Interface Sci.* **2015**, *20*, 282–292, doi:10.1016/j.cocis.2015.10.004.
52. Martinelli, A.; Maréchal, M.; Östlund, Å.; Cambedouzou, J. Insights into the Interplay between Molecular Structure and Diffusional Motion in 1-Alkyl-3-Methylimidazolium Ionic Liquids: A Combined PFG NMR and X-Ray Scattering Study. *Phys. Chem. Chem. Phys.* **2013**, *15*, 5510, doi:10.1039/c3cp00097d.

### 3. Synthesis, characterization, and application in catalysis of ruthenium nanoparticles in functionalized ionic liquids

Major part of this chapter was reproduced from Krishnan, D.; Schill, L.; Axet, M.R.; Philippot, K.; Riisager, A. *Nanomaterials* **2023**, *13*, 1459. Copyright [2023] MDPI.



#### 3.1 Introduction

The decomposition of the organometallic ruthenium complex ( $\eta^4$ -1,5-cyclooctadiene)( $\eta^6$ -1,3,5-cycloocta-triene)ruthenium(0), [Ru(COD)(COT)], with dihydrogen under mild conditions is a powerful method to access small and well-controlled ruthenium NPs (Ru NPs) for applications in catalysis [1]. As discussed in Chapter 1, using an organic solvent and a carefully chosen stabilizer (polymer or ligand), the organometallic approach allows control of the surface properties of the Ru NPs. This strategy has also proved efficient using ILs as reaction media for the formation of finely controlled Ru NPs. For instance, Santini and coworkers found for a series of alkyl-substituted imidazolium bis(trifluoromethanesulfonyl)imide ILs, namely [RMIm][NTf<sub>2</sub>] (M = methyl, R = ethyl, butyl, hexyl, octyl and decyl), [R<sub>2</sub>Im][NTf<sub>2</sub>] (R = butyl) and [BMMIm][NTf<sub>2</sub>] (B = butyl, M = methyl), that the sizes of the formed Ru NPs correlated with the solubility of [Ru(COD)(COT)] in the non-polar domains of the ILs, which increased with the alkyl-chain length

[2]. The same group also reported the synthesis of Ru NPs of various size (1-3 nm) from [Ru(COD)(COT)] in [BMIm][NTf<sub>2</sub>] IL by varying the experimental conditions. The relationship between size and catalytic performance of Ru NPs was probed by the catalytic hydrogenation of 1,3-cyclohexadiene (CYD) and cyclohexene (CYE), which showed that the catalytic activity increased with the NP size. Regarding the selectivity for cyclohexene CYE vs. cyclohexane (CYA), it decreased with larger Ru NP size [3]. The group of Moores studied the dependency of catalytic stability and activity for Ru NPs stabilized in phosphonium- and imidazolium-type ILs [P<sub>4,4,4,1</sub>][NTf<sub>2</sub>] (P<sub>4,4,4,1</sub> - tributylmethylphosphonium), [P<sub>4,4,4,8</sub>][NTf<sub>2</sub>] (P<sub>4,4,4,8</sub> - tributyl-octylphosphonium) and [P<sub>4,4,4,14</sub>][X] (P<sub>4,4,4,14</sub> - tributyltetradecylphosphonium) (X = [NTf<sub>2</sub>]<sup>-</sup>, [OTf]<sup>-</sup>, [PF<sub>6</sub>]<sup>-</sup>), [BMIm][NTf<sub>2</sub>] and [BMMIm][NTf<sub>2</sub>] with respect to the ionicity of the ILs using [Ru(COD)(2-methylallyl)<sub>2</sub>] as the precursor. They showed the most stable Ru NPs were formed in the ILs having lower ionicity (as the result of strong associations between the IL cations and anions). The IL-stabilized Ru NPs were investigated in the biphasic hydrogenation of CYE to CYA, showing that the stability and activity of the NPs depended on the nature of the IL [4]. Starting from same organometallic precursor, bis(2-methylallyl)(1,5-cyclooctadiene)ruthenium(0), [Ru(COD)(2-methylallyl)<sub>2</sub>], Dupont and coworkers reported the synthesis of Ru NPs in the cyano-FIL [(CH<sub>3</sub>CH<sub>2</sub>CH<sub>2</sub>CH<sub>2</sub>CN)MIm][NTf<sub>2</sub>] [5]. Their results showed the influence of the FILs on the catalytic properties of the so-obtained Ru NPs, which were selective towards nitrile hydrogenation of a series of nitrile-containing aromatic compounds, without displaying any arene hydrogenation which otherwise typically occurs with Ru NPs. The difference in reactivity most likely originated from interaction of the IL-nitrile functionality with the Ru surface preventing the arene hydrogenation. Pádua and coworkers studied the solvation and stabilization mechanism of Ru NPs using density functional theory (DFT) methods, demonstrating that the 2 nm size Ru NPs were solvated by both the anions and the cations of the ILs, where the interface layer was one ion thick [6]. This finding of solvation was in line with the finding of the aforementioned work by Dupont and coworkers.

Selective hydrogenation of styrene (S) into ethylbenzene (EB) is of interest in the petroleum industry, where the product is widely used in value-added aromatics and in the gasoline pool [7]. For the selective hydrogenation of S to EB, most literature describes the use of catalysts like polyethylene glycol stabilized Pd [8] carbon nanotubes (CNTs) supported Pt [9] or bimetallic



systems (Ni-CeO<sub>2-x</sub>/Pd) [10], whereas very few examples are reported for S hydrogenation using Ru NPs in ILs/FILs. Vignolle and coworkers synthesized Ru NPs stabilized with polymerized ILs (PILs) based on *N*-vinyl imidazolium and hydrogenated S as a model reaction to study the correlation between chemo-selectivity and the nature of counter anion. They showed that I<sup>-</sup>/[NTf<sub>2</sub>]<sup>-</sup> anion exchange enabled the chemo-selective hydrogenation of S to switch from EB to ethylcyclohexane (ECH) [11]. Jiang and coworkers reported the synthesis of Ru NPs from RuO<sub>2</sub>·xH<sub>2</sub>O in phosphine-FILs [BMMIm]<sub>3</sub>[tppt] (tppt = tri(*m*-sulfonyl)triphenylphosphine) and [BMMIm][PF<sub>6</sub>], and demonstrated that Ru NPs stabilized by the former FIL showed high activity and selectivity in the hydrogenation of functionalized olefins, aromatic nitro compounds and aromatic aldehydes [12]. The same group also reported the synthesis of Ru NPs from RuO<sub>2</sub>·xH<sub>2</sub>O and [Ru(COD)(2-methylallyl)<sub>2</sub>] in phosphine-FILs like [BMIm][tppm] (tppm = mono(*m*-sulfonyl)triphenylphosphine) and [BMIm]<sub>3</sub>[tppt] and their application in the chemo-selective hydrogenation of diverse substrates such as vinylarenes, aromatic ketones, aldehydes and quinolines. Here, S was converted selectively into EB (30 °C, 10 bar H<sub>2</sub>, S/Ru ratio of 500) with full conversion in 4 h [13]. These results have paved the way for exploring the capability of Ru NPs stabilized by ILs bearing other functional groups than phosphines, such as ethers, to catalyze the production of EB more efficiently under even milder reaction conditions.

In this chapter the synthesis and characterization of Ru NPs stabilized by two ether-FILs, 1-methoxyethoxymethyl-3-methylimidazolium bis(trifluoromethanesulfonyl)imide, [MEMIm][NTf<sub>2</sub>] or MEM, and 1-methoxymethoxyethyl-3-methylimidazolium bis(trifluoromethanesulfonyl) imide, [MMEIm][NTf<sub>2</sub>] or MME are reported following the organometallic approach. The novel Ru/FILs NPs systems (Ru/MEM and Ru/MME) were applied for hydrogenation of styrene and phenylacetylene to probe the surface reactivity of the Ru NPs. In particular, the influence of the ether functions on the catalytic performance was studied and compared to two counterpart catalytic systems based on Ru NPs stabilized by the non-functionalized IL 1-hexyl-3-methylimidazolium bis(trifluoromethanesulfonyl)imide (Ru/H) and the cyano-FIL [(CH<sub>3</sub>CH<sub>2</sub>CH<sub>2</sub>CH<sub>2</sub>CN)MIm][NTf<sub>2</sub>] (Ru/CN), respectively. The obtained results evidenced a clear influence of the FIL on the hydrogenation selectivity of the Ru NPs between

vinyl and aromatic hydrogenation of styrene, thus demonstrating the key role of the FIL in the catalytic systems.

## 3.2 Experimental section

### 3.2.1 Synthesis of FIL-stabilized Ru nanoparticles (Ru/FILs NPs)

In a typical synthesis, [Ru(COD)(COT)] (9.40 mg, 0.03 mmol) and a given IL (1 mL) were introduced in a Fischer-Porter reactor under argon atmosphere, and the mixture stirred (1500 rpm) at 40 °C for 24 h. The so-obtained homogeneous yellow mixture was then exposed to 3 bar of H<sub>2</sub> in dynamic flow for 10 min and then in a static mode for 22 h at room temperature, except for CN, for which a temperature of 60 °C was applied. Next, generated cyclooctane was removed under vacuum ( $\approx$  0.05 mbar) at room temperature and the resultant black colloidal suspension containing RuNPs/FIL stored under inert atmosphere inside a glovebox prior to analyses and/or catalytic reactions. The materials and characterization methods used have been provided in Chapter 7.

### 3.2.2 Catalytic hydrogenation

Catalytic hydrogenation of phenylacetylene (PA) or styrene (S) were performed in a 20 mL Fischer-Porter reactor under 5 bar of H<sub>2</sub> pressure at 30 °C using a stirring rate of 900 and 1500 rpm, respectively. In a typical experiment, a mixture containing a given Ru/FILs NPs catalyst (0.02 mmol of metal), substrate (4 mmol) and octane (0.05 mL, 0.3 mmol) as internal standard was loaded in the reactor. Aliquots of the reaction mixture were taken at different intervals of time for quantitative gas chromatography (GC) analysis in order to follow the evolution of each reaction. Recyclability tests for styrene (S) were performed after each catalytic run by washing the spent Ru/FILs NPs catalyst three times with pentane (3  $\times$  4 mL) to remove substrate and formed products, followed by drying under vacuum ( $\approx$  0.05 mbar at room temperature). The dried Ru/FILs NPs phase was mixed with a new batch of substrate and the reaction performed under the same catalytic conditions as mentioned above. This operation was repeated five times. Transmission electron microscopy (TEM) and inductively coupled plasma (ICP) analyses were performed on the spent Ru/FILs NPs after catalysis.

### 3.2.3 Solubility test of styrene and ethylbenzene

The solubility of styrene (S) and ethylbenzene (EB) in the different ILs was determined as follows: a mixture of IL (0.5 mL) and S or EB (2 mL) was stirred at room temperature for 24 h in a vial and then allowed to settle for 0.5 h. The excess of S or EB present on the top of the mixture was removed *via* cannula filtration, then pentane (5 mL) was added and the mixture vigorously stirred to extract the dissolved S or EB from the IL to the pentane. The extraction procedure with pentane was duplicated twice. The pentane phase was then analyzed by GC using octane (0.03 mmol) as internal standard and the quantitative GC data allowed to determine the concentration of S and EB dissolved in each IL.

## 3.3 Results and Discussion

### 3.3.1 Synthesis of Ruthenium Nanoparticles in ILs (Ru/ILs NPs): optimization of reaction conditions

As a first attempt to prepare Ru NPs in the synthesized ILs as described in chapter 2 (Ru/ILs NPs), [Ru(COD)(COT)] was stirred (1500 rpm) at room temperature for 24 h aiming to completely dissolve the precursor in the ILs. However, due to the relative high viscosity of the ILs, the Ru precursor crystals did not all dissolve well. To address this issue, the crystals were grinded into a powder to enhance the rate of the dissolution of the precursor in the ILs. Upon grinding and increasing the stirring temperature to 40 °C, complete dissolution of [Ru(COD)(COT)] in the ILs was achieved in 24 h. Ru/ILs NPs systems were then synthesized by introducing 3 bar H<sub>2</sub> to the Fischer-Porter reactor containing the homogeneous mixture at room temperature except for the nitrile-FIL (CN), where complete decomposition of the Ru complex required a higher temperature of 60 °C (**Scheme 3.1**). During a period of 22 h, the color of the reaction turbid mixture was observed to change from yellow to black which indicated the decomposition of the Ru complex (**Figure 3. 1**).

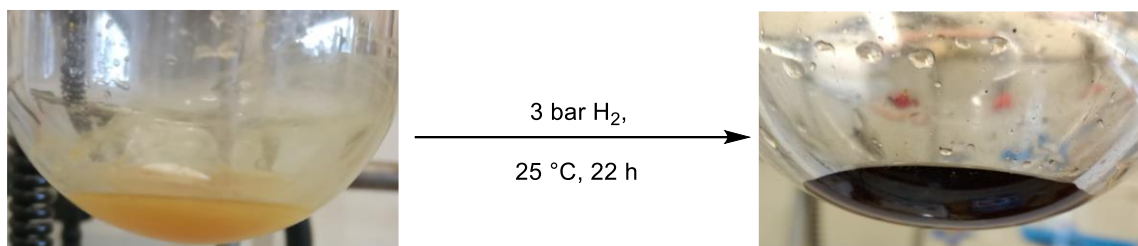
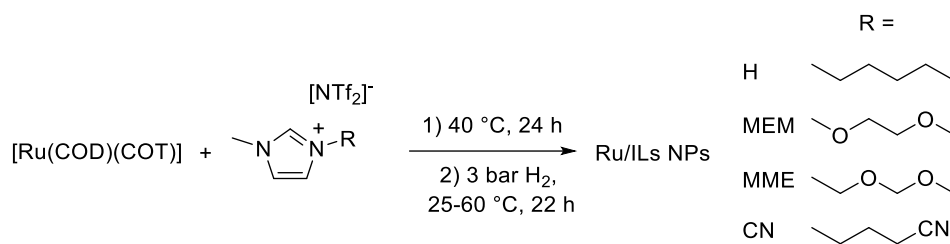


**Figure 3.1** Synthesis of Ru NPs in MEM ILs.

The metal content of each batch of Ru/ILs NPs was established by ICP analysis and found to be close to the expected value of 0.2 wt.% Ru (**Table 3.1**).



**Scheme 3.1** Synthesis of Ru/FILs NPs.

**Table 3.1** Metal content of the Ru/FILs NPs and mean size of the formed Ru NPs.

Ru/FILs NPs	Ionic liquid	Ru content (wt.%) <sup>a</sup>	Ru NP mean size with standard deviation (nm) <sup>b</sup>
Ru/H		0.16	1.5 ± 0.8
Ru/MEM		0.20	2.2 ± 0.3
Ru/MME		0.17	1.3 ± 0.1
Ru/CN		0.20	1.3 ± 0.2

<sup>a</sup> Determined by ICP analyses. <sup>b</sup> Determined from analyses of TEM images.

### 3.3.2 Characterization of the Ru/FILs NPs

#### a) TEM analysis

The synthetic procedure led to the formation of well-dispersed Ru NPs in all the ILs with a mean size ranging from 1.3 to 2.2 nm as observed by TEM analyses. **Figure 3.2** shows the TEM images of Ru NPs stabilized in the ILs. High-resolution TEM (HRTEM) and high-angle annular dark-field scanning TEM (HAADF-STEM) analyses were also performed on all the Ru/FILs NPs systems (**Figure 3.3**)

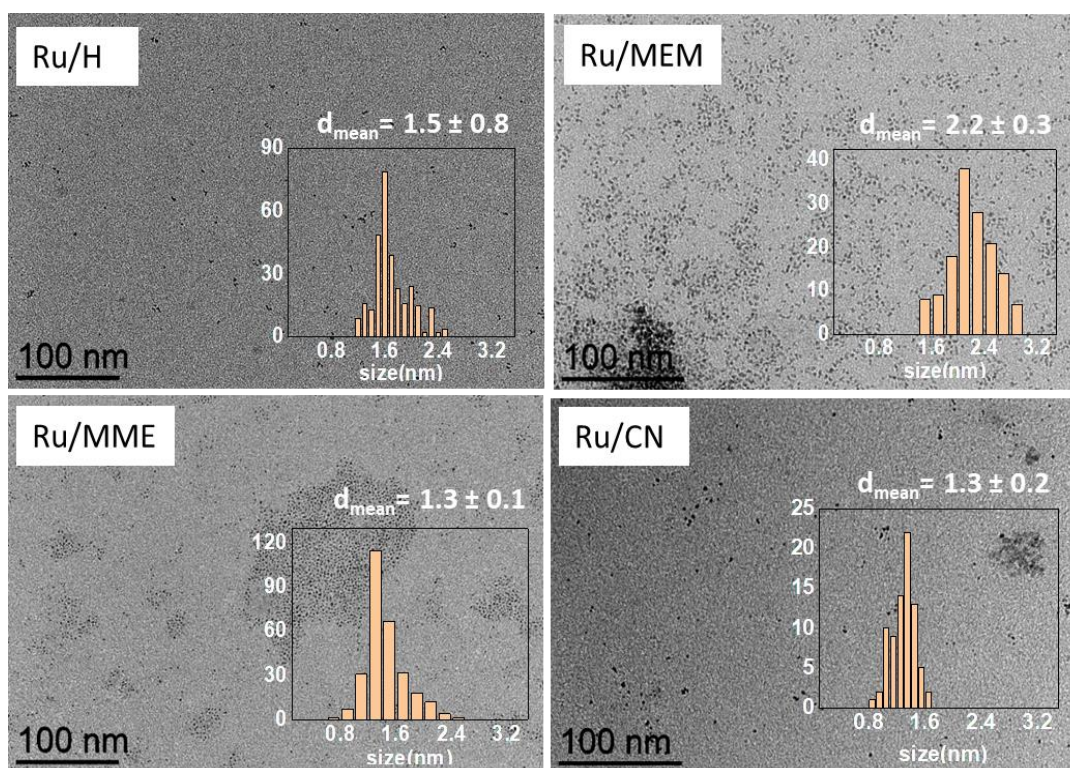


**Figure 3.2** TEM images of Ru/FILs NPs with their corresponding size distribution (scale bar = 100 nm).

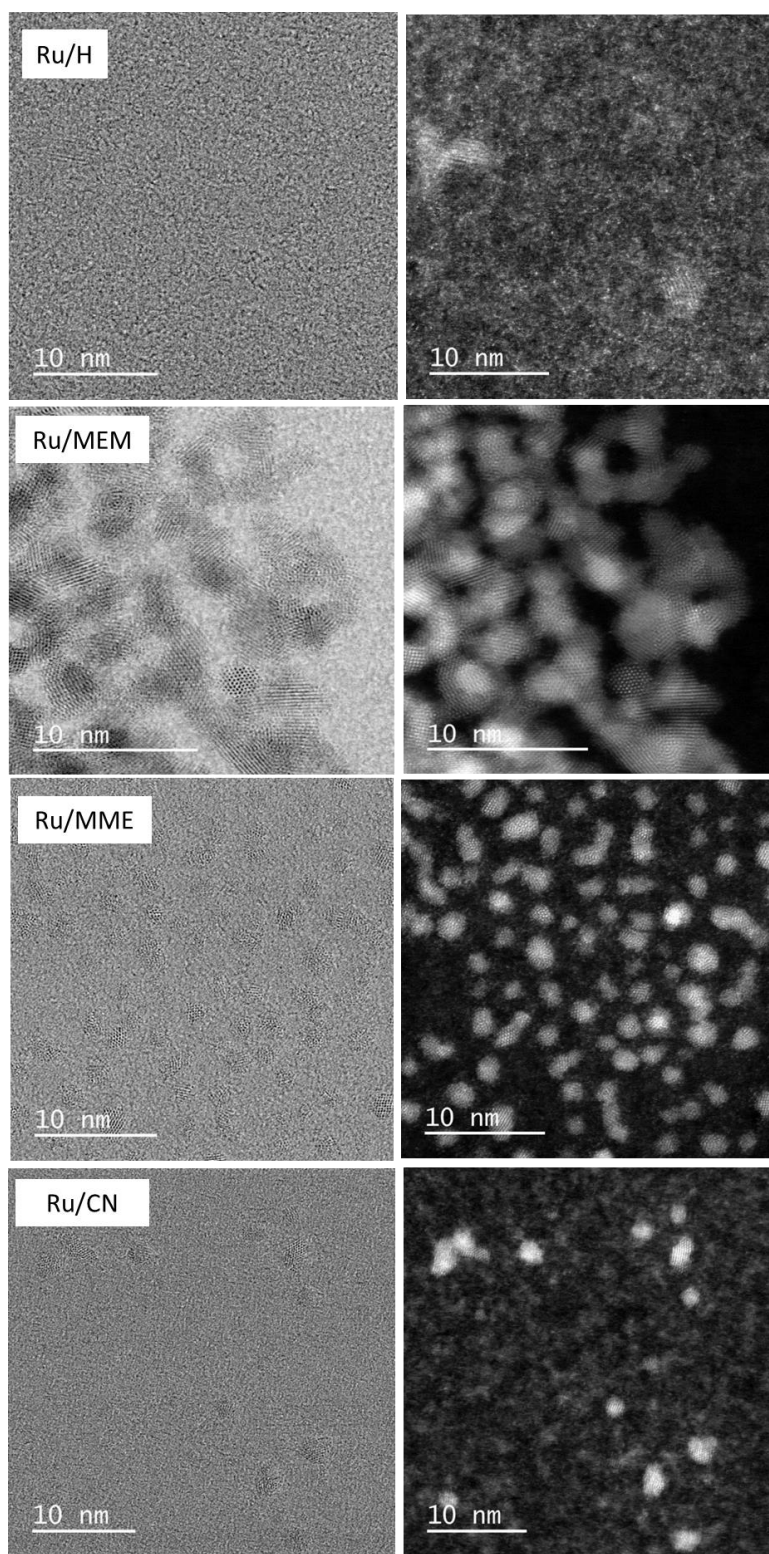


**Figure 3.3** HRTEM and HAADF-STEM images of Ru/FILs NPs (scale bar = 10 nm).

b) TG analysis

TG analyses of the Ru/FILs NPs were performed under N<sub>2</sub> and their stability compared with that of the respective ILs (**Figure 3.4 and Appendix C**) [14]. Notably, the Ru/FILs NPs showed a lower decomposition temperature  $T_{dec}$  of all the comprised ILs, thus indicating a close interaction between the ILs and the Ru NPs. The difference in decomposition temperature ( $\Delta T_{dec}$ ) of the ILs in the presence or the absence of Ru NPs was highest for H. This may result from geometrical stabilization of the Ru NPs inside the non-polar domains of H [2], leading to a maximum proximity of the alkyl chains of H with the Ru surface and favoring their decomposition. Oppositely, the smallest  $\Delta T_{dec}$  was observed for CN in which the Ru NPs are expected to interact strongly through the CN functionality, and therefore have less influence on the decomposition of the alkyl chain compared to the H counterpart [5,15–17]. Concerning the two methoxy-FILs, MEM and MME, the  $\Delta T_{dec}$  were found intermediate between those of H and CN, thus indicating some interaction between the surface of the Ru NPs and the ILs but less pronounced than with CN. Hence, overall, the Ru/ILs NPs colloidal suspensions remained robust when exposed to high temperature.

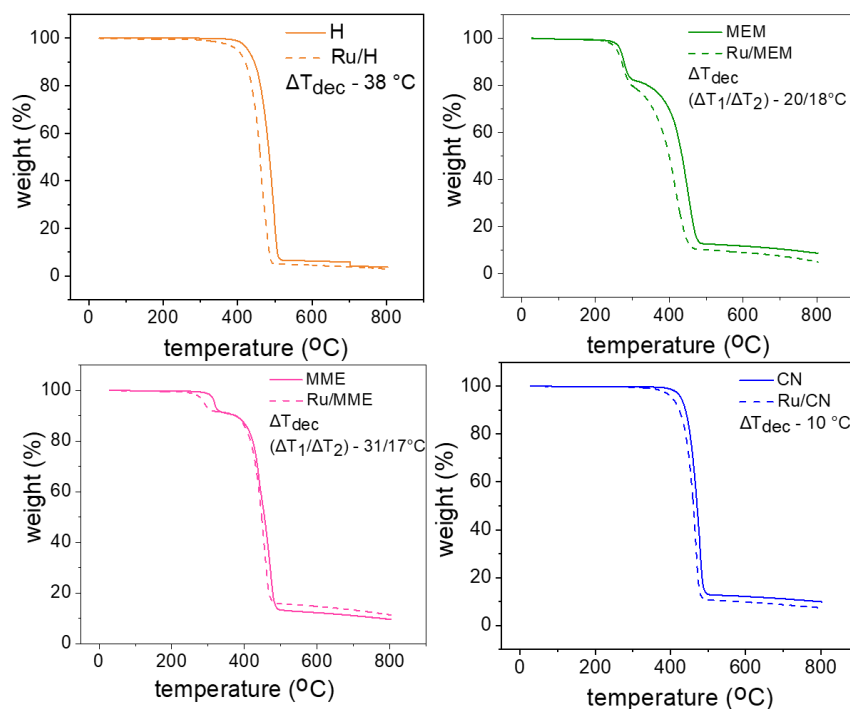


**Figure 3.4** TG profiles of the ILs (solid lines) and corresponding Ru/FILs NPs (dotted lines).

c) XPS analysis



XPS analyses were also performed on the Ru/FILs NPs, which showed similar spectra as those obtained of the ILs. The corresponding survey spectra for the Ru/FILs NPs are depicted in **Figure 3.5**. The deconvoluted high-resolution scan spectra of the different elements (C 1s, N 1s, F 1s, S 2p, O 1s) are compiled in **Appendix C**. **Tables 3.2, 3.3** and **3.4** summarize significant differences in binding energies of the Ru/FILs NPs compared to those of the ILs without Ru NPs.

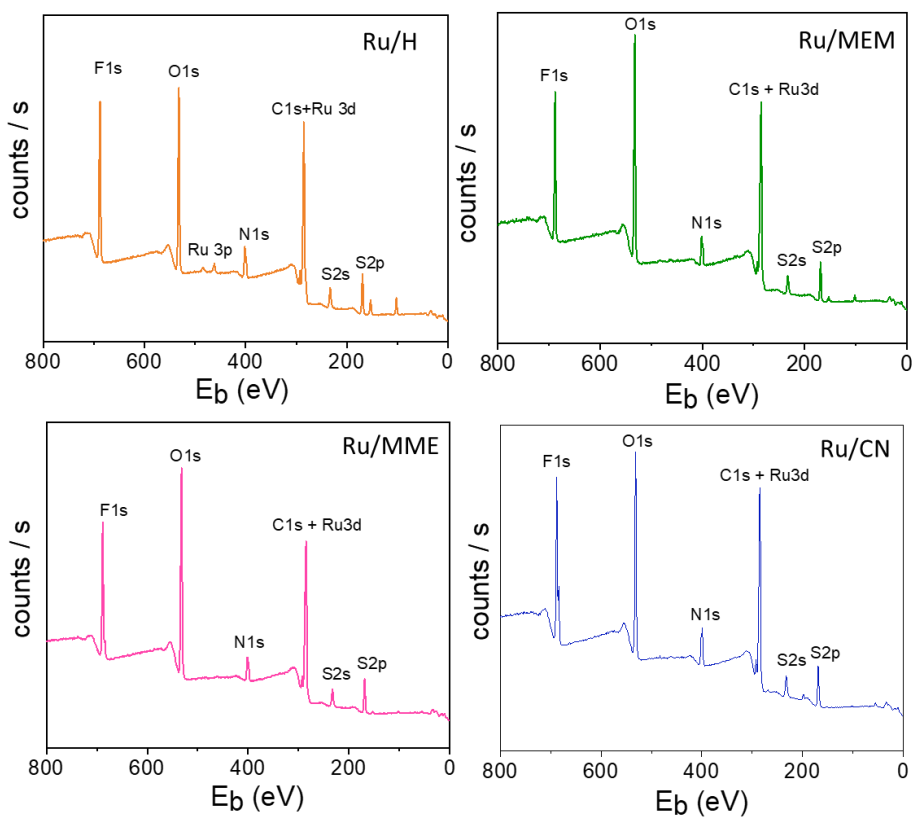


**Figure 3.5** XPS survey spectra of Ru/FILs NPs.

Noticeable shift in some binding energies was observed in the presence of Ru NPs ( $E_{RuIL}$ ) with respect to the IL, as represented by  $\Delta E$  and summarized in **Table 3.2** for the different elements. For H, the  $\Delta E_{C1s}$  was more pronounced for  $C_2$  and  $C_3$  (Table 3.3) of the cation, while it was lower for the elements present in the  $[NTf_2]^-$  anion of the IL. This could indicate a preferred solvation of Ru NPs in the non-polar domain of H with weak associated interactions. Oppositely, a higher  $\Delta E$



was found for N 1s, F 1s, O 1s, and to some extent S 2p, for the elements in the anions of MEM, MME and CN, which may be attributed to the presence of both anions and cations near the surface of the Ru NPs [6]. The higher values of  $\Delta E_{O1s}$  for MEM and MME compared to H and CN could also be due to the stabilization of the Ru NPs by the oxygen atoms from the cation in addition to the ones from the anions. A change of the  $E_{C1s}$  of C<sub>4</sub> to a lower value in the presence of Ru NPs (i.e., negative  $\Delta E$ ) would indicate formation of a nucleophilic species, e.g. *N*-heterocyclic carbene derived from the imidazolium cation [18]. However, for all the ILs  $\Delta E_{C1s}$  of C<sub>4</sub> was positive suggesting that carbene formation during Ru NPs synthesis was negligible. Likely, the very low basicity of the anion [NTf<sub>2</sub>]<sup>-</sup> and the mild conditions applied for the Ru NPs synthesis reduced the reactivity between the moderately acidic C<sub>4</sub> proton and the anion.

**Table 3.2** Difference in binding energies (eV) of the chemical states of selected elements in the ILs and Ru/FILs NPs.

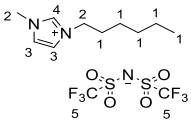
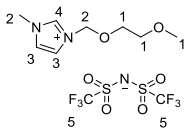
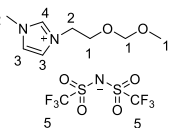
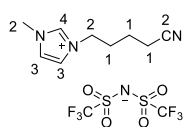
IL	$\Delta E$ cation (eV)				$\Delta E$ anion (eV)					
	C <sub>2</sub> 1s	C <sub>3</sub> 1s	C <sub>4</sub> 1s	N 1s	C <sub>5</sub> 1s	N 1s	F 1s	O 1s	S 2p <sub>3/2</sub>	S 2p <sub>1/2</sub>
H	0.10	0.27	0.07	0.09	0.07	0.16	0.12	0.04	0.15	0.17
MEM	-0.05	0.09	0.27	0.28	-0.08	0.23	0.29	0.41*	0.11	0.14
MME	0.06	0.29	0.01	0.29	0.16	0.31	0.36	0.20*	0.40	0.47
CN	0.01	-0.09	0.03	0.27	0.07	0.24	0.13	-0.04	0.35	0.28

\* $\Delta E$  cation and anion.

The binding energies ( $E_b$ ) atomic ratio (%) and the full-width-at-maximum FWHM (eV) of the C 1s and N 1s, O 1s, S 2p and F 1s of the Ru/FILs NPs have been summarized in **Table 3.3** and **Table 3.4**, respectively.

**Table 3.3** Binding energies (eV) of C 1s for the carbon atoms in the ILs and Ru/FILs NPs.

Chapter 3. Synthesis, characterization, and application in catalysis of ruthenium nanoparticles in functionalized ionic liquids

ILs	Atom <sup>a</sup>	Binding energy Ru/ILs NPs (E <sub>RuIL</sub> )	Atomic ratio (%)	FWHM (eV)
<b>H</b> 	C <sub>1</sub>	284.80	56.60	1.44
	C <sub>2</sub>	286.53	22.45	1.44
	C <sub>3</sub>	287.68	2.19	1.01
	C <sub>4</sub>	288.92	3.98	1.12
	C <sub>5</sub>	292.66	6.49	1.13
<b>MEM</b> 	C <sub>1</sub>	284.80	40.26	1.44
	C <sub>2</sub>	286.31	36.93	1.43
	C <sub>3</sub>	287.68	5.36	1.06
	C <sub>4</sub>	288.66	8.05	1.22
	C <sub>5</sub>	292.51	7.13	1.13
<b>MME</b> 	C <sub>1</sub>	284.80	32.78	1.44
	C <sub>2</sub>	286.37	35.95	1.43
	C <sub>3</sub>	287.80	11.51	1.38
	C <sub>4</sub>	288.76	3.99	1.33
	C <sub>5</sub>	292.54	8.42	1.16
<b>CN</b> 	C <sub>1</sub>	284.80	37.34	1.44
	C <sub>2</sub>	286.13	43.33	1.41
	C <sub>3</sub>	287.63	2.63	1.23
	C <sub>4</sub>	288.69	3.93	1.06
	C <sub>5</sub>	292.37	11.38	1.14

<sup>a</sup> C<sub>1</sub>-C<sub>5</sub> correspond to the carbon atoms in the ILs as numbered.

**Table 3.4** Binding energies (eV) of the chemical states of the atoms in the Ru/ILs NPs.

Chapter 3. Synthesis, characterization, and application in catalysis of ruthenium nanoparticles in functionalized ionic liquids

Element	Binding energy Ru/ILs NPs ( $E_{RuIL}$ )	Atomic ratio (%)	FWHM (eV)
H			
N 1s (anion)	399.24	39.18	1.37
N 1s (cation)	401.8	60.82	1.30
S 2p <sub>3/2</sub>	168.93	66.65	1.18
S 2p <sub>1/2</sub>	170.17	33.35	1.14
F 1s	688.5	100	1.83
O 1s (cation/anion)	532.21	86.9	1.44
H <sub>2</sub> O <sub>absorbed</sub>	533.59	13.10	1.44
Ru 3p <sub>3/2</sub>	460.90	30.49	1.44
MEM			
N 1s (anion)	399.37	40.62	1.41
N 1s (cation)	401.98	58.91	1.36
S 2p <sub>3/2</sub>	168.81	71.69	1.33
S 2p <sub>1/2</sub>	170.11	28.31	1.12
F 1s	688.73	100	1.83
O 1s (cation/anion)	532.70	77.75	1.44
H <sub>2</sub> O <sub>absorbed</sub>	533.17	22.25	1.44
Ru 3p <sub>3/2</sub>	460.70	44.83	1.44
MME			
N 1s (anion)	399.22	43.24	1.43
N 1s (cation)	401.81	56.76	1.34
S 2p <sub>3/2</sub>	168.94	80.65	1.57
S 2p <sub>1/2</sub>	170.26	19.35	1.04
F 1s (LiF)	684.36	10.69	1.75
F 1s (anion)	688.55	89.31	1.82
O 1s (CO <sub>3</sub> <sup>2-</sup> )	530.20	10.24	1.33
O 1s (cation/anion)	532.23	61.06	1.44
H <sub>2</sub> O <sub>absorbed</sub>	533.10	28.70	1.44
Ru 3p <sub>3/2</sub>	460.70	31.42	1.44
CN			

Element	Binding energy Ru/ILs NPs ( $E_{\text{RuIL}}$ )	Atomic ratio (%)	FWHM (eV)
N 1s (anion)	399.25	54.34	1.44
N 1s (cation)	401.79	45.36	1.34
S 2p <sub>3/2</sub>	168.84	64.85	1.1
S 2p <sub>1/2</sub>	170.01	35.15	1.34
F 1s	688.06	97.86	1.78
O 1s (CO <sub>3</sub> <sup>2-</sup> )	530.50	6.52	1.44
O 1s (cation/anion)	531.86	84.13	1.41
H <sub>2</sub> O <sub>absorbed</sub>	533.27	9.35	1.26
Ru 3p <sub>3/2</sub>	460.70	31.42	1.44

Despite the very low concentration of Ru NPs in the ILs, an increased number of scans enabled to acquire Ru 3p<sub>3/2</sub> spectra (**Figure 3.6**), where metallic Ru(0) (460.7 eV) and oxidized species Ru<sup>IV</sup>O<sub>2</sub>, hydrous Ru<sup>IV</sup>O<sub>2</sub>, and Ru<sup>III</sup>O<sub>3</sub> (likely formed during sample handling in air) with distinct bonding energies were identified. Notably, for all the Ru/ILs NPs was the bonding energy of the Ru(0) lower than reported values for metallic Ru (461.7 eV) in the literature[19]. These results further corroborate that the Ru NPs interacted with the ILs.

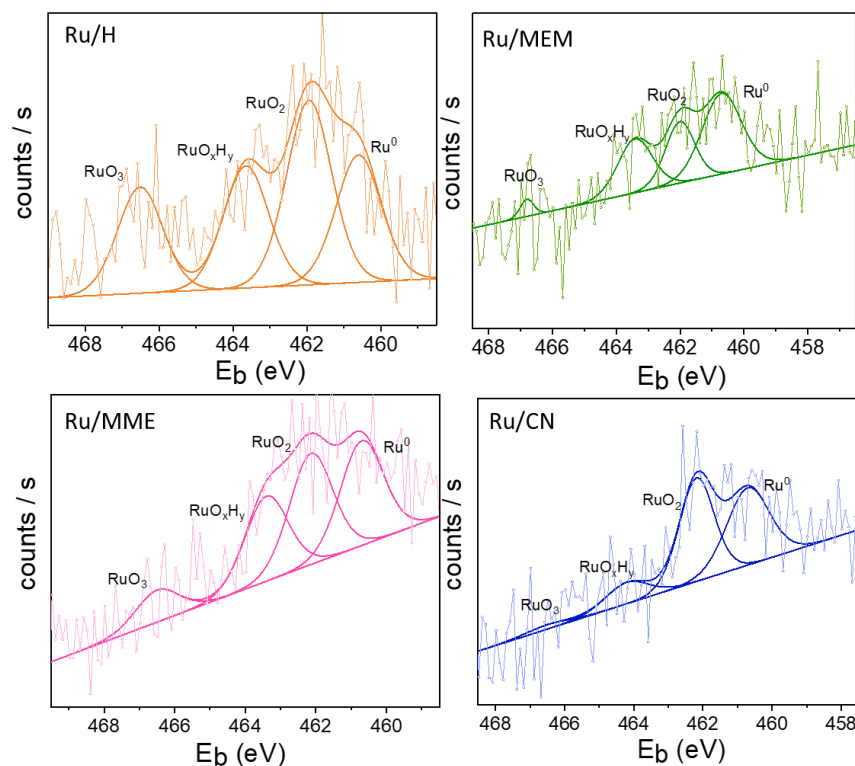


**Figure 3.6** High-resolution XPS spectra of Ru 3p for the Ru/FILs NPs systems.

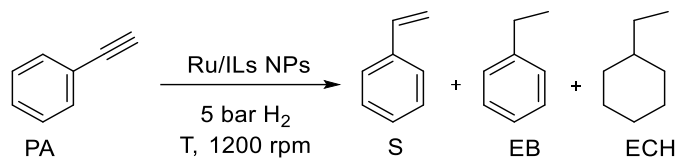
Unfortunately, NMR ( $^1\text{H}$ ,  $^{13}\text{C}\{^1\text{H}\}$ ) investigations on the Ru/FILs NPs systems did not provide clear data on the interaction of Ru NPs with the ILs, due to the presence of intense IL signals, which may have overlapped other signals if any were present. These data are available in the **Appendix C**.

### 3.3.3 Catalysis with Ru/FILs NPs

#### a) Hydrogenation of phenylacetylene

To evaluate the catalytic potential of Ru/FILs NPs, preliminary studies with Ru/H and Ru/MEM were conducted for the hydrogenation of phenylacetylene (**Scheme 3.2**). The reaction was selected because the hydrogenation of alkynes to alkenes is a challenging reaction as it is difficult to obtain chemoselectivity and stop reaction at the alkene and not reduce further to the alkane. Many literature studies rely on the use of expensive metals such as Pd (\$614/oz) [20] to catalyze this

reaction (>90% conversion and 70-97 % selectivity towards styrene), making of interest to test less costly metals [21–24].



**Scheme 3.2:** Hydrogenation of phenylacetylene (PA) to styrene (S), ethyl benzene (EB) and ethyl cyclohexane (ECH).

**Table 3.5** Reduction of phenylacetylene (PA) using Ru/FILs NPs.

Catalyst system	Time (h)	Conversion (%) <sup>b</sup>	Selectivity (%) <sup>b</sup>	
			S	EB
Ru/H	3	>99	58	42
Ru/MEM	6	89	51	49

<sup>a</sup> Reaction conditions: 0.02 mmol of Ru, 4 mmol of phenylacetylene, 0.3 mmol of octane (internal standard), 5 bar H<sub>2</sub>, 80 °C, 900 rpm. <sup>b</sup> Determined by GC using internal standard technique.

The initial studies were performed using Ru/H and Ru/MEM with mild reaction conditions (5 bar H<sub>2</sub>, 80 °C) (**Table 3.5**). **Figure 3.7** depicts the conversion vs. time plot along with the selectivity for both of the systems. For Ru/H, a complete conversion of PA was observed after 3 h with 58 % selectivity towards S, whereas Ru/MEM required 6 h of reaction to attain a conversion of 89 % of PA with 51 % and 49 % selectivity toward S and EB, respectively. Reduction of the aromatic ring of PA was not observed with any of the catalysts. In an attempt to increase S selectivity, the reaction temperature was decreased to 50 °C. This was done to reduce the rate of S hydrogenation compared to PA to S step, as literatures shows that the conversion of alkenes to alkanes proceeds at a greater rate than the alkyne → alkene [25,26], but no significant improvement of the selectivity towards S was observed, thus indicating that these Ru/FILs NPs are not appropriate catalysts for the selective formation of S from PA.

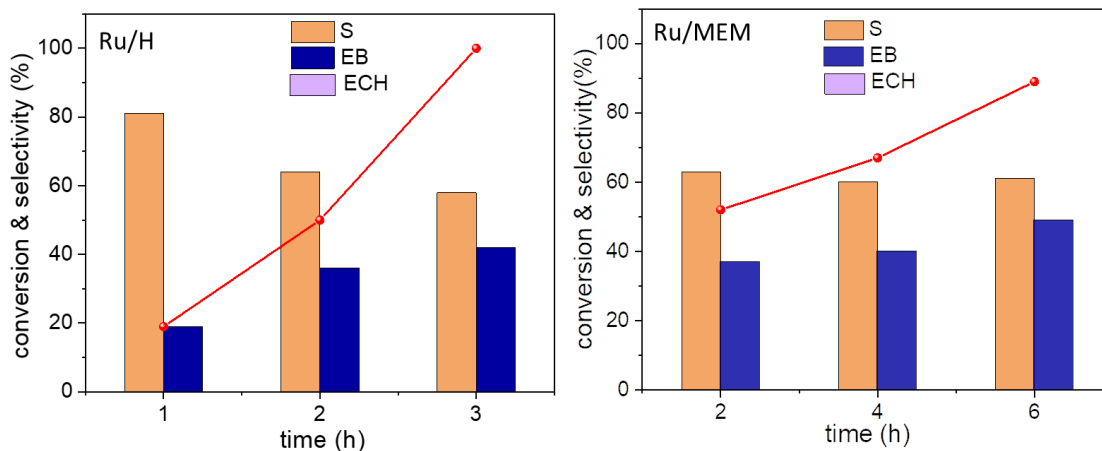
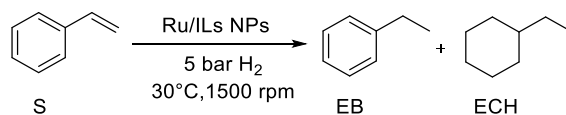


**Figure 3.7** Time-conversion curves for the hydrogenation of phenylacetylene with a) Ru/H and b) Ru/MEM catalysts. Red line = conversion, orange bar S = selectivity, and blue bar EB = selectivity.

Reaction conditions: 0.02 mmol of Ru, 4 mmol of phenylacetylene, 0.3 mmol of octane (internal standard), 5 bar H<sub>2</sub>, 80 °C, 900 rpm.

### b) Hydrogenation of styrene

Initially the hydrogenation of S was carried out under 50 °C and 5 bar H<sub>2</sub>, using a stirring speed of 900 rpm and S:Ru ratio 200:1 (**Scheme 3.3**). The catalytic systems were under these conditions found to rather active for the conversion of S. **Table 3.6** gives the conversion of S and selectivity towards EB/ECH for each catalyst after 3h of reaction.



**Scheme 3.3** Hydrogenation of styrene (S) to ethyl benzene (EB) and ethyl cyclohexane (ECH).

**Table 3.6** Reduction of styrene (S) to ethyl benzene (EB) and ethyl cyclohexane (ECH).

Catalyst system	Time (h)	Conversion (%) <sup>b</sup>	Selectivity (%) <sup>b</sup>	
			EB	ECH
Ru/H	3	>99	89	11
Ru/MEM	3	>99	86	14
Ru/MME	3	>99	>99	0
Ru/CN	3	89	>99	0

<sup>a</sup> Reaction conditions: 0.02 mmol of Ru, 4 mmol of styrene, 0.3 mmol of octane (internal standard), 5 bar H<sub>2</sub>, 50 °C, 900 rpm. <sup>b</sup> Determined by GC using internal standard technique.

To account for any varying solubility of S in the different ILs having different viscosity and minimize potential influence from mass transport limitations, a series of catalytic tests were conducted at three distinct stirring rates, 600, 900, and 1500 rpm with the Ru/MEM system. For each experiment, samples were collected and analyzed after 1 h of reaction and the results are presented in **Figure 3.8**.

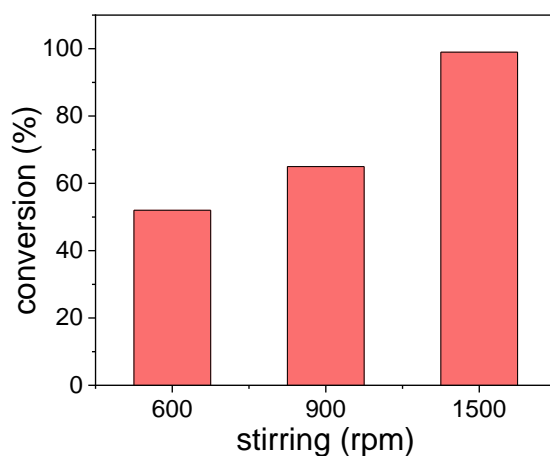


**Figure 3.8** Styrene conversion at different stirring rates for Ru/MEM. Reaction conditions: 0.02 mmol of Ru, 4 mmol of styrene, 0.3 mmol of octane (internal standard), 5 bar H<sub>2</sub>, 30 °C, 1500 rpm.

Under the given reaction conditions (50 °C, 5 bar H<sub>2</sub>, S:Ru ratio 200:1, 1 h), the conversion of S reached 52 % at 600 rpm and 65 % at 900 rpm, whereas it reached complete conversion at 1500 rpm. This clearly showed that the stirring had a significant impact on the rate of conversions for



the lower agitation speeds due to mass transport limitations. Accordingly, all further catalytic tests with the series of Ru/FIL NPs catalysts were pursued using a stirring speed of 1500 rpm. In addition, the reaction temperature was decreased from 50 to 30°C in order to follow the reaction precisely which otherwise proceeded very fast. **Table 3.7** summarizes the additional catalytic reactions obtained with the various Ru/FILs NPs catalysts.

**Table 3.7** Hydrogenation of styrene (S) with Ru/FILs NPs catalysts. <sup>a</sup>

Catalyst system	Time (h)	Conversion (%) <sup>b</sup>	Selectivity (%) <sup>b</sup>	
			EB	ECH
Ru/H	0.5	>99	>99	0
Ru/H	24	>99	93	7
Ru/MEM	1	>99	>99	0
Ru/MEM	24	>99	78	22
Ru/MME	1.5	98	>99	0
Ru/MME	24	98	>99	0
Ru/CN	6	>99	>99	0
Ru/CN	24	>99	>99	0

<sup>a</sup> Reaction conditions: 0.02 mmol of Ru, 4 mmol of styrene, 0.3 mmol of octane (internal standard), 5 bar H<sub>2</sub>, 30°C, 1500 rpm. <sup>b</sup> Determined by GC using internal standard technique.

As shown in **Table 3.7**, all the Ru/FILs NPs systems were active for the catalytic hydrogenation of S providing full substrate conversion in short reaction times (0.5-6 h). Importantly, the ILs alone did not show any conversion of S when submitted to the same reaction conditions (results not shown). **Figure 3.9** depicts the time-conversion curves for the hydrogenation of styrene with the different Ru/ILs NPs catalysts. **Figure 3.10** shows the conversion of S for each system in mmol.

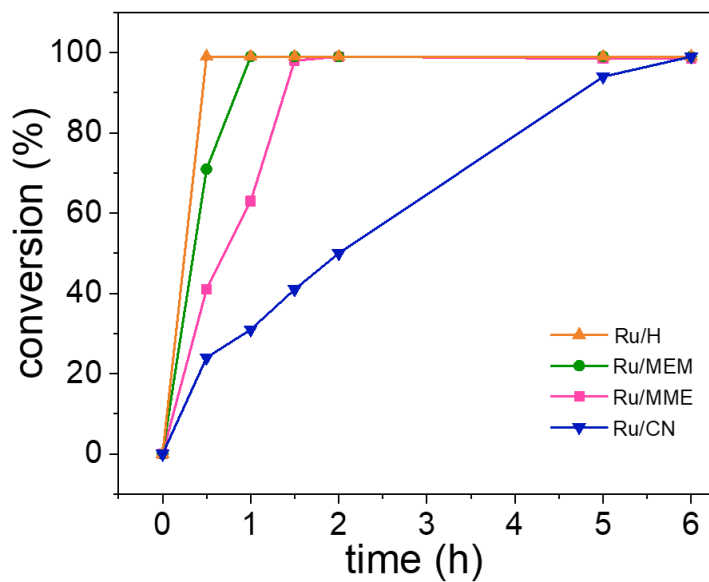


**Figure 3.9** Time-conversion curves for the hydrogenation of styrene with the different Ru/FILs NPs catalysts. Reaction conditions: 0.02 mmol of Ru, 4 mmol of styrene, 0.3 mmol of octane (internal standard), 5 bar H<sub>2</sub>, 30 °C, 1500 rpm.

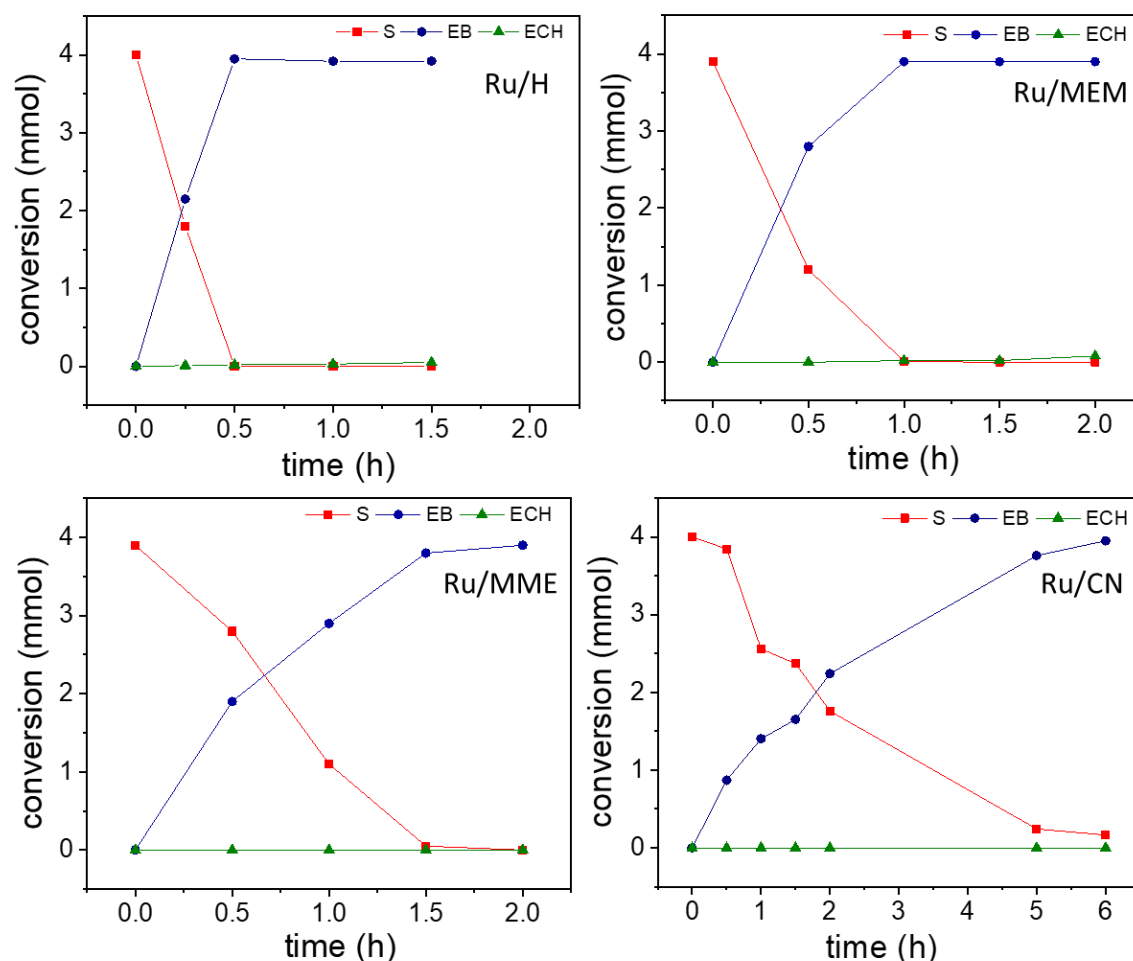


**Figure 3.10** Time-conversion curves (in mmol) for the hydrogenation of styrene with the different Ru/ILs NPs catalysts. a) Ru/H b) Ru/MEM c) Ru/MME and c) Ru/CN. Reaction conditions: 0.02 mmol of Ru, 4 mmol of styrene, 0.3 mmol of octane (internal standard), 5 bar H<sub>2</sub>, 30 °C, 1500 rpm.

The difference in the rate of conversion depending on the systems of Ru/FILs NPs was analyzed through the calculation of the turnover frequencies (TOF) at isoconversion with respect to the Ru atoms available at the NP surface (**Table 3.8**). The surface atoms were estimated according to the NP size and surface (details on the calculation procedure are given in the footnote of the same Table).

**Table 3.8** Calculation of TOFs for styrene (S) hydrogenation.

Ru/ILs NPs	NP mean size (nm) <sup>a</sup>	Ru atoms in NP <sup>b</sup>	Ru atoms in core <sup>c</sup>	Ru atoms in outer layer <sup>d</sup>	Ratio of Ru atoms at NP surface <sup>e</sup>	TOF (h <sup>-1</sup> ) <sup>f</sup>
Ru/H	1.5 ± 0.8	130	47	83	0.63	1,332
Ru/MEM	2.2 ± 0.3	409	214	195	0.48	629
Ru/MME	1.3 ± 0.1	84	25	59	0.70	212
Ru/CN	1.3 ± 0.2	84	25	59	0.70	10

<sup>a</sup> Mean size of Ru/IL NPs were determined from analysis of TEM images by considering at least 200 individual nanoparticles. Number of atoms in Ru NPs were calculated as follows: the number of Ru atoms in *hcp* cell (N) is 6. The shell thickness is assumed as half of the lattice constant, for Ru is 0.214 nm. The volume of Ru cell is 0.0817 nm<sup>3</sup>. R<sub>np</sub> represents the radius of NP. The volume of all Ru atoms in the outer layer of NP: V<sub>shell</sub> = V<sub>total</sub> - V<sub>core</sub> = 4/3·π·R<sub>np</sub><sup>3</sup> - 4/3·π·(R<sub>np</sub> - R<sub>Ru</sub>)<sup>3</sup>, V<sub>total</sub> means the volume of one Ru NP, V<sub>core</sub> corresponds to the volume of NP excluded the outer layer of atoms. <sup>b</sup> The total number of Ru atoms N<sub>total</sub> = N·V<sub>total</sub>/0.0817. <sup>c</sup> The number of metal atoms in the core N<sub>core</sub> = N<sub>total</sub> - N<sub>shell</sub>. <sup>d</sup> The numbers of metal atoms on the shell N<sub>shell</sub> = N·V<sub>shell</sub>/0.0817. <sup>e</sup> The ratio of Ru atoms on the surface of NP = N<sub>shell</sub>/N<sub>total</sub>. <sup>f</sup> TOFs calculated at isoconversion (55%) with respect to the surface Ru atom ratio.

The highest TOF value (1,332 h<sup>-1</sup>) was reached with the Ru NPs embedded in the non-functionalized IL, namely Ru/H catalyst. The two methoxy-functionalized IL systems (Ru/MEM and Ru/MME) yielded high rates (TOFs of 629 h<sup>-1</sup> and 212 h<sup>-1</sup>, respectively), while the Ru/CN had the lowest activity (TOF of 10 h<sup>-1</sup>). The differences observed in terms of reaction rates may be correlated to the variation in polarity of the ILs that can influence the solubility of the substrate, as styrene is expected being more soluble in non-polar domains than in polar ones. In line with this, the H IL that contains only alkyl chains in its structure presents the larger non-polar domains of the IL series [2] and interestingly, the Ru NPs stabilized in this IL led to the highest TOF. Oppositely, the more polar IL is expected to be the CN FIL and the CN-stabilized Ru NPs displayed the lower activity. To validate the correlation between the conversion results and the solubility of styrene in the catalytic systems, solubility tests of the substrate in the different ILs were performed (details are given in the experimental section 3.2.3). The determined solubility values are reported in **Table 3.9** and plotted against the TOF values in **Figure 3.11**. The solubility of styrene in each IL appeared to correlate well with the conversion results and the calculated TOFs, showing that the more efficient catalytic systems were those which allow the higher solubility of the styrene, with the activity order Ru/H > Ru/MEM/Ru/MME > Ru/CN.

**Table 3.9** Solubility of S and EB in ILs.<sup>a</sup>

IL	Solubility (mmol/mL)	
	S	EB
H	5.42	6.46
MEM	2.66	2.41
MME	2.63	1.61
CN	2.14	1.42

<sup>a</sup> Experimental details in **section 3.2.3**.

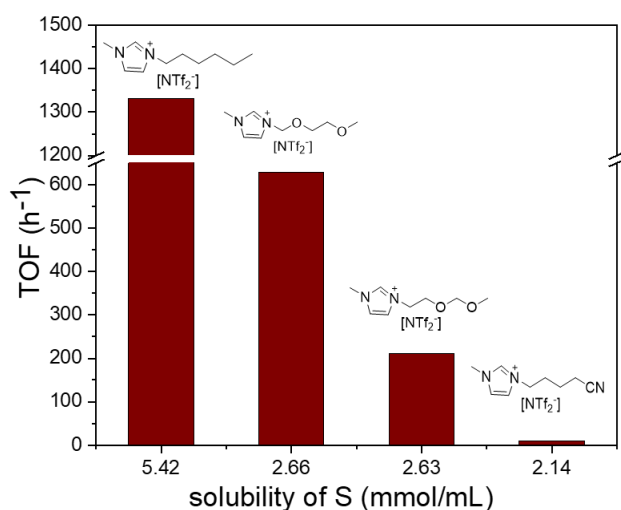


**Figure 3.11** Solubility of S in the ILs (mmol/mL) vs. TOF/surface atoms.

Besides efficient catalytic activity in the hydrogenation of S, total selectivity towards EB was obtained for all the catalytic systems at full conversion. Interestingly, a total selectivity was also observed after 24 h of reaction with the Ru/MME and Ru/CN catalysts, while some successive hydrogenation of EB to ECH occurred for Ru/H (7%) and Ru/MEM (22%) after 24 h (**Figure 3.12**). These results proved that the Ru/FILs NPs catalysts were highly selective for the hydrogenation of the vinyl group of S, but unable to hydrogenate the aromatic ring under the applied reaction conditions which is markedly different to previous literature where Ru NPs are reported to hydrogenate aromatics even at room temperature [27–29].

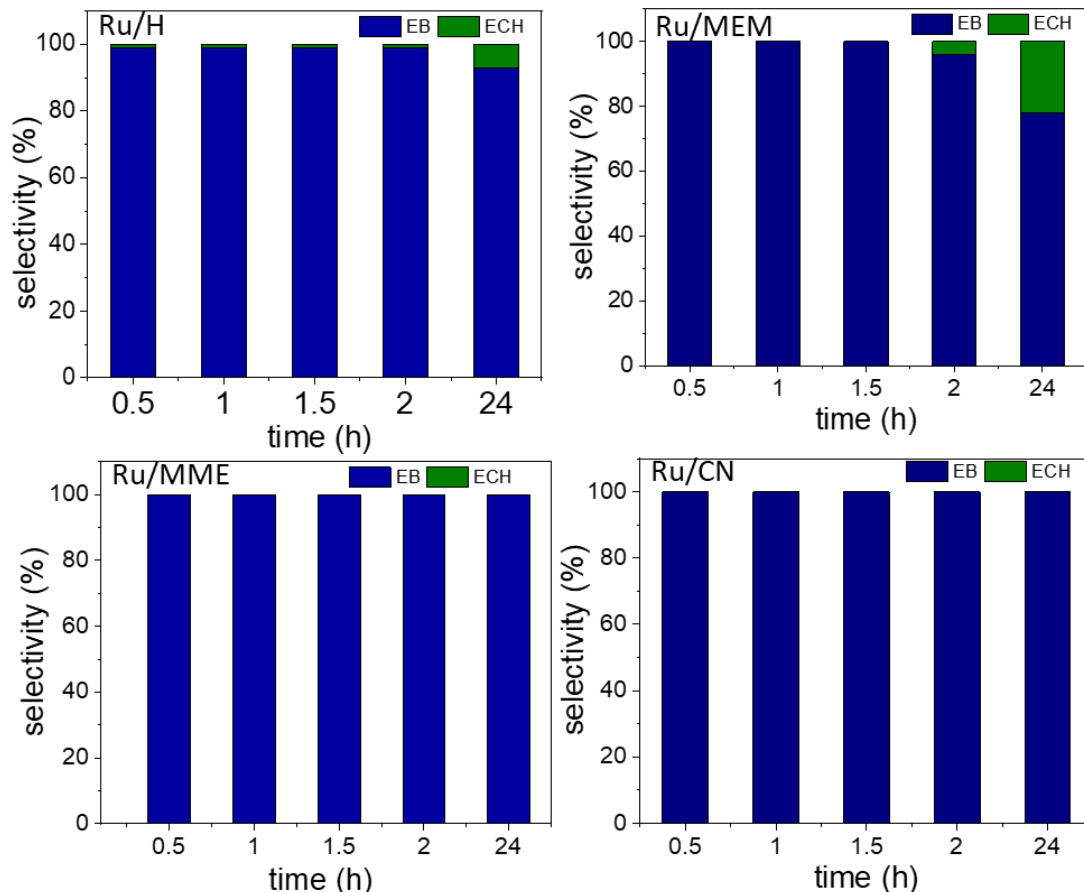


**Figure 3.12** Selectivity data of the Ru/FILs NPs at different time points 0.5 to 24h. Reaction conditions: 0.02 mmol of Ru, 4 mmol of styrene, 0.3 mmol of octane (internal standard), 5 bar H<sub>2</sub>, 30 °C, 1500 rpm.

Given the results obtained with the Ru/ILs NPs catalysts, the solubility of EB in the ILs was also measured to evaluate the influence of this parameter on the conversion of EB into ECH. As shown in **Table 3.9**, the solubility of EB was found to be similar to that of S in the ILs, thus evidencing that the high selectivity observed towards EB was not caused by the low solubility of EB in the ILs. Other key parameters can be the size of the Ru NPs and/or the accessibility of the EB at the Ru surface that may be limited by the interaction between the ILs and the surface of the Ru NPs. The hydrogenation of aromatics with Ru requires the presence of facets with an estimated minimum number of close and free Ru atoms of approximately three, which is favored in large and better crystallized NPs [30,31]. Although, Ru/H and Ru/MEM catalysts contained the larger

Ru NPs of the series with mean sizes of 1.5 and 2.2 nm, respectively (**Table 3.1**), and this could possibly account for the observed hydrogenation of EB into ECH with these catalysts, the difference in Ru NP sizes compared to the other series was only minor (mean size 1.3 nm). Hence, apart from the effect of NP size, a limitation of the surface accessibility could also derive from steric hindrance and/or blockage of Ru surface atoms, and the ILs could also have an electronic influence on the Ru surface. The Ru/MME and Ru/CN catalytic systems were found to be less prone to hydrogenate EB into ECH, indicating that less Ru surface was accessible in these systems than in Ru/H and Ru/MEM. This is supported by the smaller size of the Ru NPs in these catalysts, but it could also result from the interaction of the MME and CN FILs, *via* -O-CH<sub>2</sub>-O- and -CN groups, respectively. Such interactions may, for steric and/or electronic reasons, influence the surface properties of the Ru/IL NPs in a way that limits the hydrogenation of the aromatic ring.

To complete the catalysis study, the recyclability of each Ru/ILs NPs catalyst was tested in five successive catalytic runs at partial conversion. The obtained results are shown in **Figure 3.13**. Notably, the styrene conversion with the Ru/H catalytic system decreased gradually during the five catalytic runs, whereas the catalytic systems with the three FILs maintained similar styrene conversions upon reuse. ICP analysis of the Ru/H phase from the first run to the fifth one showed a decrease in the Ru content from 0.2 to  $\approx$  0.1 wt.%, thus confirming that Ru leaching from the IL phase during catalyst recycling was responsible for the lower conversion. In contrast, the Ru content remained essentially unchanged during the five catalytic runs with the Ru/MEM, Ru/MME and Ru/CN systems, which could indicate that Ru-FIL interactions improved the confinement of the Ru NPs in these systems compared to the Ru/H system and that the functionalization of IL had a positive influence on the stability of the catalysts [32]. Interestingly, TEM images of the spent Ru/IL catalysts (**Figure 3.14**) showed no noticeable change in the mean size nor size distribution of the Ru NPs compared to the pristine systems (**Figure 3.2**), pointing out that the Ru NPs remained stable under the reaction conditions for all the systems and leaching was not related to Ru NPs instability. Hence, more likely, the larger non-polar domains in the unfunctionalized IL compared to the FILs enhanced the catalyst solubility in the non-polar washing solvent (pentane), thus leading to a gradual catalyst loss during the intermediate washings between the catalytic runs.

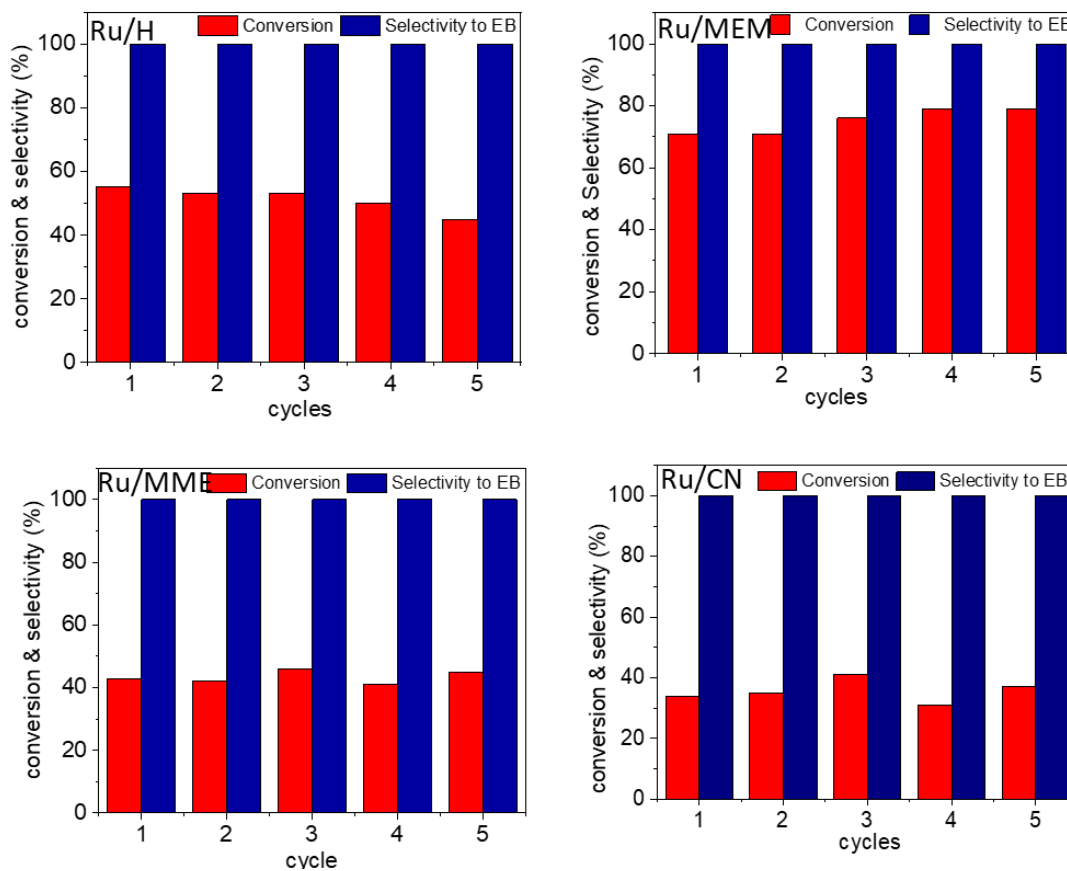


**Figure 3.13** Recyclability tests of the Ru/FILs NPs catalysts in the hydrogenation of styrene performed at partial conversion: a) H (15 min), b) MEM (30 min), c) MME (30 min) and (d) CN (60 min). Reaction conditions: 0.02 mmol of Ru, 4 mmol of styrene, 0.3 mmol of octane (internal standard), 5 bar H<sub>2</sub>, 30 °C, 1500 rpm.



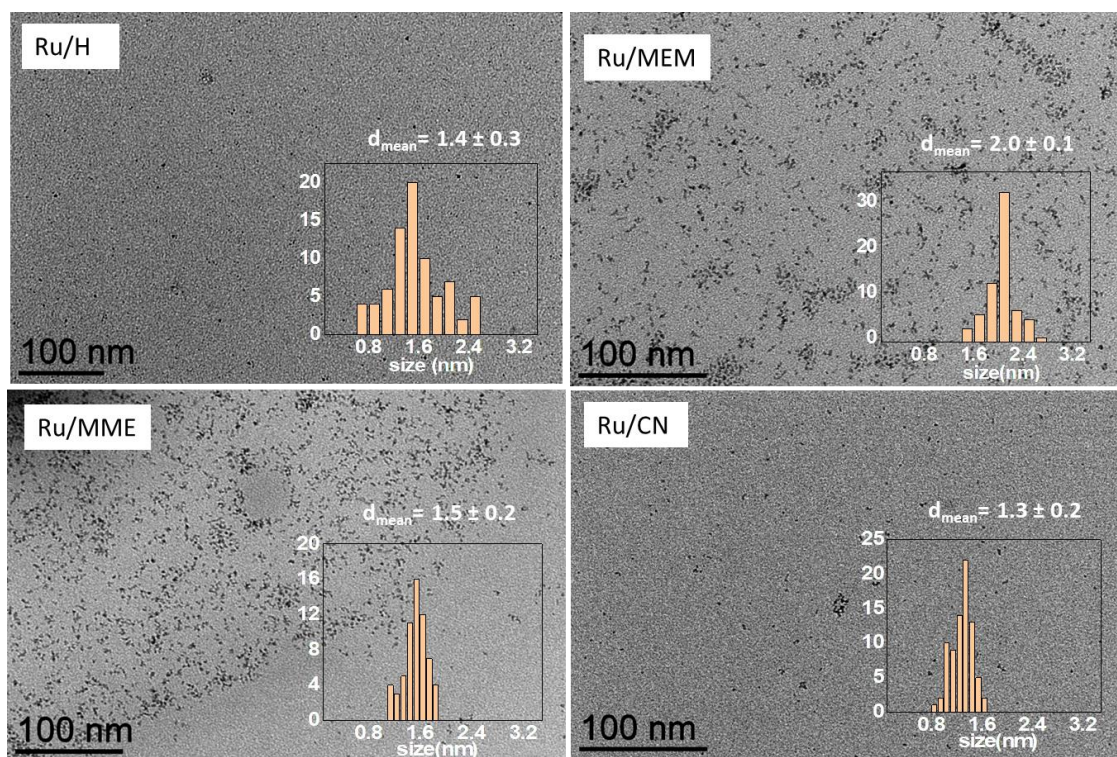


**Figure 3.14** TEM images of the Ru/ILs NPs systems after five catalytic runs with their corresponding size distribution.

### 3.4 Summary

A series of catalytic systems based on Ru NPs in a non-functionalized IL (H) and three FILs containing cyano (CN) and methoxy (MEM and MME) groups, have been synthesized, characterized, and applied for the hydrogenation of styrene. The methoxy-functionalized systems, Ru/MEM NPs and Ru/MME NPs were novel systems whereas the Ru/H and Ru/CN were reference systems previously described in literature. The collection of systems allowed to study the influence of the nature of the IL on the catalytic properties of the Ru NP catalysts. All the Ru/ILs NPs were found to be efficient catalysts for the hydrogenation of styrene under mild reaction conditions (30 °C, 5 bar of H<sub>2</sub>), providing full conversion of styrene with full ethyl benzene selectivity in short reaction times (0.5-6 h). Interestingly, a clear difference in activity (TOFs) was observed as a function of the nature of the IL, following the order Ru/H (1,332 h<sup>-1</sup>) > Ru/MEM (629 h<sup>-1</sup>) > Ru/MME (212 h<sup>-1</sup>) >> Ru/CN (10 h<sup>-1</sup>). In addition, a total selectivity for ethyl benzene was also observed at longer reaction time (24 h) for the Ru/MME and Ru/CN systems,

while some successive hydrogenation to ethyl cyclohexane occurred for Ru/H (7%) and Ru/MEM (22%) after 24 h. This shows that the Ru/ILs NPs had a strong preference towards hydrogenation of the vinyl group instead of the aromatic ring under the applied reaction conditions, which is a reactivity pattern different from typically reported for Ru NPs. Accordingly, this indicates that less Ru surface was accessible in Ru/MME and Ru/CN than in Ru/H and Ru/MEM, which can be attributed partly to lower Ru NP sizes in the former catalysts, though a contributing effect may also derive from metal-IL interactions of the MME and CN FILs *via* -O-CH<sub>2</sub>-O- and -CN groups, respectively. Such interactions may, by steric and/or electronic reasons, influence the surface properties of the Ru/ILs NPs and hamper the hydrogenation of the aromatic ring. This hypothesis is supported by the XPS results which evidenced for all Ru/ILs NPs systems a bonding energy of Ru<sup>0</sup> lower than literature values for metallic Ru, indicating that the Ru NPs and the ILs closely interact. Finally, recycling of the Ru/ILs NPs systems in five catalytic runs evidenced that the FIL-stabilized catalysts were more stable than the non-functionalized Ru/H catalyst system, where Ru leaching likely occurred due to higher solubility of the Ru/H NPs in the workup solvent of the reaction mixture between catalytic runs. Nevertheless, the results show that the functionalization of IL had a positive influence on the stability of the catalysts. In perspective, the work introduces a benign and facile co-solvent free synthesis protocol to obtain well-dispersed and narrow-sized Ru NPs stabilized by FILs containing methoxy-functionalities, which present a good balance between stability and catalytic activity. This allows Ru/ILs NPs to hydrogenate styrene with activity and total selectivity towards ethylbenzene at milder reaction conditions (5 bar H<sub>2</sub>, 30 °C) than previously reported in literature [11,13]

### 3.5 References

1. Axet, M.R.; Philippot, K. Catalysis with Colloidal Ruthenium Nanoparticles. *Chem. Rev.* **2020**, *120*, 1085–1145, doi:10.1021/acs.chemrev.9b00434.
2. Gutel, T.; Santini, C.C.; Philippot, K.; Padua, A.; Pelzer, K.; Chaudret, B.; Chauvin, Y.; Basset, J.M. Organized 3D-Alkyl Imidazolium Ionic Liquids Could Be Used to Control the Size of in Situ Generated Ruthenium Nanoparticles? *J. Mater. Chem.* **2009**, *19*, 3624–3631, doi:10.1039/b821659b.
3. Campbell, P.S.; Santini, C.C.; Bayard, F.; Chauvin, Y.; Collire, V.; Podgoršek, A.; Costa Gomes, M.F.; Sá, J. Olefin Hydrogenation by Ruthenium Nanoparticles in Ionic Liquid Media: Does Size Matter? *J. Catal.* **2010**, *275*, 99–107, doi:10.1016/j.jcat.2010.07.018.

4. Luska, K.L.; Moores, A. Ruthenium Nanoparticle Catalysts Stabilized in Phosphonium and Imidazolium Ionic Liquids: Dependence of Catalyst Stability and Activity on the Ionicity of the Ionic Liquid. *Green Chem.* **2012**, *14*, 1736–1742, doi:10.1039/c2gc35241a.
5. Prechtel, M.H.G.; Scholten, J.D.; Dupont, J. Tuning the Selectivity of Ruthenium Nanoscale Catalysts with Functionalised Ionic Liquids: Hydrogenation of Nitriles. *J. Mol. Catal. A Chem.* **2009**, *313*, 74–78, doi:10.1016/j.molcata.2009.08.004.
6. Pensado, A.S.; Pádua, A.A.H. Solvation and Stabilization of Metallic Nanoparticles in Ionic Liquids. *Angew. Chem., Int. Ed.* **2011**, *50*, 8683–8687, doi:10.1002/anie.201103096.
7. Wang, J.; Jiang, J.; Sun, Y.; Zhong, Z.; Wang, X.; Xia, H.; Liu, G.; Pang, S.; Wang, K.; Li, M.; et al. Recycling Benzene and Ethylbenzene from In-Situ Catalytic Fast Pyrolysis of Plastic Wastes. *Energy Convers. Manag.* **2019**, *200*, 112088, doi:10.1016/j.enconman.2019.112088.
8. Harraz, F.A.; El-Hout, S.E.; Killa, H.M.; Ibrahim, I.A. Palladium Nanoparticles Stabilized by Polyethylene Glycol: Efficient, Recyclable Catalyst for Hydrogenation of Styrene and Nitrobenzene. *J. Catal.* **2012**, *286*, 184–192, doi:10.1016/j.jcat.2011.11.001.
9. Li, J.; Zhang, B.; Chen, Y.; Zhang, J.; Yang, H.; Zhang, J.; Lu, X.; Li, G.; Qin, Y. Styrene Hydrogenation Performance of Pt Nanoparticles with Controlled Size Prepared by Atomic Layer Deposition. *Catal. Sci. Technol.* **2015**, *5*, 4218–4223, doi:10.1039/c5cy00598a.
10. Jiang, Y.F.; Yuan, C.Z.; Xie, X.; Zhou, X.; Jiang, N.; Wang, X.; Imran, M.; Xu, A.W. A Novel Magnetically Recoverable Ni-CeO<sub>2</sub>-x/Pd Nanocatalyst with Superior Catalytic Performance for Hydrogenation of Styrene and 4-Nitrophenol. *ACS Appl. Mater Interfaces* **2017**, *9*, 9756–9762, doi:10.1021/acsami.7b00293.
11. Parida, D.; Bakkali-Hassani, C.; Lebraud, E.; Schatz, C.; Grelier, S.; Taton, D.; Vignolle, J. Tuning the Activity and Selectivity of Polymerised Ionic Liquid-Stabilised Ruthenium Nanoparticles through Anion Exchange Reactions. *Nanoscale* **2022**, *14*, 4635–4643, doi:10.1039/d1nr07628k.
12. Wu, Z.; Jiang, H. Efficient Palladium and Ruthenium Nanocatalysts Stabilized by Phosphine Functionalized Ionic Liquid for Selective Hydrogenation. *RSC Adv.* **2015**, *5*, 34622–34629, doi:10.1039/c5ra01893e.
13. Jiang, H.Y.; Zheng, X.X. Tuning the Chemoselective Hydrogenation of Aromatic Ketones, Aromatic Aldehydes and Quinolines Catalyzed by Phosphine Functionalized Ionic Liquid Stabilized Ruthenium Nanoparticles. *Catal. Sci Technol.* **2015**, *5*, 3728–3734, doi:10.1039/c5cy00293a.
14. Ngo, H.L.; LeCompte, K.; Hargens, L.; McEwen, A.B. Thermal Properties of Imidazolium Ionic Liquids. *Thermochim. Acta* **2000**, *357–358*, 97–102, doi:10.1016/S0040-6031(00)00373-7.
15. Gieshoff, T.N.; Welther, A.; Kessler, M.T.; Prechtel, M.H.G.; Jacobi von Wangelin, A. Stereoselective Iron-Catalyzed Alkyne Hydrogenation in Ionic Liquids. *Chemical Communications* **2014**, *50*, 2261–2264, doi:10.1039/c3cc49679a.
16. Venkatesan, R.; Prechtel, M.H.G.; Scholten, J.D.; Pezzi, R.P.; MacHado, G.; Dupont, J. Palladium Nanoparticle Catalysts in Ionic Liquids: Synthesis, Characterisation and Selective Partial Hydrogenation of Alkynes to Z-Alkenes. *J. Mater. Chem.* **2011**, *21*, 3030–3036, doi:10.1039/c0jm03557b.
17. Konnerth, H.; Prechtel, M.H.G. Selective Partial Hydrogenation of Alkynes to (Z)-Alkenes with Ionic Liquid-Doped Nickel Nanocatalysts at near Ambient Conditions. *Chem. Comm.* **2016**, *52*, 9129–9132, doi:10.1039/c6cc00499g.

18. Bernardi, F.; Scholten, J.D.; Fecher, G.H.; Dupont, J.; Morais, J. Probing the Chemical Interaction between Iridium Nanoparticles and Ionic Liquid by XPS Analysis. *Chem. Phys. Lett.* **2009**, *479*, 113–116, doi:10.1016/j.cplett.2009.07.110.
19. Morgan, D.J. Resolving Ruthenium: XPS Studies of Common Ruthenium Materials. *Surf. Interface Anal.* **2015**, *47*, 1072–1079, doi:10.1002/sia.5852.
20. Chen, A.; Ostrom, C. Palladium-Based Nanomaterials: Synthesis and Electrochemical Applications. *Chem. Rev.* **2015**, *115*, 11999–12044, doi:10.1021/acs.chemrev.5b00324.
21. Shesterkina, A.A.; Kirichenko, O.A.; Kozlova, L.M.; Kapustin, G.I.; Mishin, I. V.; Strelkova, A.A.; Kustov, L.M. Liquid-Phase Hydrogenation of Phenylacetylene to Styrene on Silica-Supported Pd–Fe Nanoparticles. *Mendeleev Communications* **2016**, *26*, 228–230, doi:10.1016/j.mencom.2016.05.002.
22. Markov, P. V.; Turova, O. V.; Mashkovsky, I.S.; Khudorozhkov, A.K.; Bukhtiyarov, V.I.; Stakheev, A.Yu. Size Effect in the Liquid Phase Semihydrogenation of Substituted Alkynes over Supported Pd/Al<sub>2</sub>O<sub>3</sub> Catalysts. *Mendeleev Commun.* **2015**, *25*, 367–369, doi:10.1016/j.mencom.2015.09.017.
23. Zhang, X.; Wang, Z.; Li, S.; Wang, C.; Qiu, J. Recyclable Catalyst for Catalytic Hydrogenation of Phenylacetylene by Coupling Pd Nanoparticles with Highly Compressible Graphene Aerogels. *RSC Adv.* **2014**, *4*, 59977–59980, doi:10.1039/C4RA12029A.
24. Zheng, Y.; Gu, L.; Li, Y.; Ftouni, J.; Dutta Chowdhury, A. Revisiting the Semi-Hydrogenation of Phenylacetylene to Styrene over Palladium-Lead Alloyed Catalysts on Precipitated Calcium Carbonate Supports. *Catalysts* **2022**, *13*, 50, doi:10.3390/catal13010050.
25. SEGURA, Y.; LOPEZ, N.; PEREZRAMIREZ, J. Origin of the Superior Hydrogenation Selectivity of Gold Nanoparticles in Alkyne + Alkene Mixtures: Triple- versus Double-Bond Activation. *J. Catal.* **2007**, *247*, 383–386, doi:10.1016/j.jcat.2007.02.019.
26. Liu, W.; Otero Arean, C.; Bordiga, S.; Groppo, E.; Zecchina, A. Selective Phenylacetylene Hydrogenation on a Polymer-Supported Palladium Catalyst Monitored by FTIR Spectroscopy. *ChemCatChem* **2011**, *3*, 222–226, doi:10.1002/cctc.201000244.
27. Tang, M.; Deng, J.; Li, M.; Li, X.; Li, H.; Chen, Z.; Wang, Y. 3D-Interconnected Hierarchical Porous N-Doped Carbon Supported Ruthenium Nanoparticles as an Efficient Catalyst for Toluene and Quinoline Hydrogenation. *Green Chem.* **2016**, *18*, 6082–6090, doi:10.1039/c6gc01858k.
28. Gonzalez-Galvez, D.; Lara, P.; Rivada-Wheelaghan, O.; Conejero, S.; Chaudret, B.; Philippot, K.; van Leeuwen, P.W.N.M. NHC-Stabilized Ruthenium Nanoparticles as New Catalysts for the Hydrogenation of Aromatics. *Catal. Sci. Technol.* **2013**, *3*, 99–105, doi:10.1039/c2cy20561k.
29. Bresó-Femenia, E.; Chaudret, B.; Castellón, S. Selective Catalytic Hydrogenation of Polycyclic Aromatic Hydrocarbons Promoted by Ruthenium Nanoparticles. *Catal. Sci. Technol.* **2015**, *5*, 2741–2751, doi:10.1039/c4cy01758g.
30. Chen, C.S.; Lin, J.H.; Chen, H.W.; Wang, C.Y. Infrared Study of Benzene Hydrogenation on Pt/SiO<sub>2</sub> Catalyst by Co-Adsorption of CO and Benzene. *Catal. Letters* **2005**, *105*, 149–155, doi:10.1007/s10562-005-8684-7.
31. Hammer, B.; Nielsen, O.H.; Nørskov, J.K. Structure Sensitivity in Adsorption: CO Interaction with Stepped and Reconstructed Pt Surfaces. *Catal. Letters* **1997**, *46*, 31–35, doi:10.1023/A:1019073208575.
32. Luska, K.L.; Moores, A. Functionalized Ionic Liquids for the Synthesis of Metal Nanoparticles and Their Application in Catalysis. *ChemCatChem.* **2012**, *4*, 1534–1546, doi:10.1002/cctc.201100366.



## 4. Synthesis, characterization, and catalytic application of nickel- and nickel oxide nanoparticles in functionalized ionic liquids

### 4.1 Introduction

Nickel nanoparticles (Ni NPs) have received an increasing interest in the field of nanocatalysis due to the lower cost of nickel compared to other catalytically active transition metals [1]. Generally, Ni NPs are generated in solution by reduction of a nickel salt, *e.g.* nickel(II) chloride ( $\text{NiCl}_2$ ) with lithium and 4,4'-di-*tert*-butylbiphenyl (DTBB) [2], or reduction of nickel(II) acetate ( $\text{Ni}(\text{OAc})_2$ ) with aqueous hydrazine [3], *etc.* Another reputed synthesis method is an organometallic approach consisting of the decomposition of the organometallic complex bis-( $\eta^4$ -1,5-cyclooctadiene)nickel(0) ( $[\text{Ni}(\text{COD})_2]$ ) [4,5] in the presence of  $\text{H}_2$  in an organic solvent, as explained in Chapter 1. The addition of stabilizing species (*e.g.*, an amine as hexadecylamine, a polymer like polyvinylpyrrolidone (PVP), a mixture PVP/triphenylphosphine, a carboxylic acid as octanoic acid or stearic acid [4,6]) allow the control of the growth of the NPs. For instance, a straightforward approach was used by Keith *et al.* [7] for the synthesis of Ni NPs through the thermal decomposition of nickel(II) bis(acetylacetonate) ( $\text{Ni}(\text{acac})_2$ ) in the presence of *n*-trioctylphosphine, as capping ligand. *N,N*-diisopropylethylamine, dimethylhexadecylamine and oleylamine were introduced as size-limiting agents. A direct relationship was established between the bulkiness of the alkylamine ligands and the average diameter of the resulting Ni NPs. When the bulky oleylamine was employed Ni NPs with an average diameter of  $2.8 \pm 0.9$  nm were formed. Conversely, the use of less bulky *N,N*-dimethylhexadecylamine led to formation of larger NPs ( $4.4 \pm 0.9$  nm). Decreasing the amount of *n*-trioctylphosphine compared to the Ni source allowed further growth of the Ni NPs to  $17.8 \pm 1.3$  nm, thus explaining the role of the ligands on determining the size of the NPs during the synthesis.

Ni NPs display significant catalytic properties, facilitating various organic reactions like alkylation of ketones [8], hydrogen transfer in alkenes and carbonyl compounds [9] and alkyne hydrogenation [10]. Over the past decade, the synthesis of Ni NPs in various ionic liquids (ILs) has been also

developed due to the versatile properties of ILs that can be employed as both stabilizers and dispersion media, allowing to obtain well-dispersed NPs directly usable for catalysis applications. For instance, Jiang *et al.* [11] synthesized Ni NPs by the reduction of Ni(OAc)<sub>2</sub> with NaBH<sub>4</sub> or hydrazine using 1-butyl-2,3-dimethylimidazolium (*S*)-2-pyrrolidinecarboxylic acid IL as stabilizer. The resulting Ni NPs had an average diameter of 5.1 nm with face-centered cubic (*fcc*) structure. The catalyst was effectively employed for the chemoselective hydrogenation of quinoline and aromatic nitro compound. Dupont and coworkers [12] synthesized well-dispersed Ni NPs (size range: 4.9 ± 0.9 to 5.9 ± 1.4 nm) by decomposing [Ni(COD)<sub>2</sub>] under hydrogen pressure (4 bar) in the presence of 1-alkyl-3-methylimidazolium bis(trifluoromethanesulfonyl)imide ILs. They showed that ILs with longer side chain (from n-butyl to n-hexadecyl) induced the formation of the Ni NPs with smaller diameter and size distribution. An innovative approach for the synthesis of Ni NPs in imidazolium ILs was reported by Prechtel, Santini, Dupont and coworkers, where the imidazolium ILs acts also as mild reducing agent for the [Ni(COD)<sub>2</sub>] precursor, thus promoting the auto-decomposition of the latter under milder reaction conditions [13]. One interest of this synthesis approach relies with the absence of classical reducing agents, thus avoiding additional cost and limiting the contamination of the NPs. As another interesting example, Prechtel and coworkers [14] synthesized Ni NPs using nitrile-functionalized IL as stabilizer. A series of Ni NPs of average size ranging from 4.4 ± 0.7 to 8.3 ± 1.6 nm were prepared by varying the alkyl chain length and the substitution at the C<sub>2</sub> position of the imidazolium ring. The obtained NPs were used for the partial hydrogenation of alkynes to (*Z*)-alkenes at near ambient conditions as well as for the selective hydrogenation of benzonitrile to benzylamine [15]. Mahalingam and coworkers [16] synthesized NiO NPs in 1-butyl-3-methylimidazolium triflate ([BMIm][TfO]) by the reduction of nickel(II) nitrate hexahydrate (Ni(NO<sub>3</sub>)<sub>2</sub>·6H<sub>2</sub>O) with NaOH. The Ni(OH)<sub>2</sub> formed during the reaction was then calcinated at 400 °C to obtain the required NiO NPs. These NiO NPs exhibited superparamagnetic behavior although NiO as bulk material is antiferromagnetic. Vijayakumar and coworkers [17] reported the synthesis of cubic shaped Ni NPs stabilized by imidazolium-based poly(ionic liquids) (PILs) with hydroxide counter anion having a dimension of 11 nm. These (PIL-1)-Ni-NPs were found active in transfer

hydrogenation reactions of carbonyl compounds like acetophenone, 2-cyclohexen-1-one *etc.* Remarkably, in isopropyl alcohol, this catalyst system was able to chemoselectively reduce the carbonyl group of  $\alpha,\beta$ -unsaturated carbonyl compounds to alcohols.

Chemoselective reduction of olefinic bonds in  $\alpha,\beta$ -unsaturated carbonyl compounds holds significant importance in the synthesis of industrially and pharmaceutically relevant chemicals [18–20], and substantial focus has been provided to develop cost-effective and reusable catalysts allowing to achieve this catalytic reaction. Most of the catalytic protocols employed involve the use of precious metals like ruthenium, iridium, rhodium, platinum, and palladium [18,20–22]. Cheaper and abundant NPs of first-row transition metals like iron, cobalt and nickel [9,23,24] have also been employed to catalyze this reaction. Mokhov *et al.* [25] have reported the selective hydrogenation of substrates including linear and cyclic alkenes, styrene and norbornene derivatives, as well as pinenes, camphene, and cinnamic nitrile with Ni NPs at 1 atm H<sub>2</sub>. However, this work reports no catalyst recovery and recycling. Philippot and coworkers [6] have investigated the chemoselective hydrogenation of  $\alpha,\beta$ -unsaturated carbonyl compounds under mild reaction conditions (4 bar of H<sub>2</sub>, 60 °C) using a series of Ni NPs synthesized with different stabilizers, including polymer (PVP) and ligands with different functional groups. Their work evidenced that the hydrogenation performance appeared to be sensitive to the ligand type with carboxylic acid stabilized Ni NPs systems exhibiting the best performances. These results indicate that the nature of the stabilizing ligand is an important parameter for the catalysis performance. In addition, all nanocatalysts were found to be active in reducing only the C=C double bond. Based on extended X-ray absorption fine structure (EXAFS) and X-ray photoelectron spectroscopy (XPS) analyses, this chemoselectivity could be related to the high content of Ni metal in the NPs, whose surface allows to activate selectively the hydrogenation of the C=C bond.

In this chapter, novel Ni NPs and Ni-NiO NPs stabilized by two ether-functionalized ionic liquids (FILs), 1-methoxyethoxy-methyl-3-methylimidazolium bis(trifluoromethanesulfonyl)imide, [MEMIm][NTf<sub>2</sub>] or MEM, and 1-methoxymethoxyethyl-3-methylimidazolium bis(trifluoromethanesulfonyl)imide, [MMEIm][NTf<sub>2</sub>] or MME, were synthesized by the

organometallic approach using  $[\text{Ni}(\text{COD})_2]$  as Ni precursor, and characterized. The Ni/FIL NPs systems (Ni/MEM and Ni/MME) were then applied in the hydrogenation of  $\alpha,\beta$ -unsaturated carbonyl compounds with the aim to probe the surface reactivity in terms of conversion and selectivity. Ni NPs in the non-functionalized IL 1-hexyl-3-methylimidazolium bis(trifluoromethanesulfonyl)imide (Ni/H) and the cyano-FIL 1-Butylcyano-3-methylimidazolium bis(trifluoromethanesulfonyl)imide  $[(\text{CH}_3\text{CH}_2\text{CH}_2\text{CH}_2\text{CN})\text{MIm}][\text{NTf}_2]$  (Ni/CN) were also prepared for the purpose of comparison. In a second stage, the as-synthesized Ni NPs were exposed to air which led to Ni-NiO NPs. Hydrogenation of several substrates using these oxidized NPs, including cinnamaldehyde and 2-cyclohexen-1-one among others, was performed to understand the effect of the NP oxidation on the catalytic performance.

## 4.2 Experimental section

### 4.2.1 Synthesis of Ni/FILs in THF

In a typical reaction,  $[\text{Ni}(\text{COD})_2]$  (33 mg, 0.11 mol) was dissolved in a THF/IL mixture (4/3 mL) in a Fischer-Porter reactor under magnetic stirring (1500 rpm). The reactor was pressurized with 3 bar  $\text{H}_2$  in dynamic flow for 10 min and then in a static mode for 22 h. The generated cyclooctane (resulting from hydrogenation of the COD ligands) was removed under vacuum ( $\approx 0.05$  mbar) overnight. Upon completion of the reaction, a black colloidal suspension was obtained for H and CN ILs.

### 4.2.2 Synthesis of Ni/FILs in THF in the absence of $\text{H}_2$ and magnetic stirrer

In a typical reaction,  $[\text{Ni}(\text{COD})_2]$  (16.3 mg, 0.06 mmol) was dissolved in a THF/FIL mixture (4/3 mL) inside a quartz tube that was then closed and placed on the rotating instrument (**Figure 4.3**) at a speed of 50 rpm at room temperature for 24 h.

### 4.2.3 Synthesis of Ni/FILs in pentane

In a typical reaction,  $[\text{Ni}(\text{COD})_2]$  (16.27 mg, 0.06 mmol) was dissolved in pentane/IL mixture (1/3 mL) in a Fischer-Porter bottle. The reaction was allowed to proceed for 24 h at 80 °C and 1500



rpm using a magnetic stirrer. Next, generated cyclooctane was removed under vacuum ( $\approx 0.05$  mbar). The resultant black colloidal suspension containing Ni/FIL NPs was stored under argon.

#### 4.2.4 Synthesis of Ni-NiO/FILs

Inside the glove box, colloidal suspensions of Ni/FILs were placed in closed 20 mL vials at room temperature and then exposed to static air for 24 h under stirring (200 rpm).

#### 4.2.5 Catalytic hydrogenation

Hydrogenation of all substrates was carried out in a 20 mL stainless steel high-pressure batch reactor (**Figure D1, Appendix D**). In a standard experiment, substrate (1 mmol) was placed into a vial containing Ni/FILs or Ni-NiO/FILs (0.01 mmol of metal) and octane (0.05 mL, 0.3 mmol, internal standard). The vial was introduced into the reactor and the reactor purged three times with H<sub>2</sub> and subsequently pressurized with the required pressure of H<sub>2</sub>. To avoid external mass transfer limitation, a stirring of 1200 rpm was applied at the desired temperature for the indicated reaction time.

Catalyst recyclability tests were performed for 2-cyclohexen-1-one hydrogenation reaction using Ni-NiO/MEM as catalyst following the catalysis procedure described above. The spent catalyst phase was washed three times with pentane ( $3 \times 5$  mL) after each catalytic run to remove substrate and formed products, followed by drying under vacuum ( $\approx 0.05$  mbar) at room temperature for 1 h. The dried Ni-NiO/MEM phase was mixed with a new batch of substrate and the next reaction was performed under the same catalytic conditions as mentioned above. This operation was repeated eight times. TEM and ICP analyses were performed on the spent Ni-NiO/MEM after the last catalytic run. All materials and methods have been provided in chapter 7.

### 4.3 Results and discussion

#### 4.3.1 Optimization of the synthesis of Ni/ILs

As an initial investigation for the preparation of Ni NPs in the given ILs, the reactions were performed at 75 °C in tetrahydrofuran (THF) under 3 bar H<sub>2</sub> for 22 h. The temperature, solvent

and pressure were chosen from previous reports for the synthesis of Ni- and RuNi NPs using PVP or various ligands as stabilizers [6,26,27]. TEM images of the two systems Ni/H and Ni/CN showed well-dispersed NPs with an average diameter of 4.6 nm and 4.4 nm, respectively (**Figure 4.1**). Note that the Ni/CN NPs presented a narrower size distribution.

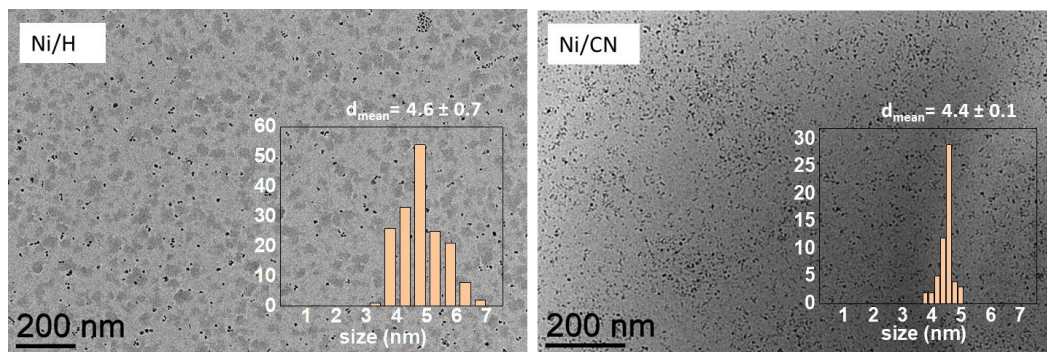


**Figure 4.1** TEM images of Ni/H and Ni/CN with their corresponding size distributions (scale bar = 200 nm).

Attempts of Ni NPs synthesis in THF with the FILs MEM and MME as dispersion media and following the protocol described above for Ni/H and Ni/CN systems, led in both cases to formation of a magnetic and adhering material onto the magnetic bar introduced in the reaction mixture for stirring (**Figure 4.2**). Due to relative high viscosities of the FILs and the magnetic nature of the formed materials, separation from the stirrer could not be achieved in a quantitative way, and thus no characterization of these materials was done.



**Figure 4.2** Magnetic Ni/MEM material.

Additionally, upon dissolution of the precursor  $[\text{Ni}(\text{COD})_2]$  in a THF solution of FILs (MEM, MME or CN), it underwent spontaneous decomposition prior to the addition of  $\text{H}_2$  noticeable by the color change of the solution from yellow to pale black. Similar decomposition of this Ni precursor in the absence of  $\text{H}_2$  was previously reported by Prechtel, Santini, Dupont and coworkers [13]. Interestingly, they observed that the decomposition occurred upon dissolution of the  $[\text{Ni}(\text{COD})_2]$  in imidazolium ILs with short alkyl side-chains ( $n = 2, 4$ ), whereas for longer chains ( $n = 6, 8, 10$ )  $\text{H}_2$  was required for NP formation. Furthermore, they revealed by TEM analysis of the obtained nanomaterials a sponge-like structure consisting of agglomerates from the auto-decomposition of the precursor. They hypothesized that the observed decomposition was induced by the cleavage of the acidic  $\text{C}_2\text{-H}$  bond and the successive generation of *N*-heterocyclic carbene (NHC) species. Additionally, they suggested that a possible interaction of the  $[\text{NTf}_2]^-$  anion with the COD ligands of the Ni complex may also support the Ni NPs formation. It has also been reported that imidazolium cations can undergo oxidative addition to low-valent and electron rich group 10 metal centers to form carbene complexes through  $\text{C}_2\text{-H}$  bond [28]. On the basis of density functional theory (DFT) calculation, Yates and coworkers [29] proposed a mechanism for reaction of imidazolium salts with Ni and Pd, which hypothesizes the formation of a molecular carbene-M-H species.

Thus, assuming a carbene involving scenario, the decomposition of  $[\text{Ni}(\text{COD})_2]$  was attempted in a THF solution of MEM and MME FILs in the absence of  $\text{H}_2$  and magnetic stirrer to avoid agglomeration of the nanomaterial on the stirring bar. To ensure a proper mixing of the reaction mixture, the reaction mixture was placed on a rotating instrument as shown in **Figure 4.3**.



**Figure 4.3** Rotating instrument used to stirrer the  $[\text{Ni}(\text{COD})_2]/\text{THF}/\text{FIL}$  reaction mixtures.

The reaction was allowed to rotate at 50 rpm at room temperature for 24 h. Upon completion of the reaction, the presence of a black supernatant together with a black precipitate was observed for the Ni/MEM system. The obtained material was found magnetically active and easily separated from THF upon applying a magnetic field by approaching a magnet on the external walls of the quartz tube (**Figure 4.4**). The THF phase was found colorless, thus leading to the hypothesis that the  $[\text{Ni}(\text{COD})_2]$  precursor was fully decomposed.

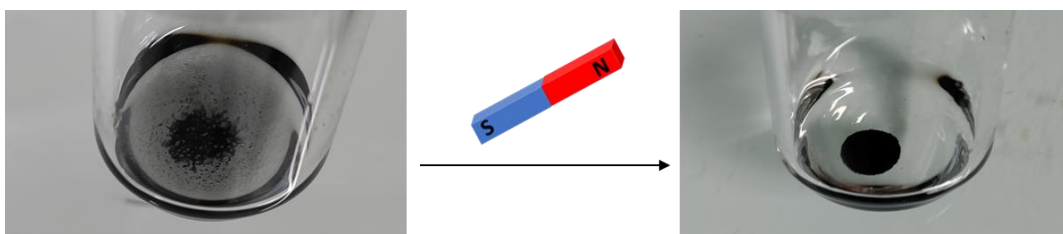


**Figure 4.4** Separation of Ni/MEM from THF by use of a magnet.

In the case of the Ni/MME, a yellowish-black solution (**Figure 4.5**) was obtained after the reaction thus indicating that unlike the Ni/MEM system the complete decomposition of the precursor was not achieved with MME. When approaching a magnet on the quartz tube, the formed material

could be separated from a yellow solution of THF, thus indicating the incomplete decomposition of the Ni precursor in the applied reaction time (24 h).

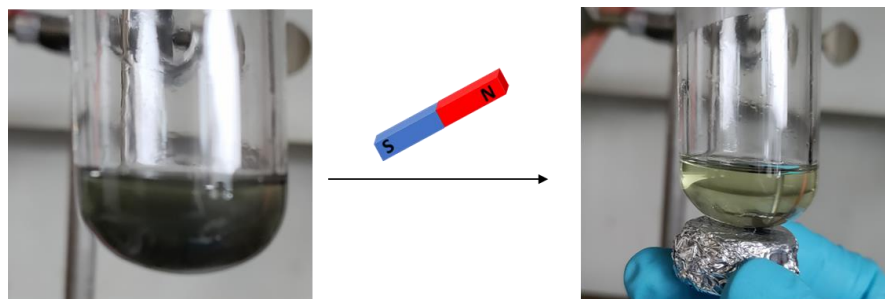


**Figure 4.5** Separation of Ni/MME from THF/rest of  $[\text{Ni}(\text{COD})_2]$  by use of a magnet.

TEM analyses were performed on the obtained materials to examine if NPs were formed (**Figure 4.6**). The TEM images of Ni/MEM and Ni/MME showed the presence of well-dispersed black dots attributed to Ni NPs. From the size histograms, a mean diameter of 6 nm and 7.3 nm was deduced for the Ni/MEM and Ni/MME systems, respectively. Thus, following this procedure, the Ni NPs displayed larger sizes than the ones obtained using  $\text{H}_2$  and mechanical stirring. Also, the Ni/MEM NPs displayed an inhomogeneous morphology, in contrast to the Ni/MME system.

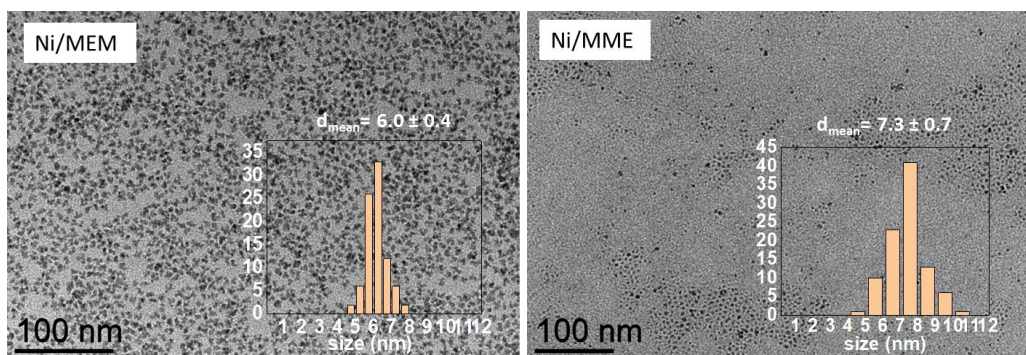
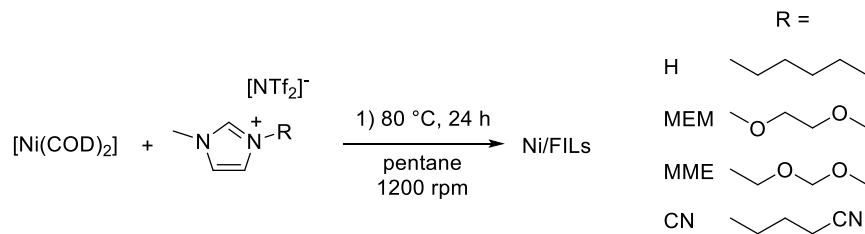


**Figure 4.6** TEM images of Ni/MEM and Ni/MME NPs prepared in the absence of  $\text{H}_2$  and magnetic stirring with their corresponding size distributions (scale bar = 100 nm).

The incomplete decomposition of the Ni precursor in the MME FIL using this methodology urged for further optimization to obtain better controlled Ni/MME NPs. Additionally, it was crucial to

establish the same method for the synthesis of Ni NPs in the four ILs to allow the comparison of the characteristics and catalytic properties of the formed Ni NPs.

Mudring and coworkers [30] have also observed a similar decomposition of  $[\text{Ni}(\text{COD})_2]$  without  $\text{H}_2$ , while synthesizing Ni NPs in a series of six mono- and bi-cationic imidazolium-based ILs bearing long alkyl chains. In this work the synthesis of Ni NPs was performed at 40-45 °C, using a co-solvent (pentane) to dissolve the lipophilic Ni precursor in the ILs, leading to the targeted Ni NPs. Thus, based on this work, the Ni NPs were here synthesized with few modifications of the procedure.  $[\text{Ni}(\text{COD})_2]$  precursor was dissolved in pentane/IL mixture (1/3 mL) in a Fischer-Porter bottle and the reaction was allowed to proceed for 24 h at 80 °C and 1500 rpm using a magnetic stirrer (**Scheme 4.1**). Upon completion of the reaction, a black colloidal suspension was obtained for the four ILs tested, indicating the successful decomposition of the precursor under these optimized conditions. The generated cyclooctane and the solvent were removed under vacuum ( $\approx 0.05$  mbar) overnight. The metal content of each batch of Ni/IL was established by ICP analysis and found to be close to the expected value of 0.10 wt.% Ni (**Table 4.1**). Other characterization data are described hereafter, first for the Ni/FILs and then for their oxidized counterparts.



**Scheme 4.1** Optimized synthesis of Ni/FILs.

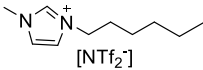
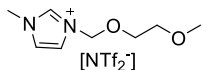
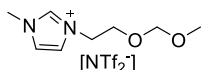
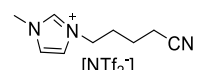
### 4.3.2 Characterization of the Ni/FILs

#### a) TEM analysis

The aforementioned synthetic procedure, using pentane and heating (80 °C) without  $\text{H}_2$  pressure, led to the formation of well-dispersed Ni NPs in all the FILs tested with mean sizes ranging from

2.8 to 6.5 nm (**Table 4.1**) depending on the FIL used. Also, the morphology and the dispersion of the NPs varied with the nature of the FIL as visible on the TEM images (**Figure 4.7**). The size of the NPs increased in the order of the FILs: CN < MEM < H < MME. Note that the range in mean sizes obtained for the Ni NPs series is different from that previously observed in the Ru/FIL series in Chapter 3 (from 2.8 to 6.5 nm for Ni NPs against 1.3-2.2 nm for Ru NPs). This is not surprising in comparison to previous results on the synthesis of Ru and Ni NPs with the same organometallic precursors in the presence of polymers or ligands which gave rise to same orders of size for Ru and Ni NPs, thus indicating that the size ranges observed are strongly related to the precursor used, either Ru or Ni. However, the influence of the FILs on the NP size in the Ni series was different than with Ru. With a mean diameter of 2.8 nm, the CN-type FIL led to the smallest Ni NPs as observed for Ru/CN NPs. The two oxygenated FILs (MEM and MME) provided in both cases larger sized Ni NPs (4.4 and 6.5 nm, respectively), while in the Ru NPs series the Ru/MME system presented a mean size similar as for the Ru/CN system. Additionally, the size of the Ni/MEM and Ni/MME NPs were close to the sizes of the Ni NPs formed in the non-functionalized IL (Ni/H, 4.4 nm), as observed in the Ru NPs series. These results evidence that the influence of the FILs on the growth of the Ni NPs is slightly different than with the Ru NPs series.

**Table 4.1** Ni content in Ni/FILs systems and Ni NP mean size.

Ni/FIL	Ionic liquid	Ni content (wt.%) <sup>a</sup>	Ni NP mean size (nm) <sup>b</sup>
Ni/H		0.11	5.6 ± 0.3
Ni/MEM		0.12	4.4 ± 0.4
Ni/MME		0.11	6.5 ± 0.3
Ni/CN		0.11	2.8 ± 0.3

<sup>a</sup> Determined by ICP analyses. <sup>b</sup> Determined from TEM analyses.



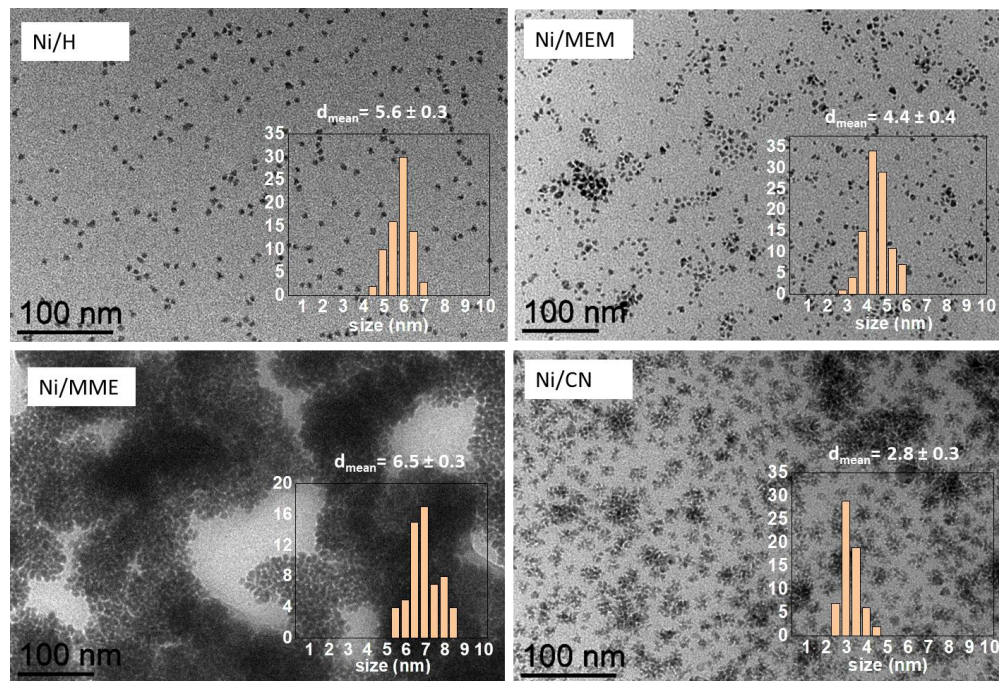
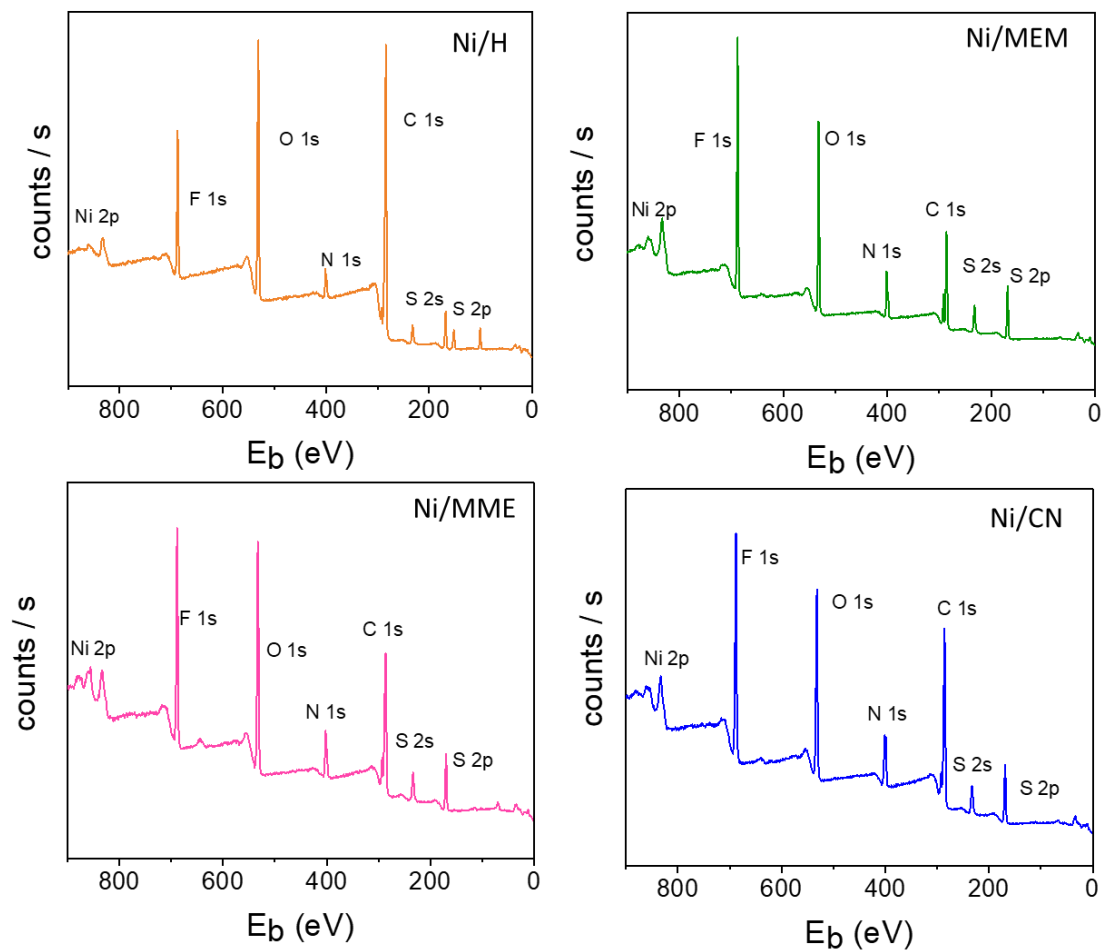


**Figure 4.7** TEM images of Ni/FILs with their corresponding size distributions (scale bar = 100 nm).

### b) XPS analysis

XPS analyses were performed on all Ni/FILs systems. The corresponding survey spectra for each system are presented in **Figure 4.8**. The deconvoluted high-resolution scan spectra of the different elements (C 1s, N 1s, F 1s, S 2p, O 1s) are compiled in Appendix D. The binding energies ( $E_b$ ), atomic ratio (%) and the full width at half maximum FWHM (eV) of the C 1s and N 1s, O 1s, S 2p and F 1s of the Ni/FILs are given in **Table 4.2** and **Table 4.3**, respectively.

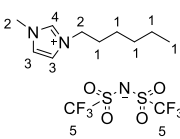
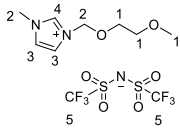
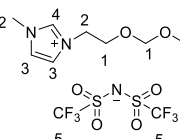
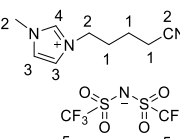




**Figure 4.8** XPS survey spectra of Ni/FILs.

Chapter 4. Synthesis, characterization, and catalytic application of nickel- and nickel oxide nanoparticles in functionalized ionic liquids

**Table 4.2** Binding energies (eV) of C 1s for the carbon atoms in the Ni/FILs.

IL	Atom <sup>a</sup>	Binding energy Ni/FILs, $E_{\text{NiIL}}$ (eV)	Atomic ratio (%)	FWHM (eV)
	C <sub>1</sub>	284.80	60.34	1.44
	C <sub>2</sub>	286.37	19.47	1.44
	C <sub>3</sub>	287.74	6.23	1.44
	C <sub>4</sub>	288.85	5.51	1.13
	C <sub>5</sub>	292.68	3.91	1.09
	C <sub>1</sub>	284.80	48.53	1.44
	C <sub>2</sub>	286.25	26.66	1.27
	C <sub>3</sub>	287.32	8.37	1.44
	C <sub>4</sub>	288.39	9.69	1.28
	C <sub>5</sub>	292.48	5.66	1.16
	C <sub>1</sub>	284.80	43.82	1.44
	C <sub>2</sub>	286.21	30.71	1.34
	C <sub>3</sub>	287.33	8.26	1.40
	C <sub>4</sub>	288.50	8.46	1.23
	C <sub>5</sub>	292.32	7.23	1.12
	C <sub>1</sub>	284.80	47.23	1.44
	C <sub>2</sub>	286.40	30.41	1.44
	C <sub>3</sub>	287.66	6.61	1.44
	C <sub>4</sub>	288.50	3.76	1.44
	C <sub>5</sub>	292.67	8.95	1.44

**Table 4.3** Binding energies (eV) of the chemical states of N, S, F and O atoms in the Ni/FILs.

Element	Binding energy Ni/FILs, $E_{\text{NiIL}}$ (eV)	Atomic ratio (%)	FWHM (eV)
H			
N 1s (anion)	399.25	37.75	1.25
N 1s (cation)	401.84	59.14	1.27
S 2p <sub>3/2</sub>	168.80	67.00	1.15
S 2p <sub>1/2</sub>	170.02	33.00	1.12
F 1s	688.56	100.00	1.77
O 1s (CO <sub>3</sub> <sup>2-</sup> )	531.33	20.07	1.66
O 1s (cation/anion)	532.28	58.37	1.37
H <sub>2</sub> O <sub>absorbed</sub>	533.44	21.55	1.65
MEM			
N 1s (anion)	399.05	41.17	1.44
N 1s (cation)	401.62	57.03	1.44
S 2p <sub>3/2</sub>	168.58	65.50	1.25
S 2p <sub>1/2</sub>	169.81	34.50	1.25
F 1s	688.33	100.00	1.86
O 1s (CO <sub>3</sub> <sup>2-</sup> )	530.34	2.03	1.92
O 1s (cation/anion)	532.16	77.79	1.65
H <sub>2</sub> O <sub>absorbed</sub>	533.44	20.18	1.52
MME			
N 1s (anion)	398.83	37.04	1.31
N 1s (cation)	401.53	46.98	1.17
S 2p <sub>3/2</sub>	168.43	61.81	1.14
S 2p <sub>1/2</sub>	169.64	38.19	1.27
F 1s (anion)	688.01	100.00	1.78
O 1s (CO <sub>3</sub> <sup>2-</sup> )	530.26	4.74	1.64
O 1s (cation/anion)	532.00	85.35	1.74
H <sub>2</sub> O <sub>absorbed</sub>	533.43	9.90	1.55

Chapter 4. Synthesis, characterization, and catalytic application of nickel- and nickel oxide nanoparticles in functionalized ionic liquids

Element	Binding energy Ni/FILs, $E_{NiFIL}$ (eV)	Atomic ratio (%)	FWHM (eV)
CN			
N 1s (anion)	399.16	44.55	1.44
N 1s (cation)	401.77	38.63	1.39
S 2p <sub>3/2</sub>	168.72	73.33	1.44
S 2p <sub>1/2</sub>	170.02	26.67	1.21
F 1s	688.38	100.00	2.00
O 1s (CO <sub>3</sub> <sup>2-</sup> )	530.64	17.07	1.92
O 1s (cation/anion)	532.15	80.53	1.79
H <sub>2</sub> O <sub>absorbed</sub>	534.36	2.40	0.85

The change in binding energies observed in the presence of Ni NPs ( $E_{NiFIL}$ ) with respect to the pure FIL, is represented by  $\Delta E$  and summarized in **Table 4.4** for the different elements. The  $\Delta E$  for H, follows the same trend as for the Ru/H system previously described in Chapter 3. The  $\Delta E_{C1s}$  of the cation is more pronounced than the elements present in the [NTf<sub>2</sub>]<sup>-</sup> anion of the IL. In the case of CN, the  $\Delta E_{C2}$  was found to be 0.47 eV, indicating a strong interaction of the FIL with the surface of the Ni NPs through the CN functionality. Such interaction through the nitrile functionality has been previously described for various metal NPs including Ni [14] as well as Ru [31], Fe [32] and Pd [33]. Unlike all the Ru/FILs systems, a change of the  $E_{C1s}$  of C<sub>4</sub> to a lower value (*i.e.*, negative  $\Delta E$ ) was observed for all FILs in the presence of Ni NPs. This can be attributed to the formation of a nucleophilic species, *e.g.* *N*-heterocyclic carbene derived from the imidazolium cation. The generation of the NHC species could be explained by the fact that, in the absence of hydrogen, the decomposition of the [Ni(COD)<sub>2</sub>] precursor took place through the cleavage of the acidic C<sub>4</sub> as described earlier [13,28]. Thus, this also means there may exist a competition for the stabilization of the NPs surface by both the NHC species and the functional groups present in the FILs (CN, MEM and MME). This can also have an influence on the size of

the NPs. The stabilization by the functional group or the carbene also depends on the strength of surface coordination by the stabilizing group.

**Table 4.4** Difference in binding energies (eV) of the chemical states of selected elements in the ILs and Ni/FILs.

IL	$\Delta E$ cation (eV)				$\Delta E$ anion (eV)					
	C <sub>2</sub> 1s	C <sub>3</sub> 1s	C <sub>4</sub> 1s	N 1s	C <sub>5</sub> 1s	N 1s	F 1s	O 1s	S 2p <sub>3/2</sub>	S 2p <sub>1/2</sub>
H	-0.06	0.33	-0.13	0.13	0.09	0.17	0.18	0.11	0.02	0.02
MEM	-0.11	-0.27	-0.27	-0.08	-0.11	-0.09	-0.11	-0.13*	-0.12	-0.16
MME	-0.10	-0.18	-0.25	0.01	-0.06	-0.08	-0.18	-0.18*	-0.11	-0.15
CN	0.30	0.37	-0.16	0.25	-0.37	0.15	0.30	0.29	0.23	0.29

\* $\Delta E$  cation and anion.

Despite the very low concentration of Ni NPs in the ILs, an increased number of scans enabled acquiring Ni 2p<sub>3/2</sub> spectra (**Figure 4.9**), where metallic Ni(0) and oxidized species (NiO, Ni(OH)<sub>2</sub>) were observed. The binding energies of the three different chemical states for each FIL are provided in **Table 4.5** and agree with the literature data [26,34,35]. The relative amount of Ni(0) out of the total Ni content in the H, MEM, MME, CN FILs were found to be 55, 52, 51 and 60 %, respectively. Considering that these Ni(0) contents are only related to the surface layers of the NPs, the results suggest the surface of the Ni NPs was mostly comprised of metallic nickel.

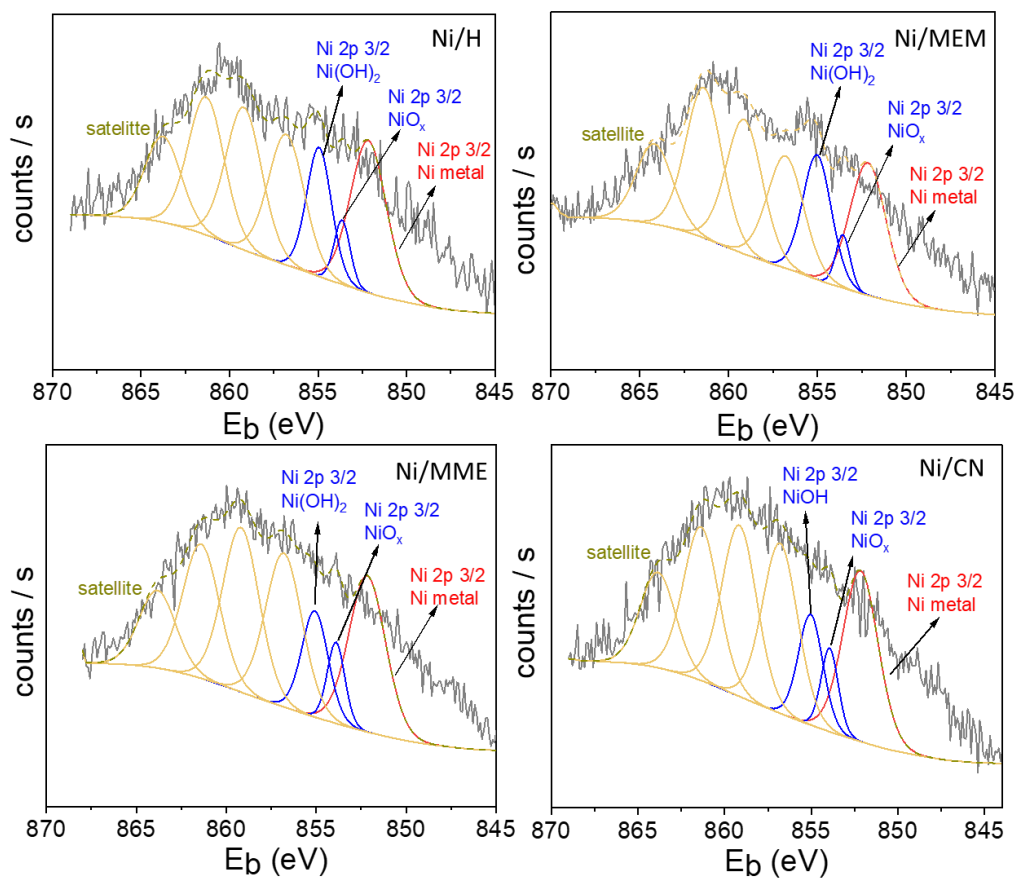


**Figure 4.9** High-resolution XPS scan spectra of Ni 2p for the Ni/FILs systems.

**Table 4.5** Binding energy of Ni 2p for the Ni/FILs systems.<sup>a</sup>

ILs	Binding energy $E_b$ (eV)		
	Ni(0)	NiO <sub>x</sub>	Ni(OH) <sub>2</sub>
H	852.16	853.64	855.00
MEM	852.16	853.86	855.06
MME	852.16	853.57	855.03
CN	852.18	853.80	855.10

<sup>a</sup> Data obtained from XPS analysis.

c) TG analysis

TG analyses of the Ni/FILs systems were performed under N<sub>2</sub> to compare their stability with that of the pure FILs (**Figure 4.10**). As shown on the TG profiles, a very good overlap of the curves of the pure FILs and the Ni/FILs systems was observed in all cases. This means that, unlike the Ru/FILs NPs systems (Chapter 3), there was not a notably change in the decomposition temperature T<sub>dec</sub> of the four FILs in the presence of Ni NPs. This could be due to the very low concentration of Ni in the FILs resulting in no effect, or if present, it is not detected.

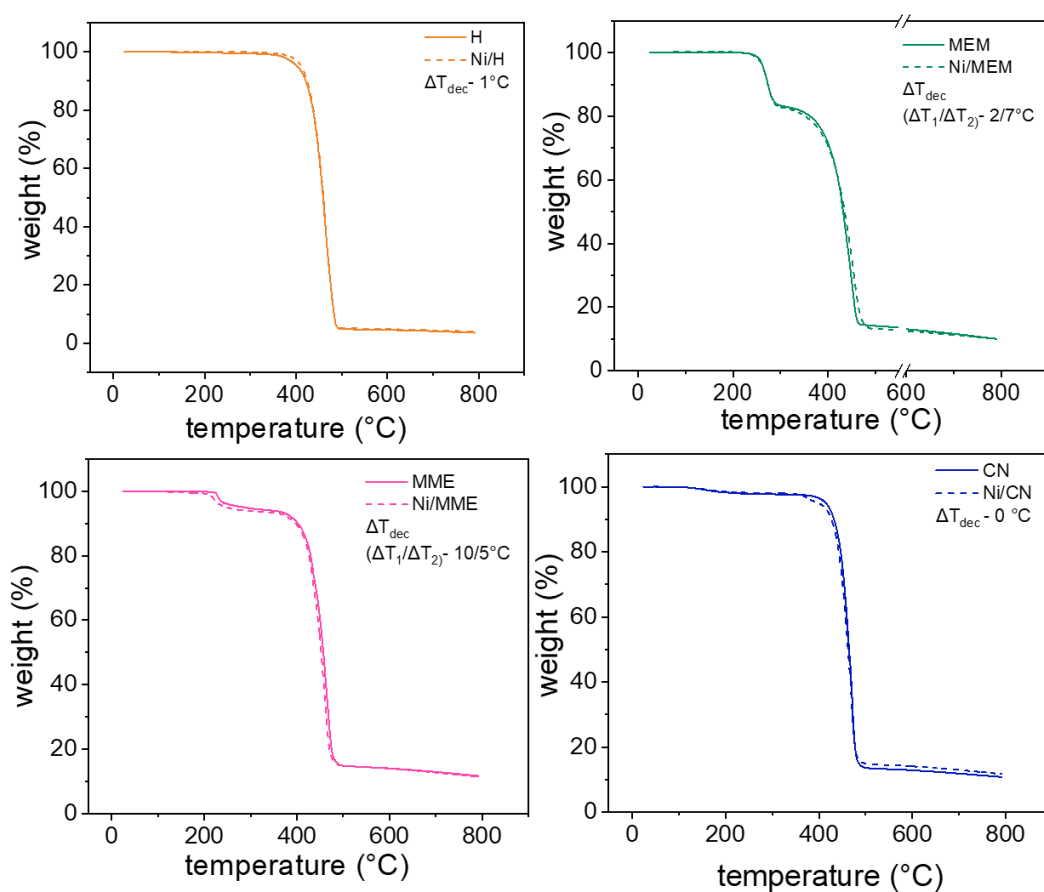


**Figure 4.10** TG profiles of the FILs (solid lines) and corresponding Ni/FILs (dotted lines).

NMR investigations on the Ni/FILs systems provided no clear data to allow concluding on the interaction of Ni NPs with the ILs, due to the presence of intense signals from the FILs, which may have overlapped other signals if any were present (**Appendix D**).

#### 4.3.3 Synthesis and characterization of the Ni-NiO/FILs

The oxidation of the Ni/FILs NPs was also a study of interest as literature points to the beneficial interest of the co-existence of Ni and NiO species for catalysis [36,37]. To facilitate this, fresh Ni/FILs samples were transferred to 20 mL vials inside a glove box, and then left to oxidize by exposing them to air for 24 h. TEM analyses of the oxidized systems were performed, and the corresponding images are provided in **Figure 4.11**. Despite a different concentration of NPs on the TEM grid, no significant difference (**Table 4.6**) in the NPs size nor morphology and dispersion before and after oxidation was observed, thus indicating that the NP systems were stable under air.

**Table 4.6** Mean size of the synthesized Ni NPs before and after oxidation.

FILs	Mean Ni NPs size (nm) <sup>a</sup>		
	Ni/FILs	Ni-NiO/FILs	Ni-Ni(OH) <sub>2</sub> /FILs
H	5.6 ± 0.3	5.5 ± 0.4	6.8 ± 0.5
MEM	4.4 ± 0.4	4.5 ± 0.5	4.4 ± 0.5
MME	6.5 ± 0.3	6.8 ± 0.5	6.9 ± 0.6
CN	2.8 ± 0.3	3.0 ± 0.4	2.8 ± 0.5

<sup>a</sup> Determined from TEM analyses.



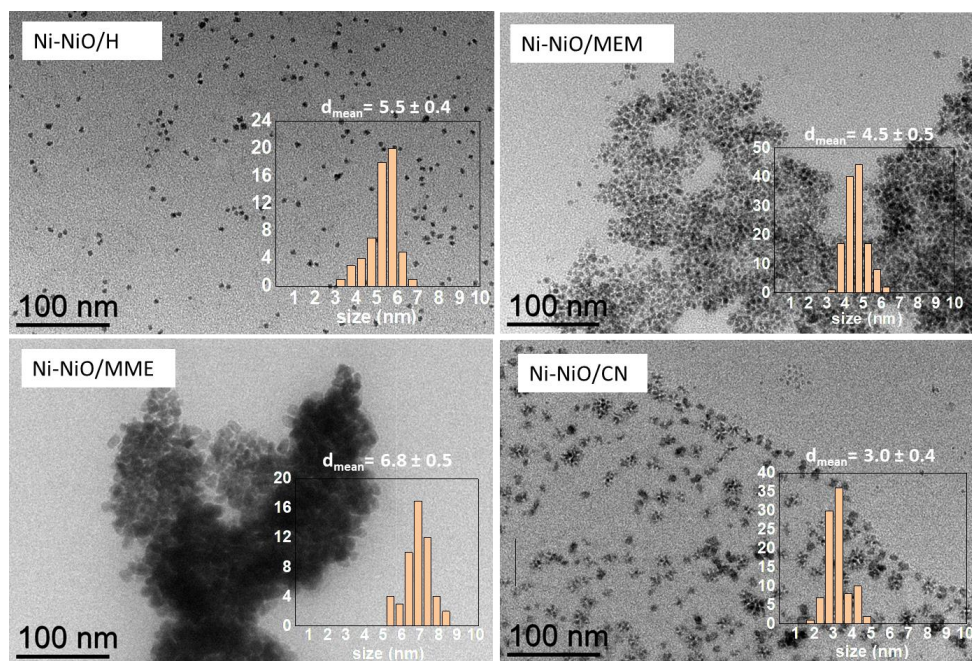


**Figure 4.11** TEM images of Ni-NiO/FILs with their corresponding size distributions (scale bar = 100 nm).

XPS analyses were also performed on Ni-NiO/FILs, which showed similar spectra than those of the FILs and Ni/FILs systems. Note that care was taken to minimize extra oxidation during sample introduction into the XPS instrument, insuring minimum exposure during the transfer of the samples into the instrument. The survey spectra for each system are presented in **Figure 4.12**.

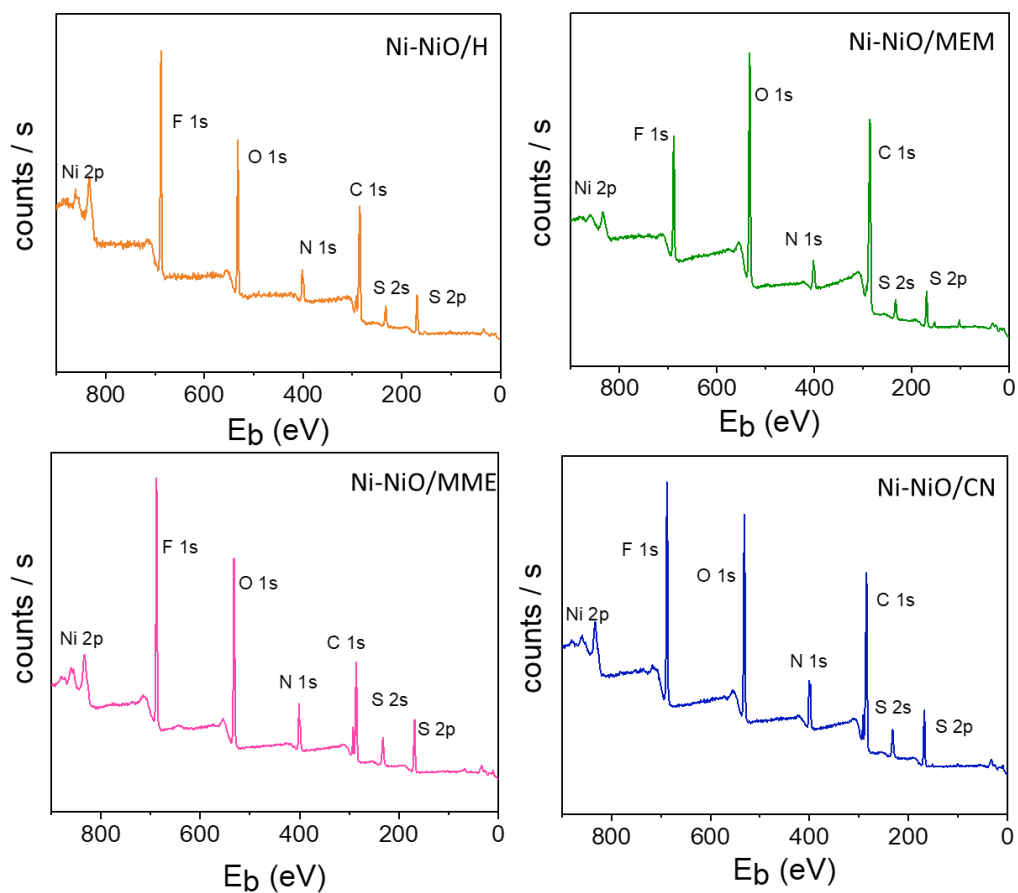


**Figure 4.12** XPS survey of Ni-NiO/FILs.

Ni  $2p_{3/2}$  spectra of the oxidized samples could be acquired (**Figure 4.13**), where metallic Ni(0) and oxidized species (NiO, Ni(OH)<sub>2</sub>) are observed. **Table 4.7** shows the percentages of the different Ni species (Ni(0), NiO and Ni(OH)<sub>2</sub>) detected as a function of the FILs.

**Table 4.7** Distribution of nickel species as a function of the FILs.

FILs	Distribution of nickel (%) <sup>a</sup>	
	Ni(0)	NiO / Ni(OH) <sub>2</sub>
H	55	45
MEM	42	58
MME	44	54
CN	59	41

<sup>a</sup> Data obtained from XPS analysis.

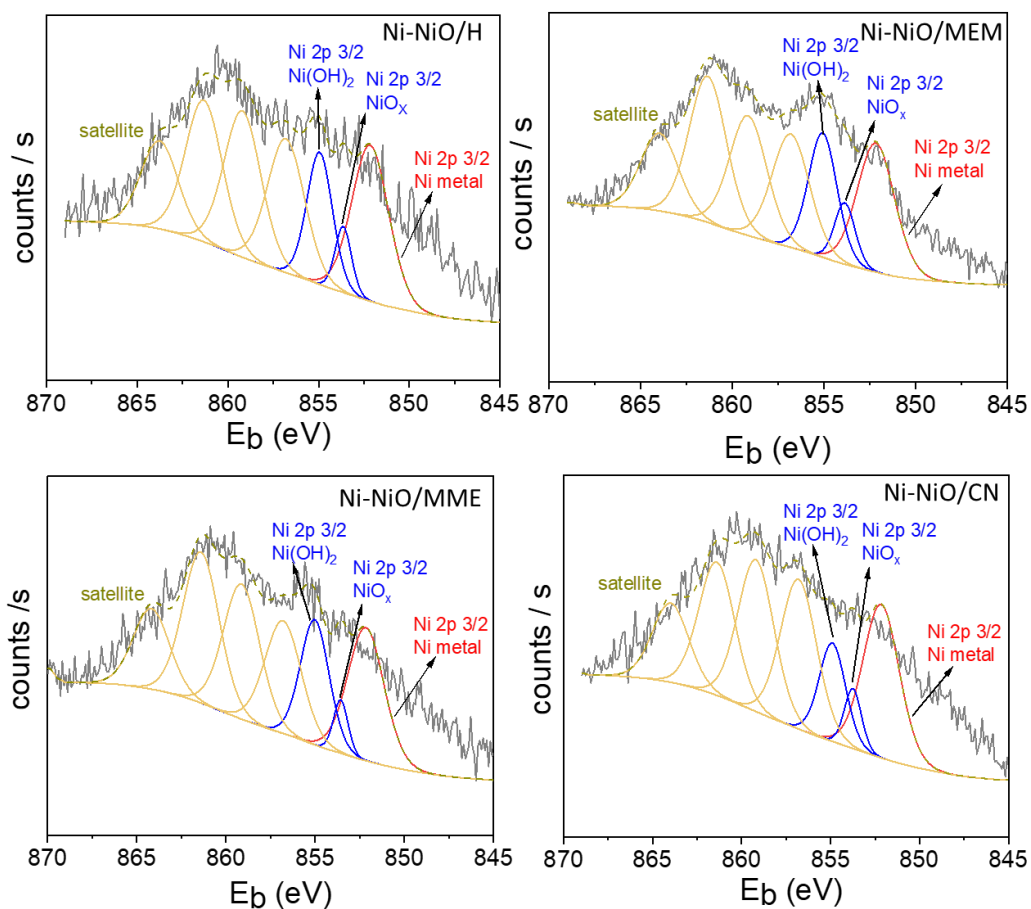


**Figure 4.13** High-resolution XPS scan spectra of Ni 2p for the Ni-NiO/FILs systems.

For H and CN FILs no significant change in Ni(0) content was observed after exposure to air, whereas for MEM and MME, the relative concentration of metallic nickel decreased by approximately 10%. This might indicate the rate of oxidation of the NPs surface is different depending on the nature of the FILs, being less rapid in the presence of CN FIL compared to MEM and MME FILs. The fact that the Ni NPs contained ca. 40-60% of metallic Ni despite exposure to air yields interesting information about their stability in air. This can be an advantage for their storage and handling in catalysis.

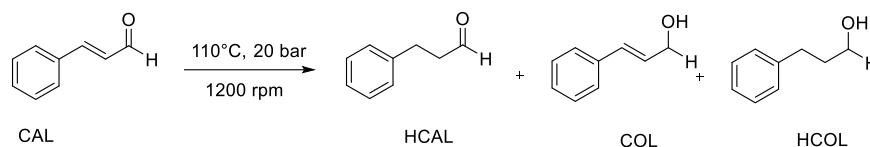
#### 4.3.4 Catalysis with Ni/FILs and Ni-NiO/FILs

##### a) Hydrogenation of cinnamaldehyde

Selective hydrogenation of cinnamaldehyde (CAL) is a challenging catalytic reaction since this molecule contains three functionalities that can be hydrogenated, namely a carbonyl group, an olefinic bond and an aromatic ring. There are several examples of selective hydrogenation of cinnamaldehyde using NPs of noble metals like Pt, Pd, Ir, Ru, Rh, Os and non-noble metals like Fe, Co, Ni, *etc.* [17,38–41]. Prakash *et al.* [42] reported the selective hydrogenation of CAL using different catalysts based on Ni NPs supported in TiO<sub>2</sub>. All catalysts exhibited 70-99% conversion under the given reaction conditions in methanol (80-140 °C, 20 bar H<sub>2</sub>, 1 h), and the selectivity was between 25-64% for hydrocinnamaldehyde (HCAL), 30-61% towards cinnamyl alcohol (COL) and 5-21% towards hydrocinnamyl alcohol (HCOL). Zhenshan and coworkers [43] synthesized Ni NPs in 1-(3-aminopropyl)-2,3-dimethylimidazolium bromide IL and employed them in the hydrogenation of CAL in aqueous phase (H<sub>2</sub>O/FILs as solvent, 90 °C, 30 bar H<sub>2</sub>, substrate/Ni ratio of 50/1, 10 min). The best catalyst was able to achieve 93.4% selectivity for HCAL with 92% conversion.

Given the previous literature data and interest of Ni as low cost and abundant metal, the performance of the synthesized Ni NPs and Ni-NiO NPs was evaluated for CAL hydrogenation. The aim was to compare the activity of the two catalyst systems and their selectivity towards the different functional groups present in CAL. The preliminary study was conducted with the Ni/MEM system as MEM provided with Ru NPs the best catalytic performances in hydrogenation

catalysis (**Chapter 3**). The hydrogenation of CAL was performed using the Ni/MEM or Ni-NiO/MEM systems at 20 bar H<sub>2</sub> and 110 °C with a CAL/Ni ratio of 100/1 (**Scheme 4.2**). The reaction conditions were set according to the previous literature works.



**Scheme 4.2** Hydrogenation of cinnamaldehyde (CAL) to hydrocinnamaldehyde (HCAL), cinnamyl alcohol (COL), and hydrocinnamyl alcohol (HCOL) with Ni/MEM and Ni-NiO/MEM NPs.

**Table 4.8** Hydrogenation of cinnamaldehyde with Ni/MEM and Ni-NiO/MEM catalysts.<sup>a</sup>

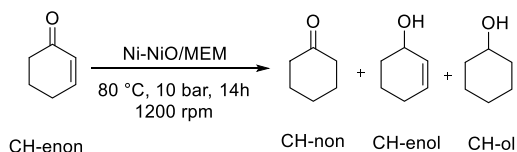
Catalyst system	Time (h)	Conversion (%) <sup>b</sup>	Selectivity (%) <sup>b</sup>		
			HCAL	COL	HCOL
Ni/MEM	24	45	>99	0	0
Ni-NiO/MEM	24	56	>99	0	0
Ni-NiO/MEM	48	87	91	0	9

<sup>a</sup> Reaction conditions: 0.01 mmol of Ni, 1 mmol of cinnamaldehyde (CAL). 0.3 mmol of octane (internal standard), 110 °C, 10 bar H<sub>2</sub>, 1 h, 1200 rpm. <sup>b</sup> Determined by GC using internal standard technique.

For Ni/MEM, 45% conversion of CAL was observed after 24 h with >99% selectivity towards HCAL. With Ni-NiO/MEM, the same reaction time resulted in a higher conversion of 56% also with >99% selectivity towards HCAL. With increased reaction time of 48 h the CAL conversion increased to 87% for Ni-NiO/MEM, but a decrease of selectivity was observed with formation of 91 and 9% of HCAL and HCOL, respectively (**Table 4.8**). In all cases, no hydrogenation of the aromatic ring was observed confirming that both the Ni/MEM and Ni-NiO/MEM system exhibited high chemoselectivity for hydrogenation of the olefinic bond. The higher CAL conversion observed after 24 h for the oxidized system could be due to a synergistic effect of the Ni-NiO surface. Such increase in catalytic activity upon oxidation of Ni has been already reported for the hydrogenation and chemical reduction of 4-nitrophenol to 4-aminophenol by NaBH<sub>4</sub> [44,45].

**b) Hydrogenation of 2-cyclohexen-1-one**

Since the Ni-NiO/MEM system showed a good hydrogenation activity in the case of CAL, the hydrogenation of 2-cyclohexen-1-one (CH-enon) (**Scheme 4.3**) was performed using only this catalyst at 80 °C with 10 bar H<sub>2</sub> (stirring rate of 1200 rpm). A complete conversion of CH-enon was obtained after 14 h with 100% selective formation of cyclohexanone (CH-non). A lower reaction temperature of 50°C resulted in a drastic drop of the conversion (5%) while the selectivity remained the same. Given the two-phase nature of the Ni-NiO NPs, one hypothesis could be that the oxidized Ni surface was not reduced at the applied temperature of 50 °C, which limited the activation of the NP surface. Thus, a temperature of 80 °C led to a more efficient hydrogenation of CH-enon.



**Scheme 4.3** Hydrogenation of 2-cyclohexen-1-one (CH-enon) to cyclohexanone (CH-non), 2-cyclohexen-1-ol (CH-enol) and cyclohexanol (CH-ol) with Ni-NiO/MEM NPs.

Recyclability of the Ni-NiO/MEM catalyst in CH-enon hydrogenation was tested using the reaction conditions described above in eight successive catalytic runs at partial conversion (**Figure 4.14**). A 18% decrease in CH-enon conversion was observed after the second catalytic run but with an unchanged high selectivity towards CH-non. However, in the subsequent seven runs (runs 3 to 8), the activity remained reasonably constant. The initial drop in conversion could correspond to an activity loss due to further oxidation of the spent catalyst upon washing with pentane in air after the first run. To examine this hypothesis, the recovered catalyst after the eight run was treated under 20 bar H<sub>2</sub> at 120°C for 24 h before employed in another catalytic run without exposure to air. Such treatment increased the conversion by 20%, recovering almost the initial activity from the first run thus clearly suggestion reactivation of the Ni surface by H<sub>2</sub> reduction of the NiO. Furthermore, this also showed that the NiO probably protected the catalyst by forming a passivation layer that made the NPs less sensitive to air.

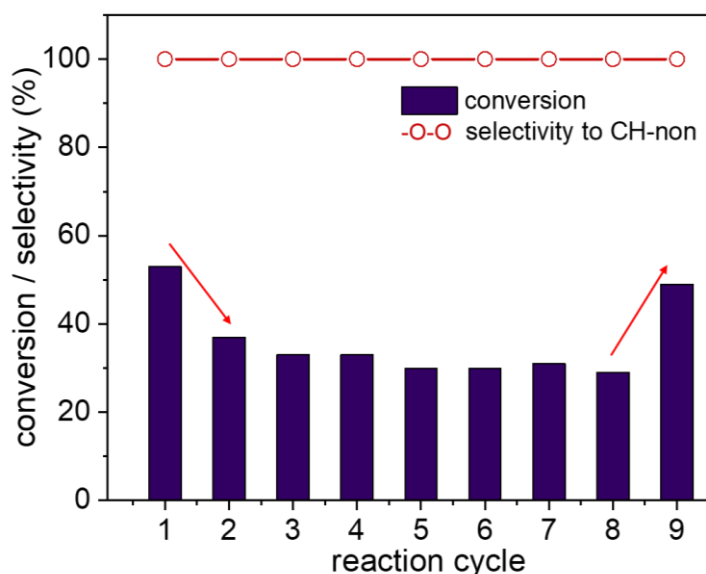


**Figure 4.14** Recyclability study of Ni-NiO/MEM in the hydrogenation of 2-cyclohexen-1-one (CH-enon). Reaction conditions: 0.01 mmol of Ni, 1 mmol of 2-cyclohexen-1-one (CH-enon), 0.3 mmol of octane (internal standard), 130 °C, 10 bar H<sub>2</sub>, 1 h, 1200 rpm.

Results of TEM analysis performed on the spent catalyst after nine catalytic runs are provided in **Figure 4.15**. The TEM images showed some agglomeration of the NPs as well as a mean NP size increase from  $4.5 \pm 0.5$  to  $6.5 \pm 0.9$  nm, thus suggesting a loss in NP dispersion or stability in the applied conditions for catalysis. However, this seems to not limit the catalytic performance of the NPs that was found similar to that of the introduced Ni-NiO NPs, when treated under 20 bar H<sub>2</sub> and handling them with caution.

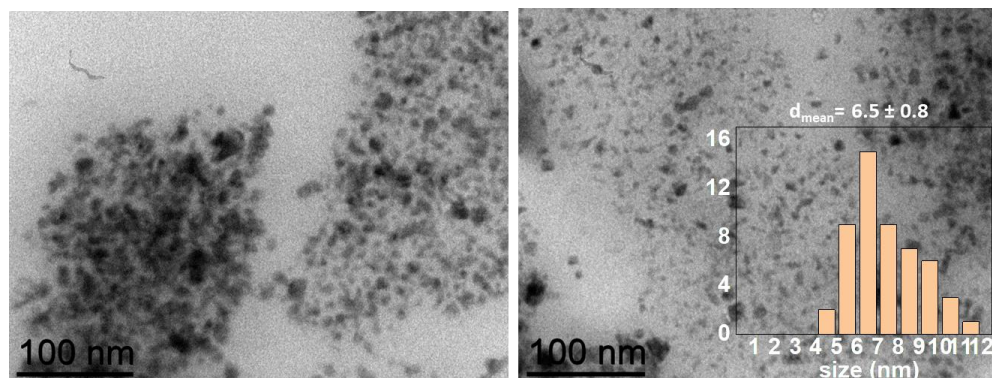


**Figure 4.15** TEM images of Ni-NiO/MEM with the corresponding NPs size distribution (scale bar = 100 nm) after nine catalytic runs in the hydrogenation of 2-cyclohexen-1-one (CH-enon).

To assess the potential impact of temperature variation on catalyst selectivity, the hydrogenation of CH-enon was also performed at 130, 150, and 170°C with the Ni-NiO/MEM system, while keeping all other parameters constant. Notably, the hydrogenation of neither the carbonyl group nor the aromatic ring was observed at 150 and 170°C and full conversion of CH-enon was observed. At 130°C the CH-enon conversion reached 78% after 1 h. Further tests were performed at 130°C to reduce the reaction time reasonably.

When the hydrogenation of CH-enon was performed using Ni/MEM (130°C, 10 bar H<sub>2</sub>, 1 h) a conversion of 97% was obtained. Given this good performance, a comprehensive study with all Ni/FILs and Ni-NiO/FILs systems was carried out under these reaction conditions. The results are provided in **Table 4.9**. All the systems were highly active for the catalytic hydrogenation of CH-enon providing substrate full conversion in 1 h with >99% selectivity to CH-enol. Unlike Ni-NiO/MEM and Ni-NiO/MME it could be noticed that the Ni-NiO/CN and Ni-NiO/H systems did not show inferior activity compared to their non-oxidized analogues. The reason could be a lower oxidation of the NPs surface during air exposure as supported by the XPS data, making these catalysts more effective in the short reaction time applied. It may be interesting to leave the Ni-NiO/MEM and Ni-NiO/MME systems to react for a longer time in order to check if they could also reach full substrate conversion, and thereby confirm if a longer induction period is linked to the reduction of NiO. To assess the extent of conversion as a function of NP oxidation, the Ni/FILs



and then used for CH-enon hydrogenation under the same reaction conditions as previously applied for 1 h. The results are also included in **Table 4.9**.

**Table 4.9** Hydrogenation of 2-cyclohexen-1-one with Ni/FILs and Ni-NiO/FILs catalysts.<sup>a</sup>

Entry	Catalyst system	Air exposure (h)	Conversion (%) <sup>b</sup>	Selectivity (%) <sup>b</sup>		
				CH-non	CH-ol	CH-enol
1	Ni/H	0	>99	97	3	0
2	Ni-NiO/H	24	>99	98	2	0
3	Ni-Ni(OH) <sub>2</sub> /H	480	73	99	1	0
4	Ni/MEM	0	97	>99	0	0
5	Ni-NiO/MEM	24	78	>99	0	0
6	Ni-Ni(OH) <sub>2</sub> /MEM	480	38	>99	0	0
7	Ni/MME	0	>99	>99	0	0
8	Ni-NiO/MME	24	89	>99	0	0
9	Ni- Ni(OH) <sub>2</sub> /MME	480	10	>99	0	0
10	Ni/CN	0	>99	>99	0	0
11	Ni-NiO/CN	24	>99	>99	0	0
12	Ni-Ni(OH) <sub>2</sub> /CN	480	30	>99	0	0

<sup>a</sup> Reaction conditions: 0.01 mmol of Ni, 1 mmol of 2-cyclohexen-1-one (CH-enon), 0.3 mmol of octane (internal standard), 130 °C, 10 bar H<sub>2</sub>, 1 h, 1200 rpm. <sup>b</sup> Determined by GC using internal standard technique.

It was observed that prolonged oxidation of the Ni/FILs resulted in a decrease of the CH-enon conversion, being not favorable for CH-enon hydrogenation. The decrease was most pronounced in the case of the Ni/MME system (Entry 9 vs 8), where the activity dropped by 79%, while for the Ni/CN system the activity drop was only 69% (Entry 12 vs 11). The conversion with Ni/MEM was found to be 38% and 73% for Ni/H, corresponding to a drop of 40% and 26%, respectively (Entries 6 vs 5 and 3 vs 2). The catalytic activity of the systems after 20 days exposure to air followed the order: Ni/H > Ni/MEM > Ni/CN > Ni/MME.

To determine the oxidation states of the Ni NPs after exposure to air for 20 days was XPS analysis of the Ni NPs performed and the Ni 2p<sub>3/2</sub> spectra are given in **Figure 4.16**. **Table 4.10** shows the

To determine the oxidation states of the Ni NPs after exposure to air for 20 days was XPS analysis of the Ni NPs performed and the Ni 2p<sub>3/2</sub> spectra are given in **Figure 4.16**. **Table 4.10** shows the percentages of the different Ni species (Ni(0), NiO and Ni(OH)<sub>2</sub>) detected as a function of the FILs. The XPS spectra showed the presence of a low peak attributed to a remaining amount of metallic Ni(0) and very strong peaks for Ni(OH)<sub>2</sub> species, for all catalytic systems. The increase in the content of the Ni(OH)<sub>2</sub> species could be caused by adsorption of H<sub>2</sub>O from the air onto the NPs surface due to the hygroscopic nature of the ILs. This may also explain the decrease in activity of the NPs observed in the hydrogenation catalysis, where the Ni(OH)<sub>2</sub> species is probably inactive for the hydrogenation of 2-cyclohexen-1-one.

**Table 4.10** Distribution of nickel species as a function of the FILs.

FILs	Distribution of nickel (%) <sup>a</sup>	
	Ni(0)	NiO / Ni(OH) <sub>2</sub>
H	40	60
MEM	36	64
MME	31	69
CN	32	68

<sup>a</sup> Data obtained from XPS analysis.

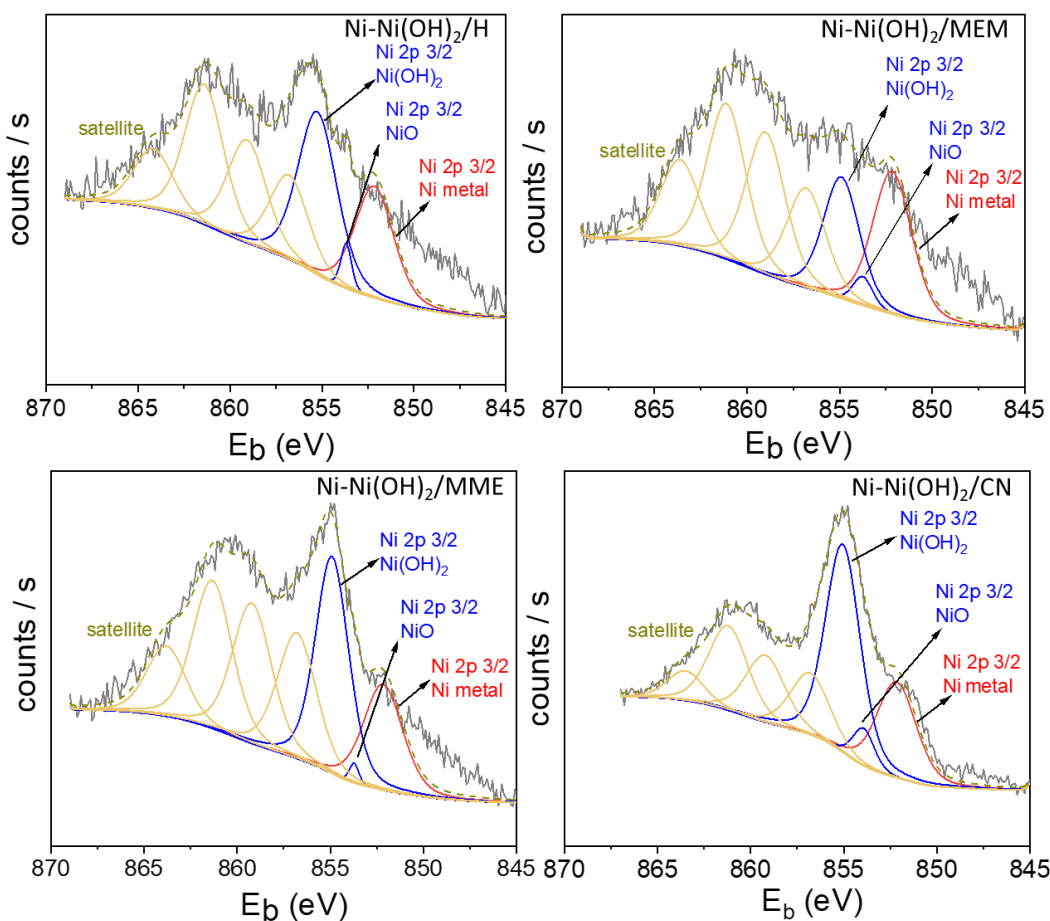


**Figure 4.16** High-resolution XPS scan spectra of Ni 2p<sub>3/2</sub> for the Ni-Ni(OH)<sub>2</sub>/FILs systems.

TEM analysis of the 20-day air exposed Ni-Ni(OH)<sub>2</sub>/ILs was performed and the TEM images are provided in **Figure 4.17**. It can be observed that the Ni NPs in H IL were strongly agglomerated, while the NPs synthesized in MEM, MME the CN remained comparatively well-dispersed after 20 days under air. The average size of the NPs stabilized in H IL had increased to ~6.8 nm, whereas the size remained unchanged for the FILs, showing that the Ni NPs synthesized in FILs provide long term stability compared to the non-functionalized H one.

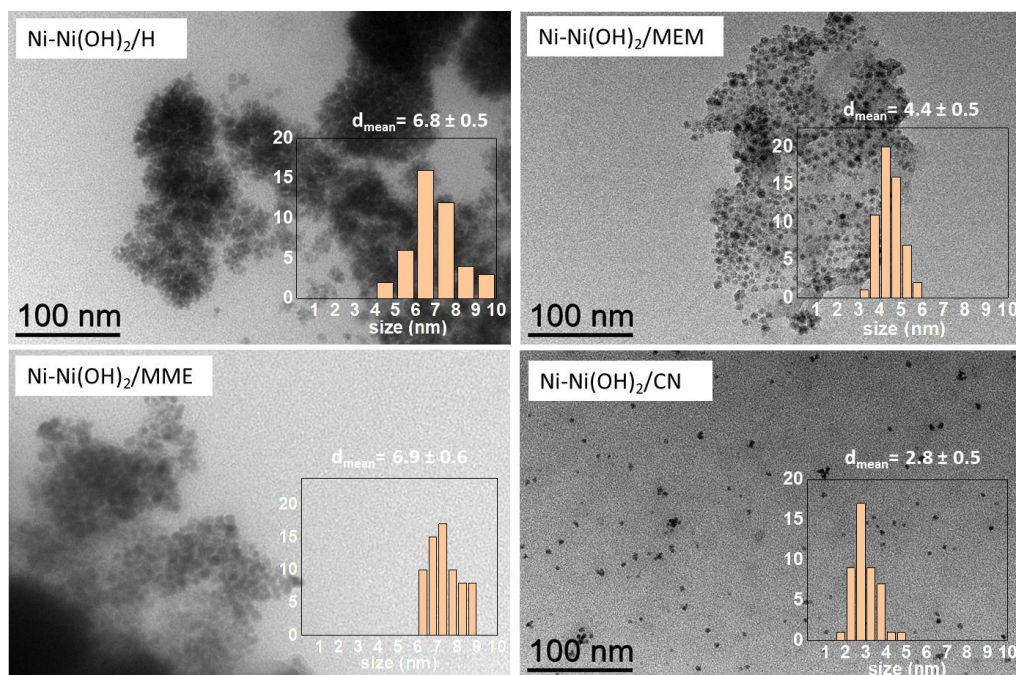


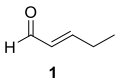
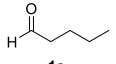
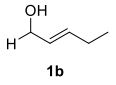
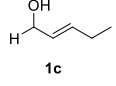
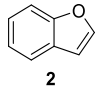
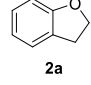
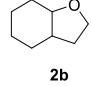
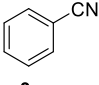
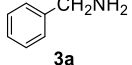
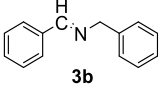
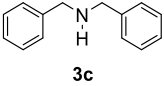
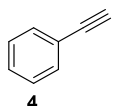
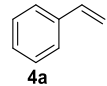
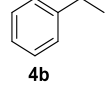
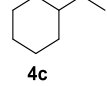
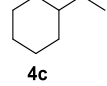
**Figure 4.17** TEM images of Ni-Ni(OH)<sub>2</sub>/FILs with their corresponding size distributions (scale bar = 100 nm).

#### 4.3.4.3 Hydrogenation of other substrates

An initial substrate screening was performed with Ni-NiO/MEM NPs under various reaction conditions without detailed optimization (**Table 4.11**). The study revealed a high selectivity towards the hydrogenation of olefin bonds in the presence of other functional groups in the tested substrates. Hence, Ni-NiO/MEM could convert *trans*-2-hexenal to 1-hexanal with 100% selectivity and a conversion of 59% after 24 h (**Entry 1**). This catalyst was also found active for the selective hydrogenation of nitriles into amines (**Entry 3**) with 51% conversion of benzonitrile into benzylamine with 75% selectivity. 2,3-Benzofuran was converted to 2,3-dihydrobenzofuran without hydrogenation of the benzene ring with a substrate conversion of 33% (**Entry 2**), whereas selective hydrogenation of phenylacetylene to styrene proved difficult and required a lowering of the reaction temperature to 60°C to limit the formation of ethylbenzene. However, by doing so the conversion dropped to 70% with 65% selectivity towards styrene (**Entry 4**). Oppositely, the

catalyst yielded 62% conversion of limonene with complete selectivity towards menthane (**Entry 5**).

**Table 4.11** Substrate screening in the hydrogenation with Ni-NiO/MEM.<sup>a</sup>

Entry	T (°C)	H <sub>2</sub> (bar)	Time (h)	Substrate	Products	Conversion / selectivity (%)
1	110	20	24			59 / <b>1a:1b:1c</b> = 100:0:0
						
						
2 <sup>b</sup>	110	20	24			33 / <b>2a:2b</b> = 100:0
						
3 <sup>c</sup>	80	10	24			51 / <b>3a:3b:3c</b> = 75:nd:nd
						
						
4	80	10	8			100 / <b>4a:4b:4c</b> = 36:64:0
	80	10	16			100 / <b>4a:4b:4c</b> = 0:100:0
	60	10	4			43 / <b>4a:4b:4c</b> = 70:30:0
	60	10	7			70 / <b>4a:4b:4c</b> = 65:35:0

Entry	T (°C)	H <sub>2</sub> (bar)	Time (h)	Substrate	Products	Conversion / selectivity (%)
5 <sup>b</sup>	110	20	24		  	62 / <b>5a:5b:5c</b> = 0:0:100

<sup>a</sup> Reaction conditions: 0.01 mmol of Ni, 1 mmol of substrate, 0.3 mmol of octane (internal standard), 1200 rpm. Product extraction and GC analysis were performed using pentane. <sup>b</sup> Et<sub>2</sub>O. <sup>c</sup> 1,4-dioxane. nd: not determined.

#### 4.4 Summary

A series of catalytic systems based on Ni-containing NPs in non-functionalized IL (H) and FILs containing cyano- (CN) and methoxy-groups (MEM and MME) have been synthesized, characterized, and applied for the hydrogenation of substrates containing different functional groups. The Ni/MEM and Ni/MME catalysts were novel systems, whereas the Ni/H and Ni/CN were previously reported and here prepared for comparison purpose. Small Ni NPs were prepared using CN (2.8 nm), compared to the previous literature (7-8 nm) [15]. All the Ni/ILs systems were found to be efficient catalysts for the hydrogenation of 2-cyclohexene-1-one under the applied reaction conditions (substrate/Ni ratio of 100/1, 130°C, 10 bar H<sub>2</sub>), providing full conversion of 2-cyclohexene-1-one with full selectivity towards hydrogenation of the olefinic bond in short reaction time (1 h). Compared to the previous literature using Ni NPs synthesized in amine-functionalized ILs [43] (substrate/Ni of 50/1, 90°C, 10 bar H<sub>2</sub>, 4 h, water solvent with isolated NPs redispersed in water), this work uses much less Ni metal content but slightly higher temperature to provide complete substrate conversion in much shorter time under neat conditions. Long time air exposure of the catalysts resulted in Ni(OH)<sub>2</sub> layer formation on the Ni/FILs, which led to deactivation and a significant drop-in catalytic activity. The implementation of recyclability tests as well as the characterization of the spent catalysts will allow to complete the evaluation of the catalytic

properties of the Ni/FILs. Another perspective could be to deposit the Ni/FILs NPs on a solid support like silica to obtain SILP systems, which can subsequently be used for hydrogenation reactions, including CO<sub>2</sub> reduction. In this context, initial experiments have been performed for grafting of the catalyst system.

## 4.5 References

1. Yu, Y.; Hou, Z. Soluble Nickel Nanoparticles for Catalytic Hydrogenation. *Curr Org Chem* **2013**, *17*, 336–347, doi:10.2174/1385272811317040004.
2. Alonso, F.; Riente, P.; Sirvent, J.A.; Yus, M. Nickel Nanoparticles in Hydrogen-Transfer Reductions: Characterisation and Nature of the Catalyst. *Appl Catal A Gen* **2010**, *378*, 42–51, doi:10.1016/j.apcata.2010.01.044.
3. Hu, Y.; Yu, Y.; Zhao, X.; Yang, H.; Feng, B.; Li, H.; Qiao, Y.; Hua, L.; Pan, Z.; Hou, Z. Catalytic Hydrogenation of Aromatic Nitro Compounds by Functionalized Ionic Liquids-Stabilized Nickel Nanoparticles in Aqueous Phase: The Influence of Anions. *Sci China Chem* **2010**, *53*, 1541–1548, doi:10.1007/s11426-010-4003-2.
4. Costa, N.J.S.; Guerrero, M.; Collière, V.; Teixeira-Neto, É.; Landers, R.; Philippot, K.; Rossi, L.M. Organometallic Preparation of Ni, Pd, and NiPd Nanoparticles for the Design of Supported Nanocatalysts. *ACS Catal* **2014**, *4*, 1735–1742, doi:10.1021/cs500337a.
5. López-Vinasco, A.M.; Martínez-Prieto, L.M.; Asensio, J.M.; Lecante, P.; Chaudret, B.; Cámpora, J.; van Leeuwen, P.W.N.M. Novel Nickel Nanoparticles Stabilized by Imidazolium-Amidinate Ligands for Selective Hydrogenation of Alkynes. *Catal Sci Technol* **2020**, *10*, 342–350, doi:10.1039/C9CY02172H.
6. Zaramello, L.; Albuquerque, B.L.; Domingos, J.B.; Philippot, K. Kinetic Investigation into the Chemoselective Hydrogenation of  $\alpha,\beta$ -Unsaturated Carbonyl Compounds Catalyzed by Ni(0) Nanoparticles. *Dalton Trans* **2017**, *46*, 5082–5090, doi:10.1039/c7dt00649g.
7. Donegan, K.P.; Godsell, J.F.; Otway, D.J.; Morris, M.A.; Roy, S.; Holmes, J.D. Size-Tuneable Synthesis of Nickel Nanoparticles. *J Nanoparticle Res* **2012**, *14*, 670-XX, doi:10.1007/s11051-011-0670-y.
8. Alonso, F.; Riente, P.; Yus, M. Alcohols for the  $\alpha$ -Alkylation of Methyl Ketones and Indirect Aza-Wittig Reaction Promoted by Nickel Nanoparticles. *Eur J Org Chem* **2008**, 4908–4914, doi:10.1002/ejoc.200800729.
9. Alonso, F.; Riente, P.; Yus, M. Nickel Nanoparticles in Hydrogen Transfer Reactions. *Acc Chem Res* **2011**, *44*, 379–391, doi:10.1021/ar1001582.
10. López-Vinasco, A.M.; Martínez-Prieto, L.M.; Asensio, J.M.; Lecante, P.; Chaudret, B.; Cámpora, J.; Van Leeuwen, P.W.N.M. Novel Nickel Nanoparticles Stabilized by Imidazolium-Amidinate Ligands for Selective Hydrogenation of Alkynes. *Catal Sci Technol* **2020**, *10*, 342–350, doi:10.1039/c9cy02172h.
11. Jiang, H. yan; Zhang, S. shi; Sun, B. Highly Selective Hydrogenation with Ionic Liquid Stabilized Nickel Nanoparticles. *Catal Lett* **2018**, *148*, 1336–1344, doi:10.1007/s10562-018-2361-0.

12. Migowski, P.; Machado, G.; Teixeira, S.R.; Alves, M.C.M.; Morais, J.; Traverse, A.; Dupont, J. Synthesis and Characterization of Nickel Nanoparticles Dispersed in Imidazolium Ionic Liquids. *Phys Chem Chem Phys* **2007**, *9*, 4814–4821, doi:10.1039/b703979d.
13. Prechtel, M.H.G.; Campbell, P.S.; Scholten, J.D.; Fraser, G.B.; Machado, G.; Santini, C.C.; Dupont, J.; Chauvin, Y. Imidazolium Ionic Liquids as Promoters and Stabilising Agents for the Preparation of Metal(0) Nanoparticles by Reduction and Decomposition of Organometallic Complexes. *Nanoscale* **2010**, *2*, 2601–2606, doi:10.1039/c0nr00574f.
14. Konnerth, H.; Prechtel, M.H.G. Selective Partial Hydrogenation of Alkynes to (Z)-Alkenes with Ionic Liquid-Doped Nickel Nanocatalysts at near Ambient Conditions. *Chem Commun* **2016**, *52*, 9129–9132, doi:10.1039/c6cc00499g.
15. Konnerth, H.; Prechtel, M.H.G. Nitrile Hydrogenation Using Nickel Nanocatalysts in Ionic Liquids. *New J Chem* **2017**, *41*, 9594–9597, doi:10.1039/C7NJ02210G.
16. Mariappan, R.; Mahalingam, S. Ionic Liquid-Assisted Synthesis of Nickel Oxide Magnetic Nanoparticles. *Asian J Chem* **2013**, *25*, 3081–3083, doi:10.14233/ajchem.2013.13524.
17. Vijayakrishna, K.; Charan, K.T.P.; Manojkumar, K.; Venkatesh, S.; Pothanagandhi, N.; Sivaramakrishna, A.; Mayuri, P.; Kumar, A.S.; Sreedhar, B. Ni Nanoparticles Stabilized by Poly(Ionic Liquids) as Chemoselective and Magnetically Recoverable Catalysts for Transfer Hydrogenation Reactions of Carbonyl Compounds. *ChemCatChem* **2016**, *8*, 1139–1145, doi:10.1002/cctc.201501313.
18. Nagendiran, A.; Pascanu, V.; Bermejo Gómez, A.; González Miera, G.; Tai, C.W.; Verho, O.; Martín-Matute, B.; Bäckvall, J.E. Mild and Selective Catalytic Hydrogenation of the C=C Bond in  $\alpha,\beta$ -Unsaturated Carbonyl Compounds Using Supported Palladium Nanoparticles. *Chem Eur J* **2016**, *22*, 7184–7189, doi:10.1002/chem.201600878.
19. Marakatti, V.S.; Peter, S.C. Nickel-Antimony Nanoparticles Confined in SBA-15 as Highly Efficient Catalysts for the Hydrogenation of Nitroarenes. *New J Chem* **2016**, *40*, 5448–5457, doi:10.1039/c5nj03479e.
20. Doherty, S.; Knight, J.G.; Backhouse, T.; Abood, E.; Alshaikh, H.; Fairlamb, I.J.S.; Bourne, R.A.; Chamberlain, T.W.; Stones, R. Highly Efficient Aqueous Phase Chemoselective Hydrogenation of  $\alpha,\beta$ -Unsaturated Aldehydes Catalysed by Phosphine-Decorated Polymer Immobilized IL-Stabilized PdNPs. *Green Chem* **2017**, *19*, 1635–1641, doi:10.1039/c6gc03528k.
21. Serhan, M.; Jackemeyer, D.; Long, M.; Sprowls, M.; Diez Perez, I.; Maret, W.; Chen, F.; Tao, N.; Forzani, E. Total Iron Measurement in Human Serum With a Novel Smartphone-Based Assay. *IEEE J Transl Eng Health Med* **2020**, *8*, 1–9, doi:10.1109/JTEHM.2020.3005308.
22. Tamura, M.; Tokonami, K.; Nakagawa, Y.; Tomishige, K. Selective Hydrogenation of Crotonaldehyde to Crotyl Alcohol over Metal Oxide Modified Ir Catalysts and Mechanistic Insight. *ACS Catal* **2016**, *6*, 3600–3609, doi:10.1021/acscatal.6b00400.
23. Alonso, F.; Riente, P.; Yus, M. Nickel Nanoparticles in Hydrogen Transfer Reactions. *Acc Chem Res* **2011**, *44*, 379–391, doi:10.1021/ar1001582.
24. Czaplik, W.M.; Neudörfl, J.M.; von Wangelin, A.J. On the Quantitative Recycling of Raney–Nickel Catalysts on a Lab-Scale. *Green Chem* **2007**, *9*, 1163–1165, doi:10.1039/b708057c.
25. Mokhov, V.M.; Popov, Y. V.; Nebykov, D.N. Hydrogenation of Alkenes over Nickel Nanoparticles under Atmospheric Pressure of Hydrogen. *Russ J Org Chem* **2016**, *52*, 319–323, doi:10.1134/S1070428016030040.



26. Cardona-Farreny, M.; Lecante, P.; Esvan, J.; Dinoi, C.; del Rosal, I.; Poteau, R.; Philippot, K.; Axet, M.R. Bimetallic RuNi Nanoparticles as Catalysts for Upgrading Biomass: Metal Dilution and Solvent Effects on Selectivity Shifts. *Green Chem* **2021**, *23*, 8480–8500, doi:10.1039/D1GC02154K.
27. Bruna, L.; Cardona-Farreny, M.; Colliere, V.; Philippot, K.; Axet, M.R. In Situ Ruthenium Catalyst Modification for the Conversion of Furfural to 1,2-Pentanediol. *Nanomater* **2022**, *12*, 328–XX, doi:10.3390/nano12030328.
28. Scholten, J.D.; Ebeling, G.; Dupont, J. On the Involvement of NHC Carbenes in Catalytic Reactions by Iridium Complexes, Nanoparticle and Bulk Metal Dispersed in Imidazolium Ionic Liquids. *Dalton Trans* **2007**, 5554–5560, doi:10.1039/b707888a.
29. Graham, D.C.; Cavell, K.J.; Yates, B.F. Oxidative Addition of 2-Substituted Azolium Salts to Group-10 Metal Zero Complexes - A DFT Study. *Dalton Trans* **2007**, 4650–4658, doi:10.1039/b709914b.
30. Yang, M.; Campbell, P.S.; Santini, C.C.; Mudring, A.V. Small Nickel Nanoparticle Arrays from Long Chain Imidazolium Ionic Liquids. *Nanoscale* **2014**, *6*, 3367–3375, doi:10.1039/c3nr05048c.
31. Pechtl, M.H.G.; Scholten, J.D.; Dupont, J. Tuning the Selectivity of Ruthenium Nanoscale Catalysts with Functionalised Ionic Liquids: Hydrogenation of Nitriles. *J Mol Catal A Chem* **2009**, *313*, 74–78, doi:10.1016/j.molcata.2009.08.004.
32. Gieshoff, T.N.; Welther, A.; Kessler, M.T.; Pechtl, M.H.G.; Jacobi von Wangelin, A. Stereoselective Iron-Catalyzed Alkyne Hydrogenation in Ionic Liquids. *Chem Commun* **2014**, *50*, 2261–2264, doi:10.1039/c3cc49679a.
33. Venkatesan, R.; Pechtl, M.H.G.; Scholten, J.D.; Pezzi, R.P.; MacHado, G.; Dupont, J. Palladium Nanoparticle Catalysts in Ionic Liquids: Synthesis, Characterisation and Selective Partial Hydrogenation of Alkynes to Z-Alkenes. *J Mater Chem* **2011**, *21*, 3030–3036, doi:10.1039/c0jm03557b.
34. Prieto, P.; Nistor, V.; Nouneh, K.; Oyama, M.; Abd-Lefdil, M.; Díaz, R. XPS Study of Silver, Nickel and Bimetallic Silver-Nickel Nanoparticles Prepared by Seed-Mediated Growth. *Appl Surf Sci* **2012**, *258*, 8807–8813, doi:10.1016/j.apsusc.2012.05.095.
35. Nesbitt, H.W.; Legrand, D.; Bancroft, G.M. Interpretation of Ni2p XPS Spectra of Ni Conductors and Ni Insulators. *Phys Chem Miner* **2000**, *27*, 357–366, doi:10.1007/S002690050265/METRICS.
36. Li, J.; Li, P.; Li, J.; Tian, Z.; Yu, F. Highly-Dispersed Ni-NiO Nanoparticles Anchored on an SiO<sub>2</sub> Support for an Enhanced CO Methanation Performance. *Catalysts* **2019**, *9*, 506, doi:10.3390/catal9060506.
37. Liu, J.; Zhu, Y.; Wang, C.; Singh, T.; Wang, N.; Liu, Q.; Cui, Z.; Ma, L. Facile Synthesis of Controllable Graphene-Co-Shelled Reusable Ni/NiO Nanoparticles and Their Application in the Synthesis of Amines under Mild Conditions. *Green Chem* **2020**, *22*, 7387–7397, doi:10.1039/D0GC02421J.
38. Richard, D.; Ockelford, J.; Giroir-Fendler, A.; Gallezot, P. Composition and Catalytic Properties in Cinnamaldehyde Hydrogenation of Charcoal-Supported, Platinum Catalysts Modified by FeCl<sub>2</sub> Additives. *Catal Lett* **1989**, *3*, 53–58, doi:10.1007/BF00765054/METRICS.

39. Ma, H.; Wang, L.; Chen, L.; Dong, C.; Yu, W.; Huang, T.; Qian, Y. Pt Nanoparticles Deposited over Carbon Nanotubes for Selective Hydrogenation of Cinnamaldehyde. *Catal Commun* **2007**, *8*, 452–456, doi:10.1016/j.catcom.2006.07.020.
40. Mahata, N.; Gonçalves, F.; Pereira, M.F.R.; Figueiredo, J.L. Selective Hydrogenation of Cinnamaldehyde to Cinnamyl Alcohol over Mesoporous Carbon Supported Fe and Zn Promoted Pt Catalyst. *Appl Catal A Gen* **2008**, *339*, 159–168, doi:10.1016/j.apcata.2008.01.023.
41. Zhou, A.; Dou, Y.; Zhou, J.; Li, J.R. Rational Localization of Metal Nanoparticles in Yolk–Shell MOFs for Enhancing Catalytic Performance in Selective Hydrogenation of Cinnamaldehyde. *ChemSusChem* **2020**, *13*, 205–211, doi:10.1002/cssc.201902272.
42. Prakash, M.G.; Mahalakshmy, R.; Krishnamurthy, K.R.; Viswanathan, B. Selective Hydrogenation of Cinnamaldehyde on Nickel Nanoparticles Supported on Titania: Role of Catalyst Preparation Methods. *Catal Sci Technol* **2015**, *5*, 3313–3321, doi:10.1039/C4CY01379D.
43. Hu, Y.; Yu, Y.; Hou, Z.; Yang, H.; Feng, B.; Li, H.; Qiao, Y.; Wang, X.; Hua, L.; Pan, Z.; et al. Ionic Liquid Immobilized Nickel(0) Nanoparticles as Stable and Highly Efficient Catalysts for Selective Hydrogenation in the Aqueous Phase. *Chem Asian J* **2010**, *5*, 1178–1184, doi:10.1002/asia.200900628.
44. Zhou, J.; Zhang, Y.; Li, S.; Chen, J. Ni/NiO Nanocomposites with Rich Oxygen Vacancies as High-Performance Catalysts for Nitrophenol Hydrogenation. *Catalysts* **2019**, *9*, 944 doi:10.3390/catal9110944.
45. Yuan, F.; Ni, Y.; Zhang, L.; Yuan, S.; Wei, J. Synthesis, Properties and Applications of Flowerlike Ni-NiO Composite Microstructures. *J Mater Chem A Mater* **2013**, *1*, 8438–8444, doi:10.1039/c3ta11219e.

## 5. Synthesis and characterization of ruthenium-rhenium nanoparticles in ionic liquids

### 5.1 Introduction

Bimetallic materials based on rhenium find a wide range of applications in catalysis, including hydrogenation reactions [1,2], Fisher-Tropsch processes [3], among others [4]. The synergistic effects arising from the presence of two different metals is the main target towards developing bimetallic catalysts. Synergy effects may potentially improve both the activity and selectivity of catalytic reactions. In the literature, different works report the enhancement of activity of a selected metal by introduction of Re. For example, Ma *et al.* [5] studied the catalytic efficiency of Al<sub>2</sub>O<sub>3</sub>/C/ZrO<sub>2</sub>-supported RuRe catalysts in the hydrogenolysis of glycerol. They observed that the introduction of Re onto Ru/Al<sub>2</sub>O<sub>3</sub>, Ru/C and Ru/ZrO<sub>2</sub> induced a considerable enhancement in the hydrogenolysis of glycerol to propanediols, which was attributed to a synergistic interplay between the two metals. Baranowska *et al.* [6] successfully synthesized a series of RuRe bimetallic NPs with different Ru/Re ratios through a microwave-assisted polyol method using RuCl<sub>3</sub> and NH<sub>4</sub>ReO<sub>4</sub> as Ru and Re precursors, ethylene glycol as reducing agent and solvent as well as polyvinylpyrrolidone (PVP) as capping agent. They obtained RuRe NPs with mean size of ca. 1.4-1.6 nm in a size range of 0.5-2.5 nm. The size of the monometallic Ru/PVP NPs (1.3 nm) prepared by the same synthesis method was slightly smaller than that of bimetallic RuRe NPs. Additionally, they synthesized RuRe NPs on  $\gamma$ -alumina- or silica-supports by *in-situ* deposition through the co-reduction of RuCl<sub>3</sub>·H<sub>2</sub>O and NH<sub>4</sub>ReO<sub>4</sub>. In another work, the same group studied the effect of Re on the dispersion of Ru in the RuRe/ $\gamma$ -Al<sub>2</sub>O<sub>3</sub> using H<sub>2</sub> chemisorption technique [7]. In this study, the catalyst was synthesized from Ru(NO)(NO<sub>3</sub>)<sub>3</sub> or RuCl<sub>3</sub> and NH<sub>4</sub>ReO<sub>4</sub> precursors, reduced in hydrogen flow (heating rate of 5 °C /min) at 500 °C for 4 h, which led to RuRe NPs with an average size < 3nm well-dispersed on the alumina support. Their results showed that the addition of Re to the Ru/ $\gamma$ -Al<sub>2</sub>O<sub>3</sub> catalyst, particularly when using the chlorine-free precursor Ru(NO)(NO<sub>3</sub>)<sub>3</sub>, led to a notable enhancement in the dispersion of ruthenium on the support. Additionally, they observed that increase in Re loading gave rise to an increase of Ru dispersion, with the highest level achieved at a composition of Ru<sub>50</sub>Re<sub>50</sub>. In contrast, the effect was less pronounced in the bimetallic RuRe NPs prepared from the chlorine-containing precursor RuCl<sub>3</sub>. Philippot, Chaudret and coworkers

[8] reported a novel route to synthesize PVP-stabilized bimetallic RuRe NPs from decomposition of the organometallic precursors (2-methylallyl)(1,5-cyclooctadiene)ruthenium(0),  $[\text{Ru}(\text{COD})(2\text{-methylallyl})_2]$ , or (1,5-cyclooctadiene)(1,3,5-cyclooctatriene)ruthenium(0),  $[\text{Ru}(\text{COD})(\text{COT})]$ , and dirhenium(II)tetraallyl,  $[\text{Re}_2(\text{C}_3\text{H}_5)_4]$ , under hydrogen pressure. Using  $[\text{Ru}(\text{COD})(2\text{-methylallyl})_2]$  this method allowed to generate very small and alloy-type RuRe NPs with an average size of ca. 1.3 nm that displayed a narrow size distribution and an hexagonal-close packed (hcp) structure. Changing the Ru precursor to  $[\text{Ru}(\text{COD})(\text{COT})]$  led to the formation of core-shell RuRe NPs displaying an average size of ca. 1.2 nm, and a narrower size distribution compared to the alloyed RuRe NPs with *hcp* structure. Whyman and coworkers [9] reported the *in-situ* synthesis of heterogeneous Ru/Re and Rh/Re nanomaterials from  $[\text{Ru}_3(\text{CO})_{12}]/[\text{Re}_2(\text{CO})_{10}]$  and  $[\text{Rh}_6(\text{CO})_{16}]/[\text{Re}_2(\text{CO})_{10}]$  precursors. The synthesis was performed by reduction of the precursors using 50-100 bar  $\text{H}_2$  and  $>150^\circ\text{C}$  during catalysis, when employed for the liquid-phase hydrogenation of cyclohexylcarboxamide ( $\text{CyCONH}_2$ ) to cyclohexylmethylamine ( $\text{CyCH}_2\text{NH}_2$ ). A 95% selectivity in the target amine was achieved in the absence of ammonia, which is usually used to suppress the formation of secondary and tertiary amines. The conversion of the amides were possible with the Rh/Re and Ru/Re nanocatalysts within the specified reaction conditions of 50-100 bar  $\text{H}_2$  using temperatures higher than  $150^\circ\text{C}$  and  $160^\circ\text{C}$ , respectively. Variations in the Ru/Re and Rh/Re ratios resulted in minor alterations in product selectivity. Furthermore, no catalyst deactivation was detected even at higher Re contents.

Considering that 1) the difficult amide hydrogenation (owing to amide stability) can be achieved with RuRe based catalysts [10], RuRe NPs of different structures can be directly synthesized [8], and 2) the relatively high thermal stability of ILs, the synthesis of RuRe NPs in ILs was targeted to use as catalysts in amide hydrogenation. So far, the synthesis of RuRe bimetallic NPs in ILs has not been reported in literature. Thus, this chapter describes the synthesis of RuRe bimetallic NPs in H and MEM ILs using the organometallic approach. For this purpose, the precursors  $[\text{Ru}(\text{COD})(\text{COT})]$  and  $[\text{Re}_2(\text{CO})_{10}]$  were used as they are commercially available and possesses ligands that can be eliminated under hydrogenation or heating conditions (see Chapter 1 for details). However, it must be noted that  $[\text{Re}_2(\text{CO})_{10}]$  is very stable at room temperature and forced reaction conditions is needed to facilitate its decomposition [11]. The reduction of the Re species may be promoted by hydrogen spillover from the reduced species of the other metal present, as

previously reported [7,12]. The  $[\text{Re}_2(\text{C}_3\text{H}_5)_4]$  precursor, which decompose under milder reaction conditions [13] than  $[\text{Re}_2(\text{CO})_{10}]$ , was unfortunately unavailable.

## 5.2 Experimental section

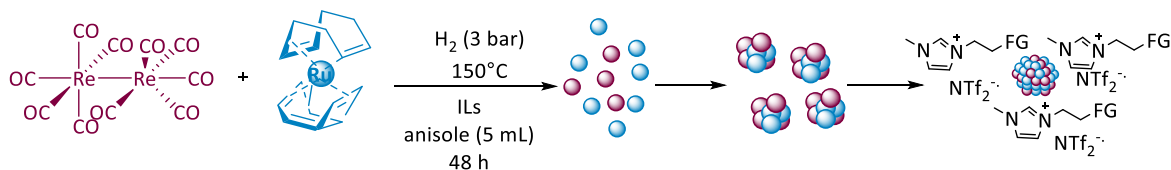
### 5.2.1 Synthesis of IL-stabilized RuRe NPs (RuRe/IL)

In a typical synthesis,  $[\text{Ru}(\text{COD})(\text{COT})]$  (27.5 mg, 0.086 mmol) and  $[\text{Re}_2(\text{CO})_{10}]$  (29.1 mg, 0.044 mmol) (1/1 molar ratio of metals), a given IL (1 mL), and anisole (5 mL) were introduced under argon atmosphere into either a Fischer-Porter reactor, pressurized with 3 bar  $\text{H}_2$  and heated to 150 °C, or into a 20 mL stainless steel high-pressure batch reactor (**Figure D1, Appendix D**), pressurized with 3 bar  $\text{H}_2$  and heated to 190 °C. The reaction was allowed to stir for 2 days at 600 rpm, where after anisole was removed under vacuum ( $\approx 0.05$  mbar) overnight at 60 °C. The resultant black colloidal suspension containing RuRe/IL was washed with pentane ( $2 \times 5$  mL) and stored under inert atmosphere inside a glovebox prior to analyses. Monometallic Ru/IL and Re/IL were prepared for comparative purposes following the same procedure using  $[\text{Ru}(\text{COD})(\text{COT})]$  (27.2 mg, 0.086 mmol) or  $[\text{Re}_2(\text{CO})_{10}]$  (28.4 mg, 0.043 mmol). Materials used and method of characterizations are provided in Chapter 7.

## 5.3 Results and Discussion

### 5.3.1 Synthesis and Characterization of RuRe/IL

As mentioned above, RuRe NPs were synthesized in earlier work using  $[\text{Ru}(\text{COD})(\text{COT})]$  and  $[\text{Re}_2(\text{CO})_{10}]$  as metal precursors employing the ligands PVP and HAD for the stabilization of the RuRe NPs (optimized reaction conditions: 3 bar of  $\text{H}_2$ , 120 °C, 48 h and anisole as solvent) [14]. Thus, in a first attempt the one-pot synthesis of RuRe/ILs was carried out following the same reaction conditions (**Scheme 5.1**). Monometallic Ru/IL and Re/IL were synthesized following the same procedure for comparative purposes.



**Scheme 5.1** Organometallic synthesis of RuRe/IL from  $[\text{Ru}(\text{COD})(\text{COT})]$  and  $[\text{Re}_2(\text{CO})_{10}]$ .

[Ru(COD)(COT)] and [Re<sub>2</sub>(CO)<sub>10</sub>] with a Ru/Re molar ratio of 1/1 were introduced into a Fischer-Porter bottle containing the desired IL (H or MEM) dissolved in anisole. The reaction mixture was pressurized with 3 bar of H<sub>2</sub> and then heated to 150 °C followed by stirring for 2 days at 600 rpm. For the H IL, the color of the solution turned from yellow to brownish with black deposits on the walls of the reactor, and upon removal of the solvent a colloidal brownish black solution was obtained (**Figure 5.1 a**). In contrast, for MEM, the color of the solution changed from yellow to black (**Figure 5.1 b**). This different behavior in terms of evolution of the reaction color could point to a different decomposition pattern of the precursors in the ILs.

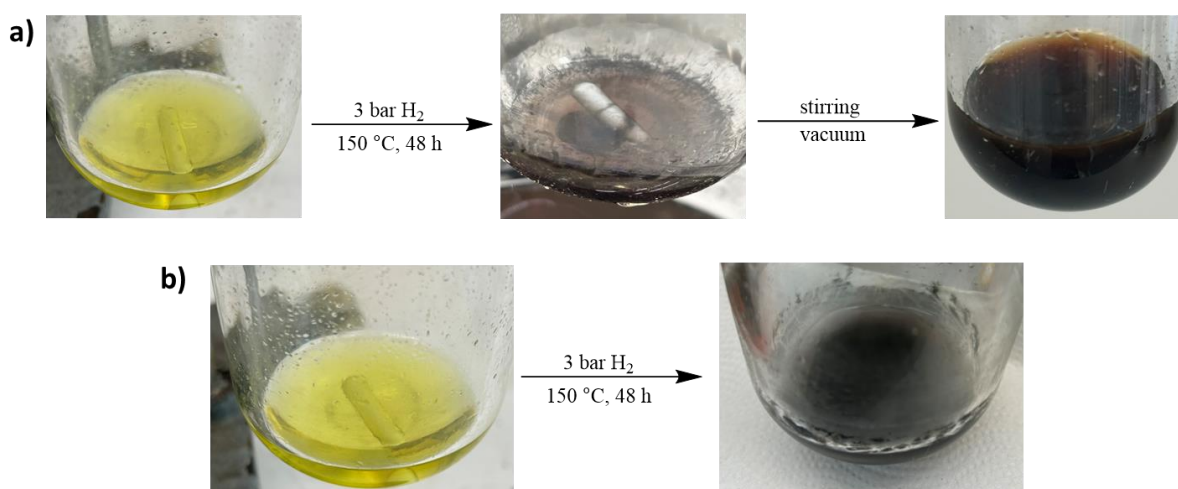


**Figure 5.1** Pictures of the synthesis of RuRe NPs in a) H and b) MEM ILs dissolved in anisole.

Ru/IL NPs synthesized using the same reaction conditions displayed the typical color change from yellow to black, whereas the color of the Re reaction mixture did not evolve to black (desired), whatever the IL used. The initial transparent solution turned clear yellowish in both cases after 48 h of reaction (**Figure 5.2**). Similar observations have been made previously (in the LCC group), when [Re<sub>2</sub>CO<sub>10</sub>] was attempted decomposed at the same reaction conditions using PVP or HDA. Here, the yellow species was proposed to be a rhenium carbonyl hydride complex, [H<sub>3</sub>Re<sub>3</sub>(CO)<sub>12</sub>], as ascertained by FT-IR, <sup>1</sup>H-NMR and WAXS techniques. Supporting this hypothesis, the synthesis of [H<sub>3</sub>Re<sub>3</sub>(CO)<sub>12</sub>] had previously been reported from [Re<sub>2</sub>CO<sub>10</sub>] and dihydrogen [15,16]. NMR and FT-IR analyses of the current samples, Re/ILs, did not allow to clarify this point as only signals corresponding to the IL were observed.

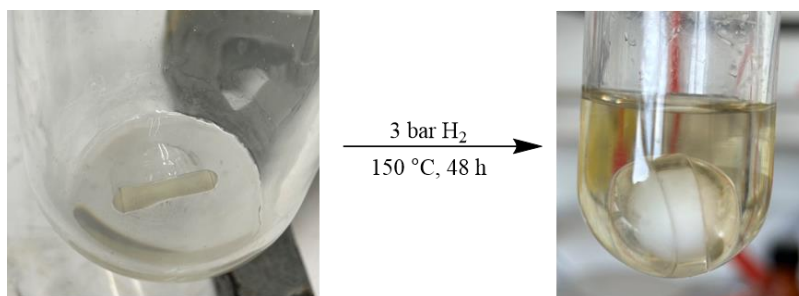


**Figure 5.2** Attempt of the decomposition of  $[\text{Re}_2(\text{CO})_{10}]$  under 3 bar  $\text{H}_2$  at 150 °C in MEM dissolved in anisole.

**a) TEM analysis**

TEM analyses were performed of both the bimetallic and the monometallic samples. The TEM images of RuRe/H and RuRe/ME showed both well-dispersed NPs with average size of  $1.6 \pm 0.2$  nm and  $3.3 \pm 0.4$  nm, respectively (**Figure 5.3**), while an average size  $2.0 \pm 0.2$  nm and  $2.1 \pm 0.2$  nm was observed for Ru/H and Ru/MEM, respectively (**Figure 5.4**). Regarding the Re samples, the TEM images confirmed the lack of formation of NPs for both Re/H and Re/MEM (**Figure 5.5**).

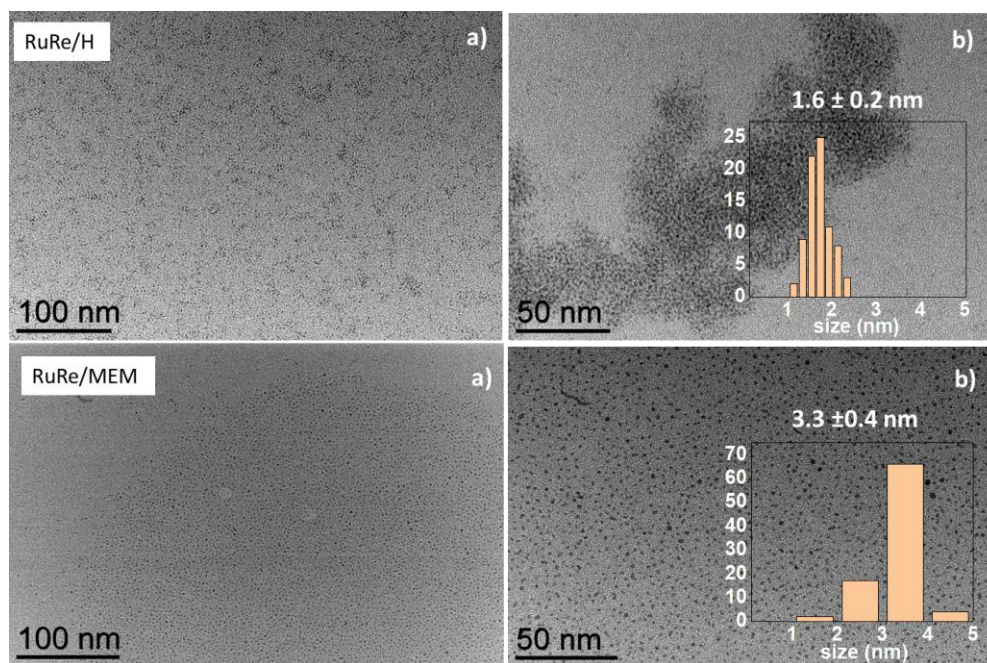


**Figure 5.3** a) TEM images and b) the corresponding NPs size distributions of synthesized RuRe/ILs NPs (150 °C, 3 bar  $\text{H}_2$ , anisole) (scale bar = 100, 50 nm).



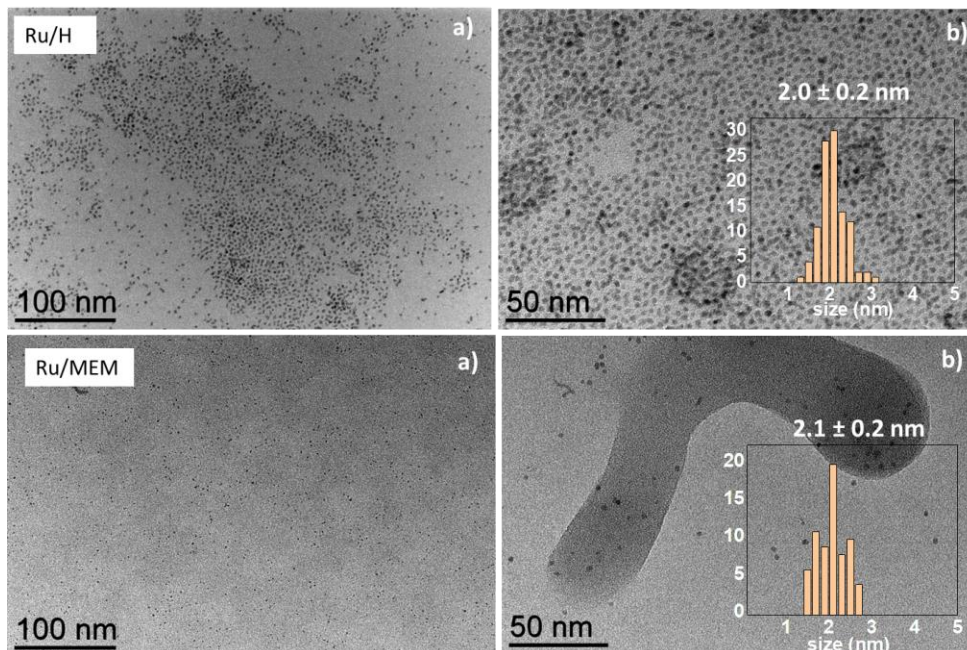


**Figure 5.4** a) TEM images and b) the corresponding size distributions of synthesized Ru/ILs NPs (150 °C, 3 bar H<sub>2</sub>, anisole) (scale bar = 100, 50 nm).

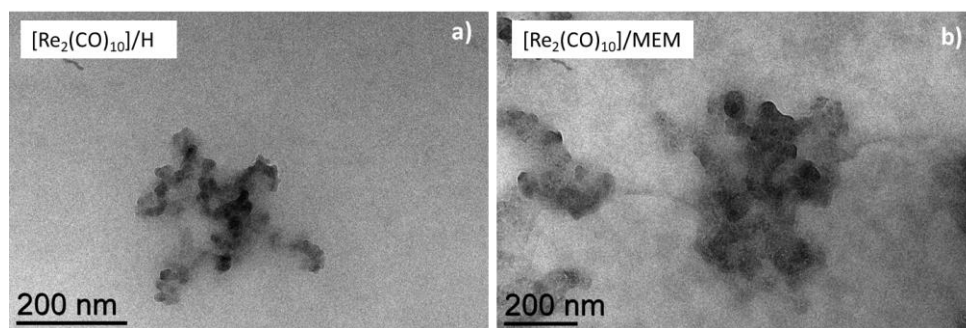


**Figure 5.5** TEM images of [Re<sub>2</sub>(CO)<sub>10</sub>] in a) H and b) MEM ILs after synthesis (3 bar H<sub>2</sub>, 150 °C, in anisole) (scale bar = 200 nm).

HRTEM and HAADF-STEM analyses were further performed on the bimetallic nanomaterials and provided for RuRe/H and RuRe/MEM in **Figure 5.6** and **Figure 5.9**, respectively. EDX analyses were also performed on the individual NPs (**Figures 5.7** and **5.10**), and the latter analysis confirmed that both metals were present in the NPs synthesized in both H and MEM. Moreover, the metal content in the NPs was quantified, with comparable results by measurements performed



at different areas of the grid, to be ~12 at% Re and ~88 at% of Ru in RuRe/H and ~34 at% Re and ~66 at% of Ru in RuRe/MEM.

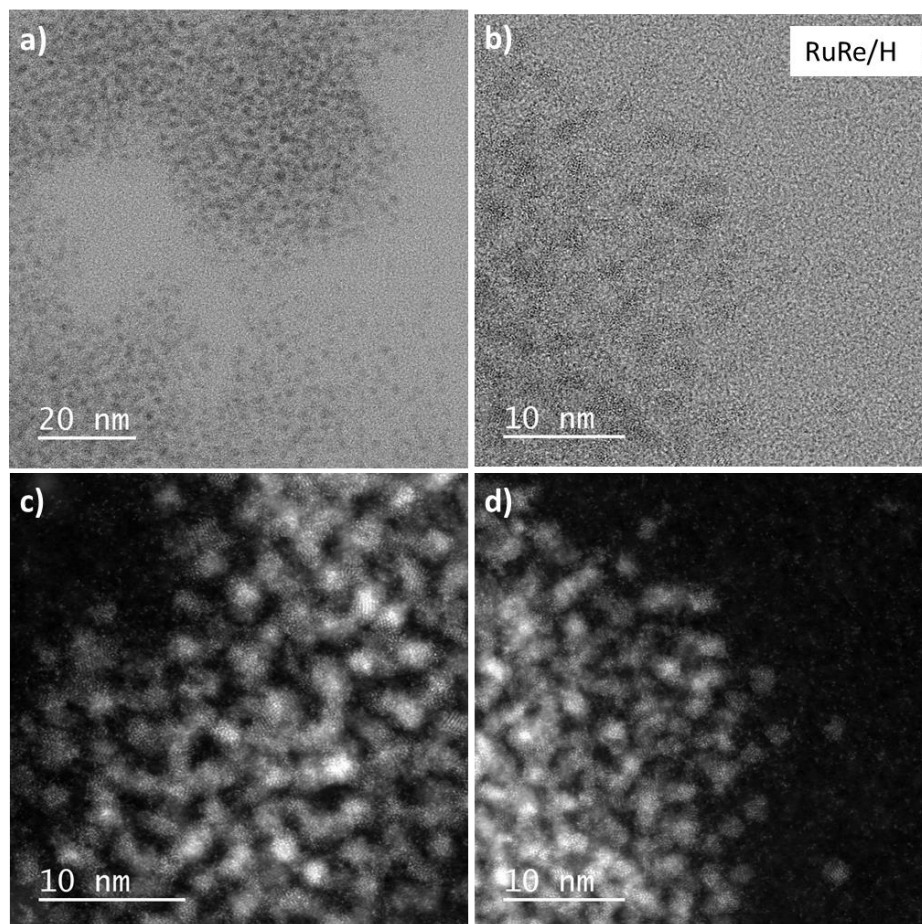


**Figure 5.6** a), b) HRTEM images and c), d) HAADF-STEM images of synthesized RuRe/H NPs (150 °C, 3 bar H<sub>2</sub>, anisole) (scale bar = 20,10 nm).

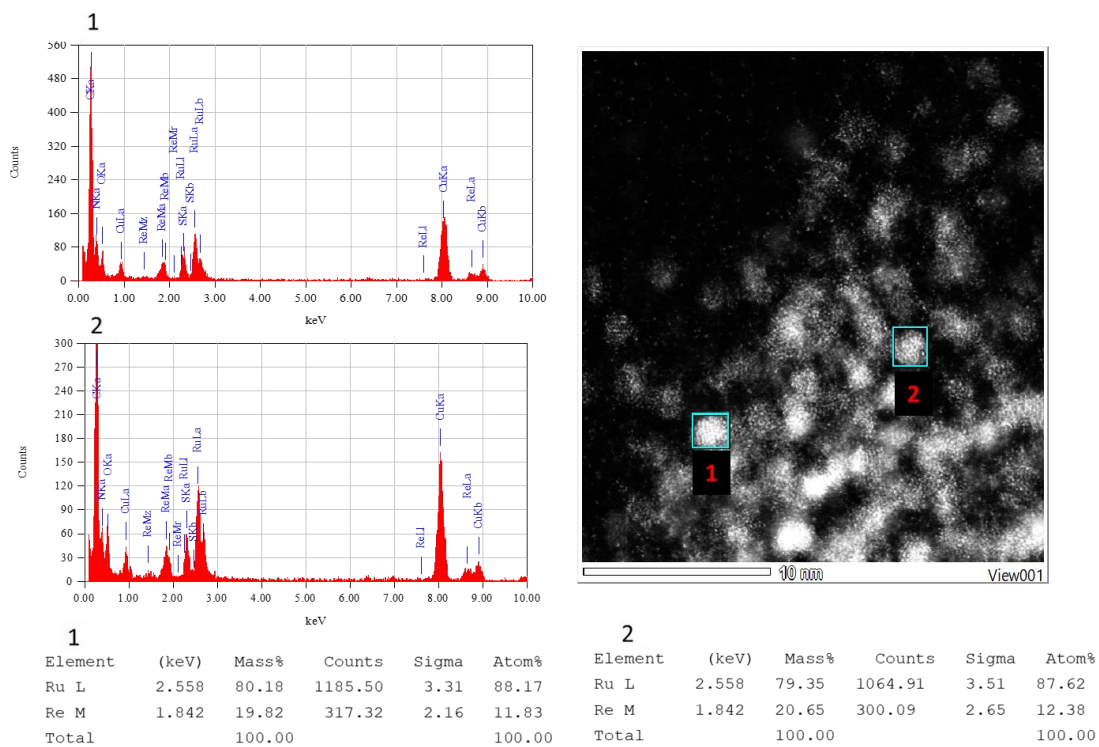


Figure 5.7 EDX analyses of synthesized RuRe/H NPs (150 °C, 3 bar H<sub>2</sub>, anisole).

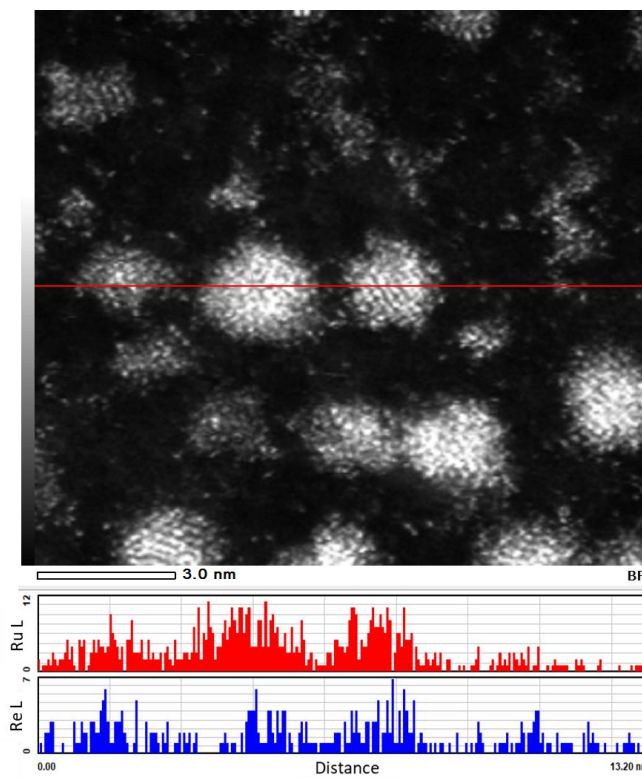
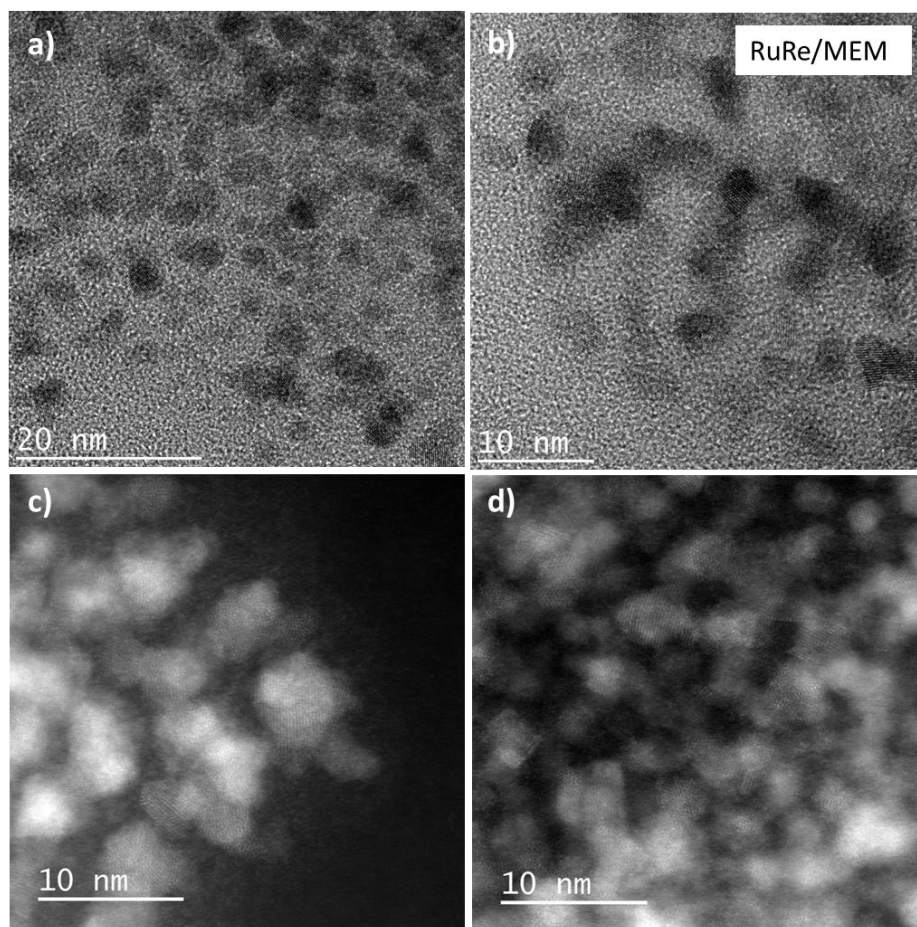
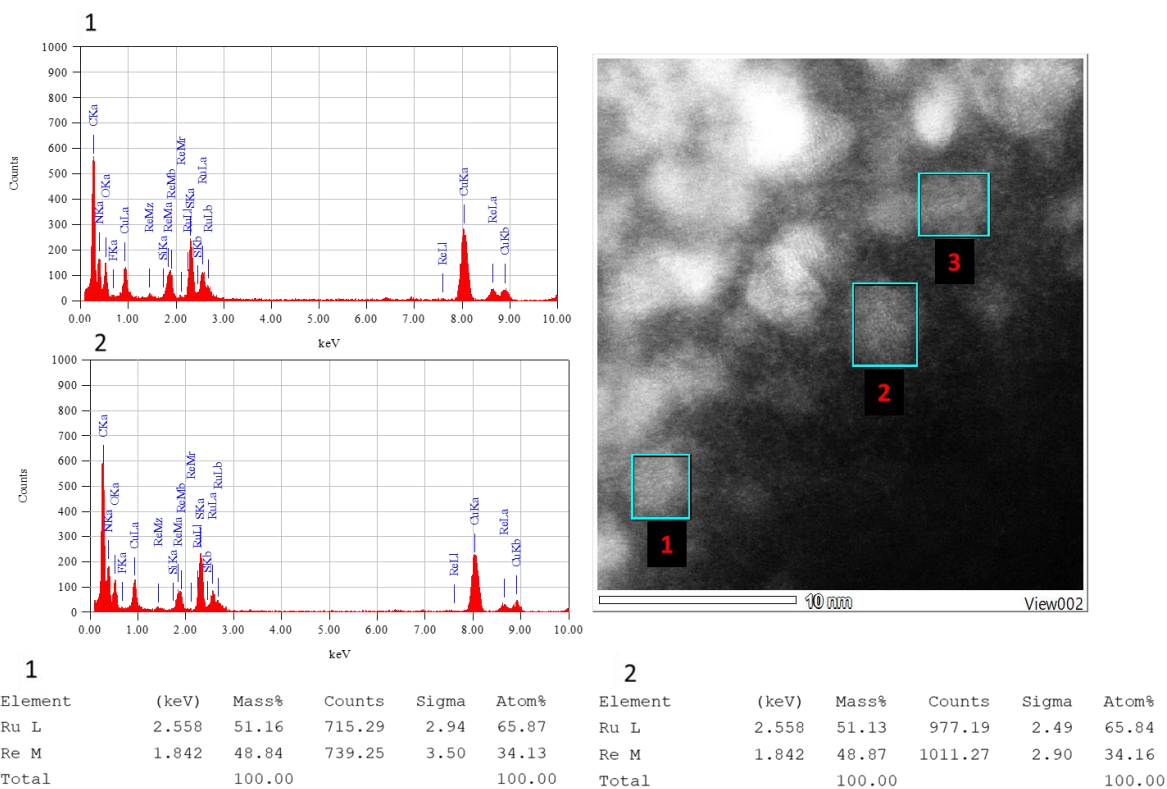


Figure 5.8 EDX line scanning profile of synthesized RuRe/H NPs (150 °C, 3 bar H<sub>2</sub>, anisole).



**Figure 5.9** a), b) HRTEM images and c), d) HAADF-STEM images of synthesized RuRe/MEM NPs (150 °C, 3 bar H<sub>2</sub>, anisole) (scale bar = 20,10 nm).



**Figure 5.10** EDX analysis of synthesized RuRe/MEM NPs (150 °C, 3 bar H<sub>2</sub>, anisole).

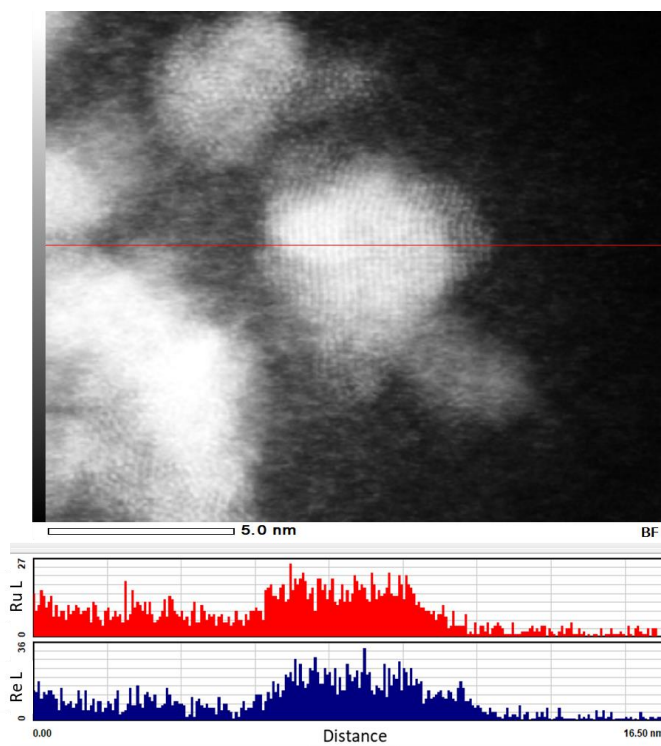


**Figure 5.11** EDX line scanning profile of synthesized RuRe/H NPs (150 °C, 3 bar H<sub>2</sub>, anisole).

The metal contents quantified from the EDX of both RuRe/H and RuRe/MEM evidenced a lower Re content than expected from the introduced amount of precursors (1/1 molar ratio). Also, a different Re content was observed depending on the IL used, being higher for the MEM IL compared to the H IL. These results strongly suggest incomplete decomposition of the  $[\text{Re}_2(\text{CO})_{10}]$  precursor or its hydride derivatives. Furthermore, elemental analyses ascertained by ICP of the purified samples that both RuR/H and RuRe/MEM had a Ru/Re = 1/1 ratio, thus indicating that the applied purification method could not eliminate the remaining Re molecular species. These results also endorse the important role of the stabilizing agent on the composition of the bimetallic RuRe NPs. Further analyses of the HRTEM images show that the formed NPs are well-crystallized. The lattice image and the corresponding numerical diffractogram for RuRe/MEM (**Figure 5.12**) demonstrated a crystalline hcp structure of both the Ru and Re metal. The angle between the pair of spots and the radial distances are in good agreement with the spot diffraction pattern of *hcp* crystals. The lattice fringes calculated for crystallites may fit with both metallic Ru and Re and the average distance measured for the lattice planes corresponded to 2.38 Å. Such observation was previously done for RuRe NPs synthesized with PVP and HAD.

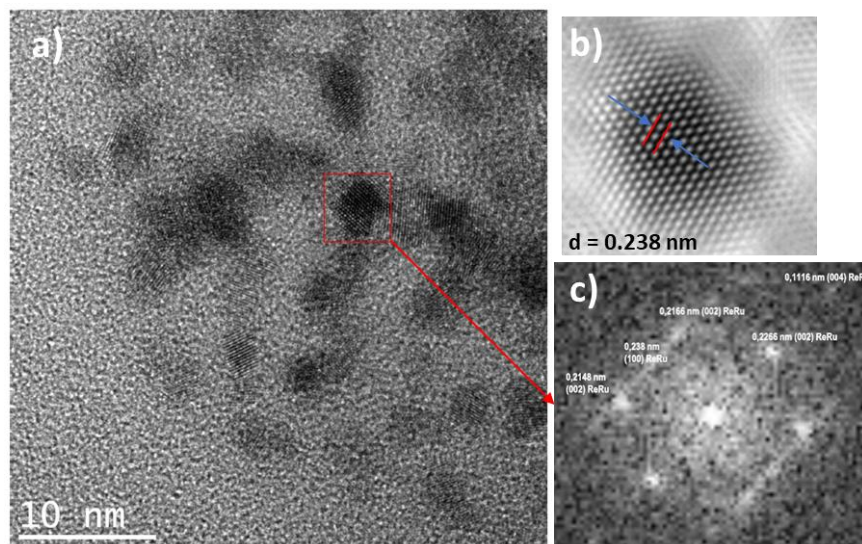


**Figure 5.12** a) HRTEM image of RuRe/MEM, b) isolated NP with a lattice spacing  $d$  of 0.238 nm obtained by inverse FFT, and c) Fast Fourier Transform (FFT) of NPs indicated by the red rectangle.

EDX line scanning profiles (**Figures 5.8** and **5.11**) provided information about the chemical order in the RuRe NPs. They also evidenced the presence of isolated Re metal on other areas of the



grid, thus confirming that a part of the introduced Re was not associated with Ru. An EDX line scanning profile for one individual RuRe/MEM NP is given in **Figure 5.13**. For this NP, Re is present at a higher quantity in the outer shell compared to the particle core, while Ru metal is more abundant in the core. This strongly suggests that the bimetallic NPs displayed a core-shell structure with an inverse gradient of the two metals from the core to the surface. However, further characterization studies, such as by WAXS or even better, EXAFS/XANES techniques, are needed to confirm this hypothesis. The core-shell structure with Ru in the core is also supported by the different decomposition kinetics known for the Ru and Re precursors. Indeed, decomposition of  $[\text{Re}_2\text{CO}_{10}]$  was found impossible in the absence of Ru in the reaction medium even at high temperature, whereas  $[\text{Ru}(\text{COD})(\text{COT})]$  decomposes very fast in IL at room temperature (see Chapter 3). Previous literature examples show similar behavior for RuNi bimetallic NPs, where a faster reduction of Ni precursor was facilitated by Ru due to hydrogen spillover [17,18].

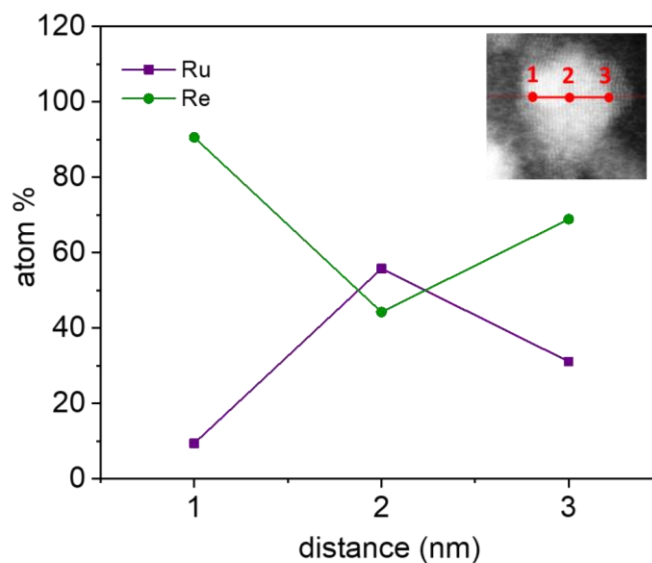


**Figure 5.13** Mapping of metal atom% along an individual NP in RuRe/MEM.

In comparison to previous work done with RuRe NPs (**Table 5.1**), the quantity of Re metal in the bimetallic RuRe NPs increased in the order  $\text{RuRe/H} < \text{RuRe/PVP} \sim \text{RuRe/HDA}$  [14]  $<$   $\text{RuRe/MEM}$ , thus suggesting a coordination effect of the stabilizers in terms of kinetics of precursor decomposition, formation of intermediate species or growth of RuRe NPs. The average

size of the RuRe NPs synthesized in the IL was found to be in the order RuRe/PVP < RuRe/H < RuRe/HAD < RuRe/MEM. Further experiments using other stabilizers such as the CN or MME ILs or other commercially available ILs could provide more information on the influence of the IL on these different possible scenarios.

**Table 5.1** Comparison of synthesized RuRe/ILs with RuRe/PVP and RuRe/HAD.

System	Average NP size (nm)	EDX composition (atom %)		Ref.
		Re	Ru	
RuRe/H	$1.6 \pm 0.2$	12	88	This work
RuRe/MEM	$3.3 \pm 0.4$	34	66	This work
Ru/H	$2.0 \pm 0.2$	-	100	This work
Ru/MEM	$2.1 \pm 0.2$	-	100	This work
RuRe/PVP	$1.5 \pm 0.4$	18	82	[14]
RuRe/HDA	$2.2 \pm 0.3$	20	80	[14]
Ru/PVP	$2.3 \pm 0.4$	-	100	[14]
Ru/HAD	-	-	-	[14]

The synthesis of RuRe NPs was also performed at 190 °C in an autoclave maintaining the other synthesis parameters the same with the aim to increase the incorporation of Re in the bimetallic NPs. TEM images obtained for RuRe/H and RuRe/MEM are displayed in **Figure 5.14**. A slightly lower mean size of  $1.4 \pm 0.2$  nm was measured for RuRe/H (**Figure 5.14 a**), to the one observed for the synthesis of the same system performed at 150 °C ( $1.6 \pm 0.2$  nm). In the case of RuRe/MEM (**Figure 5.14 b**), the size decreased significantly from  $3.3 \pm 0.4$  nm at 150 °C to  $1.5 \pm 0.2$  nm at 190 °C, thus indicating that in the case of MEM increased temperature favored the formation of significantly smaller RuRe NPs. This could be explained by a faster decomposition of the precursors or derivatives at higher temperature. However, since the effect of temperature was less important in the case of H IL, an effect of the MEM is also possible. Further analyses are ongoing to elucidate the effect of the temperature and/or IL on the structure and composition of the RuRe NPs.

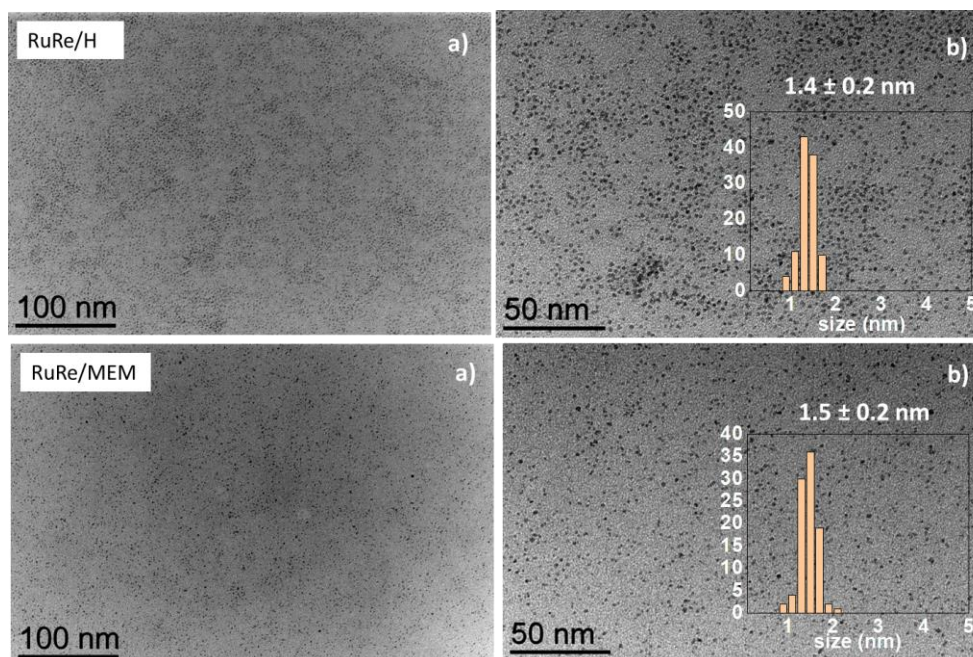


**Figure 5.14** a) TEM images and b) the corresponding size distributions of synthesized RuRe/ILs NPs (190 °C, 3 bar H<sub>2</sub>, anisole) (scale bar = 100,50 nm).

#### b) TG analyses

TG analyses of the RuRe/ILs were performed under N<sub>2</sub> and their stability compared with that of the respective ILs (**Figure 5.15**). The analyses showed similar results as the Ru/FILs (Chapter 3), namely that the decomposition temperature ( $T_{\text{dec}}$ ) of the ILs with RuRe NPs were lower than that of the pure ILs. The trend of the difference in decomposition temperature ( $\Delta T_{\text{dec}}$ ) of the ILs in the presence or the absence of NPs was also similar to the Ru/FILs systems where it was highest for H, thus suggesting a stronger interaction with the IL in this case.

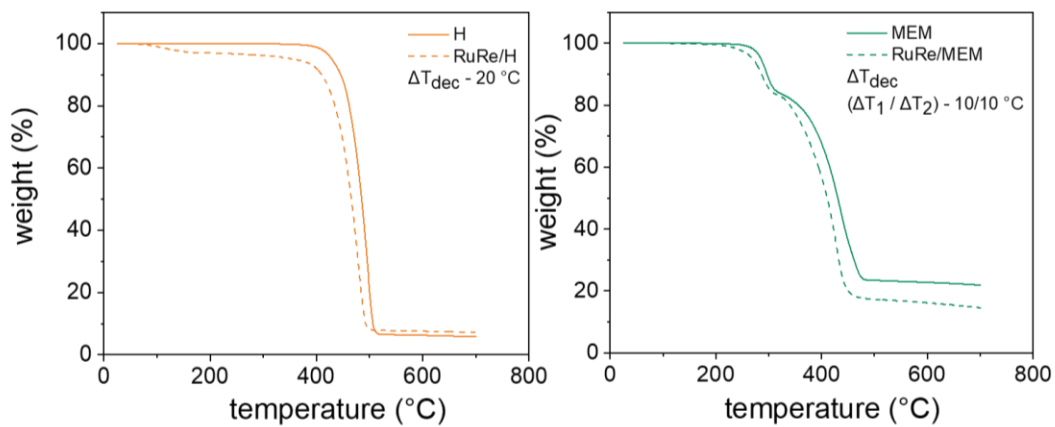


**Figure 5.15** TG profiles of the ILs (solid lines) and corresponding RuRe/ILs (dotted lines).



## c) XPS analysis

XPS analyses were also performed on the RuRe/ILs and the corresponding survey spectra for H and MEM are given in **Figure 5.16**. The deconvoluted high-resolution scan spectra of the different elements (C 1s, N 1s, F 1s, S 2p, O 1s) are compiled in Appendix E.

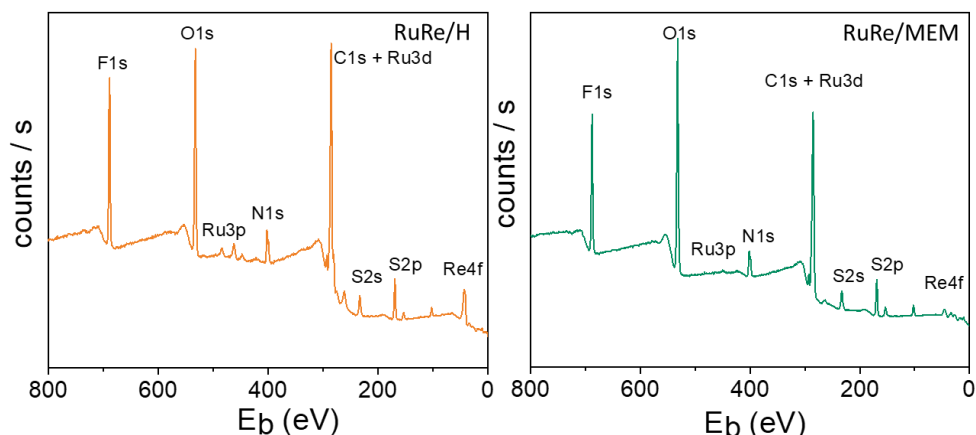


**Figure 5.16** XPS survey spectra of RuRe/ILs.

A shift in some binding energies was observed in the presence of RuRe NPs ( $E_{\text{RuReIL}}$ ) with respect to the pure ILs, as represented by  $\Delta E$  for the different elements (**Table 5.2**). For H the  $\Delta E_{\text{C}1\text{s}}$  was more pronounced compared to the  $[\text{NTf}_2]^-$  anion, which was similar to the trend observed in Ru and Ni NPs in H (Chapters 3 and 4, respectively). In the case of MEM, the  $\Delta E_{\text{O}1\text{s}}$  was more pronounced compared to the other elements, which may be due to interaction between RuRe NPs and the oxygen atoms from the imidazolium cation.

**Table 5.2** Difference in binding energies (eV) of the chemical states of selected elements in the ILs and RuRe/ILs.

IL	$\Delta E$ cation (eV)				$\Delta E$ anion (eV)					
	C <sub>2</sub> 1s	C <sub>3</sub> 1s	C <sub>4</sub> 1s	N 1s	C <sub>5</sub> 1s	N 1s	F 1s	O 1s	S 2p <sub>3/2</sub>	S 2p <sub>1/2</sub>
H	0.11	0.12	-0.02	0.07	-0.01	0.00	0.06	-0.08	0.02	0.03
MEM	0.03	0.04	0.36	-0.06	-0.07	-0.06	-0.03	0.19*	-0.05	-0.10

\* $\Delta E$  cation and anion.

The high-resolution scan spectra of Ru 3p<sub>3/2</sub> and Re 4f<sub>7/2</sub> are presented in **Figure 5.17** for RuRe/H and **Figure 5.18** for RuRe/MEM. The metallic Ru(0) (460.6 eV for RuRe/H, 460.7 eV for

RuRe/MEM) and oxidized species  $\text{Ru}^{\text{IV}}\text{O}_2$ , hydrous  $\text{Ru}^{\text{IV}}\text{O}_2$ , and  $\text{Ru}^{\text{III}}\text{O}_3$  (likely formed during sample handling in air) with distinct bonding energies were identified. The analysis of the Re 4f spectrum is difficult due to the presence of at least six distinct oxidation states of Re each with peak positions falling within a narrow binding energy range of approximately 5-6 eV, and some of them being separated by as little as 0.2 eV [19]. Additionally, the Re 4f<sub>7/2</sub> peak of a high oxidation state may overlap with the Re 4f<sub>5/2</sub> peak of a low oxidation state, thus leading to complex and heavily intertwined XPS spectra. The oxides of Re include  $\text{Re}^{\text{IV}}\text{O}_2$ ,  $\text{Re}^{\text{VI}}\text{O}_3$ ,  $\text{Re}_2^{\text{VII}}\text{O}_7$ . The presence of  $\text{Re}^{5+}$  has also been reported in rhenium oxides alloyed with cationic elements [19]. Both the RuRe/IL systems presented Re(0) (at 40.8 eV for both systems) and also contained Re with different oxidation states (likely formed during sample handling in air).

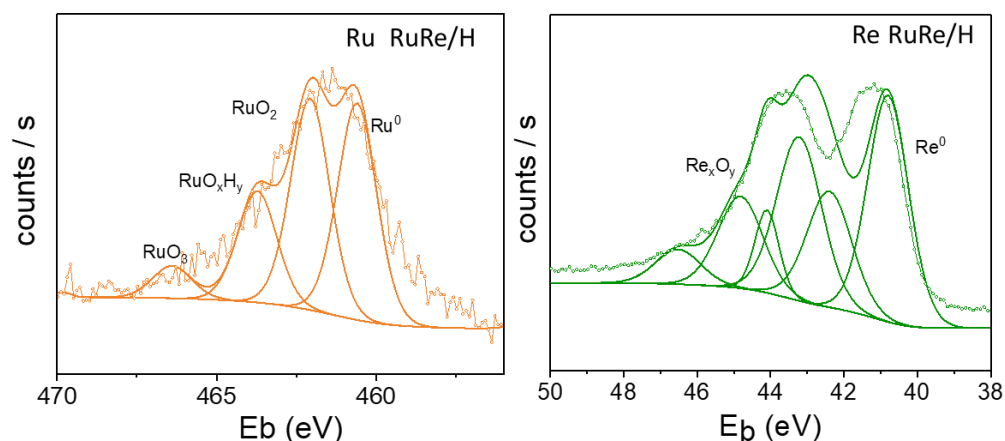


**Figure 5.17** High-resolution XPS spectra of Ru 3p and Re 4f for the RuRe/H NPs system.

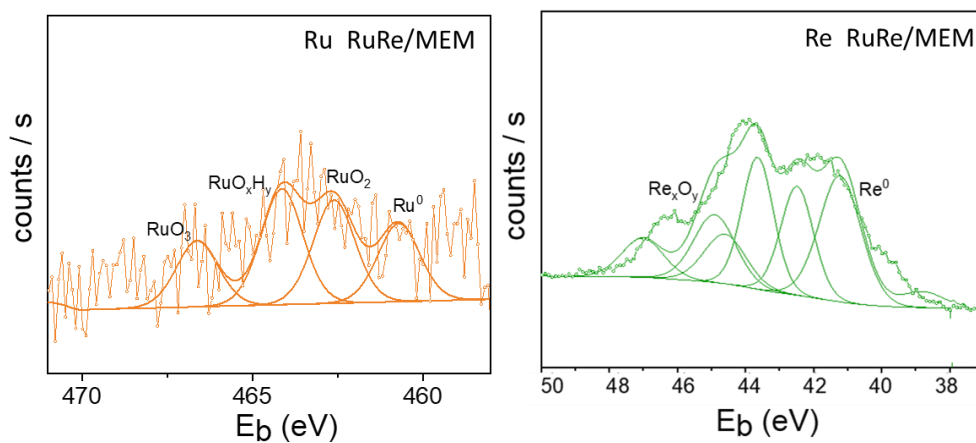


**Figure 5.18** High-resolution XPS spectra of Ru 3p and Re 4f for the RuRe/MEM NPs system.

## 5.4 Summary

Novel RuRe-containing NPs have been synthesized, using a non-functionalized IL (H) and a methoxy-functionalized one (MEM), and characterized. TEM images show well-dispersed NPs in both H and MEM ILs. Despite the Re precursor,  $[\text{Re}_2\text{CO}_{10}]$ , requires higher decomposition temperature than  $[\text{Ru}(\text{COD}(\text{COT}))]$ , EDX analysis revealed the formation of bimetallic RuRe NPs with a Re content of ca. 18% in RuRe/H and ca. 34% in RuRe/MEM. Comparing to previous work done at LCC [14], the incorporation of Re metal in the RuRe bimetallic NPs increased in the order: RuRe/H < RuRe/PVP ~ RuRe/HDA < RuRe/MEM. Owing to a incomplete decomposition of  $[\text{Re}_2(\text{CO})_{10}]$  under the applied conditions, and the difficulty to separate soluble Re species from the formed RuRe NPs, the alternative Re precursor tetraallyldirhenium(II),  $[\text{Re}_2(\text{C}_3\text{H}_5)_4]$ , is considered for future studies. If successful, the bimetallic RuRe NPs will be supported on silica to obtain SILP systems for their investigation as catalysts for the hydrogenation of amides.

## 5.5 References

1. Yoshino, K.; Kajiwarra, Y.; Takaishi, N.; Inamoto, Y.; Tsuji, J. Hydrogenation of Carboxylic Acids by Rhenium-Osmium Bimetallic Catalyst. *J. Am. Oil Chem. Soc.* **1990**, *67*, 21–24, doi:10.1007/BF02631383.
2. Pallassana, V.; Neurock, M. Electronic Factors Governing Ethylene Hydrogenation and Dehydrogenation Activity of Pseudomorphic PdML/Re(0001), PdML/Ru(0001), Pd(111), and PdML/Au(111) Surfaces. *J. Catal.* **2000**, *191*, 301–317, doi:10.1006/jcat.1999.2724.
3. Das, T.K.; Jacobs, G.; Patterson, P.M.; Conner, W.A.; Li, J.; Davis, B.H. Fischer–Tropsch Synthesis: Characterization and Catalytic Properties of Rhenium Promoted Cobalt Alumina Catalysts☆. *Fuel* **2003**, *82*, 805–815, doi:10.1016/S0016-2361(02)00361-7.
4. Gothe, M.L.; Silva, K.L.C.; Figueredo, A.L.; Fiorio, J.L.; Rozendo, J.; Manduca, B.; Simizu, V.; Freire, R.S.; Garcia, M.A.S.; Vidinha, P. Rhenium – A Tuneable Player in Tailored Hydrogenation Catalysis. *Eur. J. Inorg. Chem.* **2021**, *2021*, 4043–4065, doi:10.1002/EJIC.202100459.
5. Ma, L.; He, D.; Li, Z. Promoting Effect of Rhenium on Catalytic Performance of Ru Catalysts in Hydrogenolysis of Glycerol to Propanediol. *Catal. Commun.* **2008**, *9*, 2489–2495, doi:10.1016/j.catcom.2008.07.009.
6. Baranowska, K.; Okal, J.; Tylus, W. Microwave-Assisted Polyol Synthesis of Bimetallic RuRe Nanoparticles Stabilized by PVP or Oxide Supports ( $\gamma$ -Alumina and Silica). *Appl. Catal. A Gen.* **2016**, *511*, 117–130, doi:10.1016/j.apcata.2015.11.045.
7. Baranowska, K.; Okal, J.; Miniajluk, N. Effect of Rhenium on Ruthenium Dispersion in the Ru–Re/ $\gamma$ -Al<sub>2</sub>O<sub>3</sub> Catalysts. *Catal Letters* **2014**, *144*, 447–459, doi:10.1007/s10562-013-1169-1.
8. Ayvalı, T.; Fazzini, P.-F.; Lecante, P.; Mayoral, A.; Philippot, K.; Chaudret, B. Control of Reactivity through Chemical Order in Very Small RuRe Nanoparticles. *Dalton Trans.* **2017**, *46*, 15070–15079, doi:10.1039/C7DT02287E.

9. Beamson, G.; Papworth, A.J.; Philipps, C.; Smith, A.M.; Whyman, R. Selective Hydrogenation of Amides Using Bimetallic Ru/Re and Rh/Re Catalysts. *J. Catal.* **2011**, *278*, 228–238, doi:10.1016/j.jcat.2010.12.009.
10. Cabrero-Antonino, J.R.; Adam, R.; Papa, V.; Beller, M. Homogeneous and Heterogeneous Catalytic Reduction of Amides and Related Compounds Using Molecular Hydrogen. *Nat. Commun.* **2020**, *11*, 3893, doi:10.1038/s41467-020-17588-5.
11. Gelfond, N. V.; Morozova, N.B.; Zherikova, K. V.; Semyannikov, P.P.; Trubin, S. V.; Sysoev, S. V.; Igumenov, I.K. Investigation of Thermal Properties of the Volatile Carbonyl Compounds of Rhenium  $\text{Re}_2(\text{CO})_{10}$  and  $\text{Re}(\text{CO})_3(\text{C}_5\text{H}_5)$ . *J. Chem. Thermodyn.* **2011**, *43*, 1646–1651, doi:10.1016/J.JCT.2011.05.024.
12. Ma, L.; He, D. Hydrogenolysis of Glycerol to Propanediols Over Highly Active Ru–Re Bimetallic Catalysts. *Top Catal.* **2009**, *52*, 834–844, doi:10.1007/s11244-009-9231-3.
13. Ayvalı, T.; Lecante, P.; Fazzini, P.-F.; Gillet, A.; Philippot, K.; Chaudret, B. Facile Synthesis of Ultra-Small Rhenium Nanoparticles. *Chem. Commun.* **2014**, *50*, 10809–10811, doi:10.1039/C4CC04816D.
14. Ruthenium Rhenium. Ayvalı, T. *Rhenium Based Mono- and Bi-metallic Nanoparticles: Synthesis, Characterization and Application in Catalysis (2015)* [Doctoral, University Toulouse 3 Paul Sabatier].
15. Kaesz, H.D.; Knox, S.A.R.; Koepke, J.W.; Saillant, R.B. Synthesis of Metal Carbonyl Hydrides from Metal Carbonyls and Hydrogen at Atmospheric Pressure. *Journal of the Chemical Society D: Chem. Commun.* **1971**, 477, doi:10.1039/c29710000477.
16. Masciocchi, N.; Sironi, A.; D'Alfonso, G. Structural Characterization of the Three Rhenium Complexes  $[\text{HRe}(\text{CO})_4]_n$  ( $n = 2, 3, 4$ ), Including a Rare Example of a Square Arrangement of Metal Atoms. *J. Am. Chem. Soc.* **1990**, *112*, 9395–9397, doi:10.1021/ja00181a053.
17. Tada, S.; Kikuchi, R.; Wada, K.; Osada, K.; Akiyama, K.; Satokawa, S.; Kawashima, Y. Long-Term Durability of Ni/TiO<sub>2</sub> and Ru–Ni/TiO<sub>2</sub> Catalysts for Selective CO Methanation. *J. Power Sources* **2014**, *264*, 59–66, doi:10.1016/j.jpowsour.2014.04.075.
18. Valdés-Martínez, O.U.; Suárez-Toriello, V.A.; Reyes, J.A. de los; Pawelec, B.; Fierro, J.L.G. Support Effect and Metals Interactions for NiRu/Al<sub>2</sub>O<sub>3</sub>, TiO<sub>2</sub> and ZrO<sub>2</sub> Catalysts in the Hydrodeoxygenation of Phenol. *Catal. Today* **2017**, *296*, 219–227, doi:10.1016/j.cattod.2017.04.007.
19. Greiner, M.T.; Rocha, T.C.R.; Johnson, B.; Klyushin, A.; Knop-Gericke, A.; Schlögl, R. The Oxidation of Rhenium and Identification of Rhenium Oxides during Catalytic Partial Oxidation of Ethylene: An in-Situ Xps Study. *Zeitschrift für Physikalische Chemie* **2014**, *228*, 521–541, doi:10.1515/ZPCH-2014-0002.

## 6. General conclusion and perspectives

This PhD thesis is centered on the use of different ionic liquids (ILs) for the synthesis of ruthenium (Ru), nickel (Ni) and bimetallic ruthenium-rhenium (RuRe) transition metal nanoparticles (NPs) and their application in hydrogenation catalysis.

The work started by the synthesis and full characterization of one non-functionalized- (H) and three functionalized imidazolium bis(trifluoromethylsulfonyl)imide ionic liquids (FILs), namely, MEM, MME, and CN. These three FILs contain methoxy and nitrile functional groups, respectively, making them to potentially interact with the surface of metal NPs. All ILs were obtained in good yields (>90%) and a complete characterization, including IR, TG, DSC, NMR, XPS and SAXS analyses, was performed for all synthesized ILs. No water impurities were observed through NMR analysis, qualitatively stating that if present, water were present only in negligible amounts. IR analysis clearly showed the bands of the  $[\text{NTf}_2]^-$  anion of the ILs at 1050, 1180, 1346  $\text{cm}^{-1}$  assigned to the stretching frequencies of SN,  $\text{CF}_3$ ,  $\text{SO}_2$ , respectively. Clear bands were also detected at 1099 and 1098  $\text{cm}^{-1}$ , corresponding to the C-O stretching in MEM and MME FILs, respectively, while CN stretching of the CN FIL was found at 2248  $\text{cm}^{-1}$ . The thermal stability of the four synthesized ILs was found to be >200°C.

The next step of the PhD work focused on the synthesis, characterization, and application of IL-immobilized Ru NPs in hydrogenation catalysis using the series of ILs previously synthesized. The methoxy-functionalized systems, Ru/MEM and Ru/MME were novel systems, while the Ru/H and Ru/CN were previously described in literature and here prepared as references for comparison purpose. The synthesis of the Ru NPs was performed by following the organometallic approach involving decomposition of  $(\eta^4\text{-1,5-cyclooctadiene})(\eta^6\text{-1,3,5-cyclooctatriene})\text{ruthenium}(0)$  complex,  $[\text{Ru}(\text{COD})(\text{COT})]$ , as the source of Ru under mild condition (25°C, 3 bar  $\text{H}_2$ , 22 h). TEM analysis evidenced the formation of small and well-dispersed Ru NPs in all cases, displaying a size range of 1.5-2.2 nm and narrow size-distributions. XPS analysis confirmed the Ru(0) metallic state in all Ru NP systems and also enabled studying the interaction between the ILs and NPs. In the case of MEM, MME and CN systems, a noticeable shift in the binding energies ( $E_b$ ) was observed in the presence of Ru NPs with respect to the pure IL, clearly indicating interaction between the ILs and Ru NPs. For all the ILs, a difference in  $\text{BE}_{\text{C}1s}$  of  $\text{C}_4$  (imidazolium carbon with

acidic proton) was positive suggesting that carbene formation during Ru NPs synthesis was negligible and that the interaction of the IL and the Ru NPs was through the functional groups. All the Ru NPs/ILs systems were found efficient catalysts for the hydrogenation of styrene under mild reaction conditions (30°C, 5 bar of H<sub>2</sub>), providing full conversion of styrene with complete selectivity towards ethylbenzene in short reaction times. Notably, the excellent catalytic performance was obtained at milder reaction conditions than previously reported in literature. Also, by selectively catalyzing the hydrogenation of the vinyl group and not the aromatic ring under the applied reaction conditions, these Ru/ILs NPs display a reactivity different than typically reported for Ru NPs. Interestingly, a clear difference in activity (TOFs) was noticed as a function of the nature of the IL, following the order Ru/H (1,332 h<sup>-1</sup>) > Ru/MEM (629 h<sup>-1</sup>) > Ru/MME (212 h<sup>-1</sup>) >> Ru/CN (10 h<sup>-1</sup>). This order of reactivity was correlated to the influence of the IL nature on the catalytic properties of the Ru NP catalysts, as supported by XPS data about IL-Ru NP interaction. Finally, recycling study of the Ru/ILs NPs systems in five catalytic runs evidenced that the FIL-stabilized catalysts were more stable than the non-functionalized Ru/H catalyst system, where Ru leaching likely occurred due to higher solubility of the Ru/H NPs in the workup solvent of the reaction mixture between catalytic runs. All in all, the results obtained in the catalytic hydrogenation of styrene show that the functionalization of IL had a positive influence on the performance and stability of the catalysts, thus proving that rational design of Ru/FIL NPs may allow to reach good catalytic performances.

The third objective was the synthesis of Ni NPs in the same ILs as used for preparing the Ru/IL NPs systems. The NPs were prepared by the decomposition of bis-( $\eta^4$ -1,5-cyclooctadiene)nickel complex, [Ni(COD)<sub>2</sub>] in the absence hydrogen as the IL assisted the decomposition at 80 °C. TEM analysis indicated an average size of the synthesized Ni NPs to be between 2.8 and 6.9 nm. Well-dispersed NPs were formed in H, MEM and CN, whereas agglomerates of small NPs were formed in MME. The size of Ni NPs were found to be larger compared to the Ru NPs. Small Ni NPs were prepared using CN (2.8 nm), compared to the previous literature (7-8 nm). Unlike all the Ru/FILs system, XPS analysis showed a change of the BE<sub>C1s</sub> of C<sub>4</sub> to a lower value (*i.e.*, negative  $\Delta E$ ) for all ILs in the presence of Ni NPs. This was attributed to the formation of a nucleophilic species, *e.g.* *N*-heterocyclic carbene derived from the imidazolium cation as the result of deprotonation. However, there may exist a competition for the stabilization of the NPs surface between the NHC

species and the functional groups present in the FILs. As the stabilization by the functional group, or the carbene, can depend on the coordination strength of the stabilizing group at the Ni surface, the competition can have an influence on the size of the Ni NPs and could explain the difference in size observed in the Ni/FIL series (2.8-6.9 nm). All the Ni/ILs systems were found to be efficient catalysts for the hydrogenation of 2-cyclohex-1-ene under quite mild conditions (substrate/Ni ratio of 100/1, 130°C, 10 bar of H<sub>2</sub>), providing full conversion of 2-cyclohex-1-ene with complete selectivity towards hydrogenation of the olefinic bond in short reaction time (1 h). Compared to previous work using Ni NPs synthesized in amine-functionalized ILs (substrate/Ni of 50/1, 90°C, 10 bar of H<sub>2</sub>, 4 h, water solvent-isolated NPs redispersed in water), the work here allows using much less Ni metal, but a slightly higher temperature, to provide full substrate conversion in much shorter time under neat conditions. Remarkably, an exposure of the Ni/FILs systems to air for 24 h did not seem to affect the catalytic activity of the Ni NPs drastically. This showed that the developed Ni/FILs catalysts are quite stable in air, which may be of interest for their handling and implementation in catalysis. XPS analysis conducted on the 24 h-air exposed systems proved the existence of a remaining metallic Ni core and a NiO passivation layer, that probably protects the surface of the NPs. Recyclability of the Ni-NiO/MEM catalyst in 2-cyclohex-1-ene hydrogenation was tested. A 18% decrease in conversion was observed after the second catalytic run maintaining the selectivity. However, the activity remained reasonably constant for the subsequent seven runs (runs 3 to 8). The drop in conversion could be due to further oxidation of the spent catalyst upon washing it with pentane in air after the first run. To examine this hypothesis, the recovered catalyst after the eighth run was treated under 20 bar H<sub>2</sub> at 120°C for 24 h before implementation in another catalytic run without exposure to air. Such treatment provided almost initial activity with an increase of conversion by 20%. This result suggested reactivation of the Ni surface by H<sub>2</sub> reduction of the NiO. However, the activity was found to decrease significantly when the Ni/FILs systems were exposed to air for 20 days, as the result of the formation of Ni(OH)<sub>2</sub> species as detected by XPS. Finally, the Ni/FILs catalysts were tested in the hydrogenation of other substrates, including cinnamyl alcohol, 2,3-benzofuran, trans-2-hexen-1-ol, hexanal, benzonitrile, benzylamine, phenylacetylene and (R)-(+)-limonene.

.

Another objective of the work was the synthesis of bimetallic RuRe NPs in H and MEM at 3 bar H<sub>2</sub>, 120 °C, 2 days and anisole as solvents. The average sizes of the NPs were found by TEM analysis to be 1.6 and 3.3 nm for H and MEM, respectively. Despite insufficient decomposition of the used Re precursor, [Re<sub>2</sub>CO<sub>10</sub>], HRTEM and EDX analysis of the NPs revealed the presence of ~34% Re in the NPs in RuRe/MEM. Compared to previous work within the group that used the same Ru and Re precursors, but a polymer (PVP, polyvinylpyrrolidone) and an amine (HAD, hexadecylamine) as stabilizers, the quantity of Re metal in the RuRe bimetallic NPs increased in the order: RuRe/H < RuRe/PVP ~ RuRe/HAD < RuRe/MEM. Despite numerous attempts to achieve the complete decomposition of [Re<sub>2</sub>(CO)<sub>10</sub>] and separate the unreacted [Re<sub>2</sub>(CO)<sub>10</sub>] from the NPs through purification, this proved to be unattainable. Due to these challenges the organometallic rhenium precursor, [Re<sub>2</sub>(C<sub>3</sub>H<sub>5</sub>)<sub>4</sub>], was considered for future studies.

During the three months internship at IFPEN, Lyon (France), the synthesized Ru/ILs and Ni/ILs were screened for catalytic hydrogenation of selected amides (cyclohexanecarboxamide, *N,N*-dimethylbenzenamide and butyramide). Despite using relatively harsh reaction conditions (up to 190°C and 50-60 bar of H<sub>2</sub>), the MNPs/IL systems were not found active in the catalytic hydrogenation of the amides. Note that only a few catalytic systems are reported in the literature for the hydrogenation of amides, which is a very challenging reaction due to the high stability of amides.

The results reported in this doctoral thesis open interesting perspectives for future research:

- 1) Ru/FILs systems were found to be highly active and selective to ethylbenzene in the hydrogenation of styrene. These catalysts may be employed in the selective hydrogenation of other substrates than vinylic substrates, such as other olefinic or alkyne compounds,  $\alpha,\beta$ -unsaturated carbonyl compounds, nitriles, or even CO<sub>2</sub>. Initial studies on employing the Ru/MEM system in the hydrogenation of 2,3-benzofuran (substrate/Ru ratio 1000/1, 120°C, 10 bar of H<sub>2</sub>, 1,4-dioxane solvent) showed promising results of 20% conversion and >99% selectivity towards 2,3-dihydrobenzofuran.
- 2) The substrate screening of Ni-NiO/MEM showed potential scopes for the application of all the Ni/FILs systems for various hydrogenation reactions, thus opening avenues for their implementation in catalysis.



- 3) The RuRe/IL bimetallic system would merit to be studied deeper in the hydrogenation of amides. Change in the synthesis protocol, for example by using the organometallic precursor  $[\text{Re}_2(\text{C}_3\text{H}_5)_4]$  instead of  $[\text{Re}_2\text{CO}_{10}]$  for the synthesis of the RuRe NPs could help to achieve an active catalyst. Catalytic application of the RuRe/IL system for the hydrogenation of other substrates than amides, for example as those mentioned above, is another perspective.
- 4) All the metal NP/ILs systems developed can be immobilized onto a support like silica *via* a simple impregnation process to obtain the corresponding SILP systems with a highly accessible IL film layer. This is a convenient approach to generate materials with improved surface reactivity that facilitate a large number of reactant molecules to simultaneously reacts, thus leading to enhanced reaction rates and efficiencies when applied in catalysis.

## 7. Materials and characterization methods

### 7.1 Materials

All operations for the synthesis of metal NPs and the preparation of the catalytic reactions were performed under inert atmosphere (argon) avoid the passivation and/or oxidation of the metallic surface using standard Schlenk techniques or in a glovebox (MBraun). Pentane, acetonitrile, acetone, dichloromethane (DCM) and diethylether were purified by standard methods or using a MBraun SPS-800 solvent purification system, and further degassed using the freeze-pump thaw method or argon bubbling. 1-Methylimidazole (99%, Sigma Aldrich), 1-chlorohexane (>99%, Sigma Aldrich), 1-bromo-2-methoxymethoxy ethane (98%, Sigma Aldrich), 2-methoxyethoxy methyl chloride (99%, Sigma Aldrich), 5-chlorovaleronitrile (98%, Sigma Alrich), lithium bis(trifluoromethylsulfonyl)imide (Li[NTf<sub>2</sub>]; >99%, Chemodex) were used as received.

Styrene (98%, Sigma Aldrich), ethylbenzene (98%, Sigma Aldrich), octane (>99%, Sigma Aldrich) were purified by filtration on an Al<sub>2</sub>O<sub>3</sub> column, then degassed and dried before use. Trans-cinnamaldehyde (97%, Sigma Aldrich), cinnamyl alcohol (98%, Sigma Aldrich), hydrocinnamaldehyde (90%, Sigma Aldrich), 2-cyclohexen-1-one (>95%, Sigma Aldrich), cyclohexanone (≥99%, Sigma Aldrich), 2,3-benzofuran (99%, Sigma Aldrich), 2,3-dihydrobenzofuran (99%, Sigma Aldrich), trans-2-hexen-1-al (98%, Sigma Aldrich), hexanal (98%, Sigma Aldrich), benzonitrile (≥99%, Sigma Aldrich), benzylamine (≥99%, Sigma Aldrich), phenylacetylene (98%, Sigma Aldrich), (R)-(+)-limonene (97%, Sigma Aldrich). The Ru, Ni precursors, [Ru(COD)(COT)] and [Ni(COD)<sub>2</sub>] complex was purchased from Nanomeps, Toulouse, France. The Re precursor [Re<sub>2</sub>(CO)<sub>10</sub>] was purchased from Sigma Aldrich (98%). H<sub>2</sub> (99.999%) and Ar (99.99%) were purchased from Air Liquid, Denmark.

### 7.2 Characterization methods

Liquid nuclear magnetic resonance (NMR) spectroscopy (<sup>1</sup>H, <sup>13</sup>C{<sup>1</sup>H}, <sup>19</sup>F, <sup>13</sup>C dept-135) was performed on a Bruker Avance 300 instrument or a Bruker Avance 400 instrument using CDCl<sub>3</sub> or DMSO-d<sub>6</sub> as solvents.

Attenuated total reflection infrared (ATR-IR) spectra were recorded in the range 4000-400 cm<sup>-1</sup> under inert conditions on a Perkin-Elmer GX2000 spectrometer installed inside a glovebox.

Metal content was determined by inductively coupled plasma optical emission spectroscopy (ICP-OES) on mineralized samples using a mixture of HNO<sub>3</sub> and HCl acids with a Thermo Scientific ICAP 6300 instrument.

Transmission electron microscopy (TEM) and high-resolution transmission electron microscopy (HRTEM) analyses (Centre de microcaractérisation Raimond Castaing, CNRS-UAR 3623, Toulouse) was performed on a JEOL JEM 1011 CXT electron microscope operating at 100 kV with a point resolution of 4.5 Å or a JEOL JEM 1400 operating at 120 kV with a point resolution of 2.0 Å, and on a JEOL JEM 2100F equipped with a field emission gun (FEG) operating at 200 kV with a point resolution of 2.3 Å and HAADF-STEM on a JEOL JEM-ARM200F Cold FEG operating at 200 kV with a point resolution of >1.9 Å, respectively. The TEM samples were prepared by diluting a few drops of each MNPs/IL mixture in acetonitrile and a drop of the solution casted on a carbon-coated copper grid. Size distributions and mean sizes of the NPs were determined by measurement of at least 200 individual NPs on a given grid using the software ImageJ.

Thermogravimetric analyses (TGA) were carried out on a Mettler Toledo TGA/DSC 3+ instrument under a N<sub>2</sub> flow. Samples were placed into an alumina crucible and then heated from 25 to 800 °C at a heating rate of 10 °C/min. DSC analyses were conducted from -120 to 40 °C with a heating rate of 10 °C/min after depositing the samples in a sealed aluminum pan and using a Netzsch DSC 3500 Sirius instrument.

X-ray photoelectron spectroscopy (XPS) analyses were performed using a Thermo Scientific system at room temperature using AlK $\alpha$  radiation (1484.6 eV) and a spot size of 400  $\mu$ m. A flood gun was used to reduce sample charging effects and the obtained spectra were further corrected by setting the C 1s binding energy at 284.8 eV. Each survey scan was performed six times, MNPs scans either 35 (H sample) or 150 (other ILs) times and all other elements scanned ten times. The software's automatic survey ID function was used to obtain the atomic surface concentrations from survey scans. "Smart" backgrounds were applied to all spectra except for the metals, for which the "Shirley" method was used. Background-corrected spectra were deconvoluted using Lorentzian/Gaussian (30/70%) curves for identification and quantification of chemical species. Data processing was done using the Avantage 4.87 software.

Electrospray ionization mass spectrometry (ESI-MS) analyses were performed using a DSQ II Mass Spectrometer (Thermo Fisher Scientific) equipped with electron impact (EI) and chemical ionization (INN NH<sub>3</sub>) sources analyses up to 1000 mass at low resolution under argon.

Elemental analyses (EA) were acquired on a Thermo Fischer Flash EA 1112 analyzer (Department of Chemistry, University of Copenhagen). The water content in solvents and ILs was determined with a Karl Fisher Coulometer (Metrohm) (target value for use of solvents <5 ppm).

Small Angle X-ray spectroscopy (SAXS) analysis was performed in collaboration with Prof. John Slattery and Dr. Naomi Elstone FROM University of York using a Bruker D8 Discover diffractometer equipped with a bespoke temperature-controlled, bored-graphite rod furnace (). The radiation used was Cu K $\alpha$  ( $\lambda = 0.154056$  nm), generated from a 1 mS microfocus source. Diffraction patterns were recorded on a 2048  $\times$  2048-pixel Bruker VANTEC 500 area detector set at 121 mm from the sample (Naomi *et al.*, *J. Phys. Chem. B*, **2023**, *127*, 7394–7407).

Quantitative analysis on the mixtures from the catalytic reactions was performed by a GC with flame-ionization detection (FID) using the internal standard method. Calibration curves were obtained with commercial reference products. At LCC, Toulouse, GC analyses were performed on a Shimadzu GC-2010 equipped with a Zebrom-zb-5ms capillary column (30 m  $\times$  0.25 mm  $\times$  0.25  $\mu$ m) using He as the carrier gas (He flow: 1.25 ml/min; injector temperature: 250 °C; detector (FID) temperature: 250 °C; oven program: 50 °C (hold 3 min) to 240 °C at 10 °C/min (hold 10 min) for a total run time of 30 min. Retention times: octane 2.6 min; ethylcyclohexane 3.1 min; styrene 9.4 min; ethylbenzene 7.1 min). At DTU, the analyses were performed on Agilent 6850-5975C using a HP-5MS capillary column (30.0 m  $\times$  250  $\mu$ m  $\times$  0.25  $\mu$ m) with He carrier gas (He flow: 1.25 ml/min; injector temperature: 250 °C; detector (FID) temperature: 250 °C; oven program: 50 °C (hold 3 min) to 240 °C at 10°C/min (hold 10 min) for a total run time of 30 min. Retention times: octane 4.1 min; ethylcyclohexane 4.6 min; ethylbenzene 5.1 min; styrene 5.5 min; trans-cinnamaldehyde 5.1 min; hydrocinnamaldehyde 9.9 min; 2-cyclohexen-1-one 6.2 mi; cyclohexanone 5.6 min; 2,3-benzofuran 7.2 min; 2,3-dihydrobenzofuran 8.5 min; trans-2-hexen-1-al 5.1 min; hexanal 7.3 min; benzonitrile 7.9 min; benzylamine 7.5 min; phenylacetylene 5.3 min; (R)-(+)-limonene 7.8; menthane 7.6 min).

## Appendix A

### A.1 List of publication

Krishnan, D.; Schill, L.; Axet, M.R.; Philippot, K.; Riisager, A. Ruthenium Nanoparticles Stabilized with Methoxy-Functionalized Ionic Liquids: Synthesis and Structure–Performance Relations in Styrene Hydrogenation. *Nanomaterials* **2023**, *13*, 1459.

<https://doi.org/10.3390/nano13091459>

### A.2 List of Conference attended

#### Oral presentations

1. CEHC-2 - Cutting-Edge Homogeneous Catalysis – 2022- International conference – Leipzig, Germany - Functionalized ionic liquid stabilized ruthenium nanoparticles as hydrogenation catalysts
2. Royal Society of Chemistry - Molten Salts and Ionic Liquids Discussion Group (RSC-MSILDG) - 2022, London, UK - Ru metal nanoparticles in functionalized ionic liquids for olefin hydrogenation. D. KRISHNAN, M. R. AXET, K. PHILIPPOT, A. RIISAGER
3. DTU Symposium, 2022, Copenhagen, Denmark - Olefin hydrogenation with Ru metal nanoparticles in functionalized ionic liquids. D. KRISHNAN, M. R. AXET, K. PHILIPPOT, A. RIISAGER

#### Poster presentations

1. CEHC-1 - Cutting-Edge Homogeneous Catalysis-Toulouse 2021, on-line International Workshop, - Synthesis of ionic liquid stabilized Ru nanoparticles for catalysis. D. KRISHNAN, M. R. AXET, K. PHILIPPOT, A. RIISAGER
2. DTU Symposium, 2021\_Denmark - Synthesis of hydrogenation catalysts with ruthenium nanoparticles in functionalized ionic liquids. D. KRISHNAN, M. R. AXET, K. PHILIPPOT, A. RIISAGER

3. IRN-HC3A\_4th HC3A Meeting, 2022, Barcelona - Ruthenium nanoparticles modified by functional ionic liquids as hydrogenation catalysts. D. KRISHNAN, M. R. AXET, K. PHILIPPOT, A. RIISAGER
  
4. ISI-HSHC International School, 2023, Bucharest - Synthesis of RuRe bimetallic nanoparticles in ionic liquids for catalysis. D. KRISHNAN, M. R. AXET, K. PHILIPPOT, A. RIISAGER

## Appendix B

### B.1 XPS Analysis

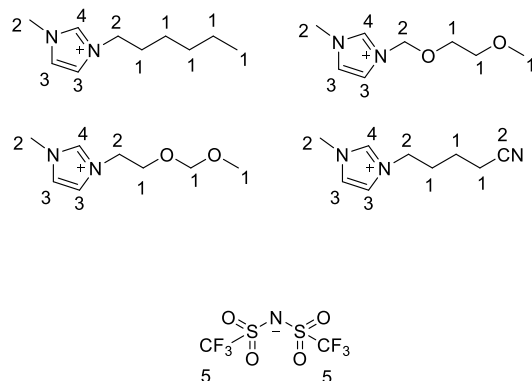


**Figure B.1** Chemical structures of the ILs with numbering of atoms.

#### 1. H

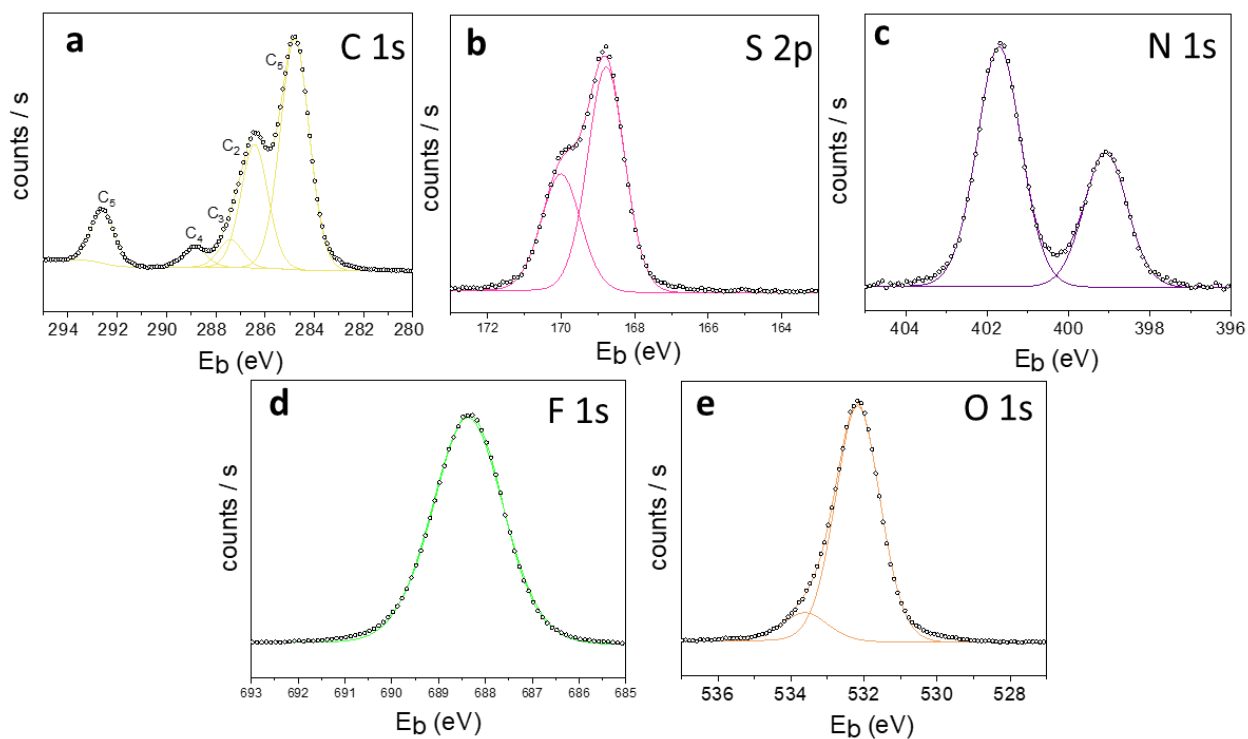


**Figure B.2** XPS high-resolution scan spectra of H a) C 1s, b) S 2p, c) N 1s, d) F 1s, and e) O 1s.

## 2. MEM

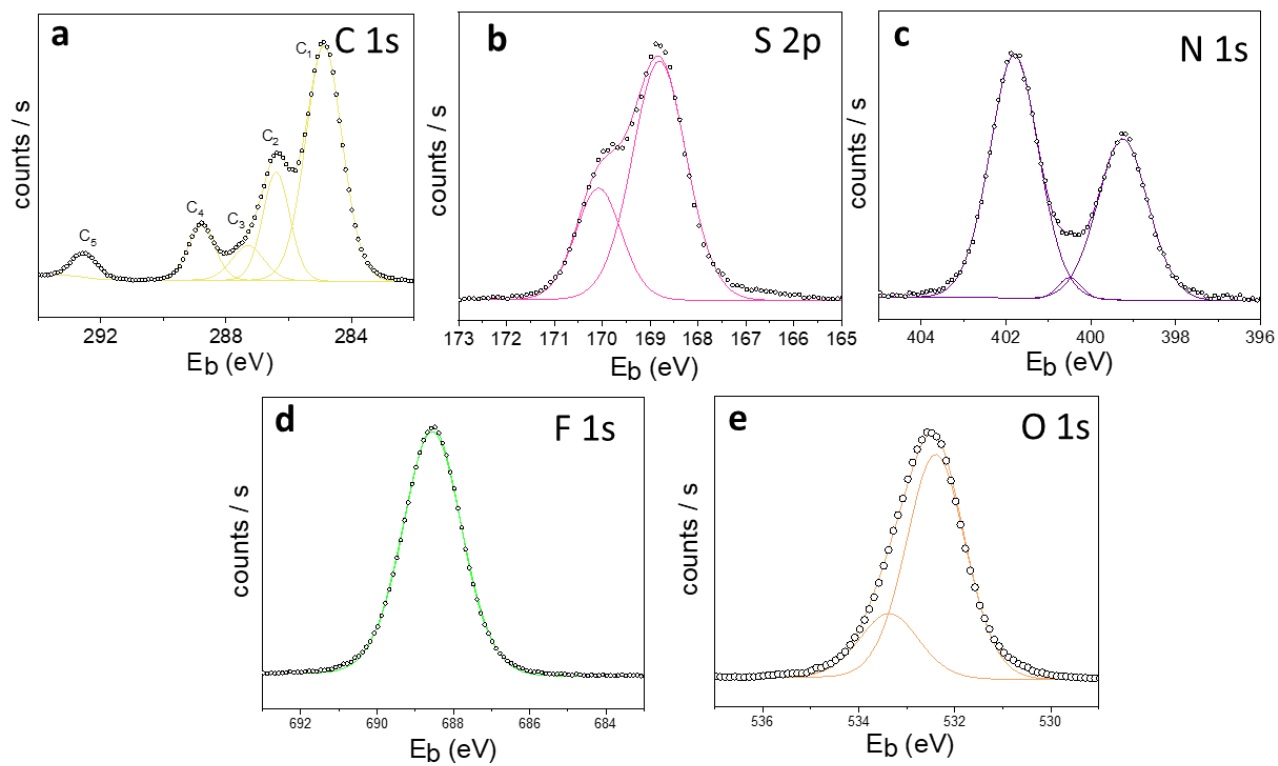


**Figure B.3** XPS high-resolution scan spectra of MEM a) C 1s, b) S 2p, c) N 1s, d) F 1s, and e) O 1s.



## 3. MME

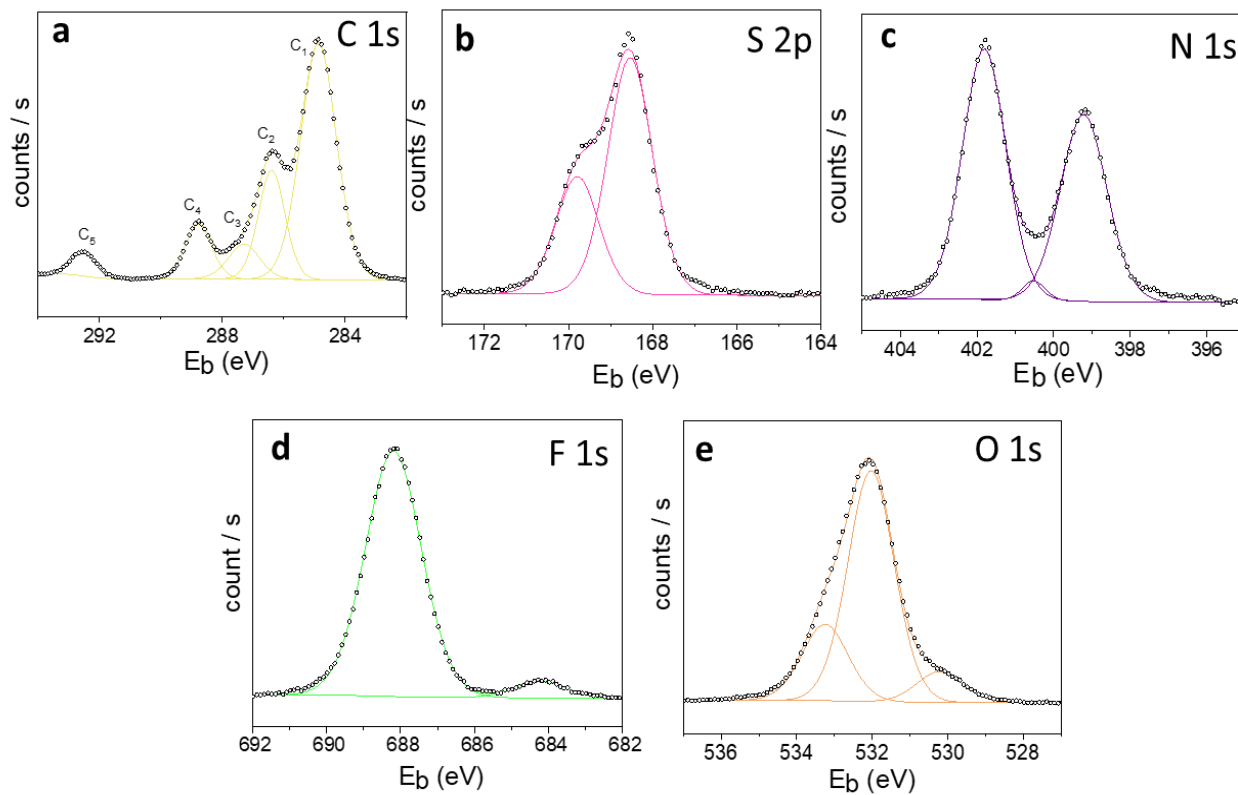


**Figure B.4** XPS high-resolution scan spectra of MME a) C 1s, b) S 2p, c) N 1s, d) F 1s, and e) O 1s.

## 4. CN

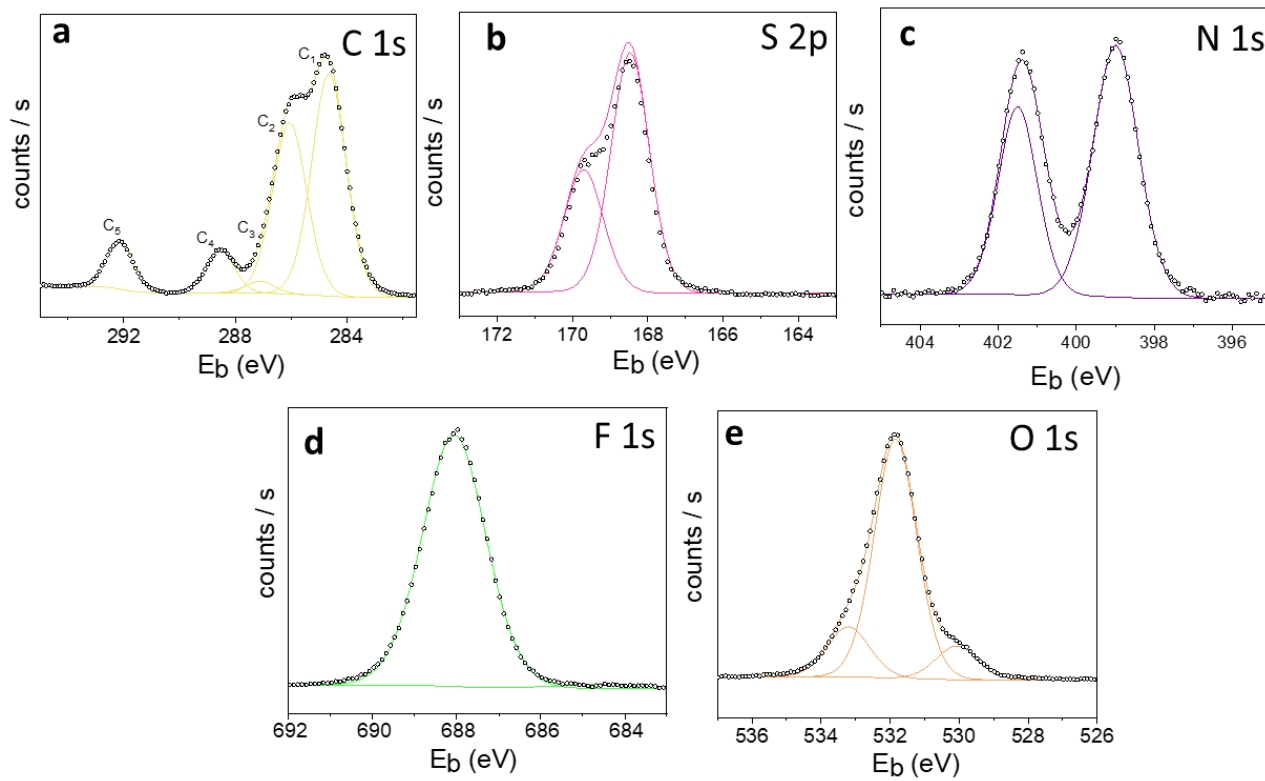


**Figure B.5** XPS high-resolution scan spectra of CN a) C 1s, b) S 2p, c) N 1s, d) F 1s, and e) O 1s.

## Appendix C

### C.1 TG analysis of Ru/FILs NPs and ILs

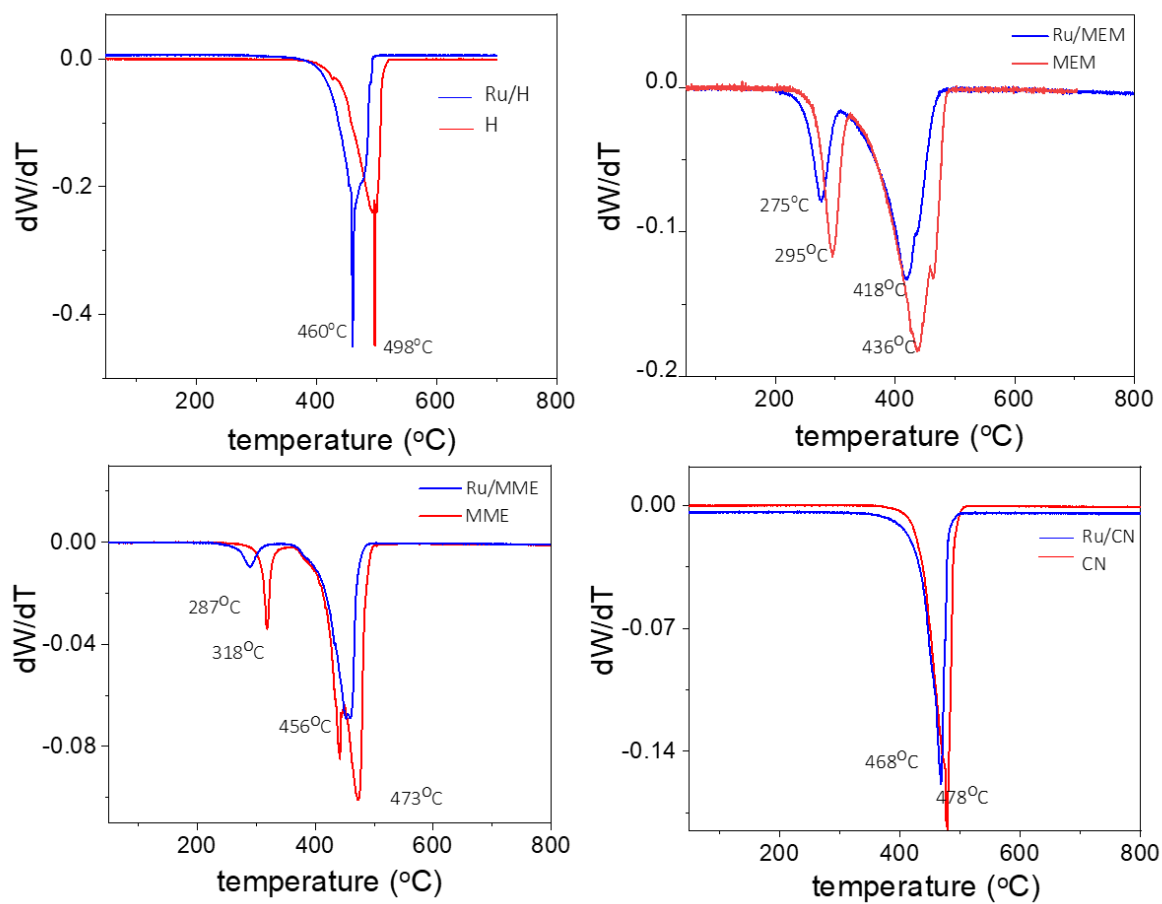
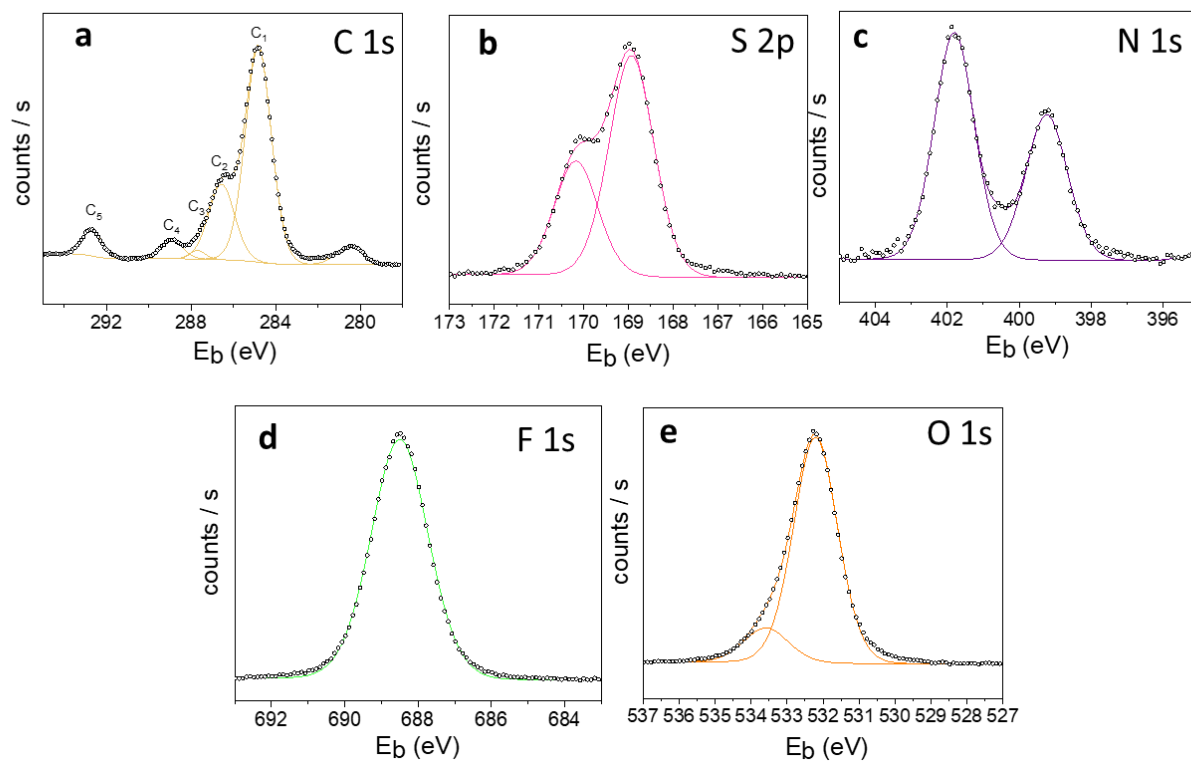


Figure C.1 TGA Analysis of Ru/FILs NPs and ILs.

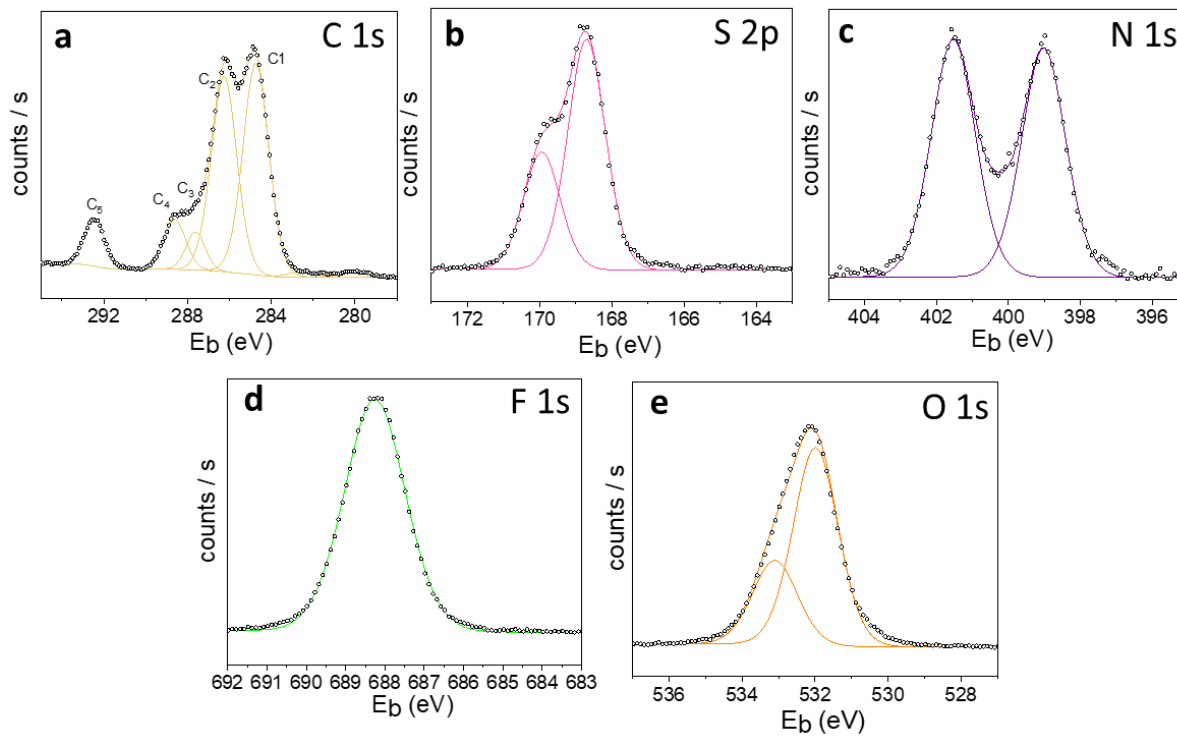
## C.2 XPS analysis

### 1. Ru/H



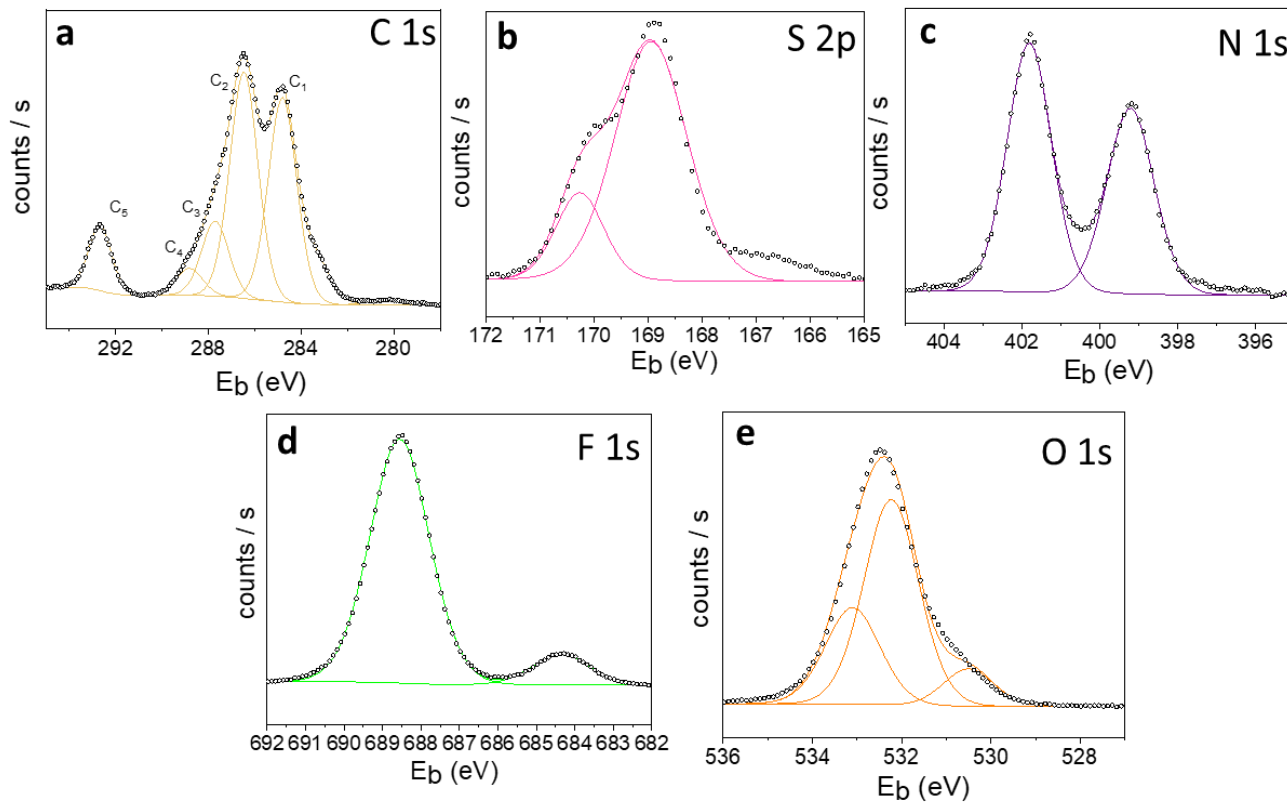
**Figure C.2** XPS high-resolution scan spectra of Ru/H a) C 1s, b) S 2p, c) N 1s, d) F 1s, and e) O 1s.

## 2. Ru/MEM



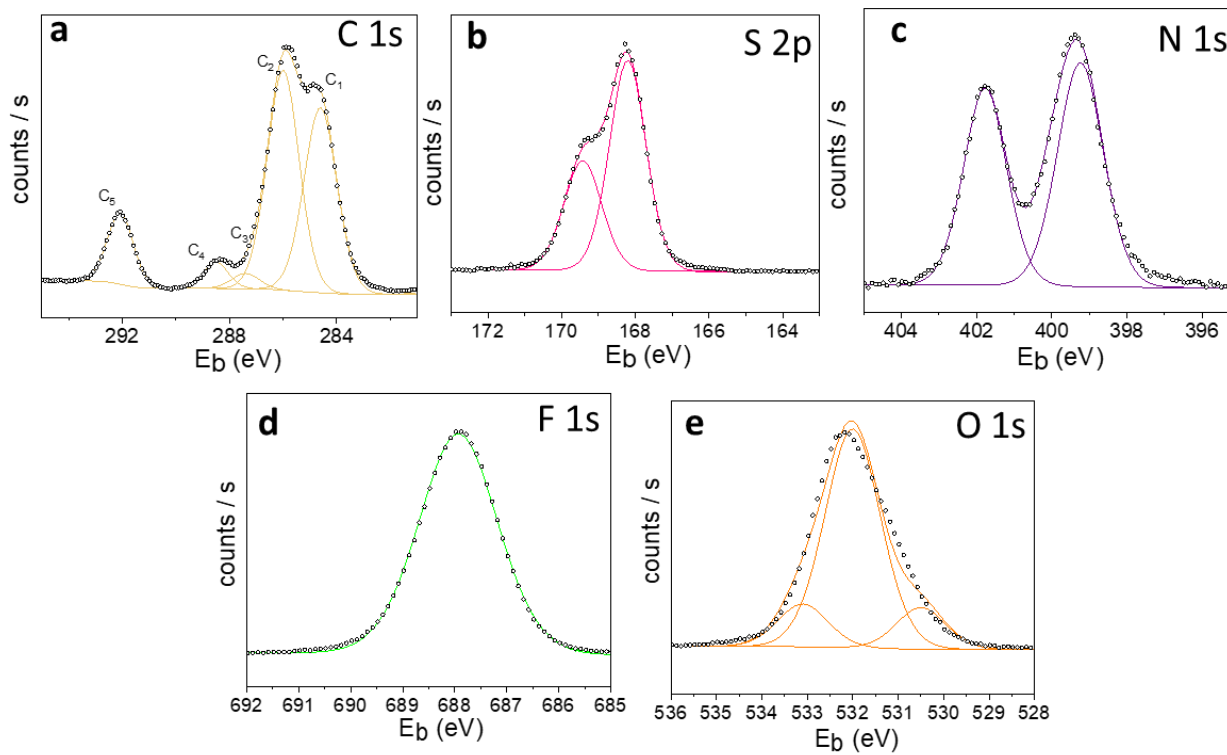
**Figure C.3** XPS high-resolution scan spectra of Ru/MEM a) C 1s, b) S 2p, c) N 1s, d) F 1s, and e) O 1s.

## 3. Ru/MME



**Figure C.4** XPS high-resolution scan spectra of Ru/MME a) C 1s, b) S 2p, c) N 1s, d) F 1s, and e) O 1s.

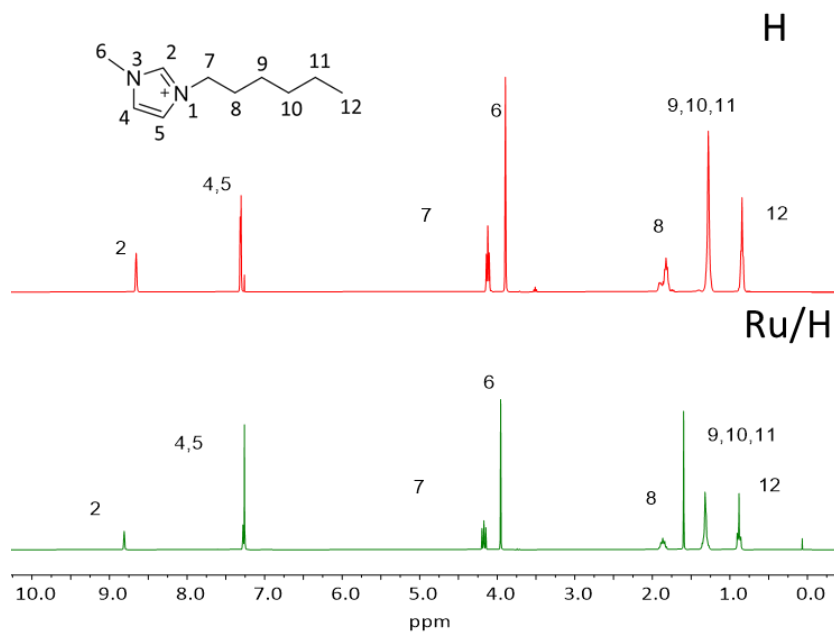
## 4. Ru/CN



**Figure C.5** XPS high-resolution scan spectra of Ru/CN a) C 1s, b) S 2p, c) N 1s, d) F 1s, and e) O 1s.

### C.3 NMR Analysis of Ru/ILs NPs

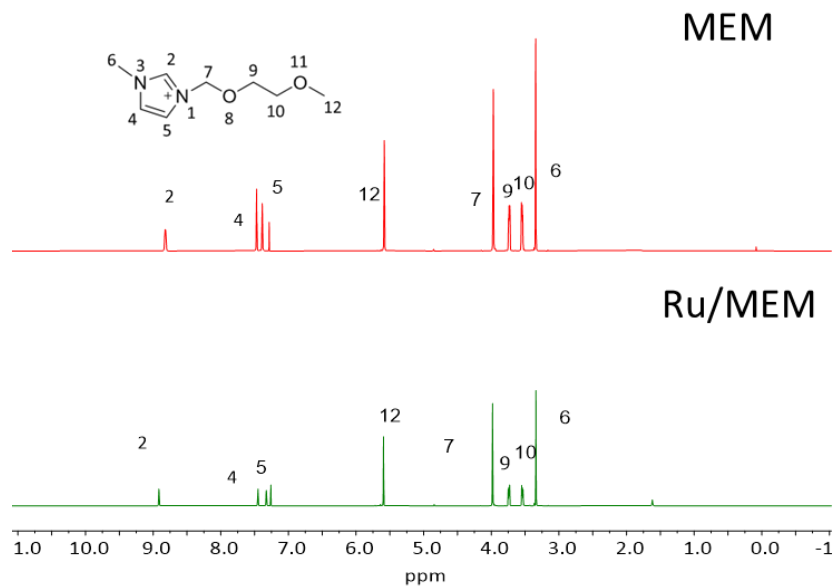
#### 1. Ru/H



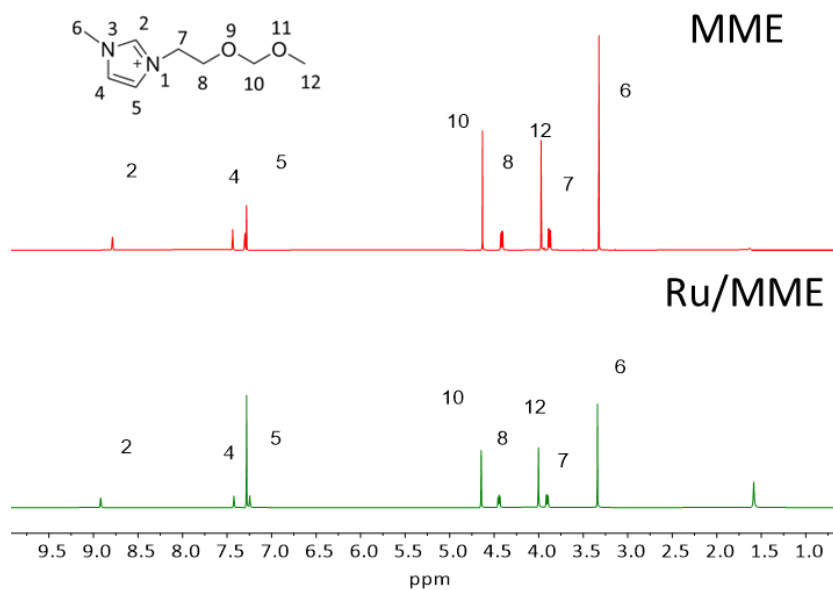
**Figure C.6** NMR spectrum of H and Ru/H in CDCl<sub>3</sub>.



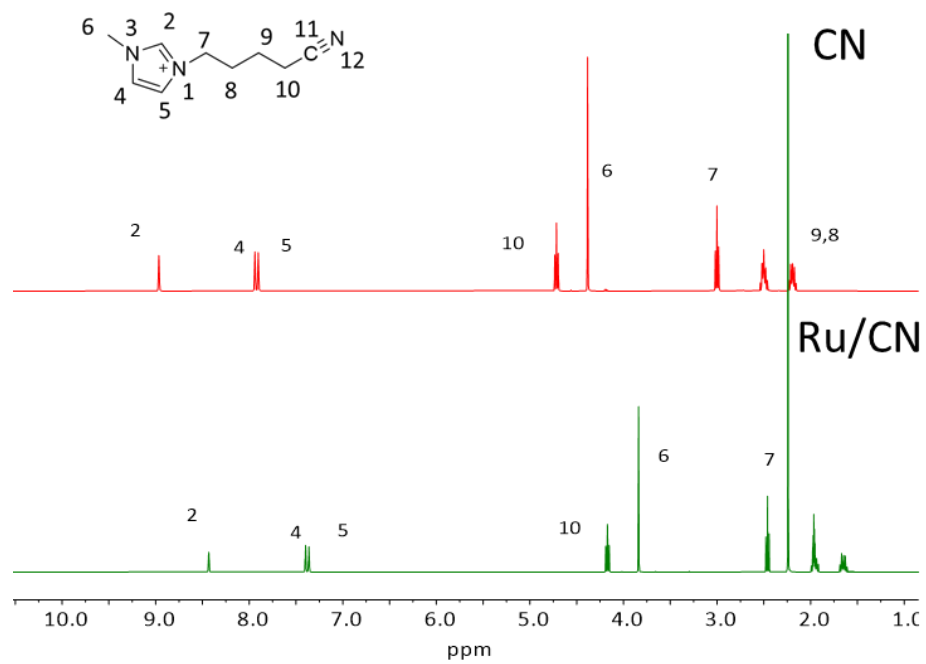
## 2. Ru/MEM

**Figure C.7** NMR spectrum of MEM and Ru/MEM in CDCl<sub>3</sub>.

## 3. Ru/MME

**Figure C.8** NMR spectrum of MME and Ru/MME in CDCl<sub>3</sub>.

## 4. Ru/CN

**Figure C.9** NMR spectrum of CN and Ru/CN in DMSO-d<sub>6</sub>.

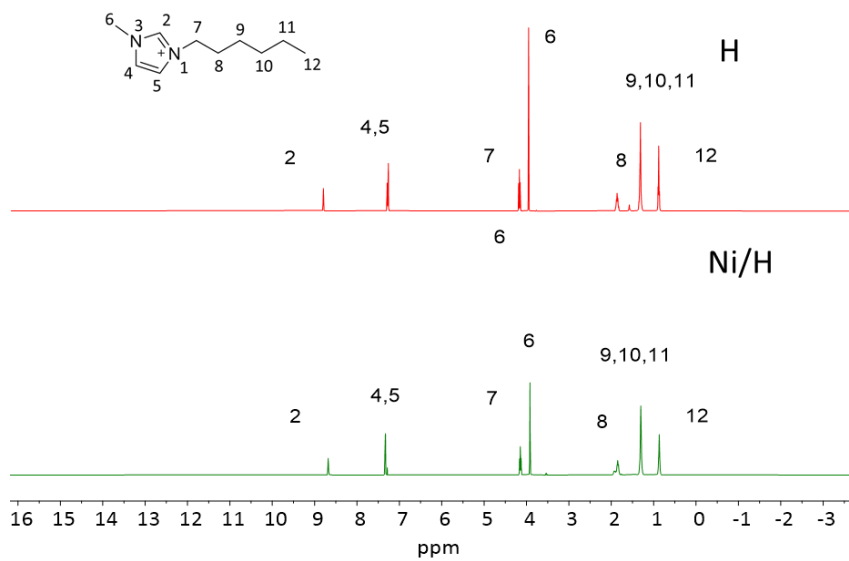
## Appendix D



**Figure D.1** Stainless steel high-pressure batch reactor.

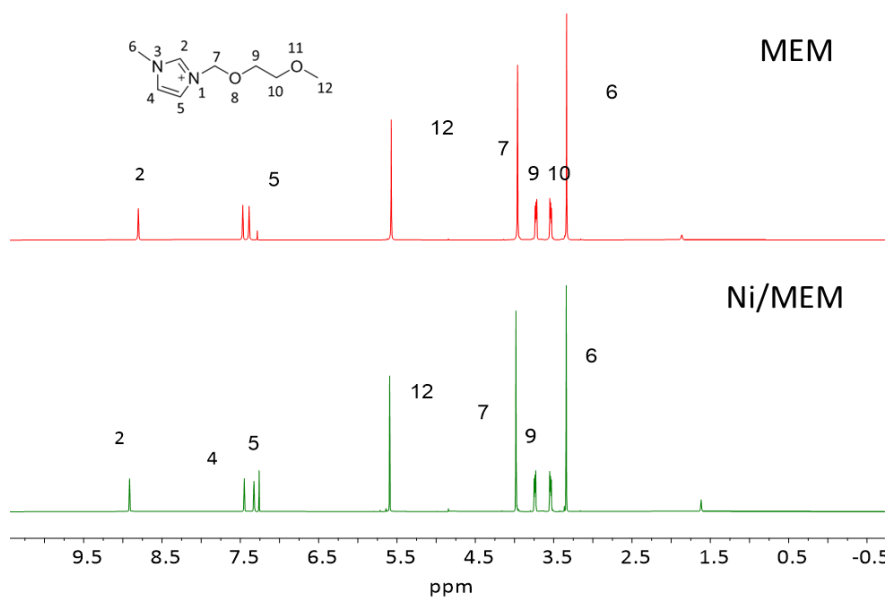
### D.1 NMR Analysis of Ni/FILs NPs

#### 1. Ni/H

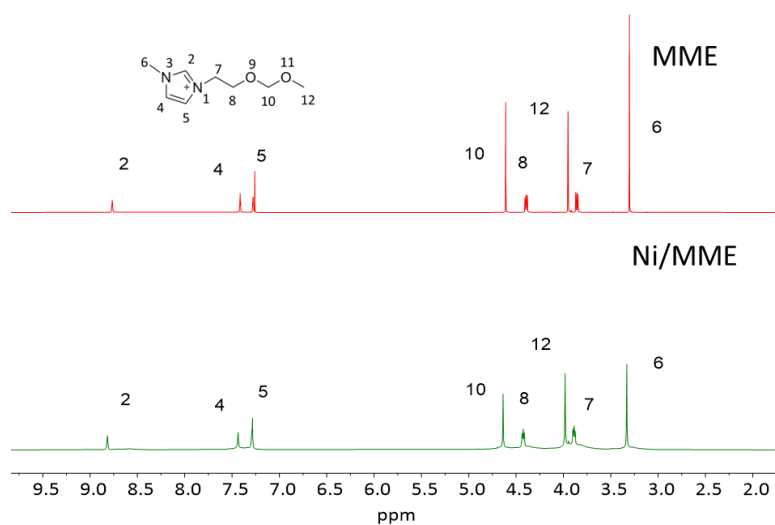


**Figure D.2** NMR spectrum of H and Ni/H in CDCl<sub>3</sub>.

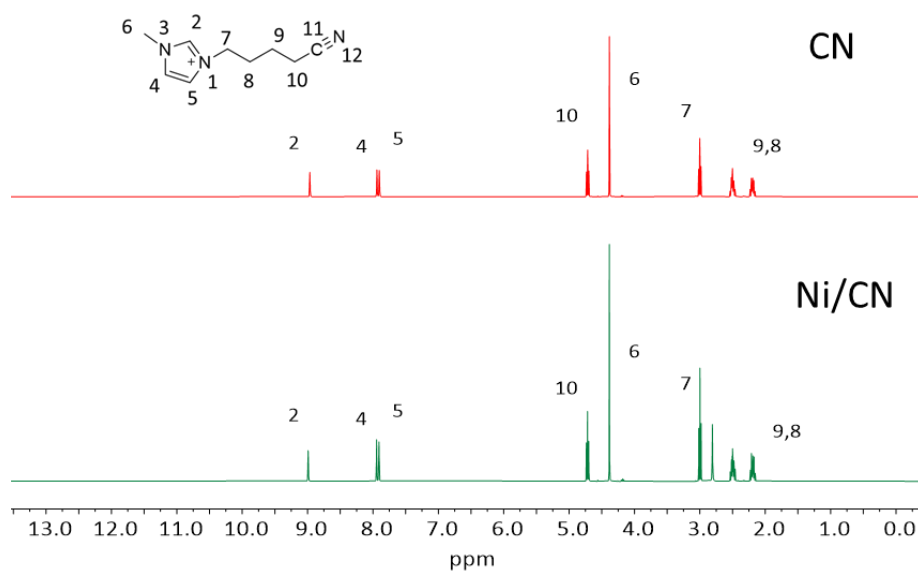
## 2. Ni/MEM

**Figure D.3** NMR spectrum of MEM and Ni/MEM in  $\text{CDCl}_3$ .

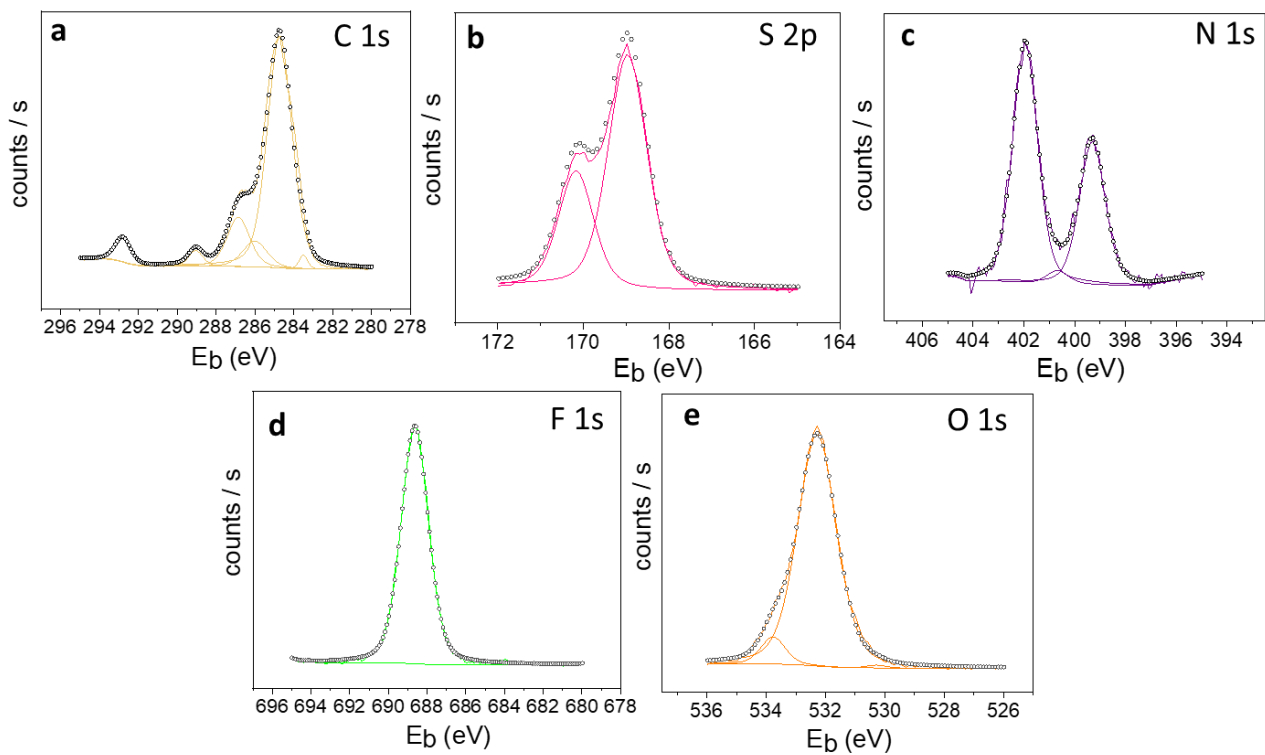
## 3. Ni/MME

**Figure D.4** NMR spectrum of MME and Ni/MME in  $\text{CDCl}_3$ .

## 4. Ni/CN



**Figure D.5** NMR spectrum of CN and Ni/CN in DMSO-d<sub>6</sub>.

**D.2 XPS analysis of Ni/FILs NPs****1. Ni/H**

**Figure D.6** High-resolution scan spectra of Ni/H a) C 1s, b) S 2p, c) N 1s, d) F 1s, and e) O 1s.

## 2. Ni/MEM

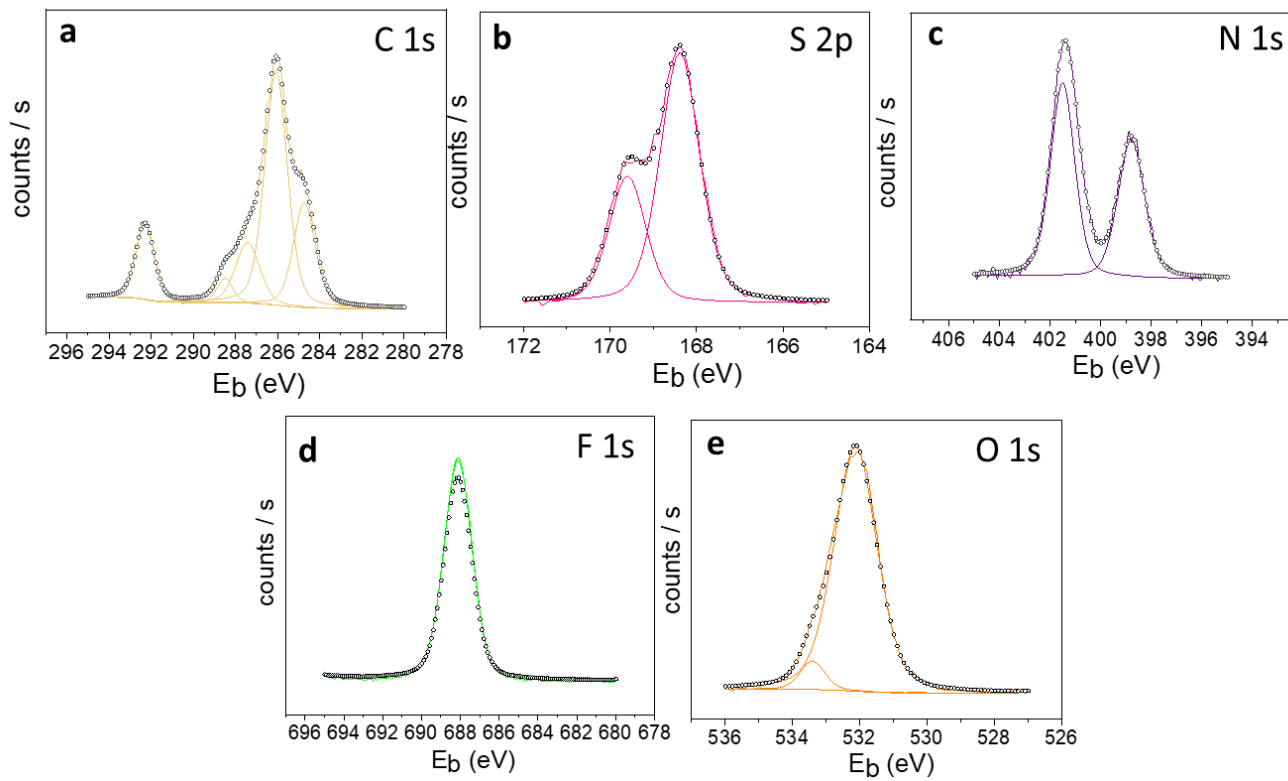


**Figure D.7** High-resolution scan spectra of Ni/MEM a) C 1s, b) S 2p, c) N 1s, d) F 1s, and e) O 1s.

## 3. Ni/MME

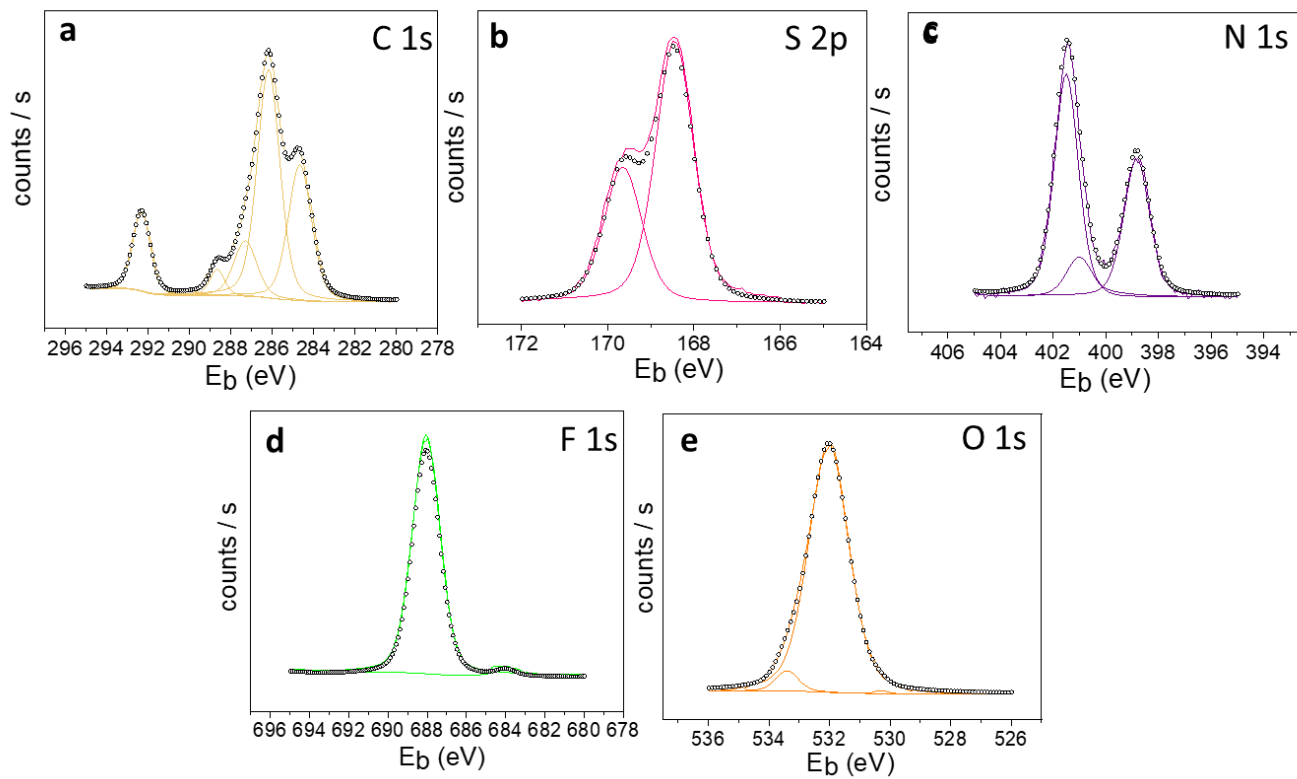


**Figure D.8** High-resolution scan spectra of Ni/MME a) C 1s, b) S 2p, c) N 1s, d) F 1s, and e) O 1s.



## 4. Ni/CN

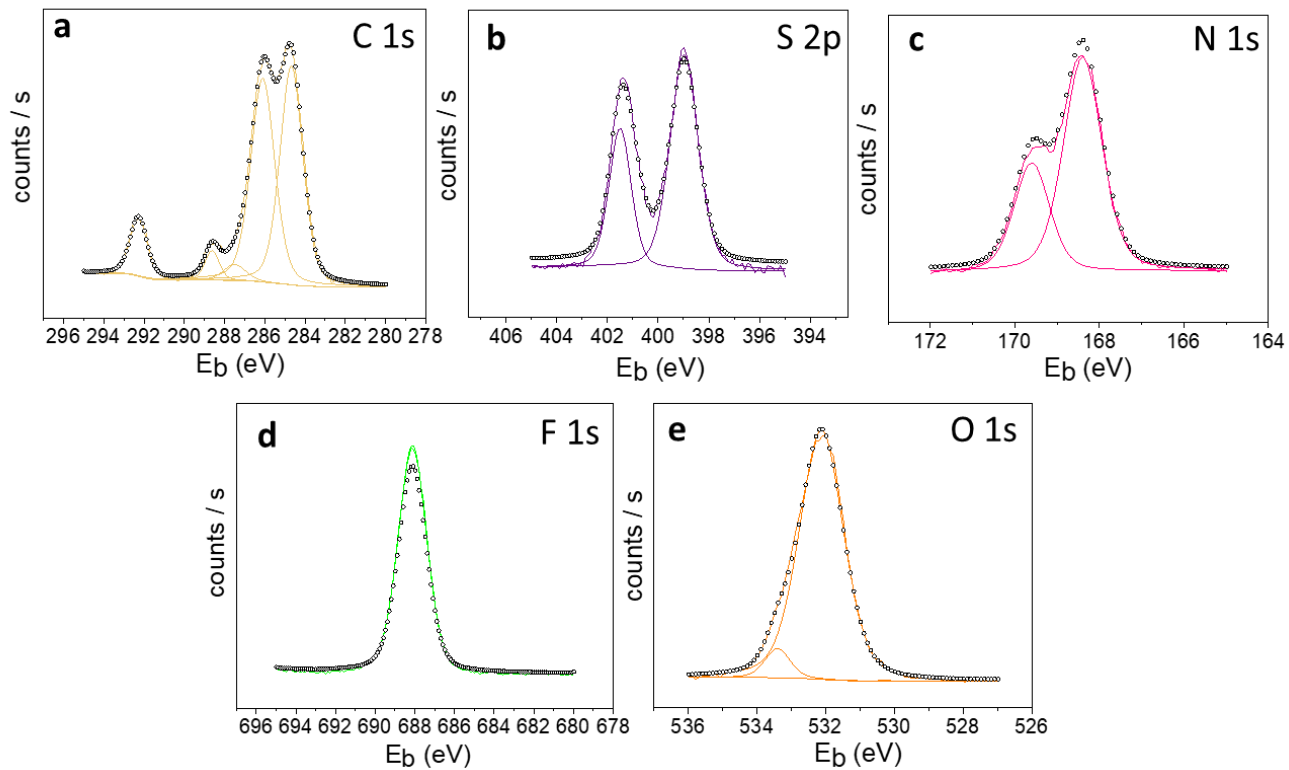


**Figure D.9** High-resolution scan spectra of Ni/MME a) C 1s, b) S 2p, c) N 1s, d) F 1s, and e) O 1s

## Appendix E

### E.1 XPS analysis of RuRe/ILs

#### 1. RuRe/H

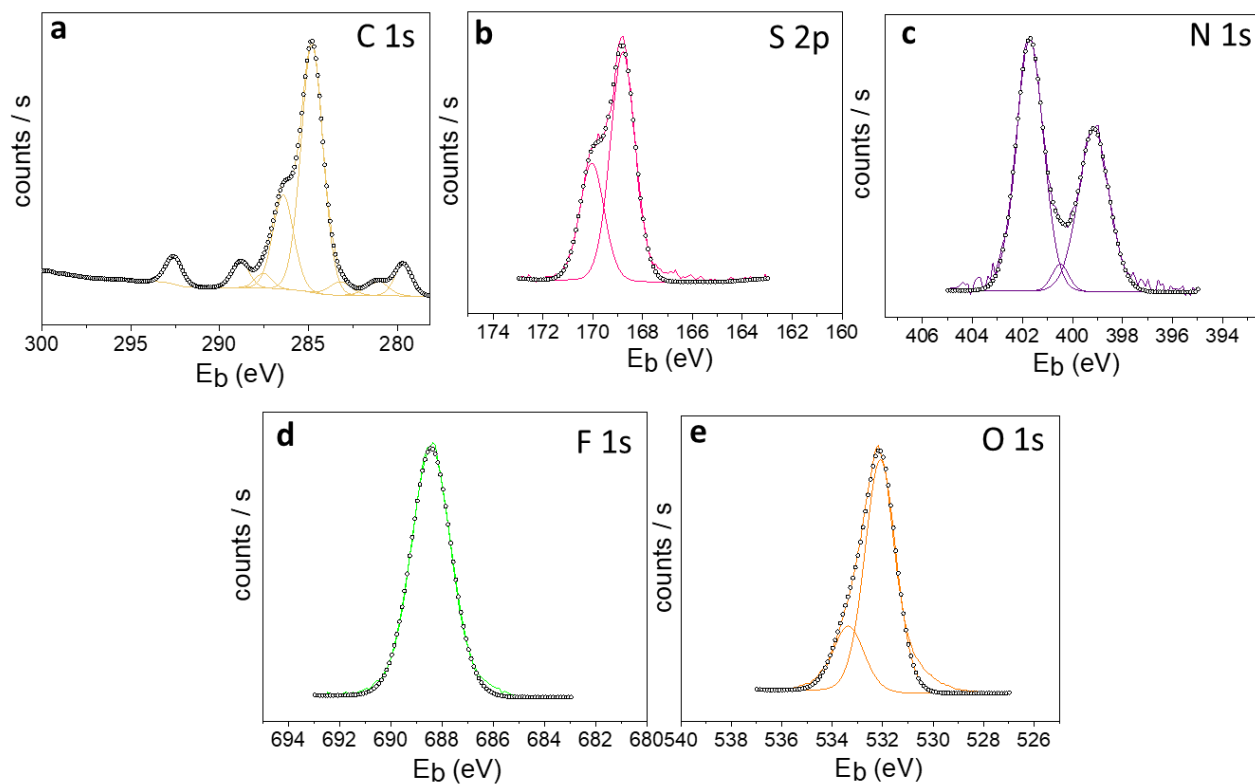


**Figure E.1** High-resolution scan spectra of Ni/H a) C 1s, b) S 2p, c) N 1s, d) F 1s, and e) O 1s.

## 2. RuRe/MEM

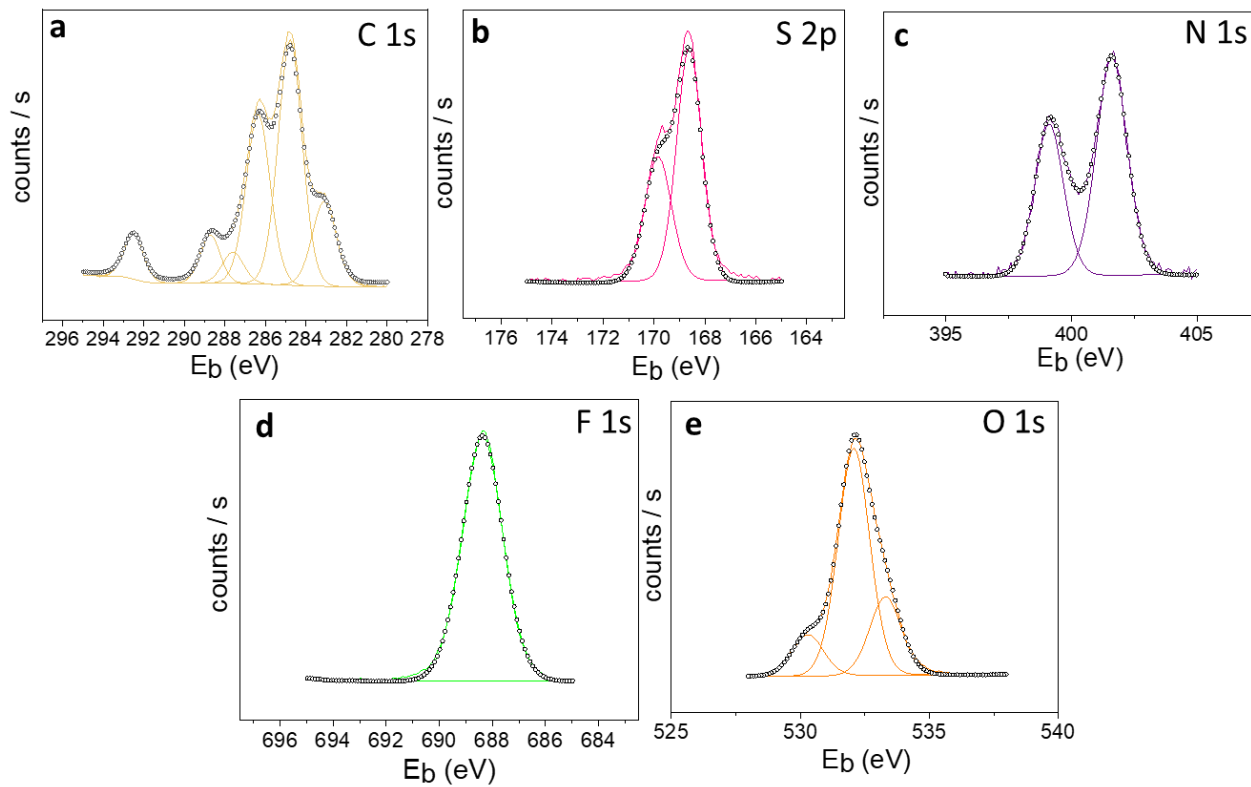


**Figure E.2** High-resolution scan spectra of Ni/H a) C 1s, b) S 2p, c) N 1s, d) F 1s, and e) O 1s.